

Monitoring of Prestressed Concrete Structures in a Nuclear Power Plant with Fibre Bragg Grating Sensors



Iain Mckeeman

Department of Electronic and Electrical Engineering
University of Strathclyde

This thesis is submitted for the degree of
Doctor of Engineering

December 2018

Declaration

This thesis is the result of the author's original research. It has been composed by the author and has not been previously submitted for examination which has led to the award of a degree.

The copyright of this thesis belongs to the author under the terms of the United Kingdom Copyright Acts as qualified by University of Strathclyde Regulation 3.50. Due acknowledgement must always be made of the use of any material contained in, or derived from, this thesis.

Iain Mckeeman

December 2018

Acknowledgements

I would like to acknowledge the help and guidance of my academic and industrial supervisors; Pawel Niewczas, Michael Johnston and Saadat Khan. I would also like to thank members of the Advanced Sensors Team in the department of Electronic and Electrical Engineering for their support throughout this project. Finally, thank you to the Nuclear Team at Vinci Technology Centre who carried out the strand stressing during the two sensor field trials.

Abstract

Monitoring the prestress level of nuclear prestressed concrete containments and prestressed concrete pressure vessels is an important maintenance activity on a nuclear site. Adequate prestress level ensures the containment or vessel is able to withstand internal pressure and contain radioactive material in the unlikely event of an accident. Prestress monitoring is currently limited to manual measurements of the total prestress force at the prestressing tendon ends. It would be beneficial to develop an online monitoring system which can measure prestress levels at several locations along a prestressing tendon. A system like this could replace existing prestress monitoring, ensure safe operation through early warning of prestress loss, and provide additional data to make informed decisions about maintenance, lifetime extension and future reactor design.

This project developed a fibre optic system capable of monitoring prestress levels. Standard 7-wire prestressing strands were instrumented with fibre Bragg grating temperature and strain sensors, while load cells measured total force at the strand ends. This provided measurement of all prestress loss effects. Sensor fabrication employed brazing to create an all-metal sensor package to reduce radiation effects in the fibre, and withstand the high stress involved in this harsh environment application. For the first time the sensors and instrumented strands were thoroughly tested in the laboratory and in two field trials representing similar conditions to the real application. Strain sensors were shown to measure strain up to $7.2 \text{ m}\epsilon$, equivalent to approximately 1300 MPa, consistently for three cycles in the laboratory. Instrumented prestressing strands were tested, during the first field trial, in two concrete beams for 170 days where sensors measured prestress levels in ambient conditions. In the second field trial several instrumented strands were stressed on a multi strain calibration rig.

The knowledge and experience gained during the project will facilitate the development of a fibre optic system capable of monitoring prestress levels in prestressed concrete containments and prestressed concrete pressure vessels.

Table of contents

List of figures	xv
List of tables	xxi
Glossary of Abbreviations	xxiii
1 Introduction	1
1.1 Research justification	3
1.2 Principal contributions	4
1.3 Thesis overview	5
1.4 Publications	6
1.4.1 Journal articles	6
1.4.2 Conference papers	6
2 Principal application: Nuclear containment buildings	7
2.1 Nuclear power generation	7
2.1.1 Nuclear fuel and reaction	7
2.1.2 Nuclear reactor classification	8
2.1.3 Reactor safety features	11
2.1.4 Ageing and decommissioning	13
2.1.5 Summary	13
2.2 Prestressed concrete	13
2.2.1 Concrete	13
2.2.2 Prestressing strands	14
2.2.3 Post-tensioned concrete	15
2.3 Prestress loss	19
2.3.1 Instantaneous prestress loss	22
2.3.2 Time dependent prestress loss	25

2.4	Current prestress monitoring	31
2.4.1	Lift-off technique	31
2.4.2	Vibrating wire strain gauges	33
2.4.3	Load cells	36
2.5	Summary	36
3	Proposal for monitoring scheme	39
3.1	Monitoring system requirements	40
3.1.1	Strain resolution	41
3.2	Strain and temperature sensors	42
3.3	Load cells	43
3.4	Structural information from sensor data	43
3.5	Summary	44
4	Fibre optic sensing of physical parameters	45
4.1	Optical fibre	45
4.1.1	Basic principle	45
4.1.2	Losses	47
4.1.3	Fabrication	49
4.1.4	Radiation induced attenuation	49
4.2	Fibre optic sensors	51
4.3	Fibre Bragg gratings	53
4.3.1	Basic principle	53
4.3.2	Fabrication	55
4.3.3	Temperature and strain dependence of the wavelength response	55
4.3.4	Radiation dependence of the wavelength response	56
4.3.5	Fibre Bragg gratings as sensors	58
4.3.6	Temperature compensation methods	58
4.4	Development in prestress monitoring with FBGs	59
4.4.1	Monitoring tendon loads with FBGs	59
4.4.2	Prestress loss from concrete strain	59
4.4.3	Fibre Reinforced Polymer instrumented strand	60
4.5	Summary	60
5	Sensor Development	63
5.1	Sensor design	63

5.1.1	Packaging	63
5.2	Brazing	65
5.2.1	Brazing alloy	65
5.2.2	Induction brazing	67
5.2.3	Capillary material	67
5.2.4	Induction heating theory	67
5.2.5	Induction heating characterisation	70
5.3	Spot welding	73
5.4	Fabrication of metal packaged FBGs	73
5.4.1	FBG inscription	73
5.4.2	FBG encapsulation	74
5.4.3	Shim attachment	74
5.4.4	Results from fabrication	75
5.5	Instrumenting a prestressing strand	78
5.5.1	Temperature sensor attachment	81
5.5.2	Strain sensor attachment	82
5.5.3	Interrogating fibre protection	82
5.6	Calibration	88
5.6.1	Temperature	88
5.6.2	Defect identification during temperature calibration	98
5.6.3	Strain	100
5.6.4	Strain transfer model	106
5.7	Sensor relaxation from vice stressing	110
5.8	Single wire tensile tests	110
5.8.1	110hr constant displacement	112
5.8.2	60hr constant displacement	114
5.9	Summary	117
6	Tensile machine tests	119
6.1	Sensor package tensile strength	119
6.2	Strain calibration	119
6.2.1	Hysteresis during tensile testing	123
6.2.2	Sensor hysteresis	125
6.2.3	Sensor strain sensitivity	127
6.3	Epoxy sensor tensile tests	129

6.4	Strain resolution and accuracy	131
6.4.1	Metal packaged sensor	131
6.4.2	Epoxy sensor	133
6.5	Summary	134
7	Field trial I: Concrete beam test	135
7.1	Beam design and sensor layout	135
7.1.1	Sensor layout	135
7.2	Sensor interrogation and data recording	139
7.3	Strand installation and stressing procedure	139
7.3.1	Strand installation	139
7.3.2	Stressing procedure	140
7.3.3	Calibration of strain sensors	140
7.3.4	Load cells	143
7.3.5	Locking off the stressed strands	144
7.4	Results from the calibration cycles and final stressing	144
7.4.1	FBG peak detection	144
7.4.2	Temperature sensors	147
7.4.3	Strain sensors	147
7.4.4	Summary of problems encountered during calibration	147
7.4.5	Possible explanations and solutions of the problems	149
7.5	Longterm results	152
7.6	Summary	161
8	Field trial II: Multi strand test	163
8.1	Aims	163
8.2	Sensor design	163
8.3	Installation of the instrumented strands	167
8.4	Stressing procedure	167
8.5	Sensor results and observations	170
8.6	Outcome of the field trials	174
8.7	Summary	175
9	Investigations into the non-ideal sensor responses	177
9.1	Non-linear wavelength response	177
9.2	Sensor hysteresis	182

9.3	Long term calibration	192
9.4	Sensor response discussion	192
9.5	Improving the sensor design	195
9.5.1	Altering the shim design	195
9.5.2	Reducing stress at sensor end	195
9.5.3	Fibre in metal tube	197
9.6	Summary	202
10	Deploying the optical system on a working nuclear site	205
10.1	Number of sensors	205
10.2	Instrument prestressing strand	206
10.3	Calibration	206
10.4	Installing strands in concrete vessel	207
10.5	Stressing the strand	208
10.6	Monitoring strand stress with the sensors	208
11	Structural information from sensor data	209
11.1	Bayesian data analysis	209
11.2	Bayesian temperature compensation	210
11.2.1	Temperature compensation model	211
11.2.2	Parameter identification	212
11.2.3	Temperature compensation results	213
11.3	Distributed force measurements	217
11.4	Sensor fusion and model fitting	220
11.4.1	Sensor fusion	221
11.4.2	Fitting the prestress loss model to experimental data	223
11.5	Summary	224
12	Conclusion and further work	225
12.1	Conclusion	225
12.2	Further work	228
12.2.1	Sensor fabrication	228
12.2.2	Different sensor design	228
12.2.3	Radiation, humidity and corrosion	229
12.2.4	Strain calibration by bending	229
12.2.5	Fibre in metal tube	229

12.2.6	Strand instrumentation procedure and final field trial	229
12.2.7	Grouted ducts	230
12.2.8	Sensor Interrogating system	230
References		231
Appendix A		243
A.1	Shrinkage strain in concrete	243
A.1.1	Autogenous shrinkage	243
A.1.2	Drying shrinkage	244
A.2	Creep strain in concrete	245
A.3	Temperature dependence of Bragg peak wavelength	246
A.4	Strain dependence of Bragg peak wavelength	246
A.5	FBG strain and temperature sensor error analysis	247
A.5.1	Strain error	247
A.5.2	Temperature error	249
A.6	Concrete beam sensor calibration cycles	249

List of figures

2.1	PWR reactor layout	10
2.2	AGR reactor layout	10
2.3	Typical PCC and PCPV dimensions	12
2.4	Post tensioned concrete	16
2.5	Post-tensioning anchor components	17
2.6	Stressing jack fitted onto a prestressing strand	18
2.7	7-strand prestressing tendons	18
2.8	Stressing a single prestressing strand	20
2.9	Strand stressing order	20
2.10	Destressing a strand	21
2.11	Strand force profile with simultaneous stressing of both ends	24
2.12	The effect of anchor slippage and friction on strand force	24
2.13	Prestress loss due to shrinkage and creep for a small concrete beam	28
2.14	The decrease in strand strain due to steel relaxation	30
2.15	Jack load against bearing plate deflection	32
2.16	Average strand lift-off force on a PCPV	33
2.17	Average strand lift-off force on a PCPV	34
2.18	Effect of the friction coefficient on strand mobilisation	35
3.1	Lift off force per strand compared to steel relaxation for a PCPV	41
3.2	Estimated strain loss due to creep and shrinkage for two PCPVs	42
4.1	Ray of light at a refractive index interface	46
4.2	Total internal reflection inside an optical fibre	47
4.3	Bragg grating in fibre	54
4.4	Reflection spectrum of an FBG with and without apodisation	54
5.1	Temperature and strain sensor components	66

5.2	Photo of induction heating rig	68
5.3	Induction heating characterisation	70
5.4	Temperature during induction heating: overview	71
5.5	Temperature during induction heating: capillary only	72
5.6	Temperature during induction heating: susceptor and capillary	72
5.7	Fibre capillary brazed joint	75
5.8	Metal packaged strain sensors	76
5.9	Brazed joint between the capillary and shim	76
5.10	FBG wavelength and reflectivity during brazing	77
5.11	FBG spectrum after sensor construction	78
5.12	Demonstration of shim strength	79
5.13	Sensors attached to prestressing strand	80
5.14	Temperature sensor attachment improvement	81
5.15	Securing a splice protector to a prestressing strand	83
5.16	Silicone tubing to protect fibre	84
5.17	Fibre protection at end of prestressing strand	85
5.18	Reinforcing the fibre at the end of the prestressing strand	86
5.19	Reinforced fibre protection at end of prestressing strand	87
5.20	Matching thermal inertia of a thermocouple and FBG	92
5.21	Temperature calibration example	93
5.22	Induction heating temperature calibration	94
5.23	Induction heating temperature calibration results	95
5.24	Room temperature fluctuation temperature calibration results	96
5.25	Error in temperature sensitivity for varying temperature range during calibration	98
5.26	Temperature error of a temperature sensor for varying temperature range during calibration	99
5.27	Temperature calibration examples	101
5.28	Temperature sensor sensitivity for multiple cycles	102
5.29	Temperature sensor defect	103
5.30	Strain calibration by strand bending	105
5.31	Sensor package on a stressed substrate	107
5.32	Substrate and capillary model strains	108
5.33	Capillary and fibre model strains	109
5.34	Strain sensor wavelength relaxation	111

5.35	Temperature and strain measurements during a 110 hr constant displacement tensile test	113
5.36	Temperature and strain measurements during a 66 hr constant displacement tensile test	115
5.37	Strain measured by a displacement gauge during a 66 hr constant displacement tensile test	116
6.1	Sensor package stressed on tensile machine	120
6.2	Steel specimen mounted on a tensile machine	121
6.3	Example of a tensile machine calibration test	122
6.4	Strain sensors calibrated up to $3.3 \text{ m}\epsilon$	124
6.5	Load cell force against sensor wavelength during $3.3 \text{ m}\epsilon$ calibration	126
6.6	A strain sensor calibrated up to $7.2 \text{ m}\epsilon$	127
6.7	A metal packaged sensor calibrated with a tensile machine	128
6.8	Epoxied FBG calibrated with a tensile machine	130
6.9	Epoxied FBG calibrated with a tensile machine	131
7.1	CAD diagram of bent duct beam	136
7.2	Prediction of prestress loss due to friction in a double harp tendon duct	137
7.3	Sensor layout on a prestressing strand	138
7.4	Copper strand end protection	141
7.5	Reinforced strand end protection	142
7.6	Stressing the instrumented strands	143
7.7	Anchor slippage	145
7.8	Erroneous peak detection	146
7.9	Strain and temperature sensor wavelengths during stressing	148
7.10	Permissible strand strain for different strain transfers	150
7.11	Thermocouple and FBG sensor temperature for the first week	153
7.12	Temperature measured by the thermocouple and wavelength of an FBG temperature sensor	154
7.13	Total strand force measured by a load cell	155
7.14	Strain sensor wavelength decrease	156
7.15	Example of strain sensor wavelength compared to load cell force	157
7.16	Example of strain sensor wavelength compared to load cell force	158
7.17	Example of strain sensor wavelength compared to load cell force	159
7.18	Prestress force loss measured by a strain sensor	160

8.1	28-strand calibration rig	164
8.2	Improved sensor design	165
8.3	Three sensors attached to a prestressing strand	166
8.4	Installing the instrumented strands into the calibration rig	168
8.5	Load cell force during stress cycle 4	169
8.6	Typical sensor responses during stressing	171
8.7	Strain response of the two epoxy sensors	172
8.8	Bare fibre exposed after strand stressing	175
9.1	The sensor and interrogating fibre before and after three stress cycles	178
9.2	Sensor response when the interrogating fibre is fixed to the specimen	179
9.3	Force profile for second non-linear sensor response experiment	180
9.4	Sensor wavelength for second non-linear sensor response experiment	181
9.5	Rupture in fibre copper coating due to it being pulled out of the capillary	182
9.6	Epoxy sensor wavelength during 200 cycles at 5 kN	184
9.7	Normalised hysteresis area for an epoxy sensor for two separate 100-cycle tests to 5 kN	185
9.8	Epoxy sensor wavelength during 200 cycles at 5 kN	186
9.9	Metal packaged sensor wavelength during 200 cycles at 5 kN	187
9.10	First stress cycle of test 1 and last stress cycle of test 2	188
9.11	Normalised hysteresis area for a metal sensor for two separate 100-cycle tests to 5 kN	188
9.12	Load cell force and machine displacement for different forces	189
9.13	Epoxy sensor hysteresis loops for different forces.	190
9.14	Metal packaged sensor hysteresis loops for different forces	190
9.15	Normalised hysteresis area for cycles of 1, 2.5, 5, 7.5 kN	191
9.16	Long term calibration evolution at 3 m ϵ	193
9.17	Metal packaged sensor hysteresis loops during 100 cycles at 9 kN	194
9.18	Sensor with old shim design calibrated up to 7.2 m ϵ	196
9.19	Revised shim design	196
9.20	Sensor with new shim design calibrated up to 7.2 m ϵ	197
9.21	Sensor with strengthened ends stress until failure	198
9.22	Stressed and un-stressed fibre in a metal tube	199
9.23	Fibre manually fed into metal tube	200
9.24	Testing the fibre in metal tube up to 3.2 m ϵ	201

9.25	Testing the fibre in metal tube up to $6.7 \text{ m}\epsilon$	202
11.1	Parameters λ and α calculated from data windows of one day	214
11.2	Parameters λ and α calculated from data windows of two days	215
11.3	Standard deviation for λ_0 measurements from temperature compensation . . .	216
11.4	Distributed strand force profile with 20 measurements	218
11.5	Distributed strand force profile with 10 measurements	219
11.6	Prestress loss comparison with model	220
11.7	Load cell force measurements combined with FBG strain sensor measurements	222
11.8	Concrete model fitted to the combined prestress loss measurements.	224
A.1	Strand 1 (bent duct) calibration graphs	250
A.2	Strand 2 (bent duct) calibration graphs	251
A.3	Strand 3 (straight duct) calibration graphs	252
A.4	Strand 4 (straight duct) calibration graphs	253

List of tables

2.1	List of active nuclear power stations owned by EDF in the UK	9
2.2	Typical properties of 7-wire prestressing strand from BS 5896:1980	15
5.1	Ferromagnetic material properties	69
5.2	Mechanical properties of model materials.	106
6.1	Strain sensitivity of several sensors	129
8.1	Least squares fit for one metal packaged and two epoxied FBG strain sensors	173

Glossary of abbreviations

ACI	American Concrete Institute
AGR	Advanced gas-cooled reactor
DIN	Deutsches institut für Normung
EDF	Électricité de France
EM	Electromagnetic radiation
EN 1992	Eurocode 2
FBG	Fibre Bragg grating
FEM	Finite element method
Fib	Fédération internationale du béton
FPI	Fabry-Perot interferometer
FRP	Fibre reinforced polymer
FWHM	Full-width half maximum
GL	Gardner and Lockman
ITS	International temperature scale
MLE	Maximum likelihood estimate
NA	Numerical aperture
NIST	National Institute of Standards and Technology
NPL	National Physical Laboratory
ONR	Office for Nuclear Regulation
PCC	Prestressed concrete containment
PCPV	Prestressed concrete pressure vessel
PWR	Pressurised water reactor
RIA	Radiation induced attenuation
RTD	Resistance temperature detector
SHM	Structural health monitoring
SMF	Single mode fibre
TIR	Total internal reflection

UK	United Kingdom
UTS	Ultimate tensile strength
UV	Ultraviolet
VWSG	Vibrating wire strain gauge

Chapter 1

Introduction

Nuclear power accounts for about 20 % of the UK's electricity supply [1]. The sources of electricity generation are currently undergoing a transition from fossil-fuel based to renewable energy such as wind and solar. During this time and in the future, nuclear power can provide a stable guaranteed base-load with relatively low greenhouse gas output compared to fossil fuels [2]. Within the UK, the nuclear industry is also undergoing a transition; many of the currently operating nuclear reactors are nearing the end of their original operating lifetime and construction of future planned reactors has not yet started, with the exception of Hinckley Point C [1]. Lifetimes may be extended provided the reactors are deemed safe by the Office for Nuclear Regulation, ONR, and indeed many of the currently operating reactors have already had their lifetimes extended.

Electricity generation by nuclear fission, during normal operation and in the event of a fault, poses a potential risk to society and the environment, therefore, there are a number of different active and passive safety systems in place to mitigate these risks. Passive systems are particularly important as they do not require human input or electricity to function. One such system, in the case of the reactors in the UK, is either the prestressed concrete containment, PCC, for pressurised water reactors, PWRs, or the prestressed concrete pressure vessel, PCPV, for advanced gas reactors, AGRs. Both the PCC and PCPV protect the outside environment from radiation and contain contaminated material in extreme events, such as a complete reactor meltdown. The PCPV is also important during normal reactor operation, it acts as the pressure containment vessel which houses the reactor, high pressure gas and the boilers. Whereas, the PCC is a low pressure structure during normal operating conditions that envelopes components such as the steel-lined reactor pressure vessel. The PCC acts as a second line of defence.

Prestressed concrete comprises of reinforced concrete and tensioned high strength steel tendons that run through ducts in the concrete. These compress the structure to compensate

for concrete's lack of tensile strength and give the PCC and PCPV their ability to withstand high internal pressure. Over time, the prestress levels of the tendons reduce so this must be monitored. In the UK, the ducts are left ungrouted so force measurements are possible on all tendons. Prestress monitoring activity is currently carried out manually, where approximately 1 % of the tendons are routinely inspected to ensure that prestress levels in the structure do not fall below the minimum design load. Prestress measurements are limited to total force measurement at the tendon end. Globally, it is more common to fill ducts with grouting to permanently fix the tendons in place. Prestress monitoring is then restricted to a number of ungrouted inspection tendons.

An online monitoring system that could continuously monitor prestress levels along the length of the tendons would be beneficial in both grouted and ungrouted tendons due to more frequent, thorough inspection at reduced cost. Such a system could replace existing prestress monitoring, ensure safe operation and provide additional data to make informed decisions about maintenance, lifetime extension and future reactor design.

The harsh environment of this application involves high stress, up to 1300 MPa, and moderate radiation and temperature during normal conditions. Water ingress may occur due to leakages in the cooling pipes and mix with carbon dioxide. Sensors must be resilient to these conditions as they will be inaccessible upon installation. Many electric sensors are unsuitable, but fibre optic sensors have attributes that lend themselves to harsh environment applications [3]. These include: excellent multiplexing potential, immunity to electromagnetic interference, safe mode of operation and radiation resistance [4]. The small 1-D shape and one-directional interrogation of fibre optic sensors is also an advantage for this application.

This project developed a fibre Bragg grating strain and temperature system capable of monitoring strain of prestressing strands in ambient conditions at different locations along a prestressing strand. An all-metal fabrication technique using brazing was used to fabricate the sensors. For the first time the sensors and instrumented strands were thoroughly tested both in the lab and in two field trials representing conditions similar to the real application. The tests were to determine whether the sensors were able to reliably measure strains of up to $7 \text{ m}\epsilon$ as required by the application and to demonstrate that such a sensing system could be retrofitted to standard 7-wire prestressing strands with the aim of replacing the unbonded strands in the UK's nuclear prestressed concrete structures.

1.1 Research justification

Prestress levels in a PCC or PCPV are currently measured manually every 1.5-5 years. Prestress loss occurs rapidly during the first few years but reduces greatly in later years. However, prestress measurements are important throughout the entire operational life because prestress loads may reach the minimum design load near the end of a reactor's life. Current prestress measurements are carried out by the 'lift-off' technique. As we will see in Chapter 2, several assumptions must be made to determine the average tendon stress from lift off measurements. Furthermore, the distribution of stress along a tendon is not uniform. This results in two motivations to develop an additional monitoring system:

- A new monitoring system could provide continuous and tendon-distributed prestress measurements allowing early indication of prestress loss development or strand failure.
- A new monitoring system could provide a more accurate representation of the prestress on the PCC or PCPV through distributed measurements.

There are numerous challenges associated with developing a monitoring system for this application as the radiation, mechanical and chemical stresses placed on the sensors require careful consideration. Conventional electric strain gages are not suitable, due to factors such as power requirements, number of interrogating leads and electromagnetic interference. Optical fibre sensors and fibre Bragg grating (FBG) sensors in particular meet the requirements necessary for monitoring prestress levels. However, the FBGs must be properly packaged to ensure that they can withstand stresses of 1300 MPa and neutron and gamma radiation in a warm moist environment. In this work, an all metal sensor construction was adopted to fabricate sensors capable of withstanding these conditions. The work in this thesis concentrates on retrofitting existing containment buildings, but the technology can be readily applied during construction of new build reactors. In the case where tendons are secured with grout the monitoring system may be especially useful as prestress load cannot be obtained from lift-off measurements. This project has provided the basis for prestressing strands, instrumented with fibre optic sensors, to be installed in operational PCCs and PCPVs to monitor prestress levels. In a wider context, the technology is applicable to other prestressed structures such as dams, bridges and oil tanks.

1.2 Principal contributions

- Optimisation of the induction brazing encapsulation technique for fabricating fibre Bragg grating strain sensors specifically designed to monitor strain of 7-wire 18 mm-diameter prestressing strands.
- Experimental investigation of FBG wavelength and reflectivity during sensor fabrication.
- Iterative sensor package improvements based on field trials replicating similar conditions to the proposed application.
- Direct comparison of FBG metal and epoxy packaging methods for measuring strain up to 7.2 mε. Metal packaged strain sensors were tested alongside epoxied FBGs in calibration cycles and sensor wavelength repeatability tests.
- Identification of limitations of metal packaging for high strain applications.
- A fabrication defect screening procedure for metal packaged sensors during temperature calibration. Calibrating multiple sensors in an environmental chamber can identify the principal defect of these sensors.
- Practical in-situ calibration procedure for temperature calibrating strain sensors attached to prestressing strands.
- Development and demonstration of optical fibre protection for the fibre interrogating sensors attached to 7-wire prestressing strands. This protection allowed fibre to survive exiting strand ducts through the wedge jaws.
- Fabrication of 4 4-metre and 2 1.6-metre instrumented prestressing strands.
- Practical demonstration of inserting instrumented prestressing strands into strand ducts and using instrumented strands to prestress concrete.
- Practical demonstration of stressing instrumented prestressing strands up to 1000 MPa with standard single-strand prestressing jacks used in on-site prestressing activities.
- Interrogation of sensors, attached to prestressing strands, where interrogating fibre is wound round strand located inside a single strand stress-jack during stressing.
- Characterisation of metal packaged strain and temperature sensors measuring the strain and temperature of a stressed prestressing strand inside a concrete beam in ambient

conditions for 170 days. The sensors measured a reduction in strain comparable to load cell force decrease.

- Practical demonstration of instrumented strands use on a hydraulic stress jack calibration rig with a 28-strand prestressing jack. Strands were stressed to approximately 1300 MPa with the sensor interrogating fibre wound around the strand inside the stress jack. Sensors were shown to survive stresses of 1300 MPa.
- Proposal for deploying the prestress monitoring fibre optic system on a nuclear site based on the experience gained during two field trials.
- Algorithmic temperature characterisation procedure for calibrating sensors with unknown temperature sensitivities based on Bayesian principles.
- Updating concrete model with experimental strain and temperature data using Bayesian principles.

1.3 Thesis overview

Chapter 2 provides background information about nuclear reactors and their safety features. The PCC and PCPV are then described in detail; they comprise of two main components: reinforced concrete and prestressing steel. Section 2.3 demonstrates that over time the prestress levels in the structure reduce. The prestress loss is monitored with several techniques described in Section 2.4. In Chapter 3, the reasons for needing a new prestress monitoring system are laid out. The requirements for such a system are also described along with reasons why optical fibre sensors are an excellent candidate. The theory behind light transmission by optical fibres and how these can be turned into sensors is detailed in Chapter 4. Fibre Bragg gratings, the chosen sensor technology are described, with examples of the use of Bragg gratings in a prestressed concrete and nuclear context. Chapter 5 concentrates on sensor development, this includes: sensor fabrication, calibration and attachment to prestressing strands. Chapter 6 demonstrates that the sensor package is of adequate strength and that the sensors can be calibrated on a tensile machine when attached to high strength steel specimens. The sensors were tested in two field trials which are documented in Chapter 7 and 8. During the field trials, the sensors demonstrated some unexpected behaviour; therefore the sensors were thoroughly tested on a tensile machine. These tests are described and results shown in Chapter 9. A detailed plan for deploying the optical system on working nuclear reactor containment is discussed in Chapter 10. Chapter 11 describes three data analysis algorithms based on Bayesian inference for obtaining

useful structural information from the sensors. Finally, Chapter 12 concludes the research carried out in this project and lists any outstanding work that needs to be completed before the system can be successfully deployed.

1.4 Publications

1.4.1 Journal articles

1. Perry, M.; McAlorum, J.; Fusiek, G.; Niewczas, P.; McKeeman, I. & Rubert, T. 2017, 'Crack Monitoring of Operational Wind Turbine Foundations'. *Sensors* , 17, 1925.
2. Mckeeman, I, Fusiek, G, Perry, M, Johnston, M, Saafi, M, Niewczas, P, Walsh, M & Khan, S, 2016, 'First-time demonstration of measuring concrete prestress levels with metal packaged fibre optic sensors' *Smart Materials and Structures*, vol 25, no. 9, 095051.

1.4.2 Conference papers

1. Mckeeman, I, Niewczas, P & Khan, S, 2017, 'A comparison of brazed metal and epoxied fibre Bragg grating strain sensors under high strain regimes'. in *25th International Conference on Optical Fiber Sensors*. vol. 10323, 103233E, Bellingham, WA.
2. Mckeeman, I, Niewczas, P & Johnston, M 2015, 'Identifying fabrication defects of metal packaged fibre Bragg grating sensors for smart pre-stressing strands'. in *2015 IEEE Workshop on Environmental, Energy, and Structural Monitoring Systems, EESMS 2015 - Proceedings*.
3. McKeeman, I, Fusiek, G, Perry, M, Niewczas, P & Johnston, M 2015, 'In-situ temperature calibration procedure for temperature and strain fibre Bragg grating sensors for monitoring pre-stressing strands'. in *24th International Conference on Optical Fibre Sensors* vol. 9634, 96345I , Curitiba, Brazil.

Chapter 2

Principal application: Nuclear containment buildings

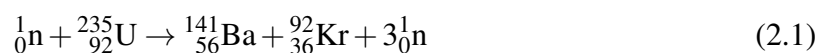
2.1 Nuclear power generation

Electricity is generated in a nuclear power station from energy released by nuclear fission. This consists of splitting a suitable element, typically using thermal neutrons, into nuclei with a lower atomic number. A large amount of energy and other particles are released during the reaction. The energy heats up the surroundings and can be used to turn water into steam to drive a turbine. The following sections concentrate on the reactor technology currently used in the UK, but there are numerous other types.

2.1.1 Nuclear fuel and reaction

Current reactors typically use enriched uranium as fuel. The most common uranium isotope is uranium-238, accounting for over 99 % of the earth's supply; however this is not fissile so raw mined uranium must be processed to enrich the uranium-235 content. This is carried out by mass separating the two isotopes using a variety of techniques; most commercial enrichment plants use the centrifuge process [5].

The fission chain reaction is initiated as follows:



A neutron source is used to start the nuclear fission reaction in the reactor core. More neutrons are produced as uranium is split into barium causing a chain reaction which will runaway if it

is not controlled. Neutron moderators (absorbers) within the core regulate the chain reaction by adjusting neutron absorption with a feedback system. The environment within the reactor is extremely harmful to humans and so it is housed within a biological shield, often comprising of a steel lining and prestressed concrete.

2.1.2 Nuclear reactor classification

Reactors can be classified into the generation within which they were designed and constructed. As the technology has developed, each reactor generation has made improvements in efficiency and safety. Reactor generations currently run from generation I - IV. Most reactors currently in operation are generation II. Generation III reactors show evolutionary improvements over generation II reactors and have become operational in the last decade or so. Generation IV reactors are still in the research and design phase and are not expected to be ready for construction until 2020-30 [6].

Another reactor classification scheme is by the type of coolant used to transfer heat away from the reactor core. Reactor coolants are critical for both stabilising the temperature of the reactor and transferring energy to turn the turbines. The output power of a reactor during safe operation is dependent on the ability of the coolant to quickly remove heat from the core. Coolants are therefore often held at high pressure to improve heat transfer. The most common coolants are described below.

Water cooled

Pressurised water reactors (PWRs) circulate superheated water at 320 °C and 15 MPa between a boiler and the reactor core, as shown in Figure 2.1. They account for roughly 50 % of all generation II reactors worldwide. The water is directly heated in the reactor and also acts as a neutron moderator. A steel shielding surrounds the PWR to contain the highly pressurised water. The reactor, boiler and cooling systems are housed in a prestressed concrete containment (PCC) that provides a biological shield should an event occur. The PCC is a second line of defence as it only serves a function, shielding, during a fault.

Gas cooled

In the UK, gas cooled reactors are more common. Modern generation II advanced gas-cooled reactors (AGRs) use CO₂ as a coolant while a graphite core and control rods act as neutron moderators, Figure 2.2. The carbon dioxide is heated by the nuclear reaction and transfers heat to water in the boilers. A prestressed concrete containment vessel (PCPV) surrounds the reactor

Table 2.1 List of the eight active nuclear power stations owned by EDF Energy in the UK . Between them, these nuclear power stations are able to generate about 21 % of the electricity in the UK [1]

Station Name	Type	Net Output (MW)	No. of reactors	Generation Start	Est. date decommissioning	Operating time (yrs)
Dungeness B	AGR	1040	2	1983	2028	45
Hartlepool	AGR	1180	2	1983	2024	41
Heysham 1	AGR	1155	2	1983	2024	41
Heysham 2	AGR	1220	2	1988	2030	42
Hinkley Point B	AGR	945	2	1976	2023	47
Hunterston B	AGR	960	2	1976	2023	47
Sizewell B	PWR	1198	1	1995	2035	40
Torness	AGR	1185	2	1988	2030	42

and houses the CO₂. Heated water exits the PCPV via pipes in the containment wall. The PCPV acts as both the the pressure containment vessel, during operation, and as a biological shield. In terms of the pressure vessel AGRs are generally safer than PWRs because a PWR's steel liner fails rapidly whereas this is prevented in an AGR by the prestressed concrete.

Liquid metal

Fast breeding reactors typical of designs from Generation III and IV can use non-enriched uranium as fuel. Fast neutrons are needed for this type of chain reaction, but as fast neutrons are not sustained in the presence of neutron moderators, conventional thermal reactors cannot be used. Liquid metal reactors use a liquid metal such as sodium as a highly conductive coolant. Energy is released as uranium-238 transmutes into plutonium-239 after absorbing a fast neutron [8]. The benefit of this is that the plutonium can be used later on as fuel, reducing radioactive waste. However, fast neutrons are hard to shield against and handling molten liquid metal can be problematic.

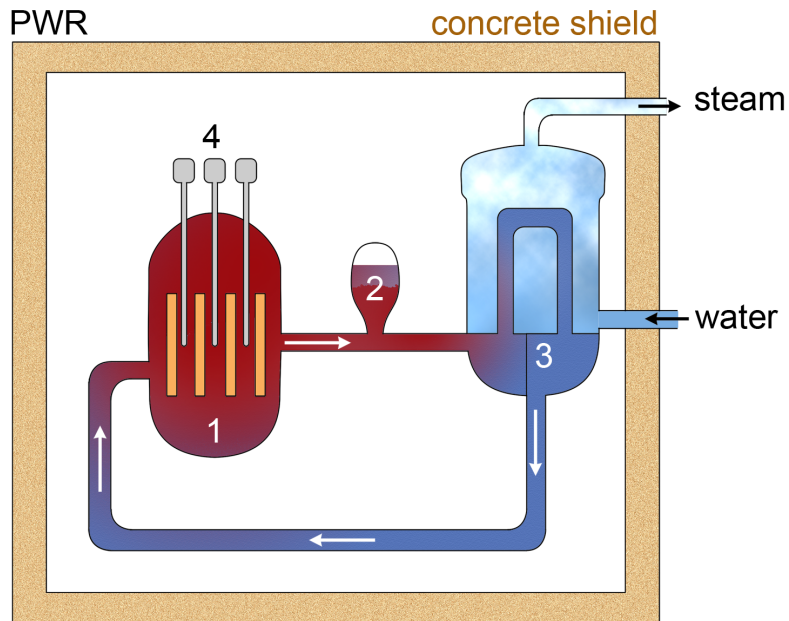


Fig. 2.1 PWR reactor layout. The reactor, in a steel vessel, and boiler are housed in a prestressed containment building. Water acts as the coolant and steam exits the containment to drive the turbines. [7].

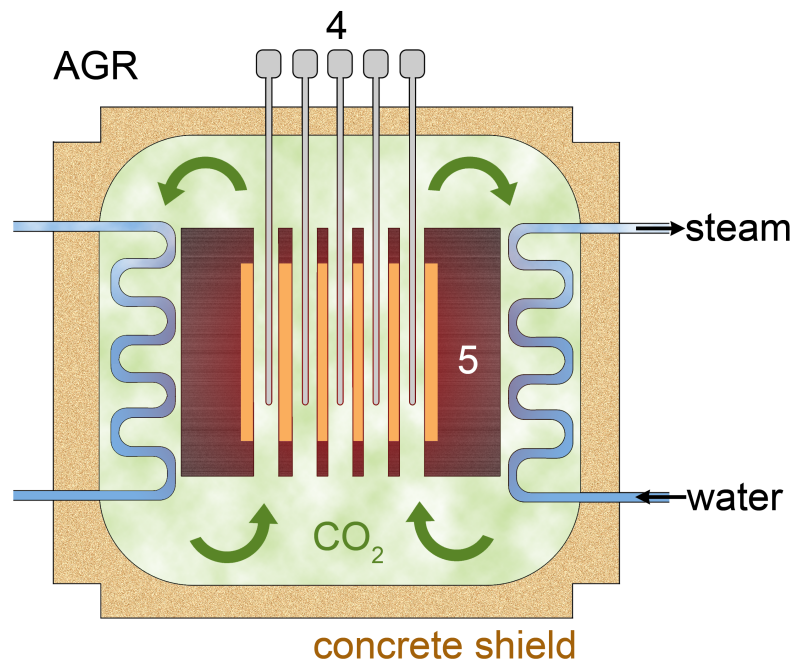


Fig. 2.2 AGR reactor layout. The reactor, boilers and coolant are housed within a prestressed concrete pressure vessel. [7].

Molten salt

Molten salt mixtures can be used as both a coolant and fuel. The high operating temperature and heat transfer of these reactors means they can operate at lower pressure with less mechanical stress on components. However, again, there are technical issues when dealing with the molten salt coolant. These reactors are planned for generation IV.

2.1.3 Reactor safety features

The above sections demonstrate that there are variety of different safety concerns for different reactor designs. But as a common theme, a safely functioning nuclear reactor must be able to remove the same amount of energy that is produced by the nuclear chain reaction. This allows a reactor to maintain a stable constant temperature. The reactor components must also be able to handle radioactive substances, high pressure and temperature. If a deviation from normal operation occurs, the physical and strategic safety management of a reactor must prepare for and mitigate worst case scenarios, such as a complete reactor meltdown. Concentrating on reactors in the UK, the following section describes the safety features, both physical and strategic, of operational and soon-to-be decommissioned reactors.

The Office for Nuclear Regulation (ONR) states, a reactor must be able to permanently shut down the nuclear chain reaction in the event that the cooling fails or if there is a runaway reaction [9]. Additionally, radioactivity must be prevented from escaping the core. There are a number of engineered, requiring active control by personnel or electronics, and passive safety systems to deal with these types of scenarios. They all work with a hierarchical structure; multiple conservatively designed fail safes operate at a very high level of redundancy [10]. Common mode failures, where similar technologies are repeatedly used, are avoided in critical areas. Several different monitoring and control technologies are chosen to complement and verify each other. However, if a technology has a proven safety record it may be used in a number of different non critical locations.

Passive safety systems include the thick concrete baseplate that the reactor sits on. In the case of a full meltdown this prolongs the time it takes for the molten mixture of reactor and fuel from burning into the ground water. Another key passive system is the PCC or PCPV surrounding the reactor. During normal operation and faults, the containment provides biological, mechanical and thermal shielding *to* the reactor; as well as protecting the outside environment *from* the reactor.

At Sizewell B, the UKs only operating PWR, a 1.5 m thick PCC houses the reactor with the plant building acting as the final containment. In the case of the gas cooled AGRs, the

reactor and primary containment are combined into the PCPV. It supports the reactor and main boilers, contains the radioactive coolant gas, is a barrier against seismic events and provides a biological shield against neutrons and high pressure gas. There is a steel lining inside the PCPV to contain the internal pressure, water pipes continually cool the liner. In both the PCC and PCPV, concrete attenuates radiation and is placed under compression to improve its tensile strength. Figure 2.3 shows an example of the dimensions and shape of a PCC and PCPV.

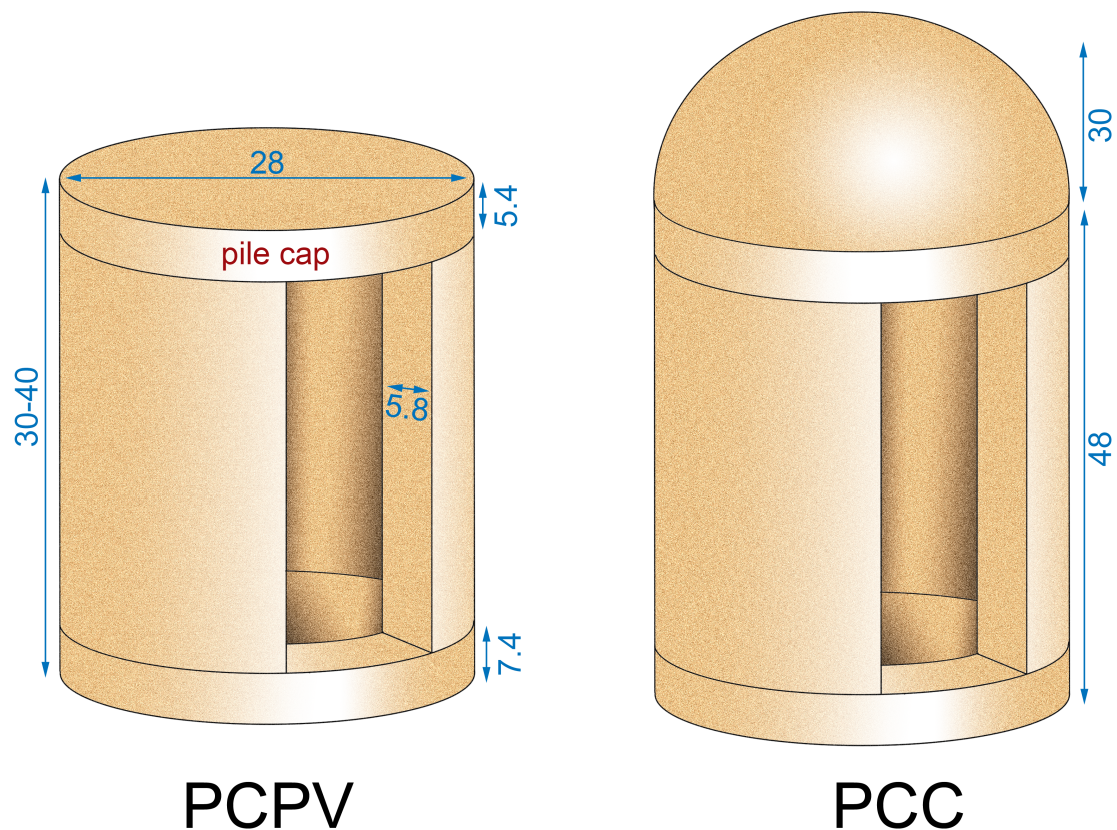


Fig. 2.3 The typical dimensions, in metres, of a PCC and PCPV. [7].

In a PCPV, the thick concrete and steel plays a key role in terms of shielding the outside environment against radiation. For example, neutrons are attenuated dramatically within 3 m of concrete, with a 10-year neutron fluence of approximately 10^{18} Gy dropping to 10^6 Gy [11], and primary gamma rays are terminated at the steel shell [12]. Secondary gamma rays are produced due to a resonance between thermal neutrons and the steel liner. But, the concrete shields these to a large extent; integrated doses drop by five orders of magnitude per metre from 1^8 Gy at the steel liner [13].

2.1.4 Ageing and decommissioning

While the designed lifetime of the nuclear reactors in the UK was around 20-30 years, many reactor lifetimes can be safely extended up to 40-50 years. Recently the ONR has agreed to lifetime extensions to several of the operating reactors [1]. These could be extended even further if rigorous inspection tests are passed. Lifetime extension is key to allow the UK to meet its energy needs. Furthermore, as we move away from fossil fuel power to more renewable energy sources, nuclear will play an important role in the transition, while also providing a guaranteed electricity base load and stabilisation of the power grid.

As most passive components degrade with age (graphite core, PCC, PCPV etc.), it is important to monitor the passive safety components to ensure the safety of the nuclear reactor. Even after power generation has stopped the passive safety barriers must remain in place as the lengthy decommissioning process begins.

2.1.5 Summary

Human or electronic failures are uncommon, but do occur as demonstrated by the events in Chernobyl and Fukushima. Therefore improving and maintaining the passive safety systems is extremely important as they don't require active input. As we have seen, the PCC and PCPV are an essential part of the safety strategy. In the case of an accident they may be the key factor in preventing a major disaster. However, these structures change over time and therefore must be monitored to ensure that they function above their minimum design level until the end of their operating life. AGRs are the most common reactor type in the UK, therefore the rest of the thesis will mainly focus on the PCPV.

2.2 Prestressed concrete

The PCC and PCPV are constructed with prestressed concrete consisting of a cast reinforced concrete structure with tensioned steelwork running through it. The steel compresses the concrete, which is necessary due to concrete's low tensile strength.

2.2.1 Concrete

Concrete is commonly composed of three main ingredients: Portland cement, water and aggregates. The aggregates, consisting of various sizes of rock and sand, form the bulk of the mixture. Portland cement and water bind the concrete together through hydration. Hydration is

a chemical reaction that occurs between the water and cement. Water allows nodes to grow out of cement particles, the nodes then link together to bind the cement and aggregates. Trapped water continues the hydration reaction, filling voids in the concrete matrix and increasing structural strength. The concrete will have reached 95 % of its full strength after one month, though there are fast drying concretes where this only takes a few days. Water content is continually reduced, so preventing its loss reduces shrinkage, which can lead to cracking. Hydration and carbon dioxide uptake continue over years causing concrete to become harder and stronger as it matures.

Concrete compressive strength varies from ~ 20 -100 MPa. During compression, the aggregates within the concrete are forced together. Due to the non-homogeneity, aggregates take up more stress than the cement matrix [14]. As compressive force is increased, stress increases on the cement nodes at the cement-aggregate interface. Chemical bonds are broken here first, leading to microcracking, energy release and relaxing stress in the entire matrix. Increasing the force further eventually causes the concrete to fail as micro cracks connect to form macroscopic ones. Concrete is an elasto-plastic material and due to its non-homogeneity it has a small linear stress-strain range.

When a tensile force is placed on concrete, only the binding cement can withstand the force. Cement has a crystalline structure which doesn't allow much displacement to dissipate the internal tensile stress the concrete is placed under. This causes the cement to crack more readily in tension and results in a low tensile strength of 2-5 MPa [15]. It is therefore desirable to design structures where concrete is under compression rather than tension due to the increased strength. Even if concrete is under uniaxial compression, the Poisson effect dictates that there may be tension orthogonal to the compression. It follows that the concrete must be triaxially compressed [16]. Prestressing concrete by deliberately compressing the structure in three dimensions with reinforced steel is one way to ensure external forces do not cause internal pressure. The compression also closes larger cracks which can lead to critical failure if left untreated. The rest of section 2.2 concentrates on the steel work and prestressing methods.

2.2.2 Prestressing strands

High tensile steel provides the compressive strength required to compensate concrete's inherent weakness. Prestressing steel is made from iron with 0-2 % dispersed carbon content. The carbon helps to inhibit the translation of iron atoms when steel is stressed, leading to higher strength and hardness. The crystal structure of steel is named Pearlite and it consists of alternating layers of iron ferrite and cementite.

Table 2.2 Typical properties of 7-wire, cold-drawn prestressing strand according to BS 5896:2012 [19]. The elasticity, yield and ultimate tensile strength are the most important features as they govern the tendon strand's ability to transfer prestressing forces.

Property	Value	Tolerance
Diameter (mm)	18	+0.4, -0.2
Cross-sectional area (mm ²)	223	+4% -2%
Linear mass density (g/m)	1750	+4% -2%
Elasticity (GPa)	195	± 10
Ultimate tensile strength (MPa)	1700	±55
Ultimate tensile strength (kN)	380	±12
0.1% offset yield strength (MPa)	1450	±60
0.1% offset yield strength (kN)	323	±13

Wire and strand fabrication

Steel is cast and rolled out into preforms as it cools. This encourages uniform thermal stress relaxation. The preforms are then cold drawn through rollers of decreasing aperture at room temperature, plastically deforming the preform into a 7mm wire. Cold rolling realigns the crystal structure to the direction that force will be applied to the wire. The steel is also work hardened as the crystal structure becomes saturated with dislocations, which help inhibit further crystal movement [17]. Low relaxation steel is further treated, so that it remains elastic almost up to the point of fracture [18]. Steel is called low relaxation after annealing at ~350 °C while under tension, this further relaxes dislocations and reduces its hardness.

Prestressing strands consist of 6 helically wound wires wound around a central straight wire. The strand can be drawn through a final die to compact the wire together. In the UK 7-wire strands should conform to BS5896:2012 the guidelines for high tensile strength steel wire and strands for prestressing concrete [19]. Table 2.2 shows the requirements a strand must have. As can be seen from the table, low relaxation steel has a much greater yield and ultimate tensile strength (UTS), 1450 MPa and 1750 MPa respectively, than concrete. It is these properties that allow the steel to transfer stress to the concrete.

2.2.3 Post-tensioned concrete

Prestressed concrete is either pre- or post-tensioned. For pre-tensioned concrete, the concrete is cast around steel tendons held under tension and the concrete bonds to the steel as it cures. Friction between the steel and concrete transfers compression to the concrete. The reliance on

friction leads to weaker compression at the extremities of the structure. Pre-tensioned concrete is usually pre-fabricated and this limits the size of the beams. For post-tensioned concrete, ducts are cast into the structure, Figure 2.4. After curing, steel tendons are inserted and tensioned with stressing jacks. They compress the concrete through anchors and bearing plates. This can be performed on-site and therefore is the method of choice for large structures.

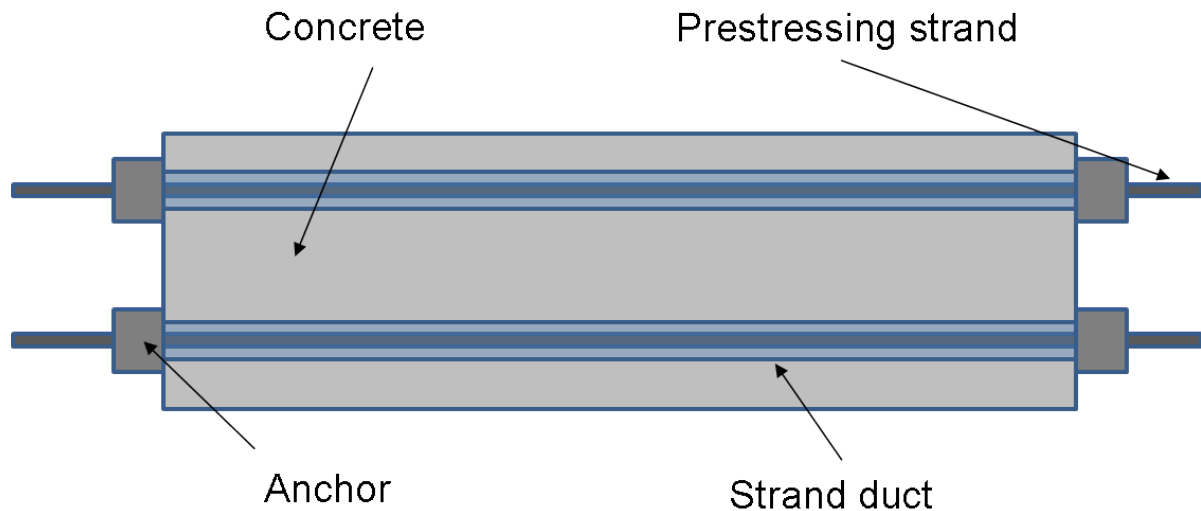


Fig. 2.4 Steel tendons are inserted into ducts that are cast into the concrete. After curing the tendons are stressed and fixed into place. The steel compresses the concrete.

Concrete compression is achieved with a post-tensioned system by the following procedure: steel strands are tensioned with a hydraulic jack, then an anchor consisting of a barrel and wedges grip the strand and transfer stress to the concrete through a bearing plate. Figure 2.5 shows the barrel and wedges fitted onto a prestressing strand, while Figure 2.6 shows the stress jack on the strand. The bearing plates house between 7 and 37 strands which form one prestressing tendon; an example of 7-strand tendons can be seen in Figure 2.7. In the UK it is common to use unbonded tendons; they are not permanently attached to the structure. An oil based lubricant is applied to the strands for lubrication and corrosion protection. It is important to protect against corrosion as this can reduce the prestressing strand area, reducing strength and potentially causing failure [20]. Unbonded strands can be inspected for corrosion and re-tensioned or replaced if necessary. A new strand can be installed by welding it onto the old strand end and pulling it into the duct. Globally, it is more common to grout the tendon ducts with cement. This prevents strand corrosion and provides a bond between the tendons and surrounding concrete. However, once a tendon is grouted, it is permanently in place.

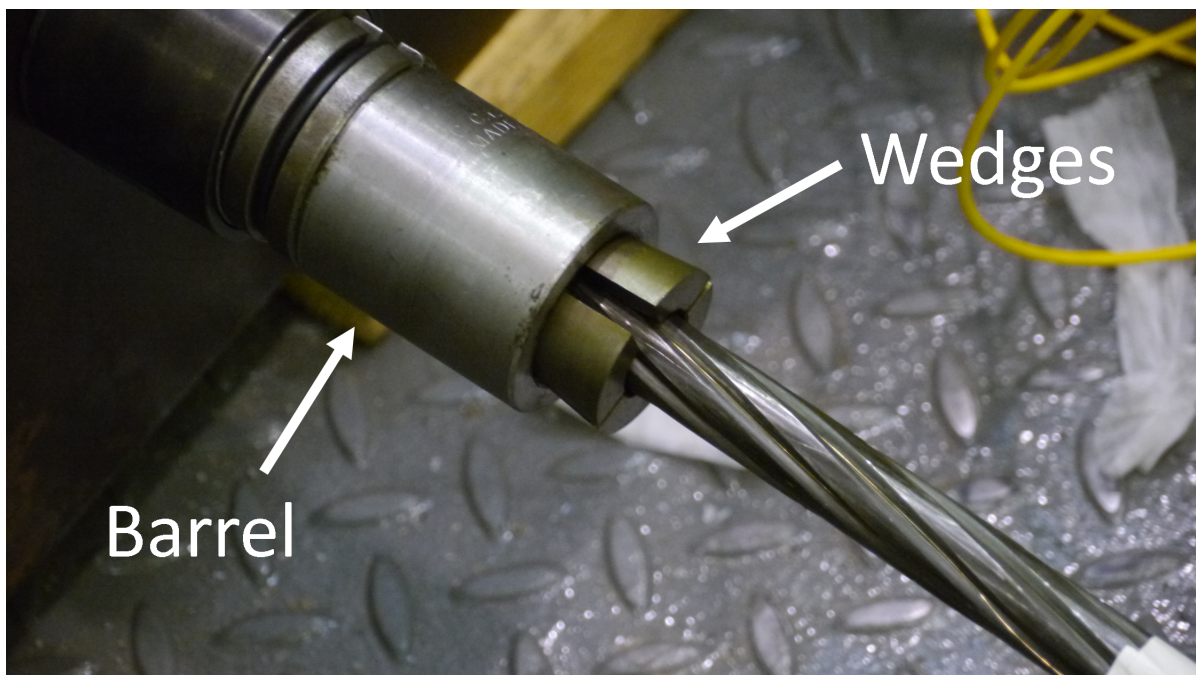


Fig. 2.5 Post-tensioning anchor components. A single prestressing strand with barrel and wedges fitted. When the strand is stressed the wedges are pulled into the barrel gripping the strand. The wedges have not been seated yet. A shim can be seen beneath the barrel to aid with the destressing process.

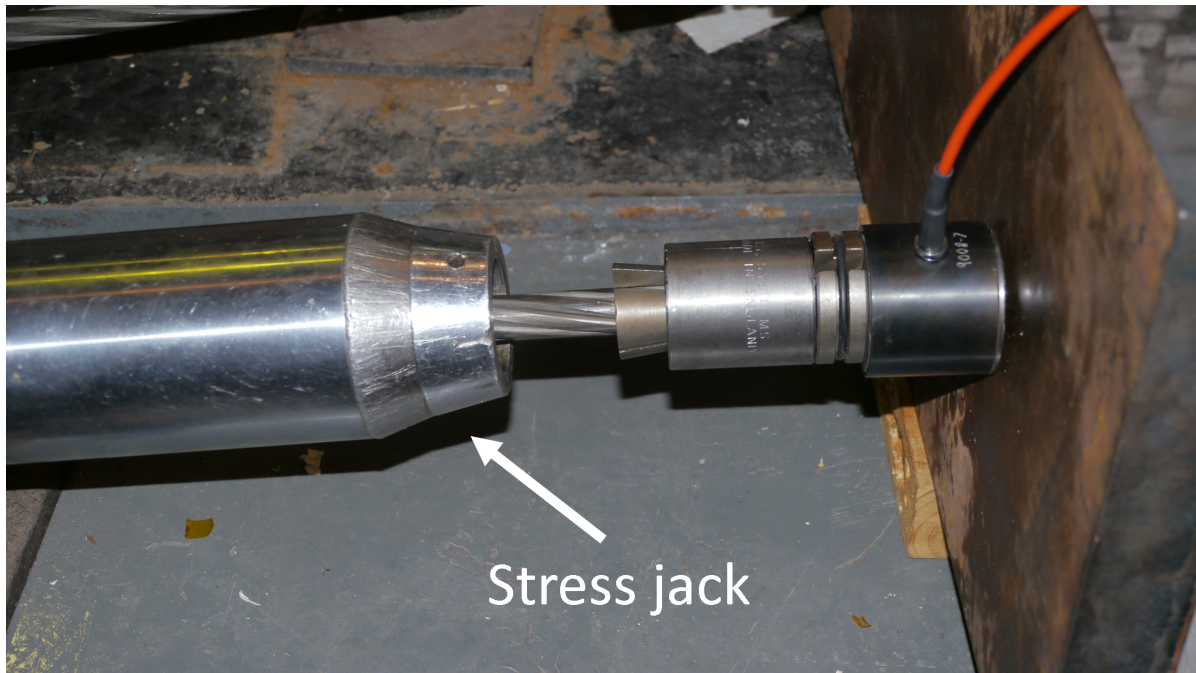


Fig. 2.6 Stressing jack fitted onto a prestressing strand. The stressing jack is moved to sit flush with the barrel, covering the wedge. It grips and stresses the strand. The stress is transferred to the concrete through the bearing plate.

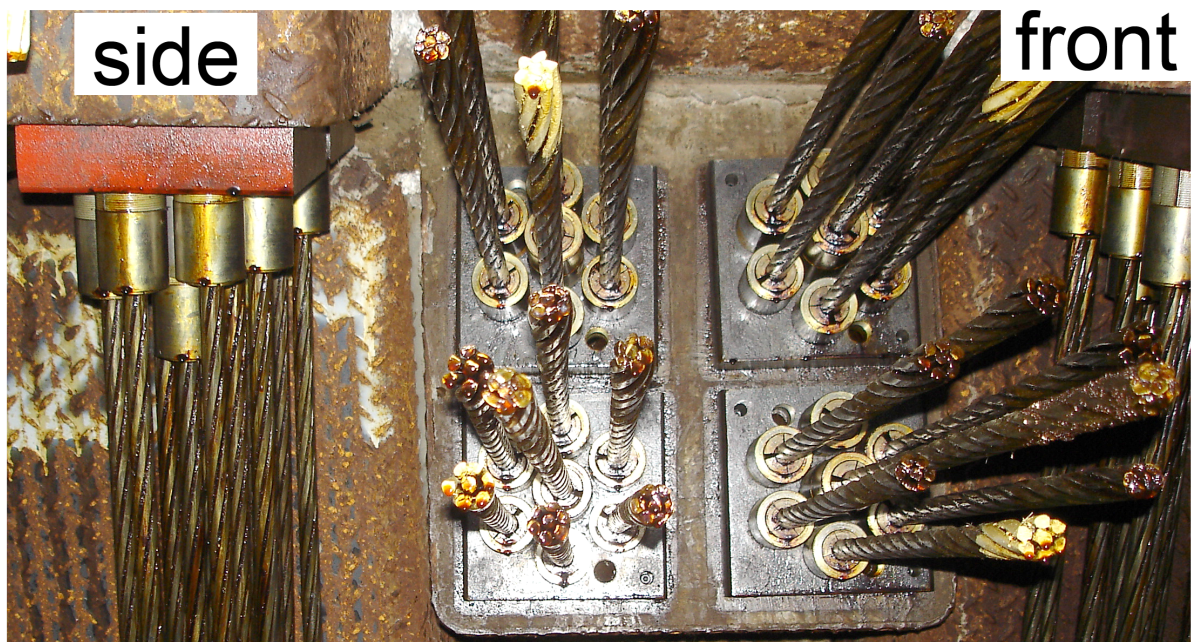


Fig. 2.7 An example of the anchor plate of 7-strand prestressing tendons. The anchor plates that transfer stress to the concrete can be clearly seen.

During the design phase, tendon duct trajectories are chosen so triaxial compression of the structure is ensured. The ducts either provide circumferential and longitudinal compression together by being helically wound round the structure like in the PCPVs at Torness, Hinkley Point B or Hunterston B. Or split the circumferential and longitudinal compression into two tendon groups like the PCPV at Hartlepool or the PCC at Sizewell B. The stressing procedure is non trivial and detailed below for a 7-strand prestressing tendon, the bearing plate is shown in Figure 2.7:

- The stressing jack is calibrated to a known primary reference standard from NPL.
- The stressing jack is fitted to the central strand.
- The stressing jack is loaded in 20, 50, 150, 304 kN stages. The force and extension are noted at each stage. At 304 kN, jack pressure and extension are taken after 60 s to check if the load needs to be topped up. Figure 2.8 shows the position of the jack during stressing.
- The jack is locked off and wedges are pushed into the barrel. The barrels transfer force to the bearing plate. The final prestressing force is around 266-304 kN, or 70-80 % UTS per strand.
- The steps above are repeated sequentially on strands 2 to 7, Figure 2.9.

Prestressing strands are normally stressed simultaneously from each end, but sometimes due to space constraints, only one end can be stressed. In this case, the dead end must be checked for slippage as this could be mistaken for extension at the live end. Should a strand need to be replaced or destressed, a stressing stool is placed on the bearing plate, as seen in Figure 2.10. The stress jack rests on top of the stool leaving room beneath to remove the barrel and wedges. Force is transferred to the stress jack, the wedges are hit and removed, and the stress in the strand is slowly reduced.

2.3 Prestress loss

PCCs and PCPVs are designed to have a minimum prestress load¹. For safe operation of the reactor, prestressing force in the tendons must remain high enough to meet this requirement, but several factors cause prestress loss during the stressing procedure and in the years after. Prestress loss can be split into two main groups: instantaneous and time dependent.

¹It must be noted that a safety factor is included in the minimum design load, therefore a reactor and containment will not fail if prestress falls below the specified level.

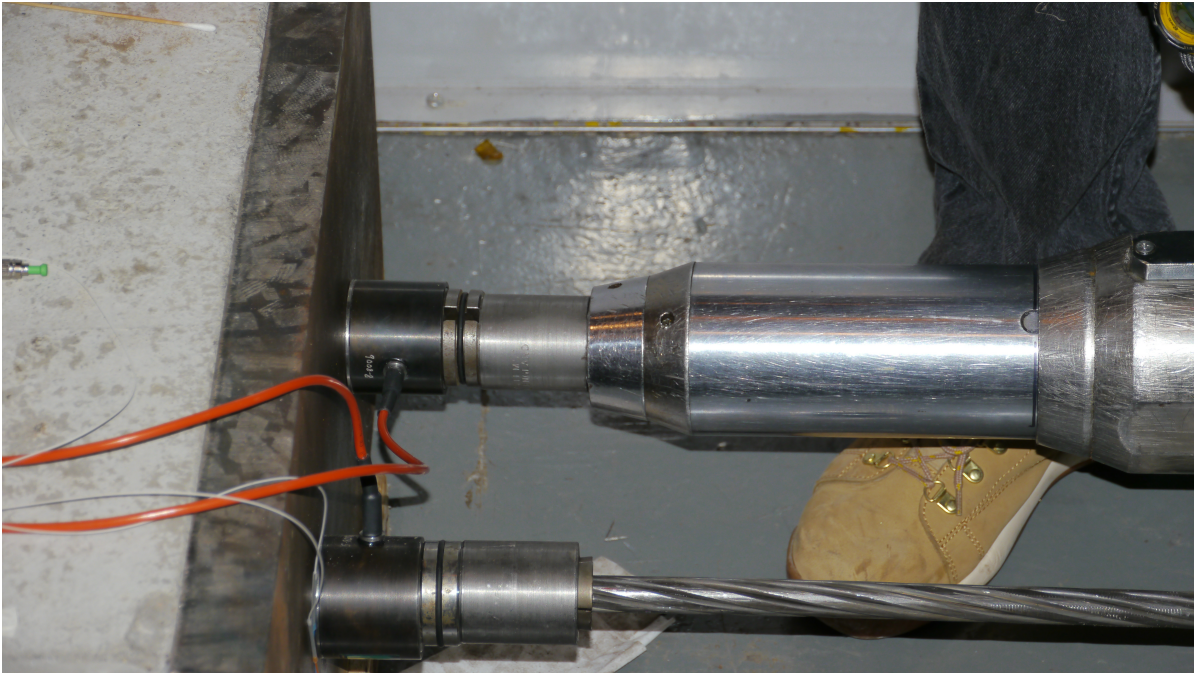


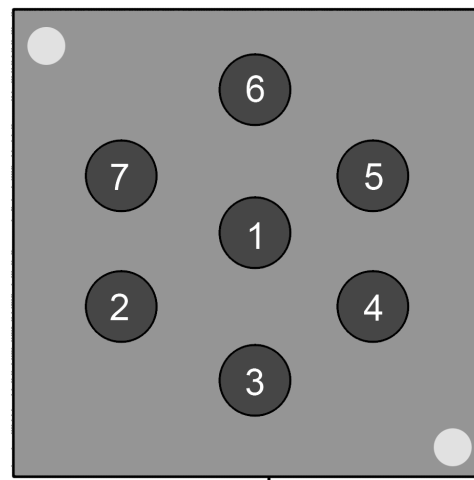
Fig. 2.8 Stressing a single prestressing strand. The stressing jack covers the wedges ensuring they are seated once the correct stress has been reached. A stressed strand is present at the bottom of the photo.

Upper anchorage:
viewed from above



locating hole

Lower anchorage:
viewed from below



bearing plate

Fig. 2.9 Strand stressing order for a 7-wire tendon.

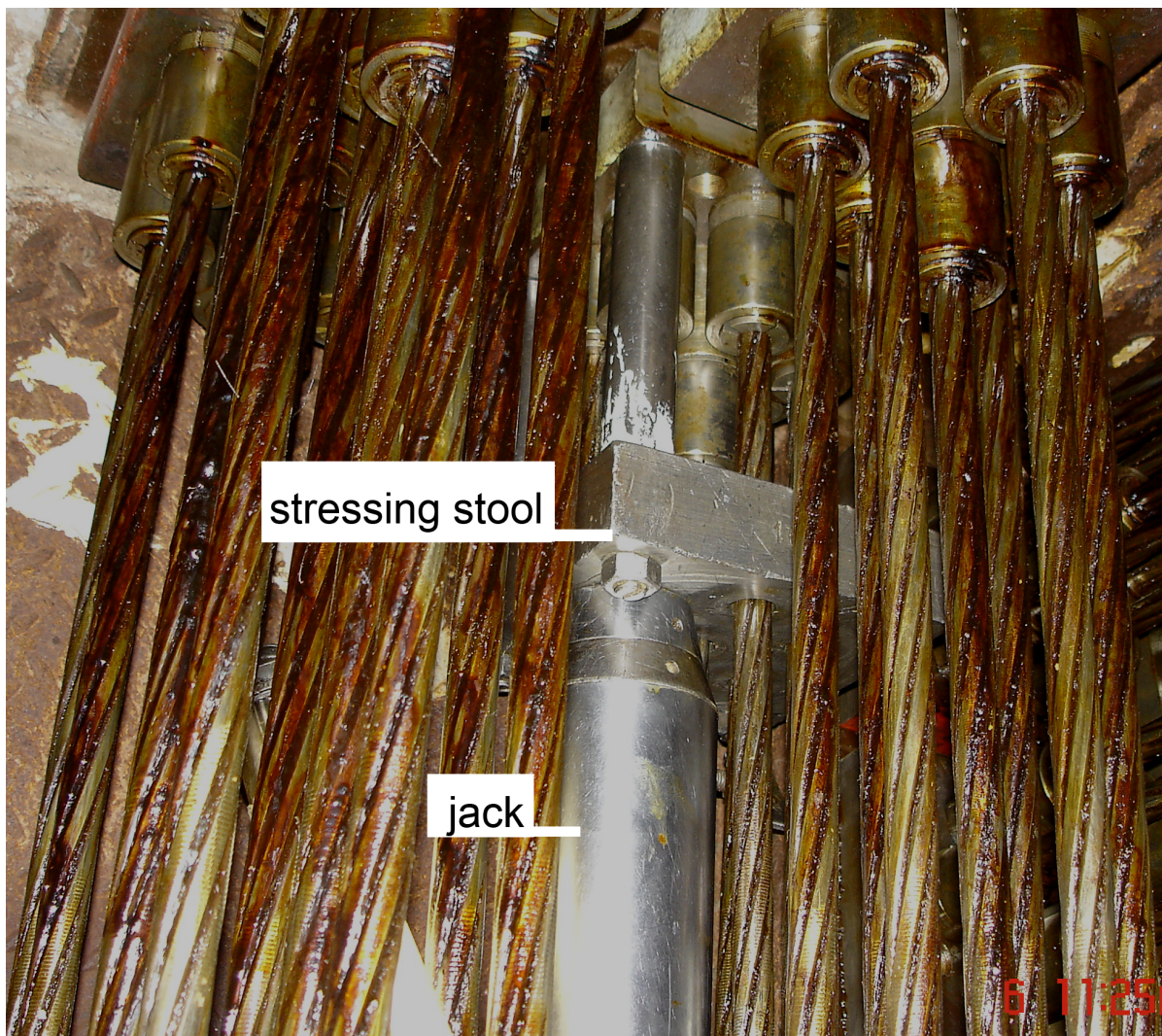


Fig. 2.10 Destressing a strand. A stressing stool is placed onto the anchorage. Once the stressing jack has transferred the load off the barrel, the wedges can be removed and the strand destressed.

2.3.1 Instantaneous prestress loss

These effects happen at the time of stressing or shortly after locking off the tendons and therefore, can generally be more easily anticipated or compensated for compared to the time dependent effects. The three main instantaneous effects are elastic shortening, anchor slippage or ‘wedge draw-in’ and friction.

Elastic shortening

During the prestressing procedure, prestress levels in the structure increase leading to elastic compression of the concrete. If all the tendons were stressed simultaneously elastic compression would not result in prestress loss. However, this is not possible with the large number of tendons present in PCCs and PCPVs. The tendons are stressed sequentially, causing the force in previous strands to reduce as the current strand further compresses the concrete. It would take too long to measure the prestress loss from sequentially stressing the tendons, so the total elastic shortening loss is empirically estimated. The simplest equation states that the force lost in each tendon is at least half of the force applied to the first tendon, ΔF_0 . The total elastic shortening loss is given by [20]:

$$\Delta f_{es} \approx \frac{M_{td}}{2} \Delta F_0 \quad (2.2)$$

Where M_{td} is the number of tendons in the system. Elastic shortening happens as the stressing takes place so it can be compensated for during the stressing procedure.

Friction and anchorage slip

Both friction between the duct and tendon and anchorage slip affect the force distribution along the length of the strand. Anchorage slip occurs as the stress in the strands is transferred from the stressing jack to the anchor plates. The wedges that grip the strand are pulled into the barrel, causing some of the strand extension to be lost, reducing the total force. Friction, on the other hand, causes decreasing strand force for an increasing distance from the anchorage. The change in force of a strand section, ∂F due to the strand turning through an angle, $\partial \alpha$ is a result of contact between the strand and duct [20]:

$$\partial F = -\mu F \partial \alpha \quad (2.3)$$

Where μ is the coefficient of friction due to the curvature effect (typically 0.2 [18]) and F is the force at the jacking end. In practice, the tendon duct is constructed with imperfect alignment,

known as the wobble effect. Combing duct geometry with the wobble effect leads to Cooleys formula; the force $F(L)$ at a given point of length, L away from the jacking end is given by [20]:

$$F(L) = F_i \exp[-(\mu\alpha + kL)] \quad (2.4)$$

F_i is the force at the jacking end, α is the cumulative angle in radians the strand has been turned through at point L and k is the wobble coefficient. The wobble coefficient (typically $6.6 \times 10^{-4} \text{rad m}^{-1}$) describes unintentional change in the strand angle per unit length. Equation 2.4 shows friction has a cumulative effect on strand force moving away from the anchorage; the maximum prestress loss due to friction occurs at the dead end. The total change in prestress due to friction, Δf_{PF} is [20]:

$$\Delta f_{PF} = f_i - f_2 = f_i(1 - \exp[-\mu\alpha - kL]) \quad (2.5)$$

Where f_i is the stress at the jacking end.

It is common to stress strands from both ends simultaneously, leading to the decreasing force profiles meeting in the middle, where strand force is at a minimum. This is known as the critical point, see Figure 2.11.

When the strand is locked off there is a force decrease at the strand anchorage, this affects the length of the strand according to the inverse Cooley formula [20]:

$$F(L) = F_i \exp[\mu\alpha + kL] \quad (2.6)$$

Reversing of the force profile is seen due to the unavoidable anchor slippage and wedge draw-in [21]. The end result is that the strand force profile has an 'M' shape, where the maximum force on the shoulders is [20]:

$$F_{max} = \sqrt{F_1 F_2} \quad (2.7)$$

Here F_1 and F_2 are the initial force and force after anchor slippage at the end of the tendon. Figure 2.12 shows the affect that anchor slippage has on the force profile.

The effect of friction on the strand force profile cannot be compensated for, so the 'M' profile remains permanently. Currently, there isn't a measurement technique capable of obtaining experimental data of the force profiles of tendons in the PCCs and PCPVs.

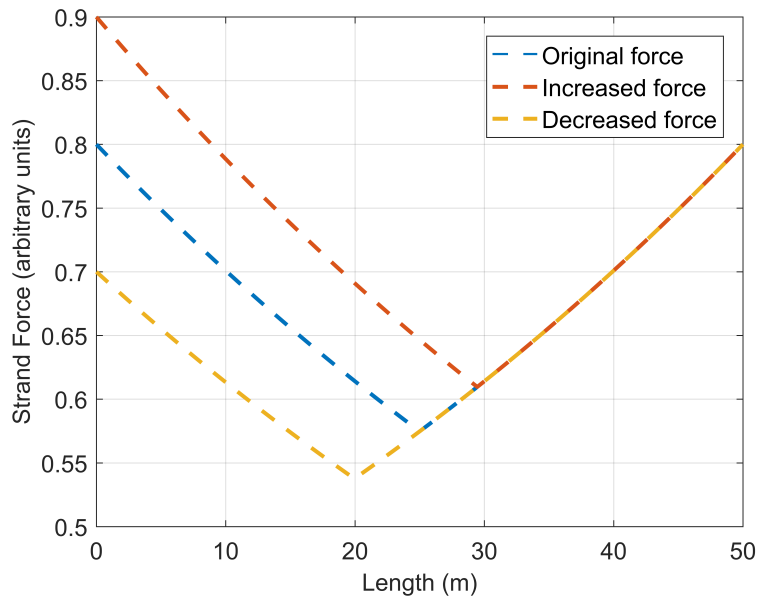


Fig. 2.11 Strand force profile with simultaneous stressing of both ends. When both ends are stressed to the same force the critical point lies half way along the strand. If the force at one end is increased, the critical point shifts away from this end. Whereas a decrease in force causes the critical point to shift towards that end. The coefficient of friction and wobble coefficient are typically 0.2 and $6.6 \times 10^{-4} \text{rad m}^{-1}$, for PCPVs.

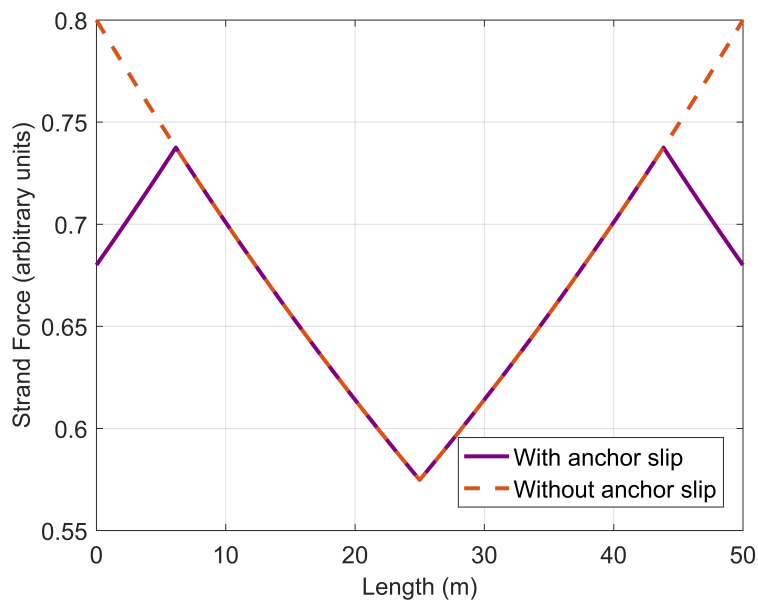


Fig. 2.12 The effect of anchor slippage and friction on strand force. Anchor slippage causes force decrease in a length of the strand near the anchorage.

2.3.2 Time dependent prestress loss

Long term prestress losses occur over the course of years and decades. Their effect on the structure is less predictable and harder to correct for.

Shrinkage

As the name suggests, shrinkage is a volume change in the concrete. It occurs over time due to the loss of water to the hydration process, termed autogenous shrinkage, and to the surrounding environment through drying shrinkage. The majority of the shrinkage takes place in the first 24 hours after curing and $\sim 80\%$ will have occurred in the first year. Therefore, a large portion of shrinkage has already taken place before prestress is applied to a structure. There is a large variation in shrinkage on practical structures due to concrete variation, the volume to surface ratio and drying conditions. This makes it difficult to predict shrinkage development. There are, however, several empirical equations to help predict shrinkage in concrete. Despite most of the shrinkage happening before a structure is stressed, it still has significant long term effect, especially if it supports or is attached to other bodies. Shrinkage can cause tension in the PCC/PCPV to cracking over long periods.

Creep

Under constant load, materials gradually flow as they adjust to the particular level of stress. Creep is a measurement of this plastic deformation or change in strain under constant stress. Only a small amount ($\sim 20\%$) of creep can be recovered [22]. The stress-strain relationship due to creep is approximately linear so creep strain, ϵ_{CR} can be related to elastic strain, ϵ_{EL} through the creep coefficient [20, 23]:

$$C_u = \frac{\epsilon_{CR}}{\epsilon_{EL}} \quad (2.8)$$

As with shrinkage there are several empirical equations that can be used to predict creep strain. It should be noted that creep only begins once load or prestress has been applied to a structure, therefore creep will generally contribute a larger portion of prestress loss compared to shrinkage. In concrete, creep can be attributed to the combination of three main effects [24]:

- Basic creep: Diffusion and movement of grain boundaries, aggregates and dislocations within the cement matrix. Old high strength concretes creep less for this reason. Basic creep is measured on loaded sealed cylindrical specimens with no moisture ingress or

egress. Therefore it is considered a constitutive material property and is independent of specimen shape and size [25].

- **Drying creep:** Concrete creeps more in a dry environment. This is known as the Picinell effect [26], and is due to the formation of micro cracks from shrinkage and water loss disrupting the stress state of microscopic gel pores, resulting in slippage in local grain boundaries. Drying creep is considered to be the remaining strain after elastic, shrinkage and basic creep strain have been removed from loaded non-sealed concrete specimens.
- **Transitional thermal creep:** A temporary increase in creep occurs after sudden changes in temperature as a result of thermally induced microcracking. The stress equilibrium in gel pores is also disrupted. Creep is promoted by temperature increases in particular because there is an increase in breakage and restoration of chemical bonds.

Creep has a decreasing rate as concrete ages and most takes place in the first year. This is because the hydration process converts water into load bearing material volumes. In other words, cement nodes are continuously generated and deposited onto capillary walls in a stress free state [27, 28]. The cement bonds are placed under less tensile stress making them stiffer. The bonds are less prone to break, reducing the creep rate [29].

Modelling creep and shrinkage

Prediction of creep and shrinkage is important for assessing the risk of concrete deflection and cracking [25]. Concrete properties are strongly affected by temperature, water availability during curing, humidity, and concrete composition. Furthermore, much of the shrinkage occurs before loading and creep is significantly reduced by concrete drying that also occurs before loading. This makes creep and shrinkage evolution complex to predict. Bazant et al. measured shrinkage of different specimens, in lab conditions, from a single mixture of concrete and found shrinkage strains to differ by $\sim 8\%$ [30]. Therefore, it is unrealistic to expect models to be within $\pm 20\%$ of test data for shrinkage, with potentially larger differences for creep [25]. For structures where creep and shrinkage are critical, prior material testing must take place, along with concrete sampling during construction; allowing the long term evolution to be extrapolated. Nevertheless, creep and shrinkage models are useful as a starting point for structural design and are sometimes adequate for less shrinkage- and creep-critical structures. As we will see in Chapter 11, the initial model can be adjusted as strain measurements from the structure become available.

A number of empirical models have been proposed to model creep and shrinkage. They include the ACI 209R-92, Bažant-Baweja B3, CEB MC90-99, fib Model Code 2010, EN1992-1-1 and GL2000 models [25, 31–33]. For all models several assumptions must be made, the most important are listed below:

- Shrinkage and creep are additive - Two concrete specimens are cured in the same conditions with the exception that one is loaded with a force of 20-40 % of the concrete tensile strength. Shrinkage is measured from the unloaded specimen, while creep is determined by subtracting shrinkage strains from the loaded specimen. Consequently, shrinkage is assumed to be independent of creep and vice versa.
- Creep strain is approximately proportional to stress - This is supported by experimental data, assuming stress is lower than 40 % of the concrete compressive strength [34, 35].
- Strains from stress follow the superposition principle [36]- Strain responses from stress increments at different times can be added using the superposition principle assuming strain reversals are excluded and temperature and moisture are kept constant.
- Stresses from curing are negligible.

During this research the fib Model Code 2010 was adopted. Due to the size and number of components to the equations, they are detailed in Appendix A.1 and A.2. To calculate the strain components, the following basic equations are used:

$$\text{Total strain} = \text{Shrinkage strain} + \text{Compliance} \times \text{Stress} \quad (2.9)$$

Total and shrinkage strain can be measured by comparing loaded and unloaded concrete specimens cured in the same conditions. Compliance is calculated from the remaining strain and is a combination of creep and elastic strain per unit stress:

$$\text{Compliance} = \frac{(\text{Elastic strain} + \text{Basic creep} + \text{Drying creep})}{\text{Stress}} \quad (2.10)$$

Shrinkage models calculate shrinkage strain, while creep models calculate either the creep coefficient of Equation 2.8 or compliance, the total load-induced strain, as seen in Equation 2.10. Figure 2.13 shows an example of model predictions for shrinkage and creep of a small concrete beam post-tensioned at day 100.

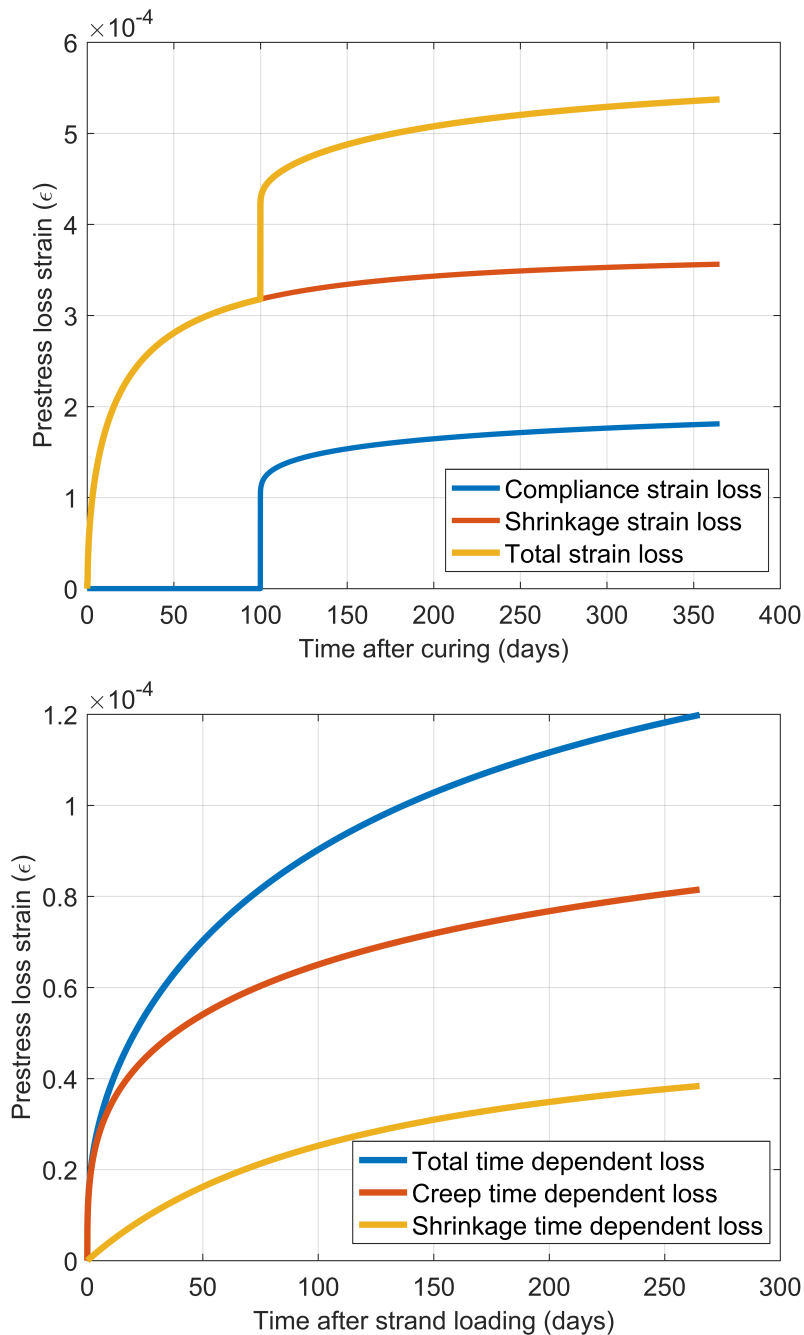


Fig. 2.13 Prestress loss due to shrinkage and creep for a small concrete beam. Figure a) shows strain reduction for one year after curing. Shrinkage occurs before and after loading the beam at 100 days. Most of the shrinkage strain happens in first few days after curing. Elastic strain at the point of prestressing causes a large decrease in strain on the 100th day. While the concrete begins to creep from this point onwards. Figure b) is an enlarged view of the time dependent losses after the concrete beam has been post-tensioned, strain reduction after prestressing is the important parameter for prestress loss prediction.

Steel relaxation

Analogous to the creep concrete undergoes, the prestressing steel grains rearrange themselves to minimise energy in their newly stressed state. Creep is a change in strain, or deformation, at constant stress, while stress relaxation is a reduction in stress at constant strain; therefore relaxation must be measured as a force.

As mentioned in Section 2.2.2, low relaxation prestressing strands undergo relaxation during their fabrication and this is known as strain tempering. Forcing the steel to creep before its use minimises the force loss during operation. Magura et al. followed by Ghali and Trevino pioneered statistical work on stress relaxation of steels, leading to the formulation of empirical equations [37, 38]. The change in prestress level, Δf_{SR} as a percentage due to steel relaxation after t hours is given by:

$$\frac{\Delta f_{SR}}{f_0} = -J\eta_t \left(\frac{f_0}{f_{uts}} - 0.4 \right)^2 \quad (2.11)$$

Where f_0 is the initial strand stress, f_{uts} is the tensile strength of the strand (~ 1.7 GPa) and $J = 1.5$ or $2/3$ for stress relieved and low relaxation strands respectively. The parameter η_t is:

$$\begin{aligned} \eta_t &= \frac{1}{16} \ln \left(\frac{t}{10} + 1 \right) && : 1 \leq t < 1000 \\ &= \left(\frac{t}{5 \times 10^5} \right)^{0.2} && : 1000 \leq t \leq 5 \times 10^5 \\ &= 1 && : t > 5 \times 10^5 \end{aligned} \quad (2.12)$$

For a stress relieved wire stressed to 80 % UTS of steel there is a 10 % loss of prestress due to steel relaxation, according to the equations. When subject to increased temperatures, steel relaxation can increase due to increased grain mobility. Figure 2.14 shows the effect steel relaxation has on concrete strains in a concrete beam.

Steel relaxation combined with other losses

Steel relaxation interacts with the other prestress loss effects like friction; it smooths out the 'M' shape profile. Cooley's formula (2.4) can be modified to [20]:

$$\frac{\partial F}{\partial \alpha} = -\mu(1-r)F \quad (2.13)$$

Where r is the stress relaxation loss ratio.

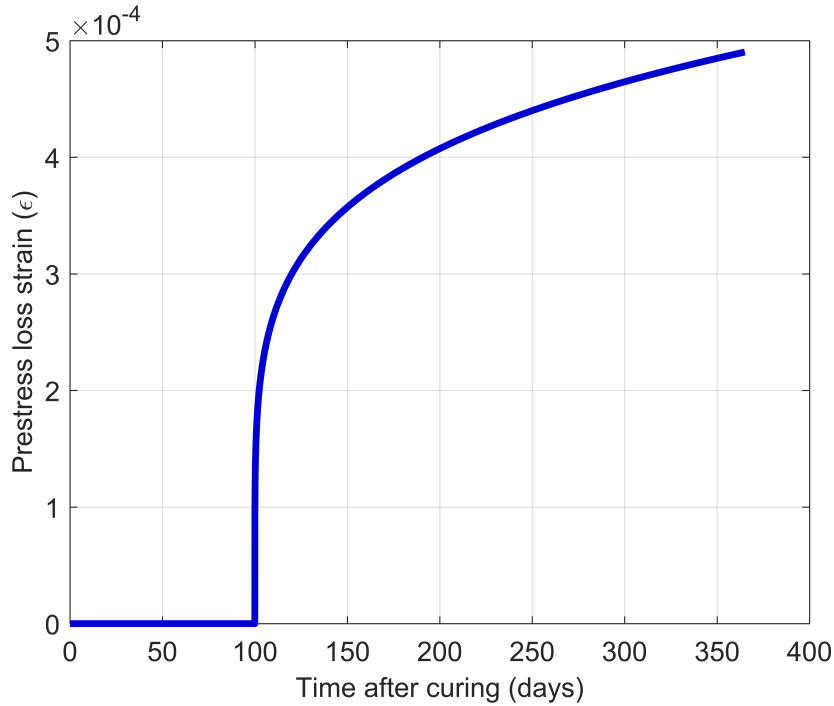


Fig. 2.14 The decrease in strand strain due to steel relaxation. In this theoretical example, a small post-tensioned concrete beam was loaded on the hundredth day to 79 %UTS of the steel.

Creep and shrinkage affect steel relaxation because they reduce the total force in the prestress tendons. Ghali and Trevino empirically derived a reduction coefficient, χ_r to take this into account [38]:

$$\chi_r = \exp \left[\left(-6.7 + 5.3 \frac{f_0}{f_{us}} \right) \left(\frac{|\Delta f_{cr} + \Delta f_{sh}|}{f_0} \right) \right] \quad (2.14)$$

Δf_{cr} and Δf_{sh} are the prestress loss from creep and shrinkage at time t hours.

To summarise, concrete creep and shrinkage and steel relaxation have a complex relationship. This changes as the structure ages and affects the force over the length of the strand. It would be useful to gather as much spatial and temporal information about the prestress level in the PCCs and PCPVs as possible. This would improve accuracy of the empirical models, increase knowledge about the state of the structure and feed back into the design phase for future reactors. However as we will see, due to practical considerations, only a limited amount of prestress level data is currently gathered.

2.4 Current prestress monitoring

Prestress monitoring is a small part of the structural health monitoring of civil structures on a nuclear site. These include [39, 40]:

- Visual inspections of the PCPV for cracks and leakages.
- Tendon anchorages are inspected for strand slippage, corrosion, mechanical damage and localised concrete cracking.
- Tendon load measurements.
- Tendon/wire withdrawal for corrosion inspection and tensile testing.
- Level surveying for monitoring settlement and tilt of the vessel which are important for fuel rod insertion and integrity of pipes exiting the reactor.
- Vibrating wire strain gauges for measurement of PCPV stress levels.
- Concrete temperature measurements.
- Inspection for cooling water leakages.
- Strand lubricant sampling for acidity and water content to determine strand oxidation and corrosion.
- Top-cap deflection for determining internal pressure and prestress.

The prestress load has an effect on many of these inspections.

2.4.1 Lift-off technique

As mentioned previously, tendons in PCCs and PCPVs are unbonded in the UK, so they can be removed and replaced if necessary. This also allows the prestress to be directly monitored by determining how much force is required to lift the strand off the bearing plate. This technique is called a lift-off measurement. Currently, some form of lift-off measurement is performed on a 1-2 % (~30 strands) random sample of strands in the structure every 1.5-5 years [41]. The trap-and-free lift-off method loads one or all of the strands in a tendon using a stress jack. The force is noted when a thin feeler gauge can be inserted between the bearing plates and barrel anchor. Loads are taken at several locations to calculate average tendon force. Other load measurement methods include potentiometric transducers or instrumented shimming feet

which measure movement or force between components in the tendon anchor. All the of these practices are time consuming, dangerous for personnel and increase reactor downtime. They also assume constant friction coefficients, but the measurements can show large variations in prestress level due to strand-duct and inter-strand friction.

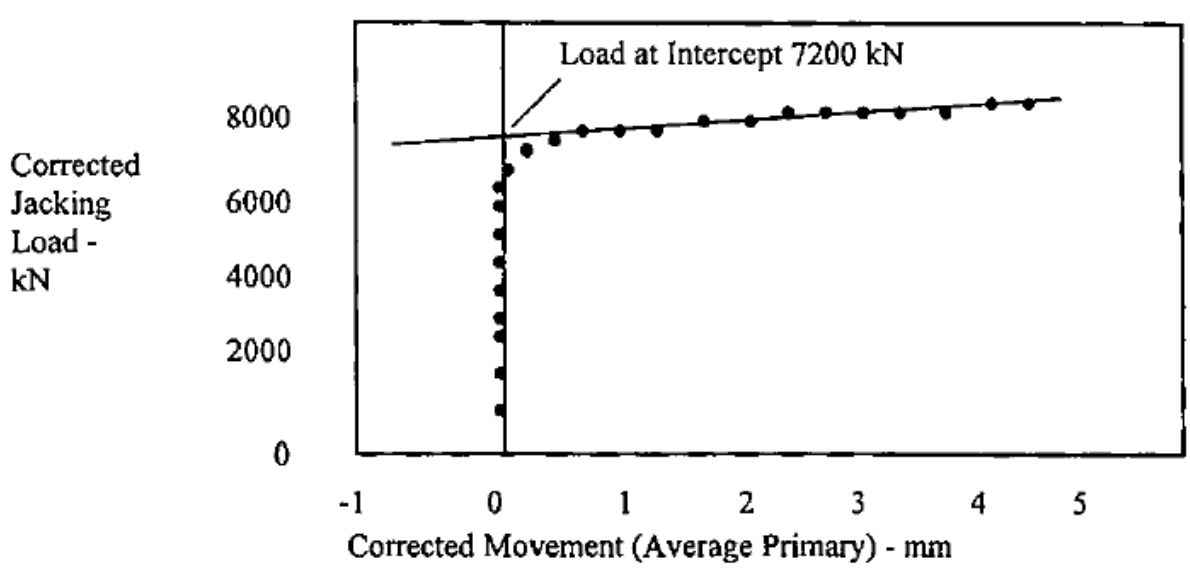


Fig. 2.15 Jack load against bearing plate deflection from a tendon in a PCPV [42]. The intercept of the straight line is the load at zero displacement and therefore the load in the tendon. Elastic deformation of the bearing plate has been corrected for.

A typical lift-off measurement is shown in Figure 2.15, the lift-off force occurs at the intercept between the horizontal and vertical lines on the graph. Loads are then reduced by 5 % to account for frictional losses, resulting in the ‘effective anchor load’. Statistical analysis is used to ensure the average tendon force is above the minimum design load. Figure 2.16 and 2.17 show over 20 years of lift-off measurements taken from two reactors; sometimes it is necessary to increase strand load by reshimming, as seen in Figure 2.17.

Lift off measurements are highly dependent on contact forces between the strand and duct. For example, if corrosion increases friction, the lift-off force will decay more quickly along the strand and won’t disturb the strand past the shoulder of the M curve, see Figure 2.18. Therefore, a shorter section of strand will be mobilised. This can be beneficial when the critical point of the strand is not disturbed, but it also makes estimating strand force more difficult because the length of mobile strand must be estimated. In real PCPVs, the apparent friction of each strand can increase from 0.2 to 0.5 after the strands are stressed due to contact between adjacent strands. However, this inter-strand friction does not affect the prestress level applied to the vessel and is another source of error for lift-off measurements. Variations in friction along the

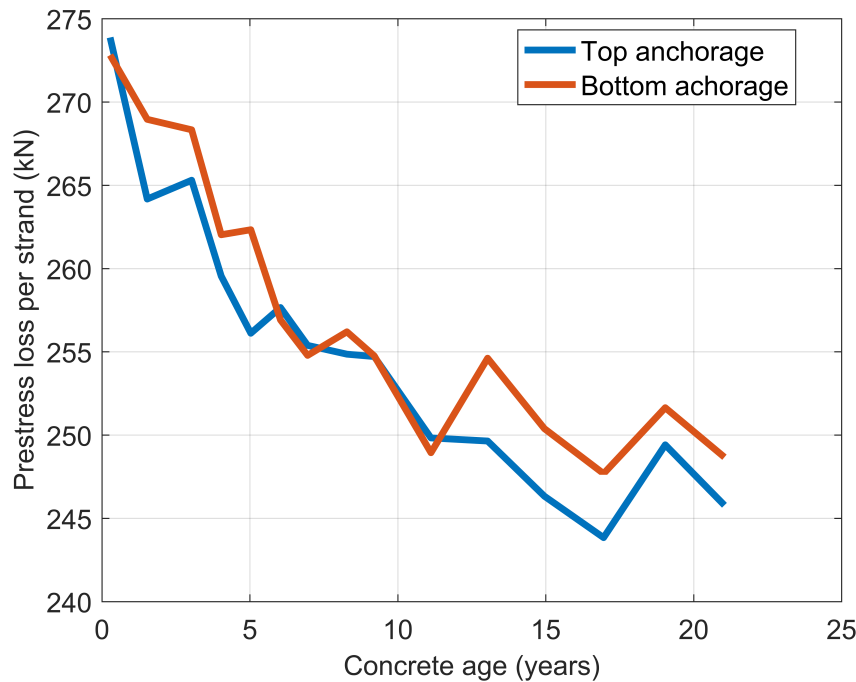


Fig. 2.16 Average strand lift-off force on a PCPV measured by a reactor operator. Measurements from 25 years of operation show that strand force has reduced by approximately 25 kN.

tendon length cannot be currently measured; a distributed force measurement would greatly help with this and complement the lift-off checks.

2.4.2 Vibrating wire strain gauges

Vibrating wire strain gauges (VWSGs) were embedded into most PCCs and PCPVs during construction. They were intended to measure vessel stress during commissioning to help demonstrate structural integrity and deduce load capacity margins during pressure tests. They are used to identify ‘hot spots’ in the containment. The wires span straight ducts and an inductive coil measures the wires electrical resistance and vibration period. Wire temperature and strain can be calculated from these and the average vessel prestress can be inferred from the wire strain. VWSGs wear out over time, but have been used routinely on all reactors as an indicator of vessel stress. While faulty VWSGs can be revived, they gradually fail², therefore they are used sparingly but still support other prestress measurements.

²Approximately 50 % of installed VWSGs are still operational

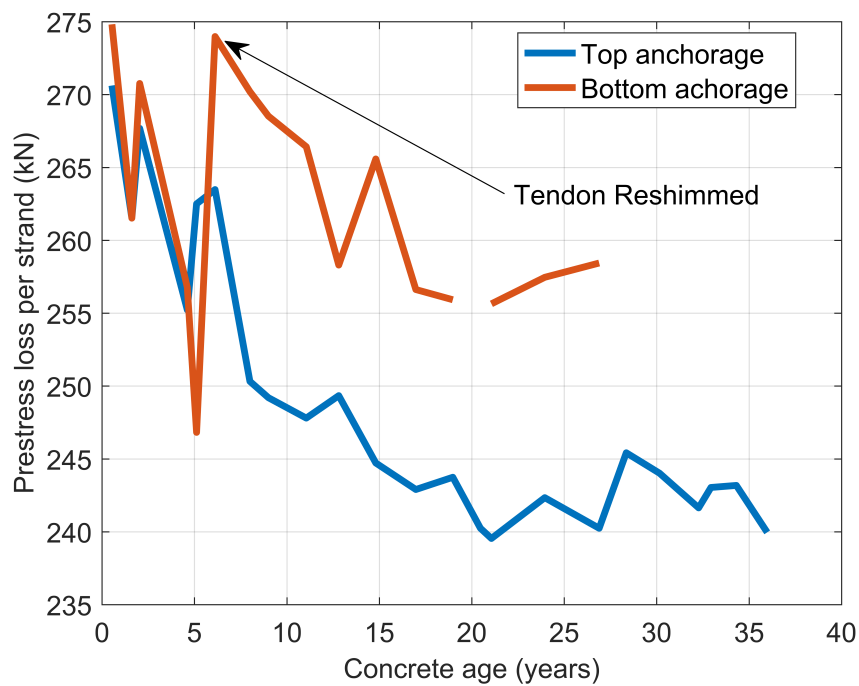


Fig. 2.17 Average strand lift-off force on a PCPV measured by a reactor operator. The bottom anchorage shows that sometimes it is necessary to increase tendon load to meet operating requirements. Shims are placed between the barrel and anchor plate to increase the load in already stressed strands.

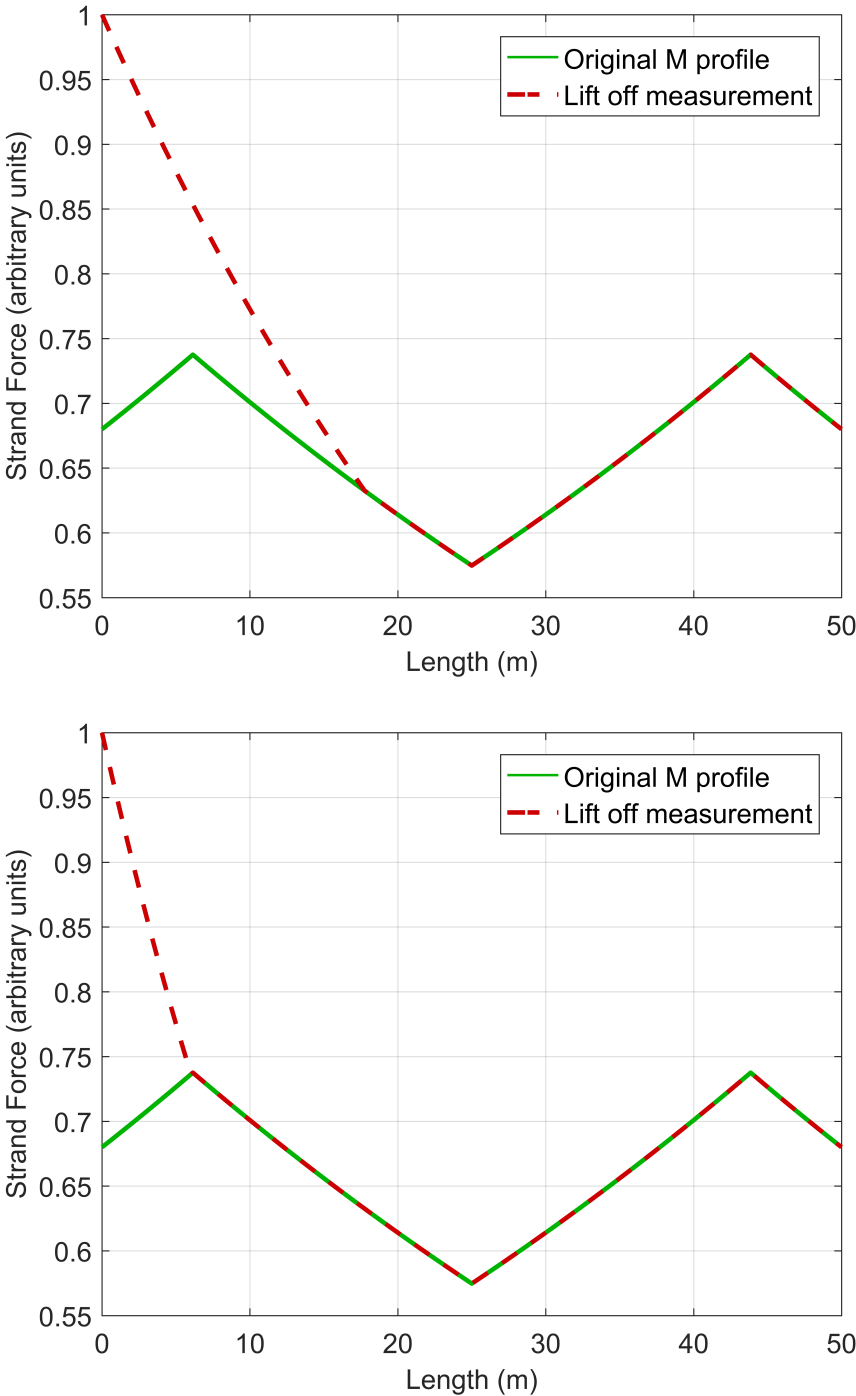


Fig. 2.18 Effect of the friction coefficient on strand mobilisation. Figure a) and b) show the difference in the length of strand mobilised during a lift-off measurement when the coefficient of friction is 0.4 or 0.8 respectively. Strands may have an increased friction coefficient due to corrosion or interstrand friction and this may cause errors in determining strand force from the lift-off measurement.

2.4.3 Load cells

Load cells are typically constructed from several electrical strain gauges. The change in resistance due to strain can be measured as a voltage signal using a Wheatstone bridge . Hartlepool and Heysham 1 have load cells installed to measure inward radial load on the vessel. Elsewhere in the world, in grouted duct prestressed concrete, load cells are used in several ungrouted ducts to calculate the average prestressing force on the structure [43]. Load cells are relatively easy to install and could complement a distributed force/strain measurement, especially as this is the only way to measure steel relaxation.

2.5 Summary

Nuclear reactors produce electricity from nuclear fission, the energy released heats water into steam to drive turbines. In the UK, the majority of the reactors currently online are advanced gas-cooled reactors. These use carbon dioxide to transfer away from the reactor. One pressurised water reactor is also still in operation. Reactors operate under high temperature and pressure and emit harmful radiation, therefore they are designed with a large number of safety features both engineered and passive. A high level of redundancy and avoidance of common mode failures ensures safe operation and containment of radiation in the unlikely event of a major incident. During normal operation the PCPV of an AGR contains operational pressure, while both the PCPV and PCC, of a PWR, are critical structures in the passive safety system. In the event of a fault, the PCC/PCPV withstand high pressure and shield the outside from radiation.

The PCC/PCPV is constructed with post-tensioned prestressed concrete. While concrete is strong in compression, it has a weak tensile strength. Prestressed concrete overcomes this weakness through the use of high strength, low relaxation steel within the structure. The steel prestressing tendons provide triaxial concrete compression, however prestress in the structure is lost through a number of instantaneous and time dependent effects. Instantaneous effects occur at the time of stressing and include: elastic effects such as concrete compression, friction on the tendon and anchor slippage. Time dependent effects occur over many years and are affected by environmental factors like temperature and humidity. These effects include concrete creep and shrinkage and steel relaxation. It is hard to predict the exact prestress loss in a structure at any given time because of variation in the environmental conditions and anisotropy in the structure. Therefore, it is necessary to monitor prestressed concrete structures and traditionally this work is carried out through manual inspection using the lift-off technique. Measuring prestress loss

this way limits measurements to the total tendon force and requires friction and the length of mobile strand to be estimated.

It would be beneficial to install a new monitoring system to complement current prestress measurements using improved technology that has become available recently. This would allow prestress loss to be monitored online rather than being measured manually once every 1.5-5 years. The following chapter describes the requirements of such a monitoring system, while Chapter 4 details the theory behind fibre optic sensing, the selected sensing technology, and highlights the benefits it has over conventional sensing methods.

Chapter 3

Proposal for monitoring scheme

The previous chapter has shown that it would be beneficial to install new prestress loss monitoring sensors and it would be useful if these sensors could be linked to an online monitoring system. The main arguments for installing new sensor technology are the following [21]:

- **Safety:** For example, a typical PCPV has a minimum design load of 1600 kN per tendon, which equates to ~ 230 kN or 1025 MPa per strand. Tendon prestress force must not fall below 1495 kN and all tendons within one reactor quadrant should be within 75 kN of the mean force. By increasing prestress surveillance coverage, the complete prestress load on the PCC/PCPV can be better monitored and predicted.
- **Reliability:** Redundancy is a key safety feature of the nuclear power plant. Additional sensor technologies can complement the existing monitoring techniques through cross-checking and combining information. This reduces common mode failure.
- **Resolution:** Current measurements calculate the average force of the moveable part of a strand. Uncertainties in friction and the length of strand that has been mobilised are accounted for by reducing the lift off measurement force by 5 %. A distributed measurement will remove this assumption. Currently, there is no spatial resolution; this would be of real industrial value as prestress nears the minimum design limit [44].
- **Costs:** Lift off measurements are expensive, time consuming and relatively dangerous for the workers that service the tendons. During a reactor outage it takes a long time to measure a small percentage of strands. Online monitoring of prestress levels may remove the need for lift-off measurements, or for them to be undertaken after longer intervals, reducing reactor downtime.

3.1 Monitoring system requirements

The system must provide a distributed strain or force measurement, of adequate accuracy, along the strand. The sensors must be installed in existing reactor containments, therefore it would be sensible to instrument current prestressing strands that meet the BS 5896:2012 standard with a number of sensors. The instrumented strands would then prestress the structure and monitor its prestress loss at the same time, providing an early warning of any tendons that fall below the minimum design load. The requirements of such a monitoring system are listed below:

- **Installation:** Instrumented strands must follow a similar installation and stressing procedure as standard strands. At the very least, the new strands must be welded onto the old one and pulled through the entire tendon duct without damage to the sensor system.
- **Retrofitted:** The reactors have already been built so any sensors that must be installed during vessel construction are not appropriate.
- **Similar strand properties:** The strands must adequately prestress the containment building and have proven reliability.
- **Measure high strain:** Sensors must be able to measure up to 7 mε. Strands are initially stressed to 1300 MPa, resulting in 6.7 mε. Table 2.2 shows the prestressing strand properties.
- **Passive:** Sensors requiring electrical power are not suitable inside the PCC/PCPV.
- **Resolution:** The majority of the concrete creep and shrinkage occurs in the first few years, therefore the strain resolution requirements differ for new and old reactors. Nonetheless, the sensors must have better than sub-millistrain resolution. This is investigated in detail in Section 3.1.1.
- **Accuracy:** Sensors must be accurate enough to be relied upon when making engineering decisions about the state of the PCC/PCPV.
- **Cost:** The sensor system must provide value of information [45]. The data acquired from the sensors must be of enough value to the reactor operators to offset the installation cost and maintenance of the interrogation system.
- **Calibration:** Sensors must be able to be properly calibrated and remain calibrated during their service life. Once installed recalibration will not be possible.

3.1.1 Strain resolution

To quantify the strain resolution that is required to monitor prestress loss, a logarithmic function was fitted to lift-off measurements taken from two PCPVs. The measured lift-off force data and the fitted line for one PCPV can be seen in Figure 3.1. The estimated steel relaxation calculated from Equation 2.11 is also shown. The expected strain measured by a sensor attached to a prestressing strand would be the difference between these two curves.

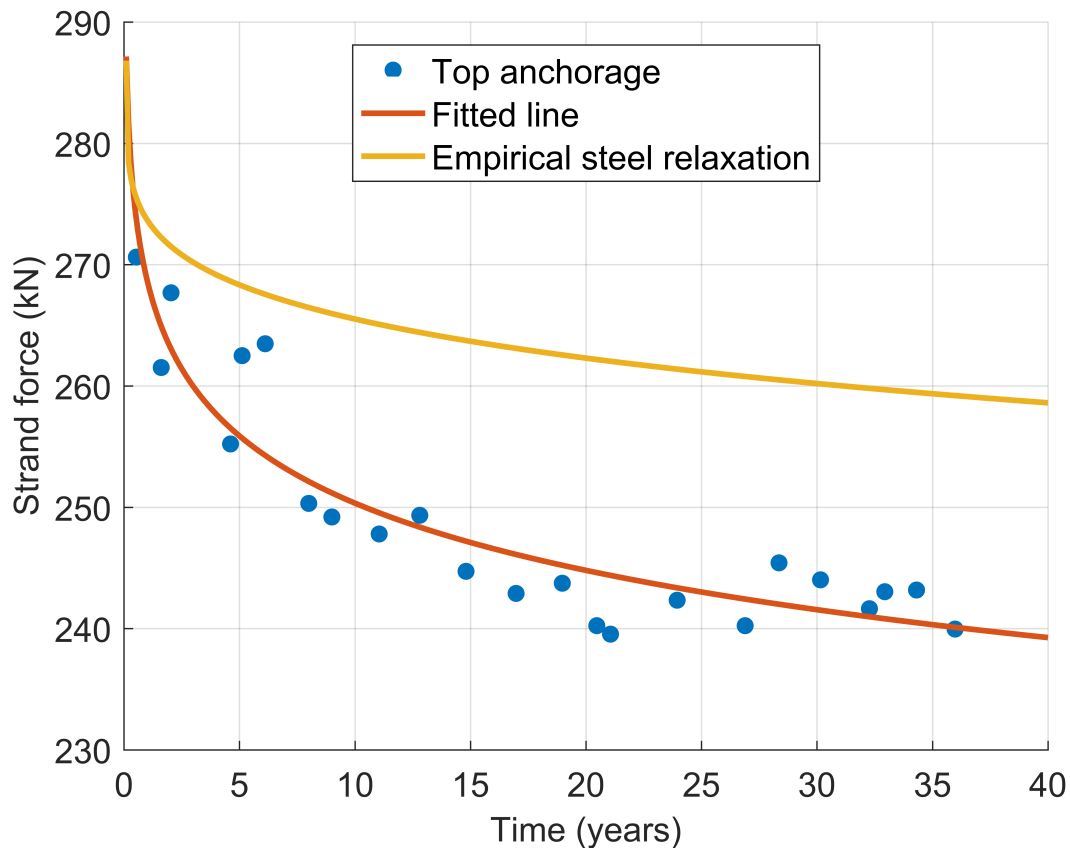


Fig. 3.1 Lift off force per strand compared to steel relaxation for a PCPV. Steel relaxation calculated from Equation 2.11 is also plotted. The difference between the log curve fitted to the data and the steel relaxation is the estimated prestress loss due to creep and shrinkage.

Figure 3.2 shows the resultant strain that would be measured by sensors attached to the prestressing strands. The total decrease in strain in PCPV 1 over 25 years was $0.38 \text{ m}\epsilon$, while in PCPV 2 the strain decrease was $0.53 \text{ m}\epsilon$ over 40 years. The majority of the decrease in prestress force occurs in the first few years, as expected from Section 2.3. For example, there is a strain decrease of $0.38 \text{ m}\epsilon$ in the first five years in PCPV 2, corresponding to a change of $76 \text{ m}\epsilon/\text{yr}$. Whereas, there is a strain decrease of only $0.03 \text{ m}\epsilon$ in the last 15 years, resulting in a change of

$2 \text{ m}\epsilon/\text{yr}$. Consequently, during the early years of a reactors operation, micro-strain resolution is required. While, in the later years the required resolution is of the order of nano-strain. This is a challenging constraint for reactors nearing the end of their operating life.

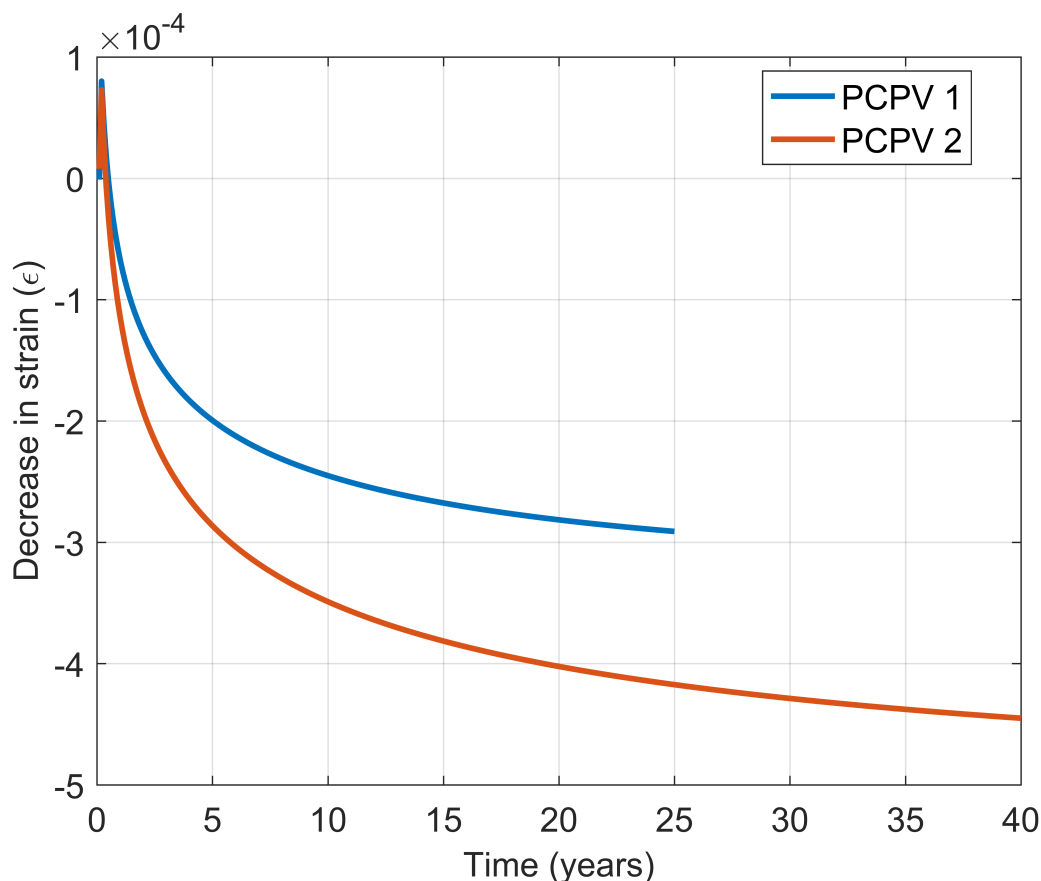


Fig. 3.2 Estimated strain loss due to creep and shrinkage for two PCPVs. The two curves are the expected measurements if strain sensors were attached to one of the prestressing strands in the PCPVs

In terms of the number of sensors, at least 6 sensors per prestress tendon are required to spatially resolve the ‘M’ shaped force profile due to duct friction. Although more than 9 sensors, with 3 on each section of the ‘M’ profile will provide better accuracy as the force gradients can be fitted with at least 3 data points.

3.2 Strain and temperature sensors

There are a few ways of measuring force, many are elastic based, such as electrical resistance strain gauges, where force on the transducer produces a repeatable deformation. Other

techniques include: utilising the piezoelectric effect, pressure based devices, linear variable differential transducers or optical strain gauges.

It is proposed that the prestress force at several points along the prestressing tendons will be obtained by elastic-based transducers; measured strain will be converted to stress via the strands elastic modulus. Temperature sensors will be required, in addition to strain sensors, to monitor thermal fluctuations and their effect on the tendon force. This will allow thermal strain in the tendons to be compensated for, resulting in a measurement of the tendons mechanical strain. The strain and temperature sensors must be small and near 1D in shape, and it must be possible to interrogate them from a distance of at least 40 m due to the length of the prestressing strands.

In addition to their desirable size and geometry for this application, optical fibre sensors are well suited to provide distributed measurements of strain and temperature in harsh conditions [3]. Within a nuclear and electricity generation context, optical fibre sensors may provide a unique solution to sensing problems due to their intrinsic properties such as excellent multiplexing potential, immunity to electromagnetic interference, safe mode of operation and radiation resistance [4]. One type of fibre optic sensor is based on the fibre Bragg grating (FBG). They are commonly used in strain sensing applications especially for structural health monitoring (SHM) [46, 47]. Chapter 4 will outline further benefits of this type of sensor and the relevant theory, while Chapter 5 describes the methods needed to fabricate optical FBG sensors suitable for this application.

3.3 Load cells

Stress relaxation occurs at constant strain, as noted in section 2.3.2, so it is not possible to measure it with elastic displacement based sensors, neither is it practical to place other types of force sensor within the strand duct. Therefore the cumulative effect of stress relaxation on total strand force should be measured at each end by load cells. These can be either electrical or optical and there is less constraint on their size, reliability and calibration as they can be serviced if necessary. The load cell force can be used to check and combine with the strain sensor measurements to measure the total prestress loss of a tendon.

3.4 Structural information from sensor data

A monitoring system with distributed temperature and strain measurements, as well as total force at the anchorages can provide information about the following things:

- Distributed strand strain/force.
- Effect of temperature on strand strain.
- Strand force profile.
- Effect of friction on force profile.
- Time dependency of creep, shrinkage, steel relaxation and thermal strain.

All of this information is useful for the safe function of the reactor, useful for analysis of the design loads and predictions, and of interest for future design improvements.

3.5 Summary

The proposed monitoring system consists of BS 5896:2012 prestressing strands instrumented with fibre optic strain and temperature sensors at several locations along the strand. Load cells at each end of the strand will measure the total force of the strand allowing steel relaxation to be determined. This monitoring system will be able to measure all the prestress loss effects and provide real measurements of the effect of strand friction on the force profile. The next chapter will demonstrate why fibre optic sensors are so well suited to an application like this.

Chapter 4

Fibre optic sensing of physical parameters

4.1 Optical fibre

Optical fibre was originally developed for communications links; however over the past 40 years it has been increasingly used as a host for sensors. The proposed sensor system uses optical fibre as the sensor interrogation link as well as for strain and temperature sensors. The basic theory of light propagation in optical fibre will be discussed, followed by how the fibre can itself be turned into a sensor.

4.1.1 Basic principle

Optical fibre is comprised of a cylindrical core and cladding made from silica glass. The core and cladding have different refractive indices allowing light to propagate down the fibre by total internal reflection.

When electromagnetic radiation, EM, propagates through a glass medium, it causes local electrons to oscillate. The electrons emit a secondary electromagnetic wave with a phase delay due to the interaction. The superposition of the original and induced wave travels more slowly and this is quantified by the refractive index. A small percentage of the light is also scattered or absorbed by the medium so that the intensity of the propagating EM wave decreases exponentially with increasing length.

Total internal reflection

As shown in Figure 4.1, light incident on an interface with angle, θ_i between two media, with different refractive indices (n_i and n_t), is transmitted with an angle, θ_t according to Snell's Law:

$$n_i \sin(\theta_i) = n_t \sin(\theta_t) \quad (4.1)$$

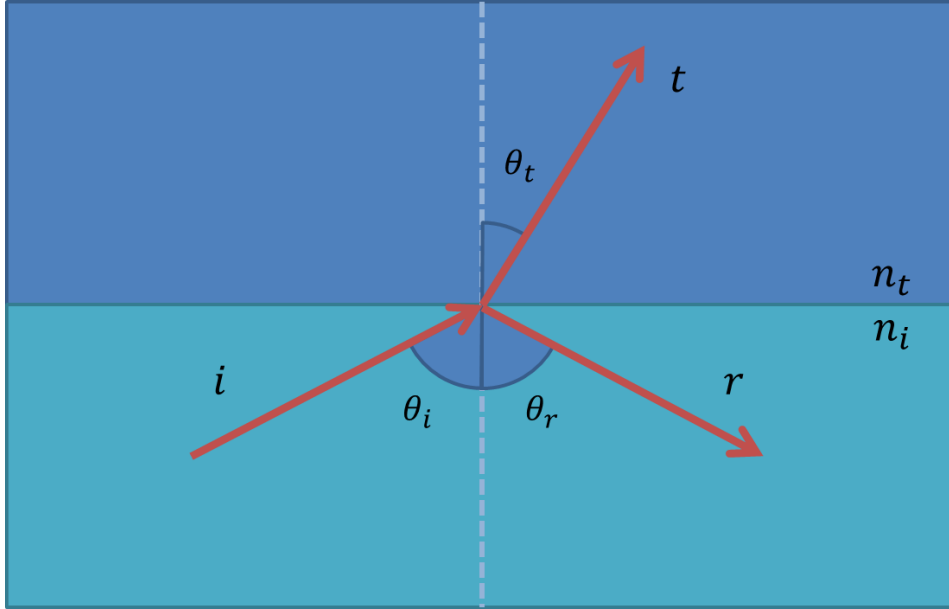


Fig. 4.1 Reflection and transmission of a ray of light at a refractive index interface.

Where the light travels in the direction from higher to lower refractive index, there is a critical incident angle θ_c when light is reflected perpendicular to the interface i.e. $\theta_t = 90^\circ$. For incident angles larger than the critical angle, light is completely reflected back into the incident medium, this is known as total internal reflection (TIR). Light is guided along multi-mode optical fibre using this principle; see Figure 4.2. A small percentage of the EM field propagates in the cladding of the fibre. This is known as the evanescent field and adds a small phase contribution to the wave.

The numerical aperture of a fibre is the sine of the maximum angle, known as the acceptance angle θ_{acc} , of an incident ray that is guided along the fibre core by TIR and is given by [48]:

$$NA = \sin(\theta_{acc}) = \frac{n_1}{n_0} (1 - \sin^2(\phi_c))^{1/2} = \frac{1}{n_0} (n_1^2 - n_2^2)^{1/2} \quad (4.2)$$

where n_1 , n_2 and n_0 the refractive index of the core and cladding and the surrounding medium (usually air), respectively. This description is valid for multi-mode fibre with a core diameter of larger than approximately 10λ . A fibre can be made to propagate a single mode for a given wavelength, λ , by reducing the core diameter and the refractive index difference. A fibre is single mode if its V number satisfies $V < 2.405$. The V number is given by [48]:

$$V = \frac{2\pi a}{\lambda} NA \quad (4.3)$$

where a is the fibre diameter. The core diameter in single mode fibre is of comparable order to the light's wavelength, so the description of propagation by TIR is not valid. Maxwells equations describe the complete mode propagation in single-mode fibre, but they are beyond the scope of this thesis. Consult Ghatak et al. for more information [49]. This work uses only single-mode fibre due to the use of Bragg gratings as sensors and due to the presence of radiation.

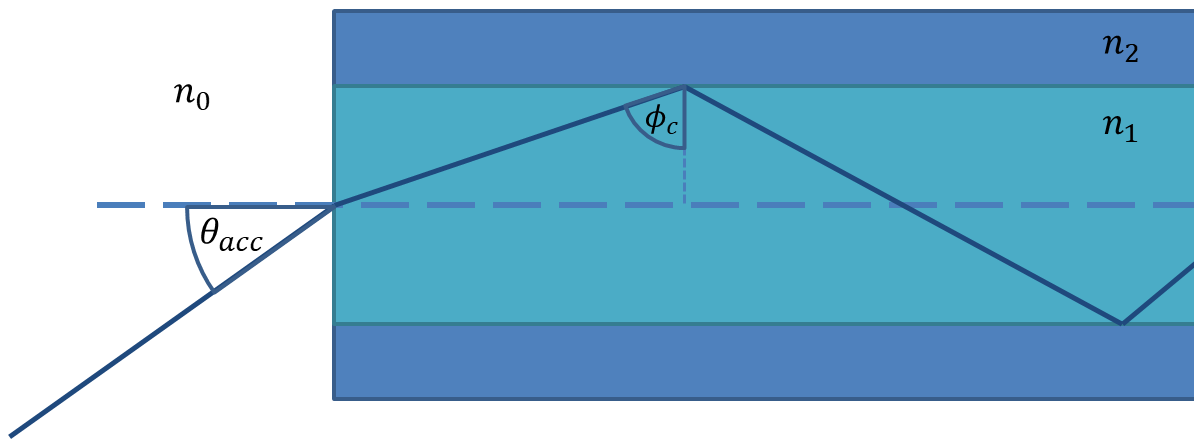


Fig. 4.2 Total internal reflection inside an optical fibre.

4.1.2 Losses

Optical losses in fibres vary with wavelength but are typically very low in the telecommunication bands and nearly reach the loss coefficient of pure silica. At 1550 nm the loss for SMF-28 fibre is typically 0.2 dB/km [50]. This is calculated using:

$$\alpha_{att} = \frac{10}{L} \log_{10} \left(\frac{P_1}{P_2} \right) \quad (4.4)$$

where P_1 and P_2 are the optical power launched into the fibre and the optical power at a distance, L , respectively. Due to the environment inside a nuclear reactor where radiation, moisture and high mechanical stress are present, fibre loss mechanisms must be considered further.

Scattering

Fibre losses are generally dominated by scattering and in particular by Rayleigh scattering. This type of scattering is caused by random density fluctuations due to the irregular microscopic

structure of silica glass. Rayleigh scattering is more prominent when the wavelength of the light is similar to the width of the scattering centres, so shorter wavelengths are scattered more readily.

Other scattering phenomena that affect optical fibres include Raman and Brillouin scattering. Both are nonlinear responses related to lattice vibrations of the silica glass. Vibrational energy in the lattice is quantised and can only be exchanged by discrete amounts, phonons. Where the vibrations are associated with optical phonons the effect is called Raman scattering, while Brillouin scattering is related to acoustic phonons. Scattering also occurs at the core-cladding interface due to imperfections.

Absorption

Absorption of photons in optical fibres occurs due to intrinsic absorption in silica glass and absorption by defects and impurities. At infrared wavelengths the main fibre loss is multi-phonon absorption. This is essentially the point where silica glass becomes less transparent and it becomes significant above ~ 1650 nm. The low loss window around 1550 nm is the result of Rayleigh scattering affecting short wavelengths and infrared absorption at large wavelengths. The intrinsic absorption of silica is increased by gamma and neutron radiation through an increased fibre density.

Defects and impurities also cause fibre absorption. Defect points in particular can cause strong, narrow absorption bands. Gamma and neutron radiation also increase the number of these defects, as such they are an important consideration for optical fibre operating in nuclear environments. Historically, optical fibre suffered from loss at 1400 nm due to OH-bond contamination, this has largely been removed through improved manufacturing. Radiation and OH ingress due to moisture can cause absorption in this wavelength region to return.

Bending

Macroscopic bending results in the incident angle of light on the core-cladding interface decreasing. At some point the incident angle becomes close to the critical angle for TIR and light is lost into the cladding. Therefore a minimum bend radius is often specified for optical fibre. Microscopic bending of the core-cladding interface also occurs, resulting in attenuation. These irregularities are created during fabrication and any time the fibre is put under stress such as during heating, coating or fusion splicing fibres.

4.1.3 Fabrication

Commercial single mode fibre is fabricated from a preform. A preform is essentially a larger scale optical fibre, typically 1m in length and a few centimetres in diameter, with a central area of higher refractive index that forms the fibre core. The preform is heated close to its melting point and pulled from the bottom, resulting in kilometres of 125 μm diameter fibre.

Fibre coatings

Fibre coatings are applied during the fabrication process to prevent nicks and scratches in the silica surface which can cause fibre failure due to its brittle nature. A variety of coatings can be applied including polymer coatings like acrylate or polyimide, metals such as gold, aluminium or copper, and carbon coatings. A hermetic seal is required in moist environments as hydrogen ingress reduces fibre strength and increases attenuation.

4.1.4 Radiation induced attenuation

Gamma and neutron radiation cause attenuation by increasing the number of point defects and through fibre compaction, an increase in fibre density. The review article by Perry et al. will be used to determine if this attenuation will be significant in the proposed online monitoring system [4].

Point defects

There are a number of naturally occurring point defects in silica glass, some are caused by contamination but these can be largely removed by coating the fibre in a protective layer. Others can be caused by neutrons and gamma rays with energies above 1 MeV. Bombardment by these types of radiation result in atomic displacements and bond breakages leading to a variety of network, interstitial and dangling bond defects [51]. For example, the presence of hydrogen in a fibre can lead to hydrogen defects under neutron and gamma radiation, resulting in increased attenuation in the infrared region due an attenuation peak comparable to the water peak [52, 53].

Compaction

Compaction is a fractional increase in fibre density, causing an increase in the fibre refractive index and the absorption coefficient. Neutron and gamma radiation both cause compaction through different mechanisms. Incident neutrons convert sections of the fibre to a denser 'metamict phase' [54]. Once the fibre has been completely saturated, there is a linear 2-3 %

increase in density [4]. Gamma compaction, on the other hand, breaks intermolecular bonds. This relaxes the entire network causing a density increase. Gamma ray induced compaction dominates at low doses.

Fibre dopants

Fibre dopants are used to increase the refractive index of the core. However, they reduce the radiation hardness to gamma rays due to increased intrinsic bond strain [4]. Dopants also act as defect centres. There are numerous studies on the effects of fibre dopants on radiation induced attenuation, including [55–58]. In summary, they show that germanium, erbium and phosphorus are detrimental to radiation hardness. While undoped, ultra pure silica or fluorine doped cores have very good radiation resistance [59, 60]. It should be noted that, multimode fibre is generally unsuitable for gamma rich environments due to the high dopant concentrations needed to increase the core refractive index.

Fibre coating

The fibre coating material has a strong influence on the degradation of fibres in fast neutron environments. Hydrogen nuclei present in polymer coatings can be embedded into the cladding when struck by neutrons. Brichard et al. irradiated polymer and aluminium coated fibre, and tested attenuation in the 400-1700 nm region. The results show that the polymer coating had increased attenuation at the water peak [51], this is an indication of hydrogen contamination [61]. Furthermore, the attenuation continued to increase after irradiation as the hydrogen nuclei diffused into the core. Therefore it is advisable to use a low hydrogen polymer or metal coated fibre for nuclear applications [4, 62].

Long term stability

For a tendon duct with 0.3 m of concrete between it and the reactor, a radiation dose for 10 years is calculated to cause a radiation induced attenuation (RIA) of <1 dB/m. The prestressing strands are roughly 30-60 m in length, so after 10 years at 60 m from the light source there would be an attenuation loss of 50 dB. However, as seen in Section 2.1.3, radiation intensity falls rapidly; therefore 1 m from the reactor, RIA is negligible and the attenuation is dominated by splices in the fibre network. This is a very conservative estimate as some of the data used for the attenuation calculations came from a fusion experiment where dose rates were higher than those observed in this application. Considering the assumptions, a fibre system placed one metre from the reactor lining will experience minimal RIA allowing the use of metal-coated

standard SMF-28 fibre for this project. Should the fibre system need to be placed closer than 1 m to the reactor, radiation resistant fibre is available, although with an increased cost. High purity silica core and fluorine doped cladding improve radiation resistance [59, 60, 63]. Photonic crystal fibres present further opportunities to improve radiation hardness too [64–67].

4.2 Fibre optic sensors

Fibre optic sensors are used for sensing physical quantities such as temperature and strain. Light sent through such a device undergoes small changes in properties which can be measured by a detector. In general fibre optic sensors have many advantages over their electrical counterparts including [3]:

- Small size.
- Passive, they do not require power.
- Immune to EM interference.
- Resistant to harsh environments.
- Distributed measurements are possible.

It is because of these advantages that fibre optic sensors have seen success in harsh environment applications where established monitoring technology is either inadequate or missing altogether. Fibre optic sensors may be based on, but not limited to, wavelength- or intensity-encoded measurements. Due to RIA, only wavelength based sensors are suitable for this application. These types of sensors can be grouped into three classes depending on the number of available sensing points on a single fibre:

- Point sensors - These sensors are used when a high accuracy measurement of a specific region is required. The most common point sensor is the Fabry-Perot interferometer (FPI). FPIs consist of a resonator cavity where light is partially reflected between two mirrors. A sharp resonance pattern is produced which is dependent on the length of the cavity; therefore, it can be used to measure temperature and strain. FPIs are accurate and can be cheap to fabricate.
- Quasi-distributed sensors - Some point based sensors can be multiplexed on a single fibre and are termed quasi-distributed as they allow many discrete measurements along

a length of fibre. Due to their narrow wavelength encoded reflection, multiple fibre Bragg gratings (FBGs) can be multiplexed together to monitor strain and temperature. FBGs have established themselves as the prominent optical sensor for structural health monitoring applications in part due to their simplicity and similarity to conventional electronic strain gauges. They have a high strain sensitivity, are capable of monitoring strains of up to $10\text{ m}\epsilon$ and are relatively easy to interrogate.

- Distributed sensors - It is possible to turn an entire length of optical fibre into a sensing medium, providing an infinite number of sensing points. This results in a highly versatile sensor where the 'sensor' or gauge length can be tuned for the application. In SHM this is an advantage as sometimes global strain values are more important than local ones [68]. There is, however, a trade off between spatial and strain resolution, in addition to the cost of the interrogator systems. Distributed sensing can be based on either Rayleigh, Brillouin or Raman scattering although their operation principles are beyond the scope of this thesis [69]. All these techniques rely on time of flight measurements to determine the section of fibre that a signal belongs to and thus require high speed electronics.

For the application of monitoring prestress of PCPVs and PCCs, strains of up to $7\text{ m}\epsilon$ need to be measured at several points along the prestressing strand. Quasi-distributed and distributed fibre optic sensors are capable of these strain measurements, however FBGs were chosen as they can offer good strain resolution at a relatively low cost. Furthermore, they are beginning to be widely implemented in industry and are the optical equivalent of the extremely well established electronic strain gauge, so they are a lower risk solution. Several other advantages for this application include the following:

- Their radiation dependence is better understood.
- They are modular and multiplexible for different tendon lengths.
- Attachment of the system to the tendon is only necessary at the sensor location.
- Higher sampling rates can be achieved compared to distributed optical sensing.

Now that FBGs have been chosen as a good match for this application their properties including strain, temperature and radiation dependence are detailed.

4.3 Fibre Bragg gratings

An FBG is a periodic modulation in the refractive index of the core of a fibre [70]. Depending on its parameters, the FBG will reflect a peak with a certain wavelength value. Figure 4.3 shows a representation of an FBG, while Figure 4.4 shows the reflected Bragg peak.

4.3.1 Basic principle

At a refractive index interface light is Fresnel reflected. Assuming a perpendicular incidence, the percentage of reflected light is dependent on the refractive index of the two medium n_1 and n_2 :

$$R = \left(\frac{n_1 - n_2}{n_1 + n_2} \right)^2 \quad (4.5)$$

The light also undergoes a phase shift of π or zero if the refractive index increases or decreases respectively. This allows the reflected field contributions from different parts of the grating to constructively interfere for a small range of wavelengths, given the grating parameters. This is a phase matching condition where the grating wavenumber matches the difference of the wave vectors of the reflected and transmitted waves; it is known as the Bragg condition [48]:

$$\frac{2\pi}{\Lambda} = 2 \cdot \frac{2\pi n_{eff}}{\lambda} \Rightarrow \lambda = 2n_{eff}\Lambda \quad (4.6)$$

Where Λ is the grating period, n_{eff} is the average effective index of the grating and λ is the Bragg peak wavelength. Side lobes around the peak wavelength are also reflected due to other harmonic wavelengths that can constructively interfere [71]. These relate to interference over multiples and fractions of the grating period, leading to a reduced reflectivity compared to the main peak. Side lobes can adversely interfere with gratings written at similar wavelengths, so they can be reduced by apodising the refractive index modulation, see Figure 4.4. A larger index modulation leads to: increased peak reflection, a broader peak full width half maximum (FWHM) and higher side lobes. Therefore, there is a trade off between grating reflectance, FWHM and side band suppression for a grating of given length. FBGs used in this project were 7 mm long, apodised, with a FWHM of approximately 0.25 nm and a reflectance of 50-60 %, see Section 5.4 for more details.

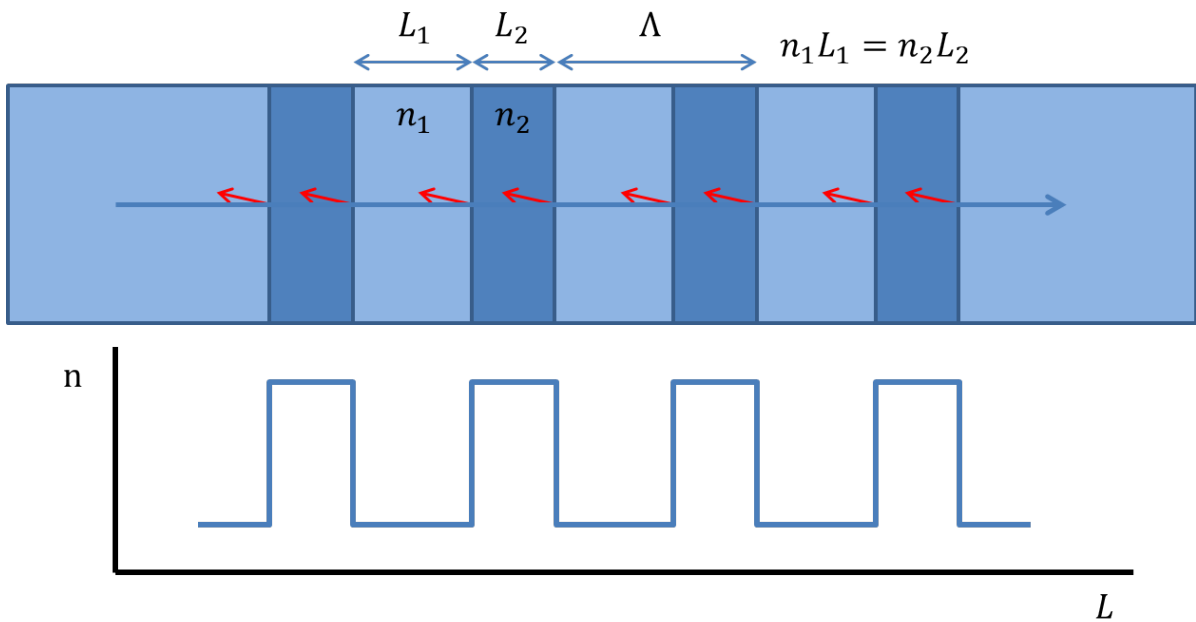


Fig. 4.3 Refractive index profile of a Bragg grating written in fibre. Reflections at each refractive index interface constructively interfere for a small range of wavelengths determined by the grating periodicity, Λ and the difference between n_1 and n_2 .

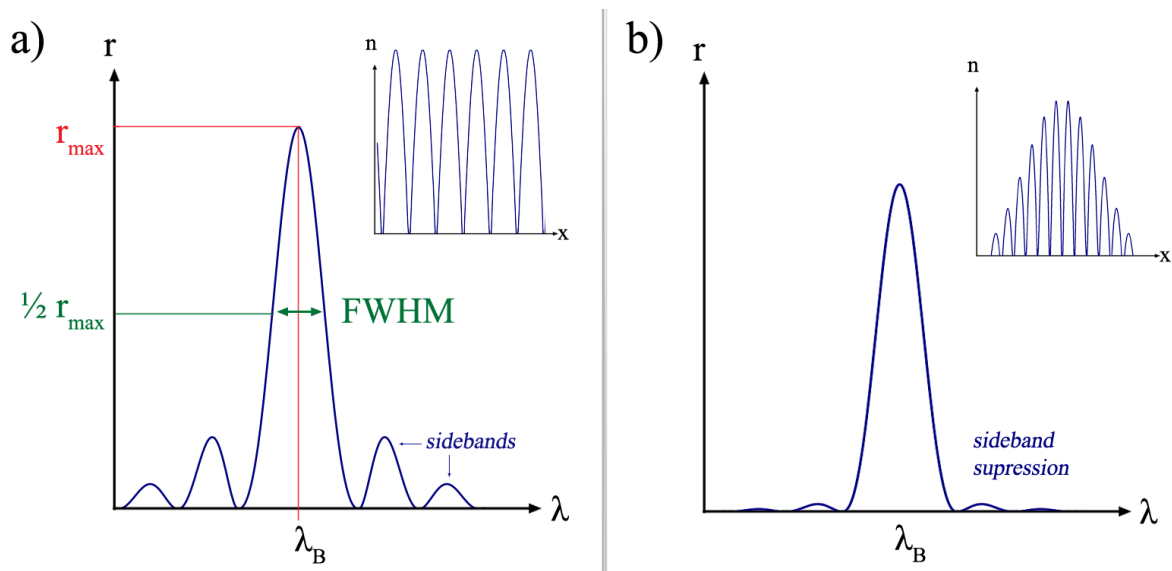


Fig. 4.4 Reflection spectrum of an FBG without a) and with b) apodisation. The sidebands of apodised FBGs are suppressed, reducing the chance of them being erroneously detected by peak finding algorithms. The refractive index profile for both resulting spectrums are shown inset. An FBG's full width half maximum is measured as shown in a) [7].

4.3.2 Fabrication

FBGs are generally fabricated by exposing the fibre core to ultraviolet (UV) light, this induces a permanent change in the refractive index. A repeating UV intensity profile along the fibre axis is achieved through interferometry or by use of a phase mask. Alternatively the areas of high refractive index can be induced with a femtosecond laser [72]. In this case, two photon absorption at the focus of the pulses allows the near infrared laser light to be absorbed. Canning provides a thorough review of the different types of FBGs, their fabrication and the mechanisms that cause the refractive index changes [73]. To summarise, gratings can be split into three main groups: Type I, Type II and Regenerated gratings. Type II differ from Type I as the grating is fabricated with laser light whose intensity is greater than the glass damage threshold. While regenerated gratings emerge from Type I gratings after they have been erased by high temperature.

Standard Type I gratings are written in photosensitive fibre, mainly Ge-doped. The UV light affects the oxygen deficiency bands around 244 nm and 320 nm, with the change in refractive index the result of a combination of polarisability and structural changes and densification [73]. Type I gratings can be further split into subgroups with subtle fabrication and therefore performance differences as sensors. For example Type IH have an enhanced refractive index change due to the presence of hydrogen [73]. Standard Type I gratings are thermally erased around ~ 320 °C, while some non damage induced gratings such as Type In can withstand temperatures of up to 800 °C for short periods of time.

The refractive index change of Type II gratings is created by fractures, void formation and filamentation due to the high intensity UV light. They can be stable for temperatures exceeding 1000 °C. Regenerated gratings can also withstand similarly high temperatures [74], they are produced by annealing out Type I gratings at temperatures higher than 500 °C.

4.3.3 Temperature and strain dependence of the wavelength response

Temperature changes result in fibre thermal expansion which affects both the periodicity and the refractive index. The normalised change in Bragg wavelength for a change in temperature, ΔT is given by:

$$\frac{\Delta\lambda_B}{\lambda_B} = (\alpha_\Lambda + \alpha_n)\Delta T \quad (4.7)$$

Where $\alpha_\Lambda = 5.5 \times 10^{-7}$ °C⁻¹ and $\alpha_n = 6.67 \times 10^{-6}$ °C⁻¹ are the thermal-expansion and thermo-optic coefficients for silica¹[75]. The refractive index change is an order of magnitude

larger than the fibre thermal expansion, but if the FBG is attached to a substrate it will also experience thermal strain related to the substrate thermal expansion. This can be significant if the FBG is attached to a metal such as steel, where $\alpha_{steel} = 16.0 \times 10^{-6} \text{ }^\circ\text{C}^{-1}$. The substrate thermal expansion is imposed on the wavelength shift through the strain dependency of an FBG.

Strain applied to an FBG along the fibre axis stretches the fibre causing an increase in the periodicity of the FBG, while the refractive index decreases due to the elongation. In terms of the Bragg wavelength, these two effects oppose each other as seen in Equation 4.6. However there is an overall linear increase in wavelength for an increase in strain:

$$\frac{\Delta\lambda_B}{\lambda_B} = (1 - p_e)\varepsilon_z \quad (4.8)$$

The strain-optic coefficient, $p_e = 0.22$ is related to the reduction in refractive index [75]. Detailed derivations of the temperature and strain sensitivity of an FBG can be found in Appendix A.3 and A.4 respectively.

4.3.4 Radiation dependence of the wavelength response

The radiation dependence of the Bragg peak wavelength is complex and still the subject of on-going research. As we have seen previously in Section 4.1.4, gamma radiation induces fibre compaction; it also normalises the refractive index modulation of FBGs causing red-shifts and peak reflection decreases [77–79]. FBGs written in Ge-doped fibre see the peak red-shift saturate after about 20pm for a dose of 80 kGy. Subsequent doses up to 1.5 MGy don't cause further peak shifts, changes in FWHM or temperature sensitivity [61, 80, 81]. This radiation dependence is not unique to Ge-doped FBGs however, most FBGs show some saturation in their peak shifts due to gamma radiation [82]. Some of the smallest red-shifts have been found in type II gratings, fabricated with a UV femtosecond laser in fluorine doped fibre cores. These exhibited shifts of less than 5 pm for a 1 MGy dose.

Peak shifts are gamma dose rate dependent; doses of 1-25 kGy/hr caused shifts of 20-80 pm in Ge-doped fibre [81]. While the temperature of the FBG during irradiation is also an issue as refractive index changes are related to glass relaxation [82]. FBGs can show post-irradiation recovery, leading to a blue shift in the FBG peak once the FBG is removed from the radiation field [83]. The result of these effects is that without proper attention they can produce strain

¹Equation 4.7 is linear, however for large temperature ranges it has been shown that a quadratic fit to the Bragg wavelength is more accurate [76]. The temperature range in this application allows a linear fit to be used with very good accuracy.

and temperature errors. These can be mitigated somewhat by irradiating the FBGs before installation to induce a controlled peak shift past the saturation point [84, 85].

Additionally, like fibre coatings, FBG coatings must be considered in the presence of radiation. Gamma radiation has been found to cause swelling in polymer coatings which can result in a strain induced peak shift; 40 kGy doses cause peak shifts of 50, 20 and 10 pm for Ge-doped fibres with ormocer, polyimide and no coating respectively [86]. Therefore it is advisable to avoid polymer coatings for FBGs in radiation rich environments.

Perhaps more important for this application are the low dose, long term effects on FBGs. Gusarov et al. subjected various Ge-doped and hydrogen loaded FBGs to fast neutrons (10^{17} cm^{-2} fluence) and gamma rays (10 MGy) over 8 years [87]. All fibres showed 60 pm shifts from neutron radiation, however shifts from gamma rays were chemical composition dependent. The smallest peak shift, of 50 pm, was found in non-hydrogen loaded, pre-irradiated fibre, coinciding with a 0.09 dB peak amplitude reduction. Pre-irradiated, pre-aged fibre had the smallest change for hydrogen loaded fibre with a 0.12 nm shift and a 0.97 dB peak reduction.

Additionally, in a strain sensing context, radiation compaction could affect fibre elasticity which would in turn affect the conversion of wavelength to strain and stress. It has been shown that FBG strain sensitivity can increase by 5 % with 400 kGy doses of gamma radiation [82]. This could be due to microscopic factors such as bond strength and conformation which have a direct effect on elasticity [88]. Strain errors could also arise where fibre is bonded to a fixed substrate, fibre compaction will subject the FBG to tensile stress as its length and cross section reduce [4].

Radiation shift dependence

While there are a lot of different effects to take into consideration, the error for a temperature or strain FBG sensor, due to radiation can be quantified with the following saturating exponential function [78]:

$$\Delta\lambda_{rad}(t) = B(1 - \exp(-t/\tau)) \quad (4.9)$$

Where B and τ both depend on the dose rate and fibre parameters. This equation is able to describe high and low dose rate environments but relative magnitudes are not accounted for. It should also be noted that to obtain the equation parameters for a specific fibre composition and dose rate, experimental data is required. Such a requirement is not detrimental for this application as the fibre chemistry and dose rate will generally be consistent. Therefore the parameters can be determined prior to sensor installation.

4.3.5 Fibre Bragg gratings as sensors

The full description of a bare FBG in an irradiated environment is the combination of Equation 4.7, 4.8 and 4.9:

$$\frac{\Delta\lambda_B}{\lambda_B}(t) = (1 - p_e)\varepsilon_z + (\alpha_\Lambda + \alpha_n)\Delta T + B(1 - \exp(-t/\tau)) \quad (4.10)$$

Equation 4.10 demonstrates that an FBG can be used as either a strain or a temperature sensor. Other physical quantities such as voltage, curvature, pressure or even gases can be detected and measured by inducing strain on an FBG or altering its reflection spectrum in a particular way. It is clear that to reliably measure one quantity an FBG must be properly characterised so that other dependencies can be compensated for. For example a strain sensor in an irradiated environment must have its temperature and radiation dependence compensated.

One of the most important parts of an FBG sensor is the sensor package itself. The package determines what physical parameters affect the FBG. For example, a humidity sensor can be made by coating an FBG in a layer that swells with moisture, producing a quantifiable wavelength shift for a given humidity. The sensor package requires careful design and this will be discussed in detail in Chapter 5.

Strain transfer of an FBG strain sensor

The wavelength dependence of an FBG, packaged for use as a strain sensor, is also dependent on the strain transfer from substrate strain to strain measured by the FBG. This can be represented by the following expression:

$$\frac{\Delta\lambda_B}{\lambda_B} = (1 - p_e)K_e\varepsilon_z \quad (4.11)$$

where K_e is the strain transfer coefficient of the sensor. The strain transfer of an FBG strain sensor must be determined through calibration, unless the fabrication process is consistent enough to assign a common value to every sensor. This is discussed in more detail in Section 5.6.3.

4.3.6 Temperature compensation methods

Temperature fluctuations at a strain sensor site are guaranteed for a large number of applications resulting in the common problem of removing the thermal response of an FBG. There are a number of methods for temperature compensating FBG strain sensors, but the most common is to monitor a nearby FBG that is isolated from strain. It is assumed that changes in wavelength

of the strain isolated FBG are due to temperature alone. This allows temperature shifts in the strain sensor wavelength response to be subtracted. As radiation affects the FBG peak wavelength in a similar way, the co-located strain isolated FBG could be used for simultaneous temperature and radiation compensation.

Other temperature compensation methods include utilising the two polarisation modes of birefringent fibres [89], writing FBGs in two fibres of different diameter [90], writing two gratings on top of each other [91], or measuring the first and second order diffraction pattern of a single grating [92]. However due to the presence of radiation in this application a co-located FBG will be used for compensation of the strain sensors.

4.4 Development in prestress monitoring with FBGs

FBG sensors have been implemented in civil engineering in recent years [93–96]. There are a few examples relating to either prestressed concrete or directly to nuclear reactors.

4.4.1 Monitoring tendon loads with FBGs

The shims of 20 90-wire tendon anchorages on a nuclear containment vessel were instrumented with FBG strain and temperature sensors [97]. In this pilot project the aim was to replace expensive periodic measurements with permanent online monitoring, with a 20 year lifetime requirement. The sensors were successfully installed while the shims were compressed by tensioned prestressing tendons. During scheduled maintenance shutdown, tests showed the strain sensors had good correlation with pressure changes inside the containment.

4.4.2 Prestress loss from concrete strain

Prestress loss can be estimated by placing strain sensors into the concrete surrounding the tendons, where stress levels are lower. Hughs et al. embedded fibre optic sensors inside concrete prestressed beams. By analysing the strain data they could ascertain material properties of high performance concrete [98]. Rather than relying on empirical equation based properties, these real measurements could be used to approximate the creep and shrinkage effect and evaluate prestress losses in the structure [99]. Abdel-Jaber et al. provide a framework for finding prestress loss using pairs of long gauge sensors embedded above and below a concrete beams centroid at a number of locations [100]. Long gauge sensors give more reliable global strain measurements in concrete as they are less sensitive to local strain variations and defects that are commonly found [68]. The framework can be used in both healthy and cracked beams. However,

prestress force estimation is dependent on the accuracy of the strain measurements, the modulus of elasticity of the concrete and the concrete thermal expansion. Concrete properties generally have a larger variation than properties of steel for instance. Additionally, embedding sensors in concrete requires planning at the design stage and does not allow for retrofitting.

4.4.3 Fibre Reinforced Polymer instrumented strand

Alternatively, FBGs can be mounted onto the tendons giving a direct localized strain measurement. This reduces the assumptions and consequently increases the accuracy of the measurement. However, this subjects the sensors to greater strains and so correct packaging is essential if they are to survive installation and remain reliable for years afterwards. Several studies have shown that it is possible to replace the central wire in a steel prestressing strand with one made from fibre reinforced polymer (FRP) with an FBG optical fibre embedded into it [101–103]. This may protect the sensors from damage, but replacing the central wire changes tensile and load bearing properties of the strands. FRPs may also be unsuitable for nuclear applications due to their low shear strength and unproven radiation hardness [104, 105]. Retrofitting sensors to standard, steel prestressing strands is another potentially cheaper universally available option, but one that is rarely investigated due to a lack of suitable attachment techniques.

4.5 Summary

In this chapter, the operation of optical fibres has been described along with their fabrication and losses from scattering, absorption and bending. Fibres subject to gamma and neutron radiation experience an increased attenuation due to compaction and point defects. Polymer coated fibre should be avoided in radiation rich environments, while high purity silica and fluorine doped cladding fibres provide the greatest radiation resistance. Due to concrete shielding, metal-coated standard smf-28 fibre is sufficient for this project.

Fibre optic sensors are well suited for monitoring strain and temperature of prestressing strands due to their size, passivity and immunity to electromagnetic radiation. Fibre Bragg gratings are the most appropriate sensor for this application because of their good strain resolution, multiplexibility and ease of interrogation, as well as their similarity to conventional electrical strain gauges. FBGs have a linear temperature and strain dependence; their radiation dependence is not as well understood, however it can be characterised for a specific fibre type and radiation conditions. In general, the effect of gamma radiation on the FBG peak causes

a saturating red shift which is fibre composition dependent. Whereas, the peak shift due to neutron radiation is not.

The previous chapters have described: the details of nuclear reactor PCC/PCPVs and their prestressed concrete, that there is a need for a new monitoring system and that fibre optic sensors, specifically FBGs, are able to provide this. Now that the theory for the sensors has been described, the next two chapters will show how FBGs may be packaged and calibrated to reliably measure strain in a harsh environment. Following on from this, results of several large field trials are reported.

Chapter 5

Sensor Development

5.1 Sensor design

As mentioned previously in Chapter 4, FBGs are extremely well suited to measure strain and temperature. However, one of the most important considerations for an FBG sensor is how it can be packaged in a proper manner for the given application.

5.1.1 Packaging

The packaging of an FBG sensor has two roles. Primarily, it must act on the FBG so that the given environmental response can be measured. Secondly, it must protect the brittle fibre from damage. A strain sensor package must securely grip the FBG so that strain can be reliably transmitted from a substrate to the FBG. A temperature sensor package must isolate the FBG from strain and be able to measure temperature changes at a suitable rate.

Epoxy

The most common way to attach a bare FBG to a structure for sensing strain is with epoxy. This technique is similar to attaching electric strain gauges that have been used for decades [106]. Epoxy is a thermosetting plastic. Long and highly branched chain molecules form during the curing process, creating strong bonds between the polymer. The FBG is completely covered in epoxy, and once set, the epoxy transfers substrate strain to the FBG with a slight reduction in absolute strain. The strain transfer mechanism for bare epoxied fibres has been well researched [107–111]. While the epoxy layer provides some additional protection to the FBG itself, the interrogating fibre and FBG must be further protected with a cover and ideally sealed with waterproof sealant. The epoxy cure time, which can range from 30 minutes to 24

hours must also be considered when installing FBGs in the field. However, bare epoxied FBGs have excellent strain transfer and provide a simple way to monitor strain. There are a number of commercial sensors available based on an epoxy construction, including sensors from HBM [112]. These strain sensors are constructed with additional packaging for protection. In some cases the sensor can be either spot welded or rigidly fixed by screws to the structure. This removes the epoxy cure time from the installation procedure and is potentially a more permanent attachment. These sensors are rated to a specified strain range and for the first 3.5 years of this research project commercial sensors were unable to measure up to the aforementioned desired maximum strain of $7 \text{ m}\epsilon$. Furthermore, no commercial strain sensor has a small enough footprint to fit the prestressing strand geometry.

Metal

There are several reasons why it may be beneficial to remove epoxy from the sensor construction for certain applications. By moving to an all metal strain sensor and metal coated fibre, radiation compatibility can be improved [4]. Exposure to radiation can have a detrimental effect on the strength of certain epoxies due to their high hydrogen content [113]. Significant mechanical creep in epoxies is probable beyond 50 % of their UTS [114] and water uptake in humid environments can lead to premature epoxy joint failure [115]. Metals also creep below their UTS, however their relative high melting point and UTS allow them to withstand higher stresses before creep occurs. High temperature epoxies are available, and epoxies continue to function above their glass transition temperature, but in general metal bonded joints can withstand a higher temperature. Creep in the fibre attachment joint may be further reduced by using a solder with a high liquidus temperature compared to a low temperature one [116]. Due to the benefits of an all metal package it is proposed that the strain and temperature sensors are constructed this way.

Metal sealing techniques are similar to glass sealing techniques commonly used in the packaging of optical components and in one case for strain sensing [117]¹. A metal filler material is heated beyond its melting temperature and used to create a joint between two objects. There are three main types of metal joining/sealing techniques: soldering, brazing and welding. In both soldering and brazing, a metal filler or solder is melted to form the joint. The filler material has a lower melting point than the main components being joined. The only difference between soldering and brazing is the temperature at which the solder material melts. Solders used in soldering melt below $\sim 350 \text{ }^\circ\text{C}$ [116]. Welding is differentiated by taking place at a

¹These strain sensors are rated up to $2.5 \text{ m}\epsilon$. It is expected that the glass seal will not be able to withstand the stress applied at $7 \text{ m}\epsilon$ [118, 119]

higher temperature, as well as the two joined components being heated above their melting points in addition to the filler material.

Soldering and brazing are suitable for making the high precision joints needed for small components such as those involving optical fibres. As a general rule, creep in metals will become significant at $\sim 35\%$ of the melting point [120]. Therefore this project used brazing for constructing strain sensors as the optical fibre and FBGs can withstand temperatures of 500-600 °C for short periods.

The brazing fabrication process for this project has been previously documented [121, 122], however the brazing process has been further optimised and the specific sensor design in this project has not been used before. Furthermore previous sensors were only briefly tested in lab conditions. The current project has built upon the existing work and attempted to properly calibrate and demonstrate brazed-package strain sensors for use in concrete containment buildings.

The temperature sensors had two main components: a metal coated fibre with FBG written into it and a metal capillary. The strain sensors consisted of three main components: a metal coated fibre with FBG written into it, a metal capillary and two metal shaped shims. Both are shown in Figure 5.1. The metal coated fibre was sealed into the capillary and shims attached via induction brazing. While the shims were spot welded to the prestressing strands. The following section describes the brazing process and spot welding.

5.2 Brazing

5.2.1 Brazing alloy

Brazing solder or filler is available in a variety of forms such as paste, paint, foil or machined preforms. The solder is made from a combination of two or three metals. The type of solder is chosen based on the following considerations:

- **Wetting:** The ability of the molten solder to flow over the work pieces. The solder may contain other chemicals to improve this property.
- **Mechanics:** The finished joints strength, shear strength, elasticity and creep.
- **Melting point:** A key consideration if the base work pieces are sensitive to high temperature. High melting point solders are harder and are less prone to creep than ones with a lower melting point [123].

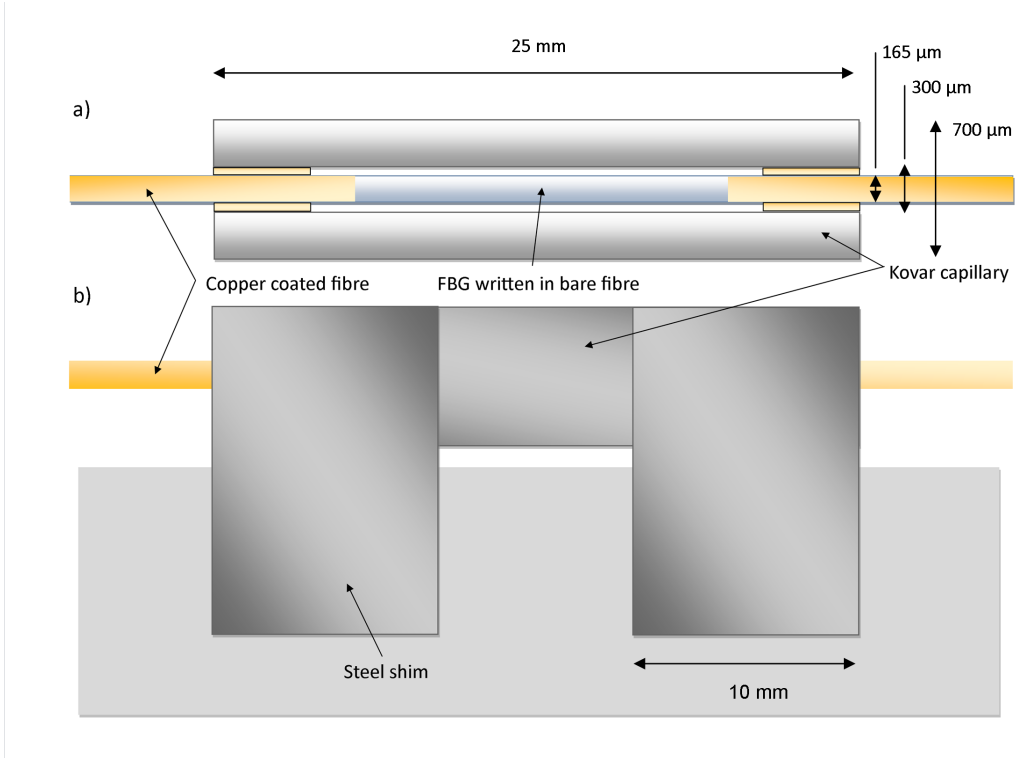


Fig. 5.1 Temperature a), and strain sensor b), components. The metal coated fibre was sealed into the capillary with brazing solder. The strain sensors were attached to the prestressing strands via spot welding.

The brazing alloy chosen for this project was 50 % silver metal in paste and foil form with a melting point of ~ 650 °C. The primary consideration was the solder melting point due to the trade off between reducing joint creep and ensuring the fibre and FBG remain functional after encapsulation. Brazing must take place in a vacuum, inert or protective atmosphere as an oxide layer forms on metals and can lead to weaker joints. Flux shields workpieces from the air and removes oxide layers, however it is corrosive so must be removed after the joint is made.

5.2.2 Induction brazing

Induction brazing uses induction heating in ferromagnetic metals to form the brazed joint. Figure 5.2 shows an induction heating setup, the induced alternating current, from the coil, melts the solder through friction heating. This type of brazing is ideally suited to making small and precise joints as it allows heating schedules with a high degree of control. Furthermore, the Curie transition of the ferromagnetic material can be exploited which significantly reduces the heating effect once the material reaches its Curie temperature. This can be used to protect the FBG within the capillary.

5.2.3 Capillary material

There are several metals that are suitable to use for the capillary. A comparison is shown in Table 5.1. The obvious choice would be steel as it matches the prestressing strand. However the large thermal expansion compared to silica glass may place the fibre-capillary joint under undue stress. Furthermore, upon cooling the FBG may be placed under compression due to the large thermal expansion mismatch. Kovar and Invar, iron-nickel alloys, better match the thermal expansion of the fibre. Due to the high stress of the application and the melting point of the brazing solder, kovar was chosen as the best suited material.

5.2.4 Induction heating theory

The current in an induction coil produces a magnetic field, \mathbf{B} . The flux, Φ_m on a conductor's surface subject to this magnetic field is given by:

$$\Phi_m = \iint_S \mathbf{B} \cdot d\mathbf{S} \quad (5.1)$$

A changing magnetic field induces an electro-motive force within the conductor, which depends on the rate of change of the \mathbf{B} -field and is opposite in sign:



Fig. 5.2 The induction heating rig. An alternating current flows through the coil, heating the ferromagnetic material within.

Table 5.1 A comparison of ferromagnetic materials properties. The most suitable capillary material should be matched to both the prestressing strand and silica glass. Due to its lower mechanical strength and thermal expansion, silica properties should be considered first.

Material	Silica	Steel	Nickel	Kovar	Invar 42
Yield Strength (MPa)	-	415	210	345	276
Tensile strength (MPa)	-	540	520	517	517
Young's modulus (GPa)	72	200	170	159	148
Poisson's Ratio	0.17	0.29	0.3	0.32	0.3
Thermal conductivity ((W/mK)	1.3	65.2	70	17.3	10.7
Thermal expansion ($\mu\text{m}/^\circ\text{C}$)	0.55	11.5	13.3	5.5	4.7
Curie Transition ($^\circ\text{C}$)	-	750	360	435	380

$$\varepsilon_{emf} = -\frac{d\Phi_m}{dt} \quad (5.2)$$

Due to resistance, R , in the conductor, a rapidly alternating coil current leads to Joule heating with a total power given by:

$$P = I^2 R \quad (5.3)$$

The current density of the eddy currents, that lead to Joule heating, decreases exponentially from the conductor edges towards the centre. The majority of the eddy currents exist within the conductor's skin depth of thickness [121]:

$$\delta = \sqrt{\frac{2\rho_r}{\omega\mu_r\mu_0}} \quad (5.4)$$

where ω is the alternating current angular frequency, ρ_r and μ_r are the conductor's resistivity and relative magnetic permeability and μ_0 is the permeability of free space. From the definitions of resistivity, skin depth and Ohm's law, a general equation for the induction heat power can be derived as:

$$P = GH^2 \sqrt{\rho_r \omega \mu_r \mu_0} \quad (5.5)$$

where the constant G is defined by the conductors geometry and H is the surface magnetic field strength.

The large permeability of a ferromagnet restricts its skin depth and confines the current to a small high resistance area leading to high Joule heating. The heating gradually reduces electron

spin alignment and therefore permeability. Eventually, the ferromagnet Curie temperature is reached and the material becomes paramagnetic, electron spin is disordered. This significantly reduces permeability leading to an increase in the skin depth of the conductor. Increased skin depth reduces resistive heating which makes it difficult to induction heat the ferromagnet beyond its Curie temperature. It must be noted that as the Curie temperature of kovar is around $435\text{ }^{\circ}\text{C}$, the brazing paste will not melt if only the capillary is placed inside the induction coil. Therefore steel heat concentrators or susceptors are placed at the end of the capillary to locally heat the joint area by heat radiation. As the FBG sits in the middle of the capillary it is still protected from the additional heating due to the susceptors.

5.2.5 Induction heating characterisation

Induction heating on the brazing rig was characterised prior to this project by Perry et al. [121]. An FBG was placed onto the brazing rig to monitor the temperature of different induction heating configurations with the kovar capillary and steel susceptors. Type I FBGs are thermally erased above temperatures of $300\text{ }^{\circ}\text{C}$ therefore a high temperature regenerated grating, [124], was used to temperature characterise the induction heating process, see Figure 5.3. The main results are summarised below.

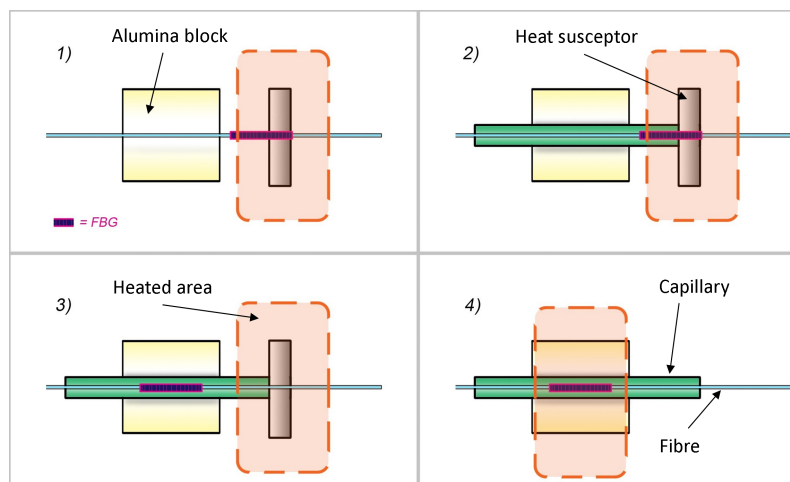


Fig. 5.3 Four different cases from the induction heating characterisation. Case 1: the FBG was placed inside the heat susceptors. Case 2: the FBG was inserted into a kovar capillary and steel heat susceptors were placed around the capillary end. Case 3: the FBG was placed in middle of the capillary with the induction coil heating the susceptors at the end of the capillary. Case 4: the FBG inside the kovar capillary was directly heated. [121].

Figure 5.4 shows the temperature during 35 s of induction heating when the steel susceptors (case 1) and kovar capillary (case 4) were placed separately into the induction coil, and also

when both were used (case 2). In case 1, the temperature increases continually until the induction current is switched off, afterwards radiative, convective and conductive radiation cool the FBG. When just the capillary is placed on the brazing rig (case 4), the temperature in the capillary quickly reaches 480 °C but does not increase further for the duration of the heating. Figure 5.5 shows the resultant temperature of capillary heating due to different induction currents. At low currents the heating rate is not large enough to overcome cooling losses. At higher currents the temperature increases beyond kovar's theoretical Curie temperature. This is because there is still some residual induction heating even though the paramagnetic state of kovar above 435 °C significantly reduces heating.

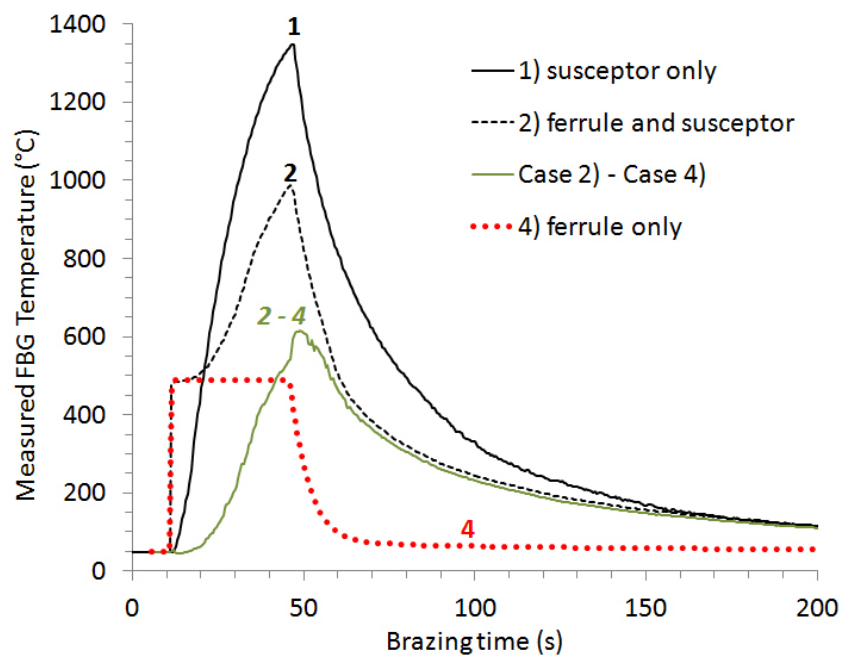


Fig. 5.4 Temperature during induction heating for different cases. Case 1: the bare fibre was exposed directly to susceptor radiation. Case 4: the fibre was placed inside the kovar capillary. Case 2: the steel susceptors were placed around the capillary end. In each case the coil current was 200 A with a heating time of 35 s. [121].

When the steel susceptors were placed around the capillary end (case 2), the temperature exceeded 480 °C, Figure 5.6. This is because the susceptor radiates heat onto the capillary. For heating times of 25 s and 35 s the capillary end becomes hotter than the melting point of the brazing paste. When the regenerated grating was placed in the middle of the capillary and the capillary end was heated with susceptors there was no noticeable difference in maximum temperature reached compared to case 4. This shows that the technique can be used to seal the capillary end while still protecting type I FBGs from significant damage.

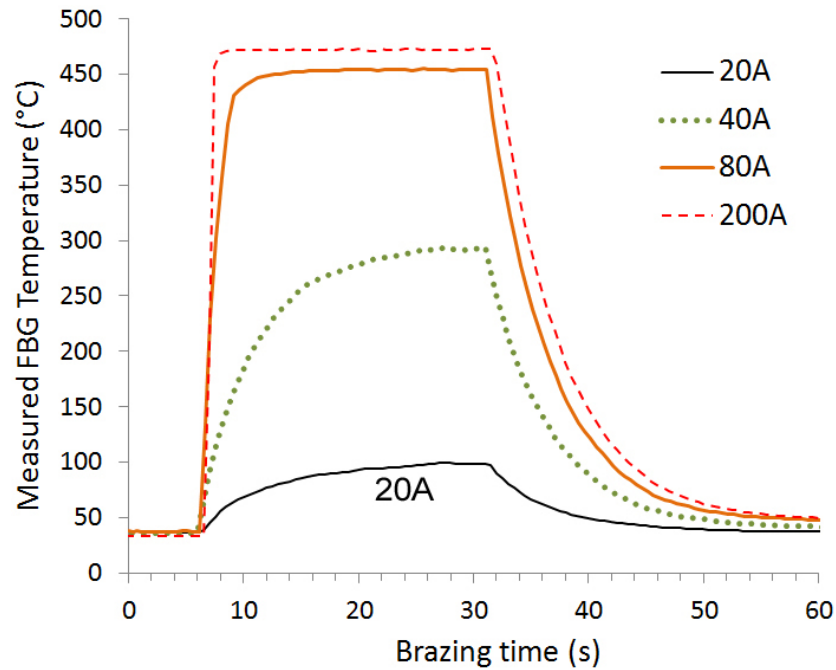


Fig. 5.5 Temperature reached during induction heating of the kovar capillary only. Note the maximum temperature reached due to the Curie transition in kovar. [121].

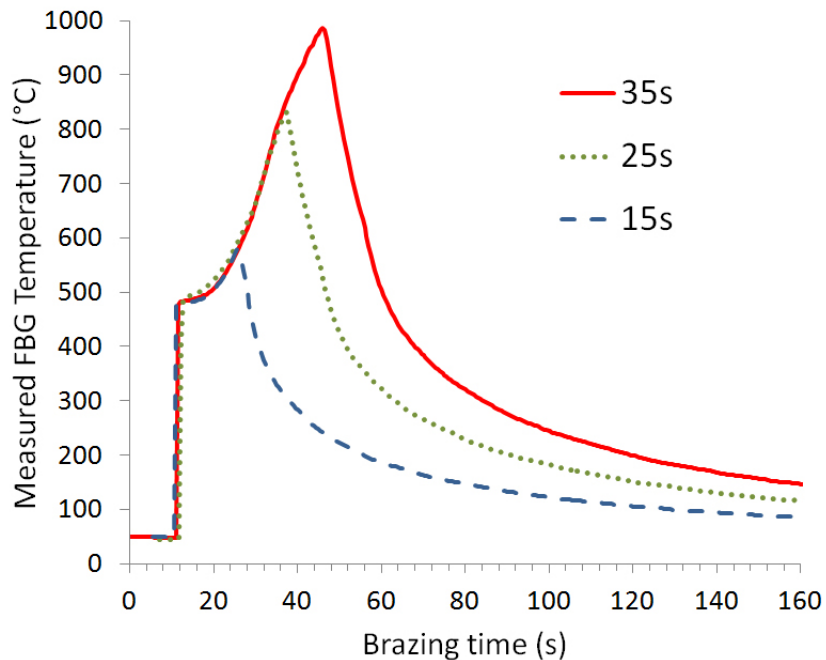


Fig. 5.6 Temperature when induction heating the capillary with susceptors surrounding it for different heating times. The temperature reaches above the kovar Curie temperature due to radiative heating by the susceptors. [121].

5.3 Spot welding

Resistance spot welding is relatively simple and is widely used to attach fibre sensors to metallic structures [125]. A current is passed through a localised area with oppositely poled copper electrodes. It is used to attach 0.05-3 mm thick metal sheets to a base work piece. The electrical resistance generates heat and melts the sheet to the base. The low copper resistivity ensures more heat is generated between the shim and strand. The weld energy, Q_s is roughly given by:

$$Q_s = I^2 R t \quad (5.6)$$

where I is the current flowing through the metal pieces, t is the weld time and R is the total resistance. Total resistance is a combination of the resistance of each component and the contact resistance between the components. The contact resistance is dependent on its area and the presence of grease and oxides which form insulating layers. These layers can result in a high contact resistance which may lead to damage due to electrical arcing. Therefore it is extremely important to ensure that the work pieces are thoroughly cleaned by sanding and wiped with solvent. The solidification of the melted joint occurs quickly and the steel crystals align in the cooling direction, this might lead to welds with poor shear strength.

To ensure that spot welding does not have a detrimental effect to the tensile strength of the strand, a number of strands were tested to failure with and without spot welded shims attached [126]. There were two main conclusions from this test; firstly, the individual wires of the strand move relative to each other when the strand is stressed. Therefore, the sensor must be attached to one wire of the strand only. Secondly, spot welding shims to the strands did not affect the ultimate tensile strength of the strands. All strands had a yield and ultimate strength higher than that specified in British Standard BS5896:2012, regardless of whether a shim had been attached. The modulus of elasticity of all strands was 185 GPa.

5.4 Fabrication of metal packaged FBGs

Now that the basic fabrication and attachment techniques of the strain and temperature sensors have been described in detail. The application specific sensor details can be described.

5.4.1 FBG inscription

The methods to inscribe an FBG into optical fibre have been described in Section 4.3.2. FBGs used in this project were 7 mm long, apodised, with a FWHM and reflectance of approximately

0.25 nm and 75 %, respectively. High reflectivity was chosen to compensate for its loss during sensor fabrication and the FWHM was chosen based on the design of the Micron Optics interrogators used in this project. The metal fibre coating must be removed before the inscription process to allow the FBG to be written. A 10 mm section of the metal coating was removed with 65 % concentration nitric acid. If a carbon underlayer is present this must also be removed by burning the layer off with a naked flame or arc. Great care must be taken during this stage as it is extremely easy to weaken the fibre.

5.4.2 FBG encapsulation

Once inscribed, the FBG was encapsulated into a 25 mm metal capillary. Compared to plated fibres, fibre encapsulated into capillaries are more rigid and are often used to provide additional mechanical strength [125, 127, 121]. The capillary also provided guidance to the FBG for off axis forces.

The FBG was inserted in the capillary and brazing paste was applied to one end. The joint area was heated via induction heating and the brazing paste melted forming the joint. Capillary action helped the molten paste to flow into the capillary. Steel heat susceptors were placed around the joint area to concentrate heat so the brazing solder melted completely. The melting point of the chosen brazing paste was 650 °C to reduce the creep rate of the sensor joints when subject to the high stress levels of this application [123, 128]. Therefore the brazing process was optimised to obtain the required capillary action of the brazing material into the metal capillaries without reducing the structural integrity of the optical fibre and reducing the FBG reflectivity due to heat exposure [129].

The joints were visually inspected after brazing for defects; the brazing paste should create a smooth joint without cavities as shown in Figure 5.7. If the brazing paste does not reach a high enough temperature a porous structure is created. This is due to the non metal components of the paste burning off leaving the unmelted metal. The encapsulated FBGs formed the main body of the strain sensor and also the temperature sensor. The temperature sensor was secured at one end into the prestressing strand groove to ensure strain was not transferred to it.

5.4.3 Shim attachment

To allow the encapsulated FBG to measure strain, a 10 mm steel shim was attached to each end of the capillary, Figure 5.8. The shims were brazed onto the sensor body one at a time. The shim was shaped around the capillary with the ends bent away. This allowed the shim to sit on the brazing rig and prevented brazing material from flowing too far up the shims. Brazing

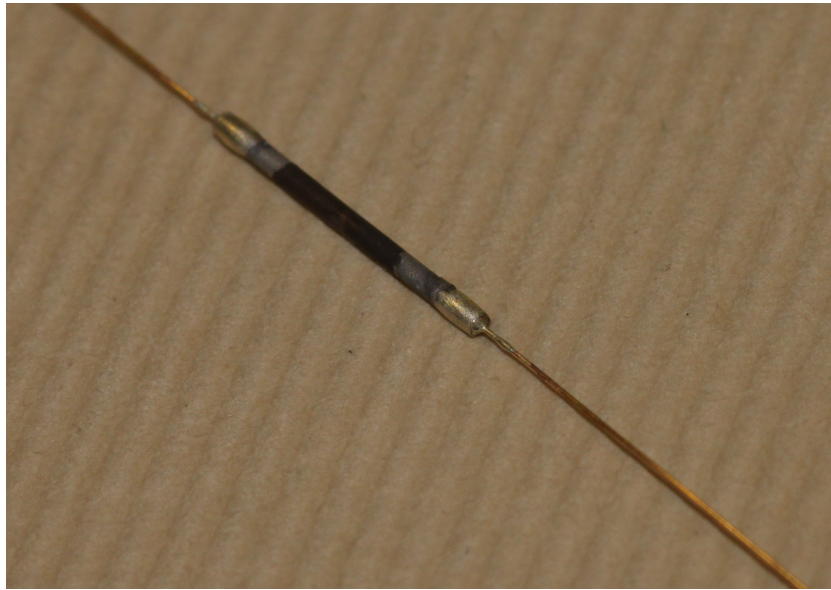


Fig. 5.7 An example of a good brazed joint between the copper coated fibre and the kovar capillary. The brazing material has created a smooth joint showing that the correct temperature has been reached and that the brazing material has flowed into the capillary.

paste was spread into the shaped bottom and the capillary was inserted, after this a 1 mm x 10 mm strip of brazing foil was placed on top of the capillary. Flux was placed on areas of shim to protect it from oxidation. Finally the shim and capillary were heated without susceptors as the shims themselves acted as heat concentrators. After brazing, residue from flux and the brazing paste was removed from the shims. The shims and sensor body were cleaned with water first, this dissolved and removed flux residue. They were then sanded several times and cleaned with alcohol. Figure 5.9 shows a cleaned sensor.

5.4.4 Results from fabrication

A sample of four sensors was monitored for reflectivity losses during the fabrication process, one can be seen in Figure 5.10. During the FBG encapsulation stage, the wavelength response of the FBG was similar to that found previously [121]; the temperature was capped at a certain value due to the Curie transition in kovar. When the shims were attached to the capillaries, the susceptors were not used as the shims themselves acted as heat concentrators. However, the wavelength response of the FBG was still expected to reach a maximum temperature and not increase further. The observed wavelength response did not show this property (see Figure 5.10 top, last two peaks), but this was likely due to the thermal expansion of the capillary straining the FBG to some extent. Furthermore, the shims made a physical contact with the capillary

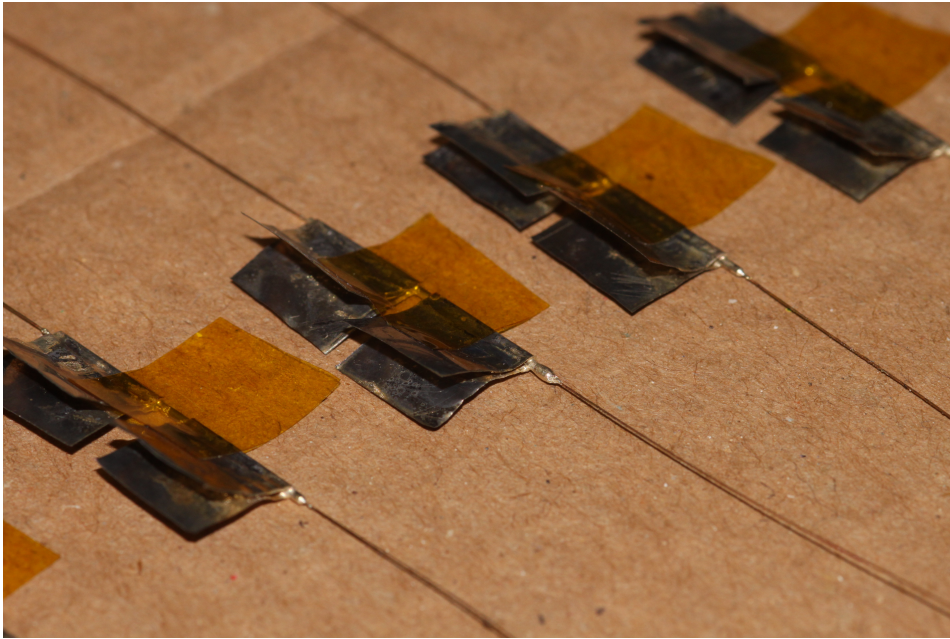


Fig. 5.8 Metal packaged sensors ready for attachment to the prestressing strands.

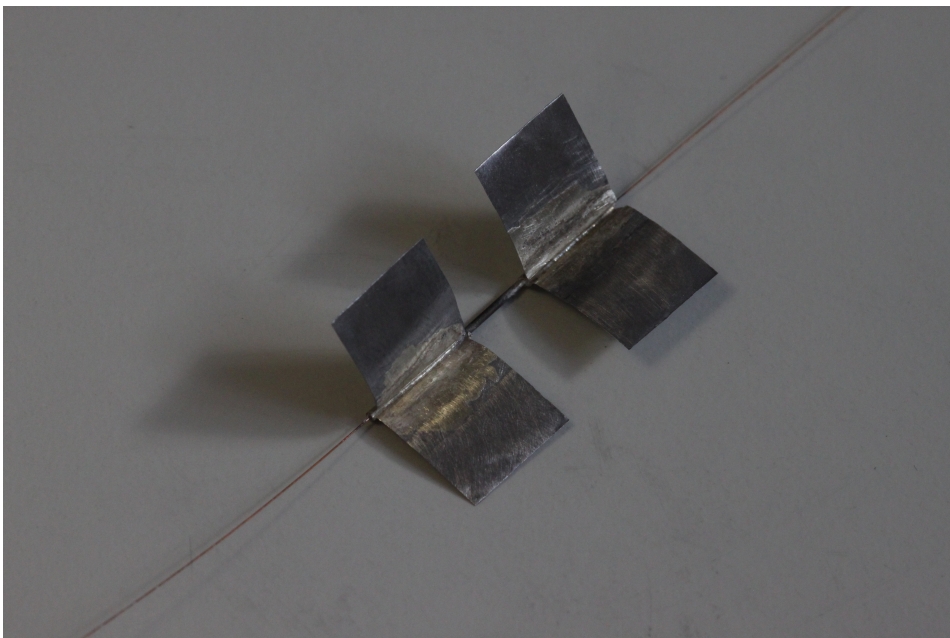


Fig. 5.9 A fabricated sensor with shims open showing the brazed joint between the capillary and shim.

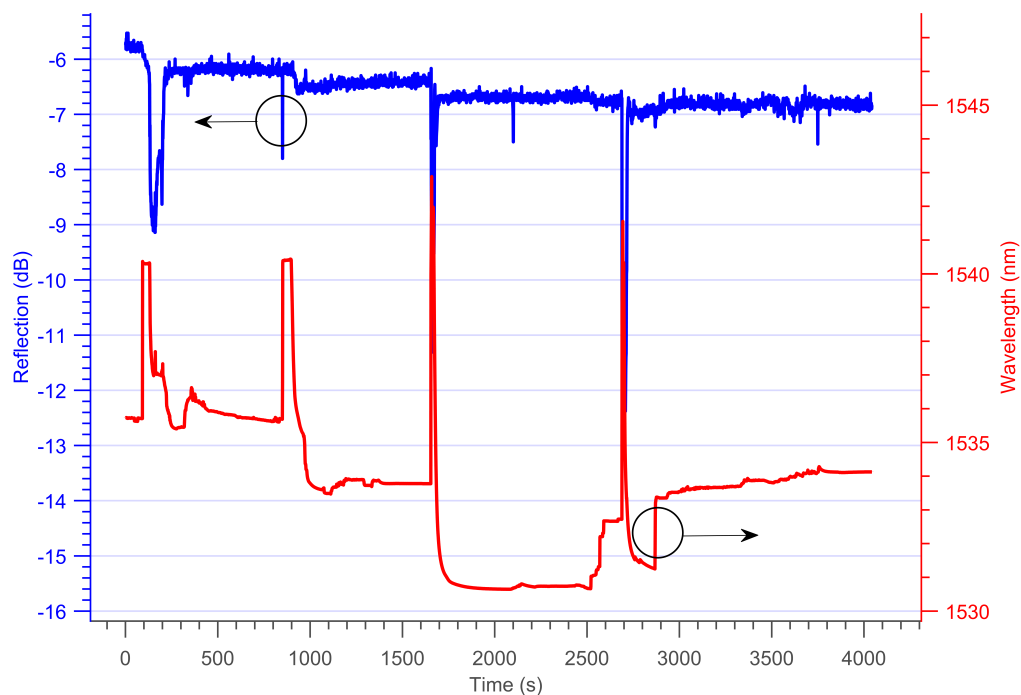


Fig. 5.10 FBG peak wavelength and peak reflectivity during brazing of the metal capillary and shims. The first two peaks with the flat tops (in the wavelength response) are the two ends of the capillary being brazed while the last two peaks occurred during brazing the shims to the capillary.

near the FBG, whereby heat was transmitted more readily to the FBG. The peak wavelength reached whilst brazing the second shim onto the capillary was generally smaller than the first one. The heating times for the induction coil were kept constant, so the temperature reached whilst brazing both shims was expected to be the same. This difference in peak wavelength shift was likely due to the initial joints between the fibre and the capillary being melted slightly. When the capillary thermally expanded the fibre would not stay in the same position if the brazed joint had melted. This could therefore reduce the strain sensitivity of the strain sensor. On average the peak reflection reduction after stabilisation of the FBGs was 35 %, showing good agreement with previous studies [121]. The rapid decay in peak reflectivity was due to thermal annealing of the grating index modulation and is characteristic of Ge-doped FBGs [129]. A spectrum from one of the constructed sensors is shown in Figure 5.11. The main peak has an amplitude of 10 dB greater than the side lobes. These results further confirmed the suitability of this technique to package FBGs for temperature and strain sensing.

The capillary-shim joint was tested to failure on a stressing vice three times; the broken sensors can be seen in Figure 5.12. This revealed that the metal capillary failed first, proving the

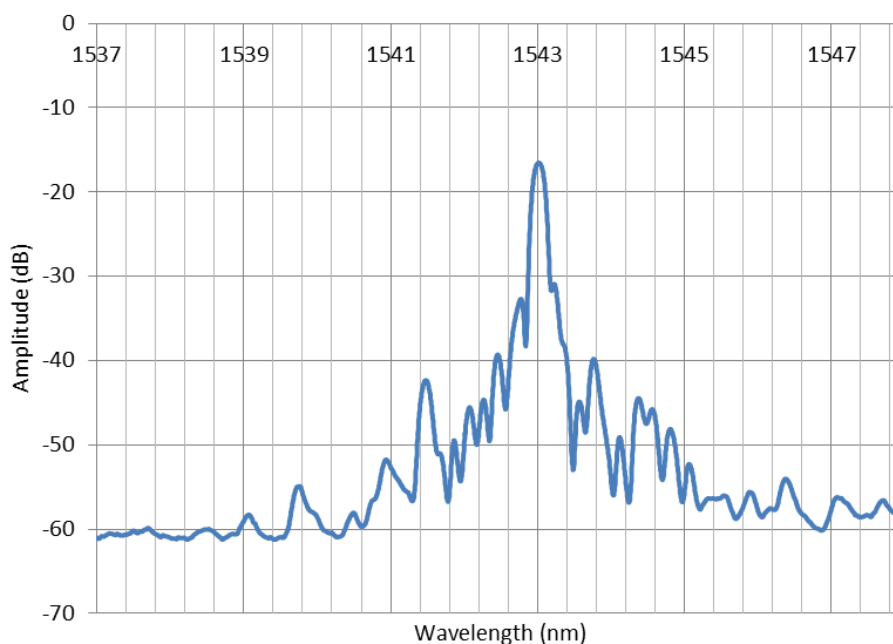


Fig. 5.11 FBG spectrum of a sensor after sensor construction.

brazing process is able to create capillary-shim joints that are stronger than the tensile strength of the capillaries themselves. The kovar capillary is predicted to break at 160 N. Comparing the yield strength of kovar and steel (276-345 MPa and 1450 MPa respectively) shows that the stress transfer must be less than 19-25 % if the capillary is to remain below the yield stress of kovar. Future studies may benefit from experimenting with capillaries made of materials exhibiting a greater yield strength than kovar.

5.5 Instrumenting a prestressing strand

One of the main considerations for the sensor design was the very specific geometry of the prestressing strands. The helically wound wires and very tight tolerances when they are installed mean that the sensors and interrogating fibre must lie within the strand grooves. This does, however, afford the sensors some protection and they are unlikely to be disturbed if they remain within the groove. Figure 5.13 shows a temperature and strain sensor installed onto a prestressing strand.



Fig. 5.12 Three FBG strain sensors tested to failure; each time the capillary broke first demonstrating that the brazed joints between the shim and capillary are of adequate strength.

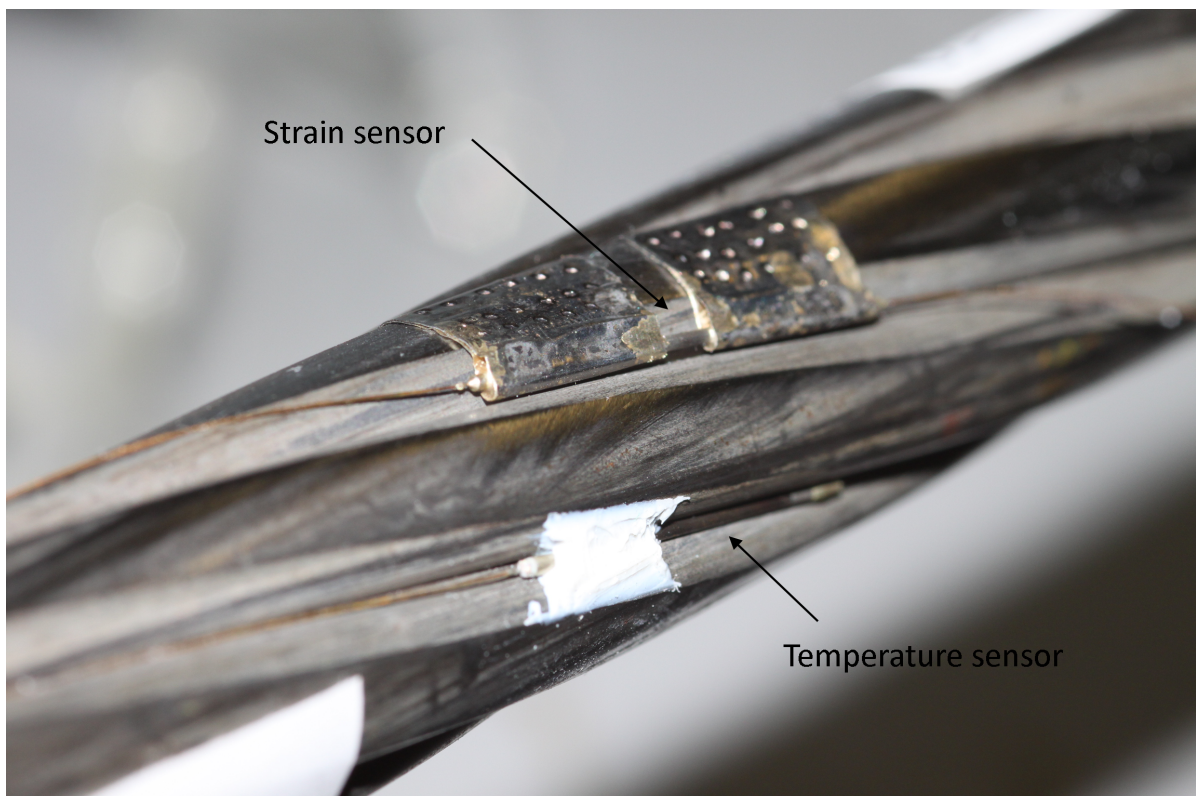


Fig. 5.13 A strain sensor and a temperature sensor attached to a pre-stressing strand. The strain sensor was spot welded, while in this case the temperature sensor was attached with silicone. Note the fibre from the strain sensor is not in its final position; once secured it sat in the groove.

5.5.1 Temperature sensor attachment

The temperature sensor attachment went through several iterations. Initially the sensors were secured at one end into the prestressing strand groove to ensure strain was not transferred to them. The attachment was tested by bending the strand in three axial directions so that the section where the sensor was mounted experienced tension, compression and side loading. The attachment was shown to be adequate in isolating the FBG from strain. During the field trial described in Section 7, the temperature sensors showed some sensitivity to strain. Therefore a second attachment method was developed. The temperature sensors themselves were not secured to the strand, but were held in place by their interrogating fibre inserted into silicone tubing, Figure 5.14.



Fig. 5.14 When the temperature sensors were attached with silicone sealant at one end they showed some strain sensitivity. Consequently, for further tests, they were not attached to the strand but held in place by the interrogating fibre inside silicone tubing.

5.5.2 Strain sensor attachment

The shims were shaped to fit the geometry of the strand so that they lay on the outside of the strand but the capillary and FBG were bent into the groove to protect them. It is important to note that due to movement between the individual wires of the strands, a strain sensor must be mounted to one wire only if it is to survive stressing. The strain sensor was temporarily taped onto the strand to secure it. Three to four rows of spot welds secured both sides of the shim to the structure. The energy for each individual spot weld was 30-40 J. Both sensor and strand surface were thoroughly cleaned prior to spot welding to reduce the chance of electrical arcing.

5.5.3 Interrogating fibre protection

Similar to the sensors themselves, protection of the interrogating fibre was improved throughout the project. For the first field trial described in Section 7, the bare fibre interrogating all sensors was helically wound round the strand in the groove. The splice joint protectors were secured into the groove with silicone sealant to prevent them catching when the strands were inserted, as seen in Figure 5.15. Later on, the fibre was placed inside silicone tubing to prevent it from exiting the groove if the strand was bent, this is shown in Figure 5.16.

The instrumented prestressing strands must be inserted into ducts in the concrete therefore the optical fibre exiting the grooves at the ends of the strands must be protected. The optical fibre must transition from the metal coated fibre, wrapped round the strand, to an armoured cable once the fibre leaves the strand. Initially, this was achieved using copper tubing glued onto the ends of the tendon in the grooves as seen in Figure 5.17. However, due to the very tight tolerances of the stressing jack this protection method was not suitable for use at the stressing end. Therefore, a more robust solution was developed. This ensured the end was smaller than the 18 mm diameter stressing strand to allow the stress jack to fit over the top. Two of the six outer wires were cut about 25 cm from the end, leaving an area for the splice protectors and armoured fibre to sit. The remaining strands provided rigidity to the fibre. The metal coated fibre was spliced to the armoured cable, silicon tubing was placed over the top and glued to the remaining strands, Figure 5.18. Once secured, the whole area was covered in Araldite 2014-1 epoxy to fix the fibre and provide a smooth surface to the end of the strand, Figure 5.19. This modification did not affect the structural integrity of the strand as the cut wires were beyond the required length of strand exiting the barrel and wedge.



Fig. 5.15 Securing a splice protector to a prestressing strand with silicone sealant.



Fig. 5.16 The interrogating fibre was inserted into silicone tubing to prevent it coming out of the groove if the strand was bent.

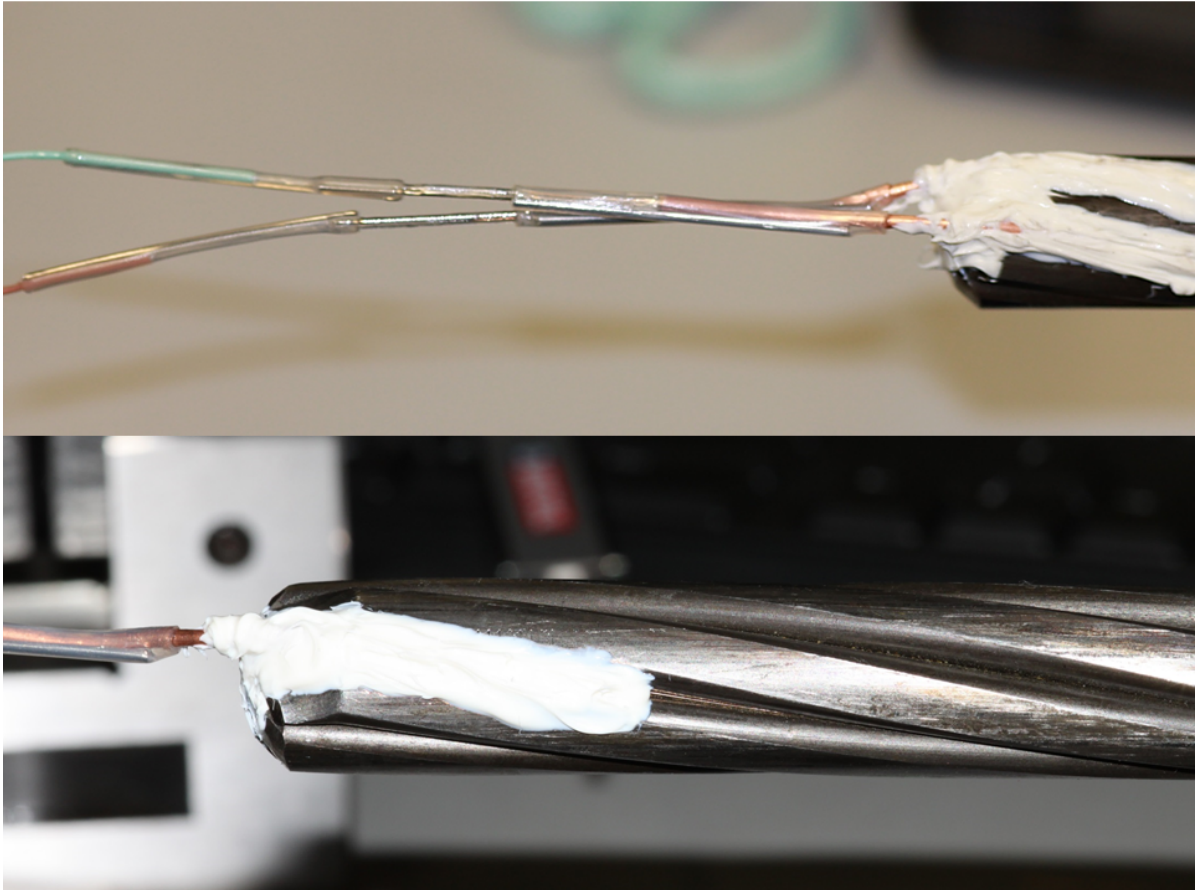


Fig. 5.17 Protection at tendon ends using copper tubing and splice jackets. During field trials it was found that the stressing jack would not fit over the end of the strand because the tubing protruded about 2 mm from the strand groove. An improved protection scheme was demonstrated.

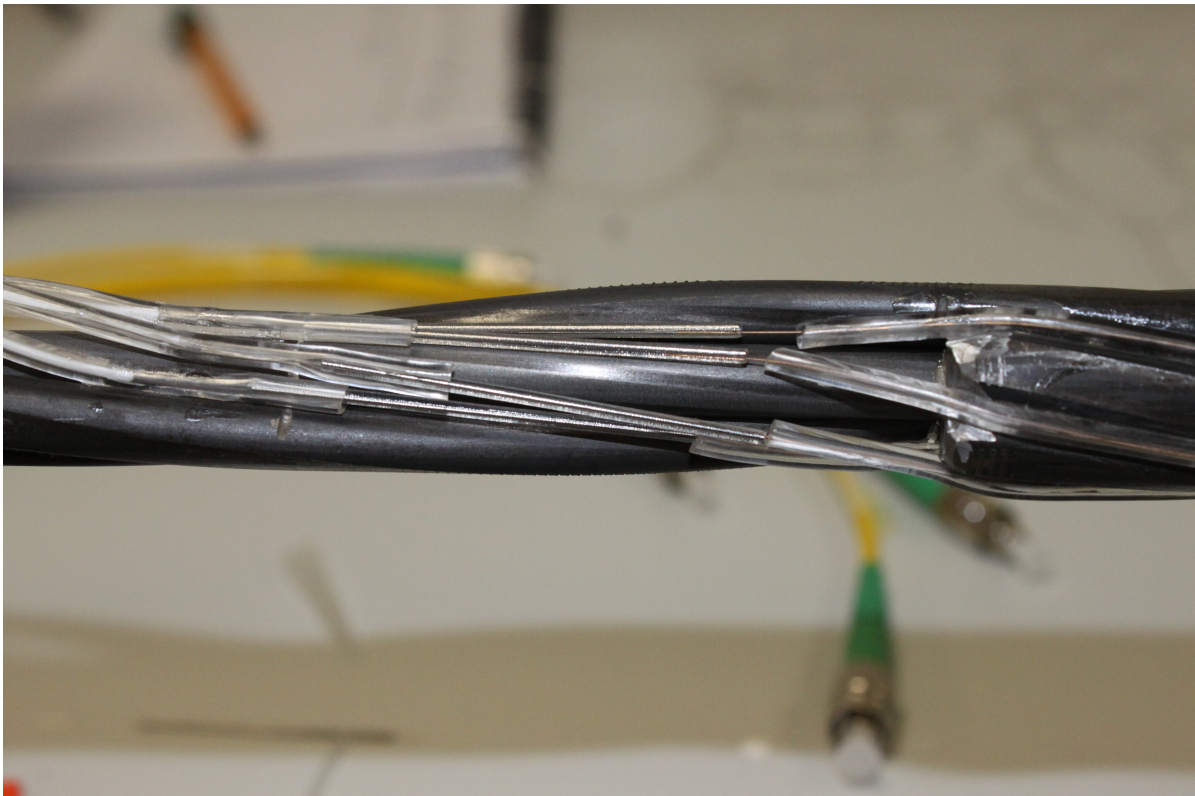


Fig. 5.18 At the end of the strand, two of the wires were cut off. The metal coated fibre was spliced to a rugged fibre cable and the bare fibre sections were protected with silicone tubing. Afterwards epoxy was applied to the whole area.



Fig. 5.19 Photos of the cut outer wire and reinforced fibre cable exiting the strand. Epoxy covers the splice protectors and fibre cable holding them in place.

5.6 Calibration

After the sensors have been constructed they are ready to measure strain and temperature. There are several options in terms of converting the sensor wavelength. From the theory laid out in Chapter 4, it is possible to convert wavelength to temperature and strain using the assumptions of strain and temperature sensitivity. The strain transfer of the strain sensors must also be considered. It is possible to characterise a number of sensors and assume that all other sensors react in the same way. Here, there is the assumption that there is a near perfect fabrication process and every sensor has the same sensitivity. However, if the sensors are to measure their given parameters to a high degree of accuracy, they must be individually calibrated. Moreover, if the sensors were to become commercially available, calibration provides rigorous fault screening and customer confidence in the sensors. In this project temperature sensors must be calibrated for temperature. The strain sensors must be calibrated for temperature and strain due to an FBG's inherent temperature sensitivity.

5.6.1 Temperature

In general temperature calibration of temperature FBG sensors is a relatively straightforward task. However, controlled temperature characterisation of individual strain sensors is challenging in SHM applications as the structures are generally large². As such, sensors may be temperature calibrated before attachment to the strands. The total strain of a structure is a combination of the mechanical and thermal strain, therefore the thermal strain component needs to be removed. In this case the thermal expansion and strain transfer of the sensor must be accurately and reliably known. Once again, accuracy and confidence in the sensor reading can be greatly improved if the temperature sensitivity of the strain sensor incorporates the thermal strain component of the structure.

Temperature reference

Another consideration for temperature calibration is the temperature reference used to compare the FBG sensor wavelength shift. There are a number of temperature references available which vary in accuracy and repeatability.

²For example, prestressing tendons in helical duct PCCV/PCPVs are 70 m on average, although this is heavily dependent on the vessel geometry and the path of the tendon ducts. The shortest tendons are around 30 m in some PCPV designs and can reach up to 150 m in the PWR PCC

The physical quantity known as thermodynamic temperature, with unit kelvin, is currently defined as the reciprocal of the thermodynamic temperature of the triple point of water [130]³. Accurate measurement of temperature requires a primary thermometer with a well understood physical mechanism whose temperature is based on other quantities. This is difficult and time consuming and therefore not of practical use for general temperature measurements. For this reason, the International Temperature Scale (ITS) was devised [132]. It presents an internationally recognised method for practically determining a wide range of temperatures. In its current form, ITS-90, it covers the temperature range from 0.65 K to the highest temperature practicably measurable using monochromatic radiation and the Planck radiation law. The Provisional Low Temperature Scale handles temperatures from 1K - 0.9 mK.

The basic idea behind ITS-90 is to define temperature at fixed points along the scale corresponding to physical transitions of elements. The transitions include vapour pressure points, triple points and freezing or melting points; the temperature near these fixed points is then extrapolated. For example, around room temperature the temperature is defined by platinum resistance thermometers calibrated at specified sets of fixed points. This creates a type of hierarchy for calibration. ITS-90 is used by National metrology labs, such as NPL or NIST, to calibrate a temperature reference to a certain accuracy. Industrial companies then calibrate their temperature references to these certified temperature references. This way multiple sensors can be calibrated at once with an increasingly poor accuracy for each sensor in the calibration hierarchy. In any case, an extremely high accuracy is not needed for the large majority of applications. It must be noted that calibration accuracy is different to the inherent accuracy of a given sensor. The two must be combined for total accuracy. For industrial and lab applications, the resistance temperature detector (RTD) and the thermocouple are two common temperature sensors.

Platinum Resistance Thermometer Detector

Resistance temperature detectors contain a fine coil wire wrapped around a ceramic or glass core. The resistance of the wire changes with temperature in a controlled manner. Platinum is often used for the wire as it produces a linear, stable and repeatable measurement. In general RTDs have excellent accuracy and repeatability as demonstrated by their use in ITS-90. There are two RTD industry resistance tolerances based on the European DIN standard [133]. Their accuracy in degrees Celsius is given below:

³This definition will change in 2018 by assigning a value to the Boltzmann constant [131]

$$\frac{1}{3}DIN = \pm \frac{1}{3}(0.3 + 0.005T)^{\circ}C \quad (5.7)$$

$$\frac{1}{10}DIN = \pm \frac{1}{10}(0.3 + 0.005T)^{\circ}C \quad (5.8)$$

where T is the temperature of the measurement. The tolerances are a combination of resistance tolerance and the temperature coefficient of resistance. Platinum RTDs with accuracies of $\pm 0.03^{\circ}C$ at $0^{\circ}C$ are readily available.

Thermocouple

A thermocouple is made of two different metal wires joined together. The voltage across the wires varies with temperature due to the thermoelectric effect. The voltage at the junction must be compared with a voltage at a known temperature to reliably calculate the temperature. Therefore, a secondary temperature reference near the instruments location often applied, this is known as cold junction compensation [134]. Thermocouples are cheaper than RTDs but less accurate. There are however a few reasons why they may be chosen over RTDs; they cover a larger temperature range compared to RTDs and have a faster response time. These reasons do not affect slow controlled temperature calibration around room temperature; therefore an RTD is the preferred temperature reference for calibrating the FBG sensors.

Temperature calibration results

Initial heating cycles were carried out in a small oven, without active cooling, to test the calibration procedure. The oven was heated to $60^{\circ}C$, once this temperature was reached the oven was switched off and left to cool. A J-type thermocouple was initially used as the temperature reference for all the sensors; it had a resolution of $0.1^{\circ}C$ and an accuracy of $\pm 1.5^{\circ}C$. The results of the heating cycles showed a difference in the thermal inertia of the thermocouple and the FBGs. In Figure 5.20 a), the thermocouple was faster to respond to the increase in temperature than the FBG. When left to cool, a slower process, the two were linearly correlated. Silica glass has a specific heat capacity that is approximately 1.5 times larger than that of nickel, J-type thermocouples are made from nickel alloy wires. Therefore an optical fibre requires more energy to raise its temperature than a nickel wire. Assuming a constant heating rate within the oven this would increase the time an optical fibre, and therefore FBG, takes to reach the same temperature as the thermocouple. In order to carry out accurate

temperature calibration, it is critical to ensure that the temperature reference and the FBGs are the same temperature.

In order to better match the heating rates of the thermocouple and FBGs, they were mounted on an aluminium plate. Aluminium has a relatively high thermal conductivity; therefore, temperature fluctuations between the thermocouple and FBGs is reduced. Additionally as the aluminium plate has a relatively large mass it requires more energy to raise its temperature compared to the thermocouple and FBGs. The thermocouple and FBGs measured the temperature of the aluminium rather than the air in the oven, allowing the heating rates to be better matched. Repeating the heating cycle in the oven showed the difference in the heating rates was reduced, Figure 5.20 b). After it was confirmed that the heating rates of the temperature reference and the FBGs were matched, the calibration procedure was moved to an environmental chamber. The chamber was stable to ± 0.1 °C once it had reached the programmed temperature. It was programmable and had active cooling this allowed the temperature cycles to be carried out over a number of days.

All temperature FBG sensors for the field trials were calibrated at the same time in an environmental chamber using this arrangement. They were subject to four heating cycles from 10-50 °C. A J-type thermocouple was used as the temperature reference for Section 7, while a platinum RTD was used for Section 8. It was mounted on an aluminium plate together with the FBGs as discussed previously. The temperature was stepped in 10 °C intervals and held at each point for two hours to allow the temperature to stabilise; data points from the end of the two hours of constant temperature were then used for calibration. A temperature conversion (pm/°C) coefficient was obtained from a least squares fit to the data, see Figure 5.21. The temperature sensors typically had a temperature sensitivity of 14-17 pm/°C. Sensors with defective brazing joints can be discovered during the temperature calibration process, as demonstrated in Section 5.6.2.

Portable temperature calibration

Following from the discussion at the beginning of Section 5.6.1, a portable in-situ method was developed to obtain the temperature sensitivity coefficients for FBG strain sensors which were attached to prestressing strands. Two methods of temperature calibration are outlined. The first is an active method, in which the FBGs are locally heated using an induction heater. The second method monitors the wavelength shifts passively during natural, daily temperature fluctuations in room temperature. By comparing these two measurement techniques, the first with its large range and larger temperature instabilities, the latter with its smaller range and

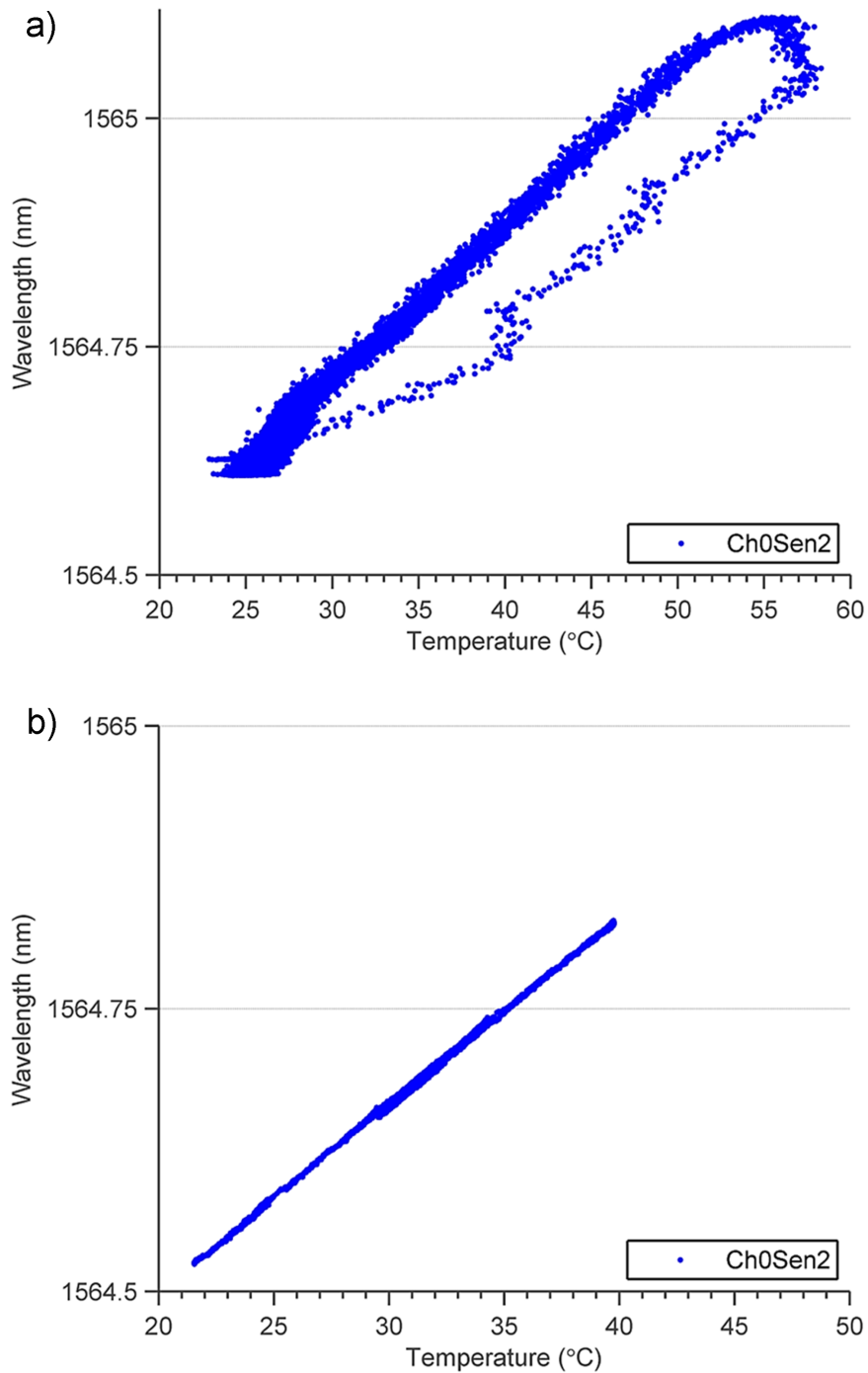


Fig. 5.20 a) Initial hysteresis obtained by heating and cooling a thermocouple and FBG . The hysteresis is due to the difference in temperature response between the FBG and thermocouple. b) After mounting on an aluminium plate the heating rates of the two are much better matched.

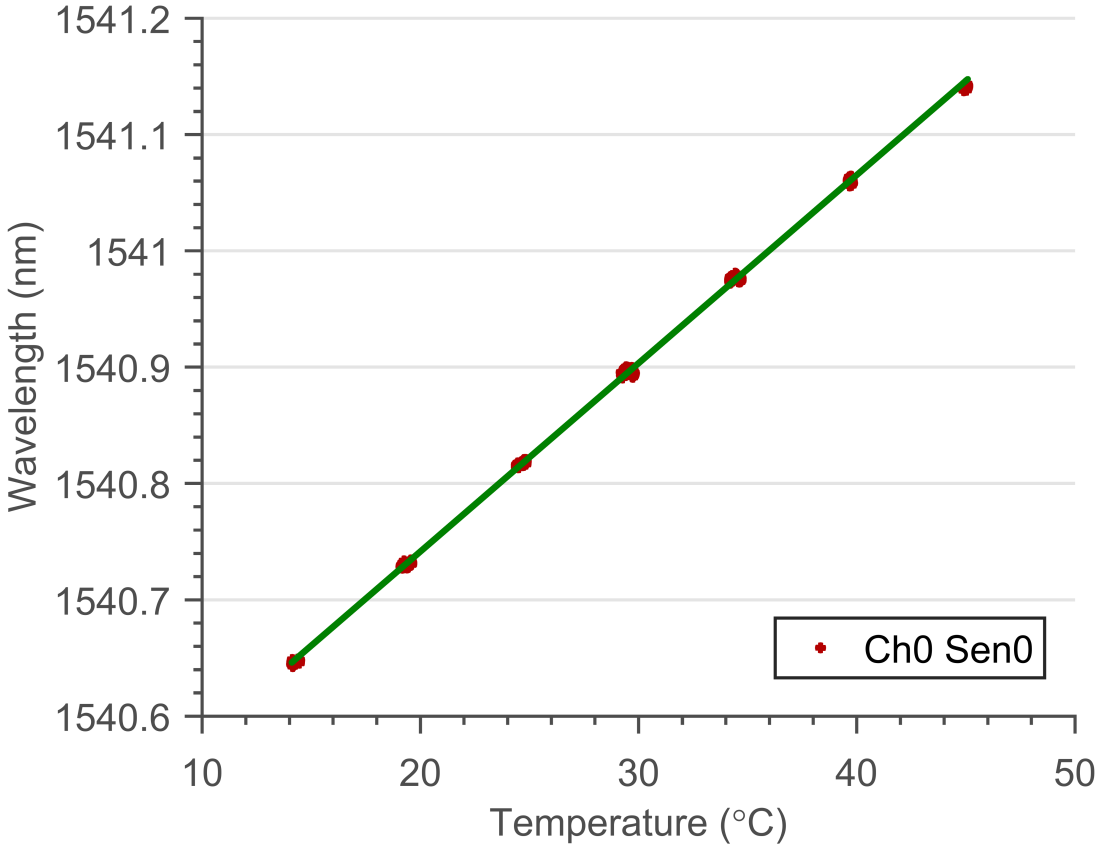


Fig. 5.21 Wavelength response of a temperature FBG sensor for four temperature cycles.

smaller temperature instabilities, a reliable temperature coefficient for FBG sensors can be derived. The calibration procedure tested with pre-calibrated FBG sensors.

In the active method, an induction heater was used to heat a section of steel strand at the location of each strain sensor. To allow higher temperatures to be realised, strand sections were also heated indirectly by enveloping them in an insulated steel box, Figure 5.22. The box acted as a heat susceptor and also reduced convective heat loss. The strand was heated to approximately 60 °C and then left to cool. The wavelength response of the strain sensor was compared to an in-situ temperature FBG (pre-calibrated) and a J-type thermocouple (± 1.5 °C accuracy), placed in thermal contact with the strand using a thermally conductive gel.

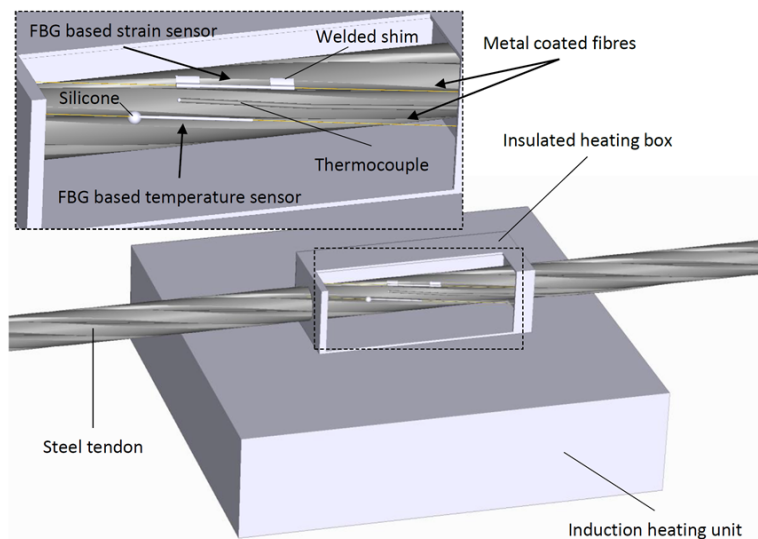


Fig. 5.22 Induction heating set-up, an insulated metal box surrounds the section of strand where the sensors are attached. The thermocouple was situated in between the two sensors and in contact with the strand. Rapid, non-uniform heating can create spatial temperature variations within the insulated box. The temperature distribution is stabilised to some extent by allowing the strand and sensor to cool from the maximum temperature achieved.

The rapid and non-uniform temperature increases during induction heating led to temperature instabilities and variations between the sensors and the strand. As such, only cooling of the strand, exhibiting much slower temperature variation, was used to characterize temperature coefficients. In each case, it took approximately 3.5 hours for strand sections to cool from 60 °C to room temperature.

Figure 5.23 shows the wavelength response of the pre-calibrated temperature sensor compared to temperature measured by the thermocouple during cooling from induction heating. The temperature coefficient matched the previous calibration (15.9 ± 0.6 pm/°C) within the

error estimate. The thermocouple data plotted shows a relatively high noise level; comparing the variance between the thermocouple and the FBG data, indicates that a more accurate temperature reference would reduce the error and increase the accuracy of the calibration substantially.

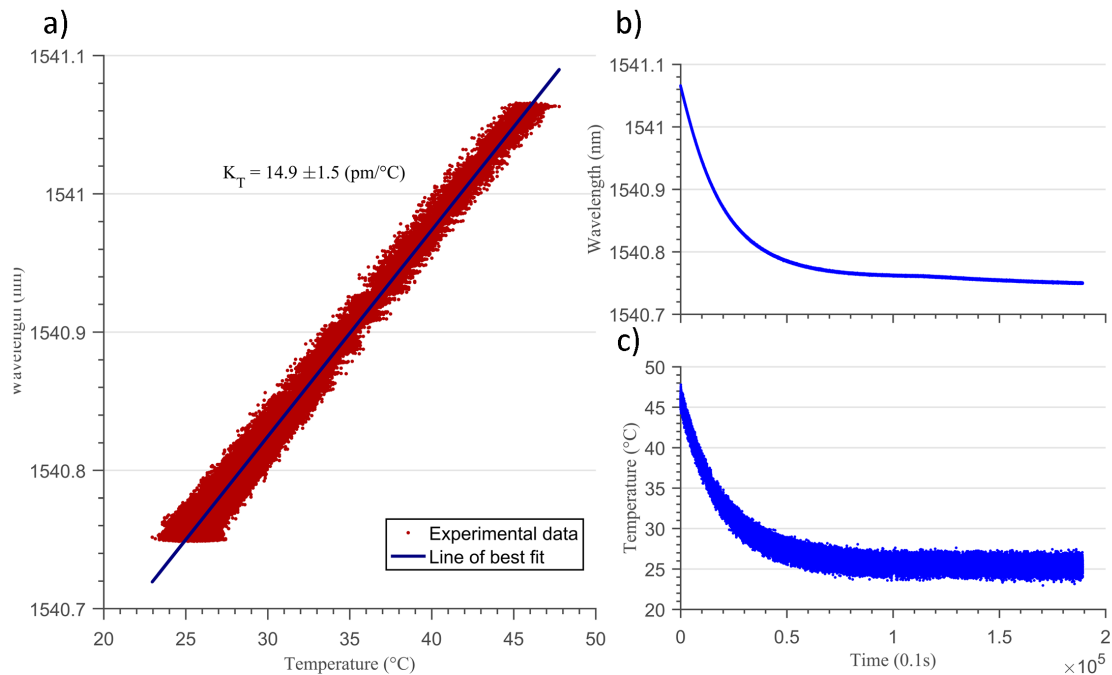


Fig. 5.23 a) Temperature response of a temperature FBG sensor during cooling after induction heating. b) The cooling profile of the FBG. c) The cooling profile of the thermocouple.

Fluctuations in room temperature can also be monitored over several days along with FBG wavelength shifts to accomplish a passive temperature calibration technique. The change in room temperature is relatively slow, so there is less likelihood of errors in temperature between the sensors and the thermocouple. In this work, the natural range of temperature variation was, at most, 7 °C each day. In the real application, sensors can be monitored when the strands are in different locations before installation. This will provide a larger temperature variation, increasing the temperature range that this calibration can be compared to the active heating method.

The results from room temperature fluctuations can be seen in Figure 5.24. The FBG temperature sensor is able to repeat the thermocouple trend with additional features seen due to the high resolution of the sensor. A calibration coefficient of 15.3 pm/°C was obtained from these measurements; this was comparable to the coefficient obtained from induction heating.

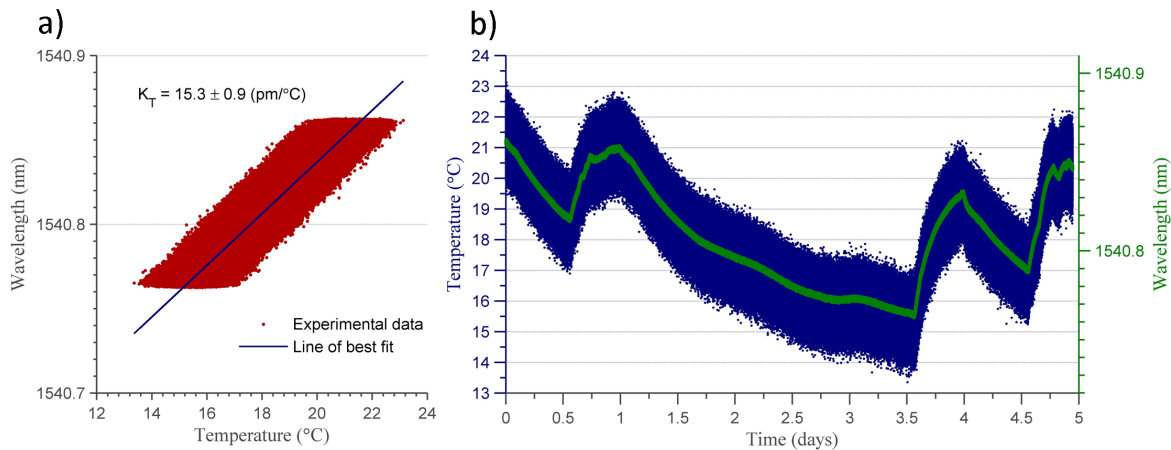


Fig. 5.24 a) Temperature response of the same temperature FBG sensor during room temperature fluctuations. b) The FBG sensor (narrow line) is able to measure smaller deviations in the temperature compared to the thermocouple. Note that these results are highly comparable to the calibration performed inside the environmental chamber, with $K_T = 15.9 \text{ pm}/^\circ\text{C}$, demonstrating that both techniques are applicable in the field.

Finally, the procedure was repeated for a strain FBG sensor, yielding values of $18.1 \pm 1.8 \text{ pm}/^\circ\text{C}$ and $17.1 \pm 1.0 \text{ pm}/^\circ\text{C}$ (induction heating and room temperature variation respectively) for its temperature coefficients. The temperature sensitivity was larger than the temperature FBG sensor due to the thermal expansion of steel that was also present in its temperature dependence. Temperature variations while measuring strain can now be compensated for, allowing the mechanical strain of the steel strands to be determined.

This section outlines a practical solution for calibrating in-situ strain sensors, mounted on steel strands for prestress monitoring. The results show that both the active and passive method were able to replicate, within the error estimate, the temperature coefficients obtained from temperature cycling in an environmental chamber. The calibration error may be reduced by using more accurate temperature references.

Temperature resolution and accuracy

The resolution of the temperature sensors is dependent on the optical interrogator resolution and the temperature sensitivity of the FBG temperature sensor. On average the temperature sensors have a sensitivity of $15 \text{ pm}/^\circ\text{C}$. Given that commercial interrogators generally have a resolution of around 0.5 pm , the resolution of the temperature sensors is approximately $0.03 \text{ }^\circ\text{C}$.

The accuracy of the temperature sensors is affected by a number of factors, see Equation A.36. One of these is the calibration error of the temperature sensitivity (K_T), which is considered first. The temperature sensitivity calibration error of the temperature sensors is given by Equation A.35. It is dependent on the accuracy of the interrogator, the accuracy of the temperature reference used for the calibration and error from fitting a line of best fit to the temperature calibration data. Assuming that the interrogator accuracy is 1 pm and the temperature reference has an accuracy of 1 °C, the error in the temperature sensitivity for the environmental chamber calibration is below 0.4 pm/°C. This value is typical when a thermocouple is used as the temperature reference. A platinum RTD is at least an order of magnitude more accurate, therefore errors can be reduced to below 0.04 pm/°C.

Another error contribution to the temperature sensitivity error is the error introduced by the interrogator accuracy, this error is dominant when using a platinum RTD for temperature calibration. Finally, there is the error from fitting a straight line to the data. When using the two practical methods (induction heating and room temperature, see section above) to calibrate the temperature sensors, the line of best fit error increases from 3.5×10^{-6} nm/°C to $\sim 5.5 \times 10^{-6}$ nm/°C when compared to the environmental chamber calibration. However, this error is more than 10 orders of magnitude smaller than the other two error contributions. The fitting error for the induction heating calibration is higher than for room temperature fluctuation calibration, but the temperature range during calibration has a much greater effect on the temperature sensitivity error. This is shown in Figure 5.25; the error in K_T is less than 0.25 % for temperature ranges greater than 30 °C, but increases to greater than 2.5 % for temperature ranges smaller than 3 °C⁴. The results show that if the room temperature fluctuation method is used for temperature calibration, the temperature range must be at least 10 °C to ensure there is an adequate temperature accuracy. This could be achieved by taking sensor measurements when the strands are outside and inside a temperature controlled building. The calculations show that the two practical temperature calibration methods can achieve error values comparable to the environmental chamber calibration as long as their temperature range is greater than approximately 30 °C. This is because the largest error contributions come from the temperature reference and interrogator which remain the same for the three methods.

The absolute temperature accuracy of a typical temperature sensor is given by Equation A.36; the first and third term in the expression are dominant by three orders of magnitude. Figure 5.26 shows the absolute temperature error of a temperature sensor at 25 °C for different

⁴Extrapolation of a sensors temperature sensitivity fit would required for calibration ranges smaller than the temperature range of the application. All evidence suggests that this would be a valid method as the temperature sensors display linear correlation with temperature. Ideally a temperature sensor should be tested to the complete temperature range it will experience during the application as this would identify if the sensor was faulty.

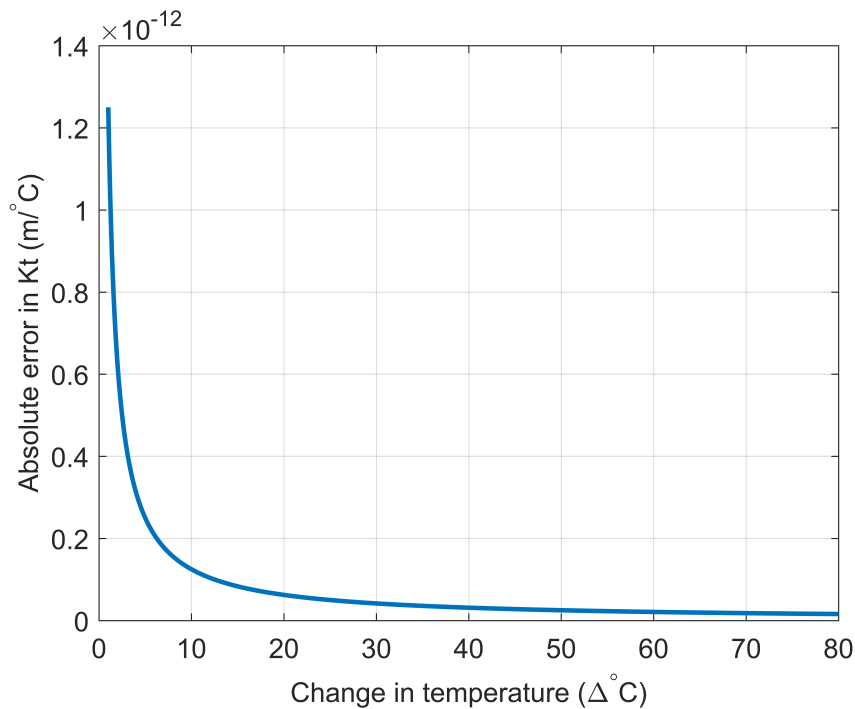


Fig. 5.25 Error in temperature sensitivity for varying temperature range during calibration.

temperature ranges during temperature calibration. The error follows a similar trend to the error of the temperature sensitivity. For a temperature range of greater than 60°C the error is smaller than 0.06°C .

5.6.2 Defect identification during temperature calibration

The two main defects from the sensor fabrication process occur due to the fibre-capillary joint either being exposed to high temperature for too long or, conversely, for too short a time. When the metal coated fibre is exposed to high temperature for a prolonged period, the molten brazing solder removes the metal fibre coating, leaving a bare exposed section at the end of the capillary. Conversely, if the brazing paste does not reach the required temperature to melt all its constituent components then a brittle, porous, inadequate joint is made. By encasing the sensor in resin and exposing the joints by lapping, the joints can be inspected under a microscope and these two types of fabrication defects can be identified. However, such a destructive technique renders the sensor unusable. External inspection is sufficient in most cases, but a joint can appear free from defect externally, while internally it may be of poor quality. Furthermore, faulty sensors may appear fully operational when tested. Such sensors can be identified during

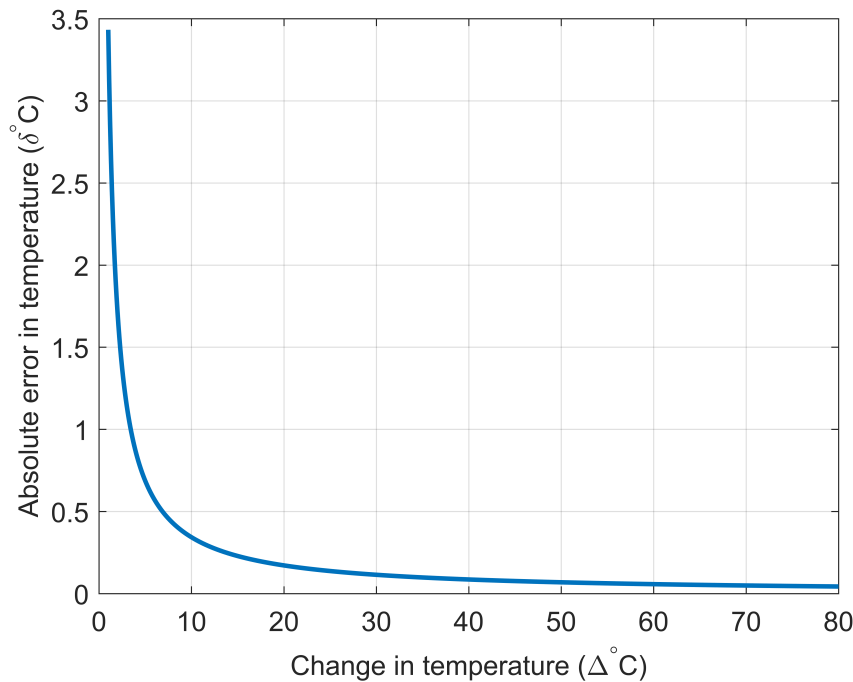


Fig. 5.26 Temperature error of a temperature sensor for varying temperature range during calibration.

the batch temperature calibration process. This defect identification technique constitutes a form of environmental stress screening procedure.

During temperature calibration the metal packaged sensors are heated and the metal capillaries linearly expand. The larger thermal expansion of the capillary stresses the joints between the optical fibre and the capillary. An imperfect joint between the fibre and capillary will allow their relative movement, resulting in an inconsistent temperature coefficient ($\text{pm}/^\circ\text{C}$) for the sensor. By temperature characterising multiple sensors in one run, the experimental variation between each temperature cycle can be tracked providing an indication of the repeatability of the calibration process. Sensors that do not match the trend in experimental variation between cycles can be identified. As discussed above, the most likely cause of an inconsistent temperature coefficient for the sensors is a defective joint between the capillary and fibre.

Figure 5.27 shows plots obtained from four temperature cycles for two different temperature sensors. It is clear from the graphs that the data points obtained for sensor Ch2Sen1 (b) are further from the line of best fit compared to Ch0Sen0 (a), both graphs have the same wavelength range for clarity. To investigate further, the temperature coefficients obtained for each individual cycle for the twelve temperature sensors were plotted on the same graph; this can be seen in Figure 5.28. Most of the sensors had the same magnitude of variation in the temperature

coefficient between each cycle. Collective temperature coefficient variations can be attributed to experimental variation of the temperature calibration procedure. The average temperature coefficient placed in the range 15.5-16.5 pm/°C, therefore any sensors with a coefficient smaller than this should be investigated further as this suggests there was an imperfect contact between the capillary and fibre. There were two sensors, namely Ch2Sen1 and Ch3Sen0, which did not follow the general temperature coefficient trend of the other sensors. Therefore, calibrating multiple sensors in one run can reveal that a specific sensor is unsuitable for deployment, and so the technique has great potential as an environmental stress screening procedure. Without calibrating multiple sensors at once, it would be hard to distinguish between experimental variation and defects in the brazed joints, risking deployment of a defective sensor.

Figure 5.29 shows further evidence that the two sensors identified in Figure 5.28 did indeed have a defective brazed joint. The two sensors (Ch2Sen1 and Ch3Sen0) were held at 35 °C for approximately 8 hours. Their wavelength response, converted to temperature in the graph, clearly showed a large decrease in wavelength over a short time scale. This indicates that under stress, the fibre exiting the capillary slipped due to the tension in the fibre reaching the critical magnitude needed to overcome the fibre-capillary bond. Sensors that were identified as functioning properly did not show the rapid decrease in wavelength seen in Figure 5.29. Therefore it is proposed that prior to calibration, sensors are held at a temperature around 60 °C for 8 hours for a preliminary defect screening. Afterwards, the temperature calibration procedure will identify any additional sensors that do not perform consistently compared to the other sensors in the sample.

This was the first time a relatively large number of sensors (13) had been fabricated together allowing for a statistical sample to be investigated for defects. Through optimising the brazing process, a high percentage (92 %) of consistently performing sensors were fabricated. Batch calibration is able to distinguish between experimental variation in the temperature coefficient and inconsistency due to defective brazing joints. By discovering inconsistent sensor performance before permanent attachment to the steel strands, the reliability and performance of this temperature and strain sensing technique can be improved.

5.6.3 Strain

Similar to temperature calibration, strain calibration of sensors attached to large structures is difficult. Ideally, a strain sensor attached to a prestressing strand should be stressed to the maximum operational force. Stressing the entire length of a strand is not practical outside of the containment due to its long length. Similarly, stressing a section of the strand around the

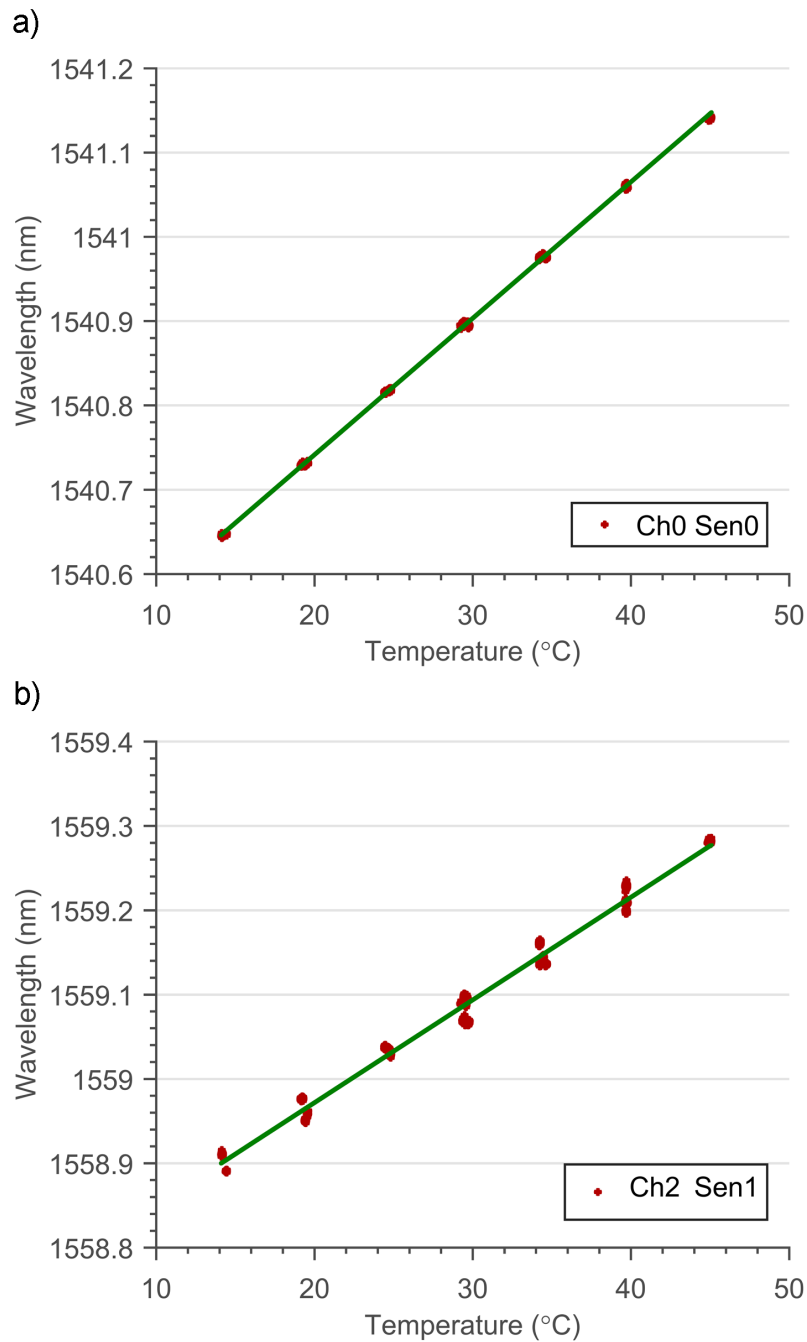


Fig. 5.27 a) Example of a temperature sensor calibration (four temperature cycles) in an environmental chamber. The data points are placed tightly on the least squares line of best fit. b) A second example of temperature sensor calibration from the same batch. Here it is clear the calibration is not as repeatable as the sensor before. This could be due to either the calibration procedure, such as large spatial temperature variations within the environmental chamber or the sensor itself.

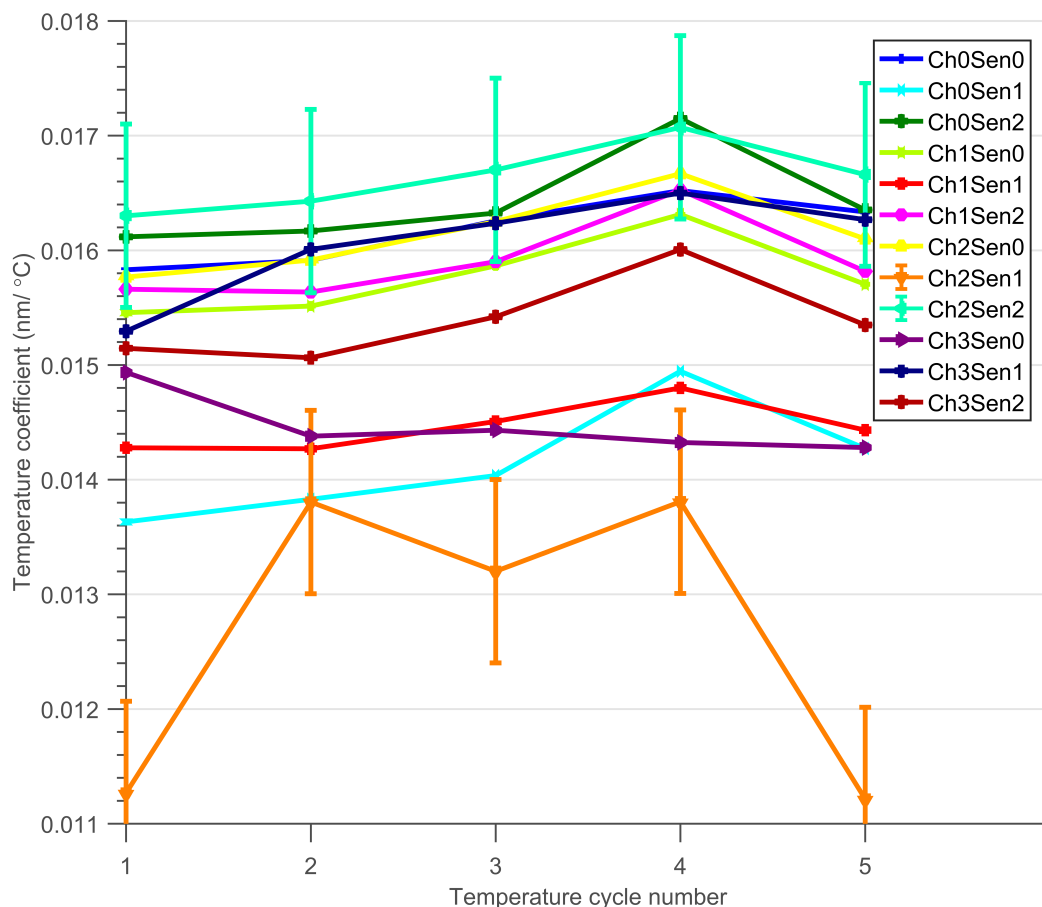


Fig. 5.28 Variation in the temperature coefficient for five temperature calibration cycles. The twelve temperature sensors shown here were calibrated in one run, allowing the experimental variation of each cycle to be monitored by following the general trend of the majority of the sensors. Sensors with inconsistent temperature coefficients can be identified, i.e., sensor Ch2Sen1 and sensor Ch3Sen0. Error bars are shown for the highest and lowest sensitivity sensor for clarity.

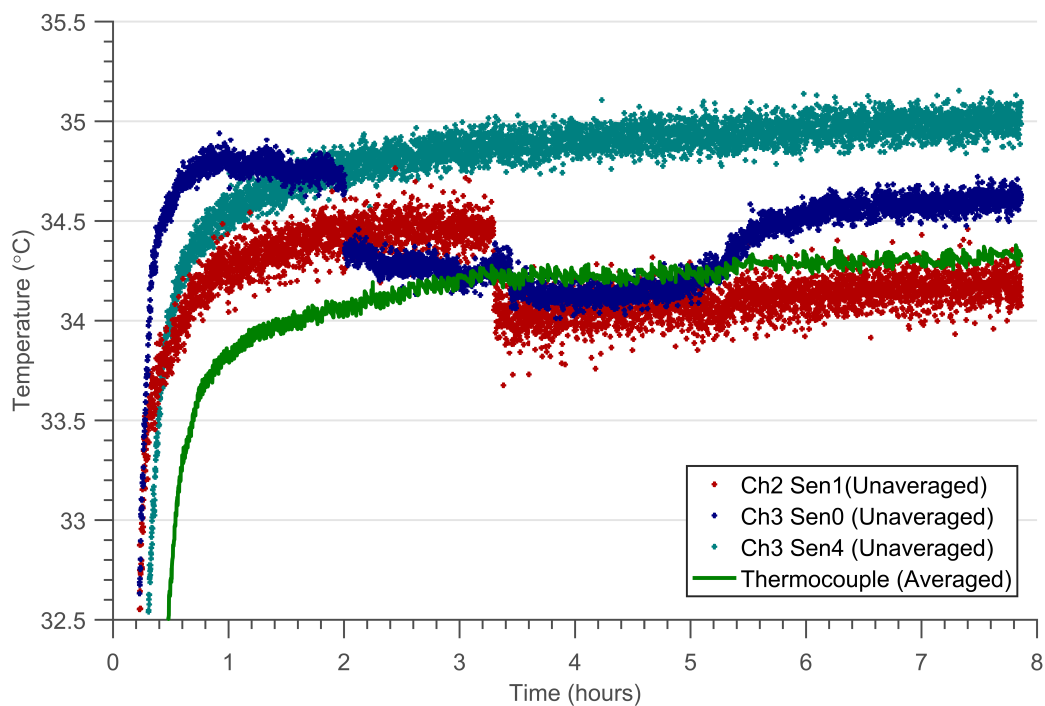


Fig. 5.29 The wavelength response converted to temperature of two temperature sensors held at around 35 °C for 8 hours. A significant blue-shift in the wavelength of both was observed. This indicates that the fibre slipped in the capillary as the brazed joint was put under stress due to thermal expansion. An additional sensor (Ch3 Sen4) is also plotted; this is the response of a sensor without a defect, for reference.

sensor also has its practical issues. Gripping strands with enough holding force to stress them up to 1300 MPa requires a locking system such as the barrel and wedges shown in Figure 2.5. The wedges and strand permanently deform as the load increases so that grip marks are left on the outer surface of the strand. These could be a source of corrosion or a failure initiator. Therefore, when installed in a concrete containment, sensors should initially be calibrated before they are attached to the strands. This will provide an initial sensor calibration and providing the attachment of the shim to the steel strand is consistent enough an average strain transfer coefficient can be applied, allowing sensors to measure strain to an accuracy defined by the strain transfer variation of the sensors.

To confirm that the bare sensor calibration and strand-shim strain transfer is valid for a particular sensor, it is proposed that the instrumented strands are manually bent around a cylinder with the sensor located on the outside of the bend. This will allow the sensor to be strained to a nominal strain without permanently deforming the strand surface. Four-point bending was initially considered, however the problem of securing the strand without damaging it remains with this technique. The sensors can also be checked during strand stressing in the containment. This will provide a final check of the sensors before the strand is locked off permanently. Stress cycles in the containment building will be affected by friction, however, so it is important that there is a high degree of confidence in consistent fabrication and calibration of the sensors before installation of the strands. There are rigorous mathematical frameworks for combining sensor calibration prior to and after attachment to the prestressing strands. One such framework is Bayesian inference which incorporates confidence values for each measurement, see Chapter 11. A demonstration of calibration by stress cycling is carried out in the two field trials in Chapter 7.

Strain calibration by bending

As mentioned previously the sensor calibration can be checked by bending the strand at a certain radius and checking the change in wavelength. Bending a section of strand, where the sensor is located, around a cylinder will allow a reliable and consistent measurement of one strain value. Depending on the consistency of the spot weld attachment, the strands could be bent around a number of cylinders of different radii, to give a full strain calibration of the sensor attached to the prestressing strand. The strain on the outer side of a prestressing strand bent around a cylinder is calculated below.

The arc length of a circle is related to the radius of curvature as follows:

$$L_0 = \rho \theta \quad (5.9)$$

Where ρ is the radius of curvature of the beam and θ is the angle of the sector. L_0 is defined as the initial length of the straight wire, see Figure 5.30. The arc length at the neutral axis remains constant for any bend radius. At a distance y from the neutral axis, the arc length L is:

$$L = (\rho - y)\theta \quad (5.10)$$

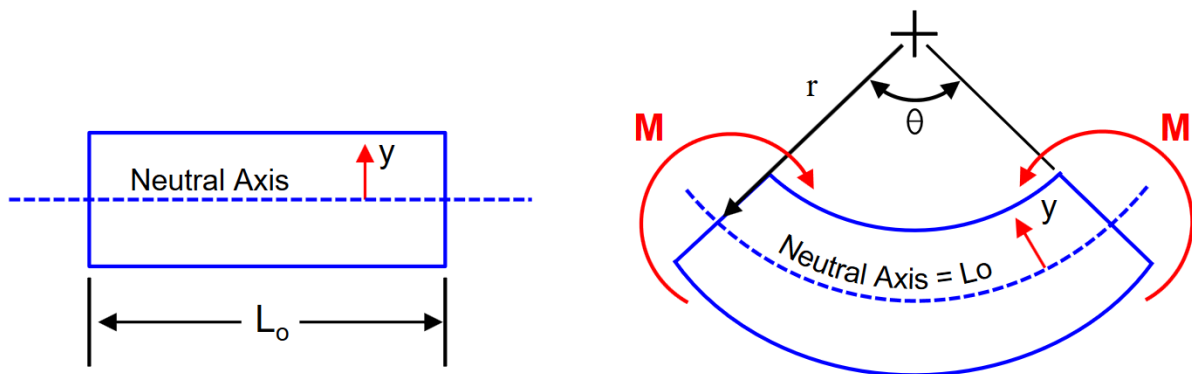


Fig. 5.30 Strain calibration by strand bending. The initial and bent state are shown on the left and right respectively. Zero strain occurs at the neutral axis, while strain is positive below, and negative above the neutral axis. [135]

If the wire is bent, the strain at a distance from the neutral axis can be found from the following equation:

$$\varepsilon = \frac{L - L_0}{L_0} \quad (5.11)$$

Substituting L_0 and L gives the equation for strain at a distance y from the neutral axis:

$$\varepsilon = \frac{-y}{\rho} \quad (5.12)$$

For a strain of $3.5 \text{ m}\varepsilon$, a cylinder with a radius of 2.57 m is required ($y = -9 \text{ mm}$ for the prestressing strands). Therefore, this technique appears feasible to calibrate strain sensors attached to the pressing strands. If calibration for multiple values is required, the strands could be bent around several cylinders with different diameters. For example, for strain measurements between 1 and $7 \text{ m}\varepsilon$, several cylinders with radii between $9 - 1.29 \text{ m}$ are required.

Table 5.2 Mechanical properties of model materials.

Material	Elasticity (GPa)	Density (kg/m ³)	Poisson Ratio
Steel	200	7850	0.33
Kovar	138	8380	0.345
Copper	110	8700	0.35
Brazing Alloy	100	9000	0.33
Silica Glass	73	2203	0.17

5.6.4 Strain transfer model

The sensor package and fibre were simulated in the finite element method (FEM) program Comsol, to investigate the strain transfer between a substrate and the optical fibre. Strain transfer is affected by the sensor package geometry and materials and the attachment method of the FBG to the package. The fibre can be fixed into the package at two points or attached continuously along its length. The simulation for this particular sensor was split into two sections to aid meshing and computation. First, a steel substrate was stressed to 1300 MPa with a bare sensor package attached. The stress from the shim surrounding the capillary from this 3D model was then used in a 2D axisymmetric model that included the shim, capillary, brazed joint and copper coated fibre. The components were modelled as elastic objects so the simulations were not able to replicate non-linear behaviour like creep. They also assumed perfect attachment between the materials. In reality this is not the case and there may be slipping between components such as the silica fibre and copper coating.

The size and geometry of each component in the strain sensor was modelled accurately, with the exception of solidified brazing alloy that forms the joint between the capillary and the fibre. The penetration depth of the brazing alloy into the capillary is not accurately known and is likely to vary between each sensor due to inconsistencies in the capillary flow during brazing. It was assumed that the joint thickness was the space between the fibre and inner radius of the capillary. Another assumption was the composition of the brazing alloy; as it consisted of 55 % silver and once the flux material has burnt off only molten metal remains, the brazing alloy was modelled using the properties of silver. Table 5.2 shows the material properties of the simulations.

Figure 5.31 shows the sensor package attached to the stressed steel specimen. The stress in the shim surrounding the capillary varies, with the largest stress in the region near the middle of the sensor. This can be seen more clearly in terms of strain in Figure 5.32. The graph shows that capillary strain for the section between the two shims ($z=45-55$ mm) is comparable to the

$\sim 6.5 \text{ m}\epsilon$ in the steel specimen. However, capillary strain underneath the shims decreases from $6.5 \text{ m}\epsilon$ to zero. The fibre is fixed to the capillary within this section which will lead to strain transfer of $\sim 50 \%$, although this is dependent on the exact attachment point.

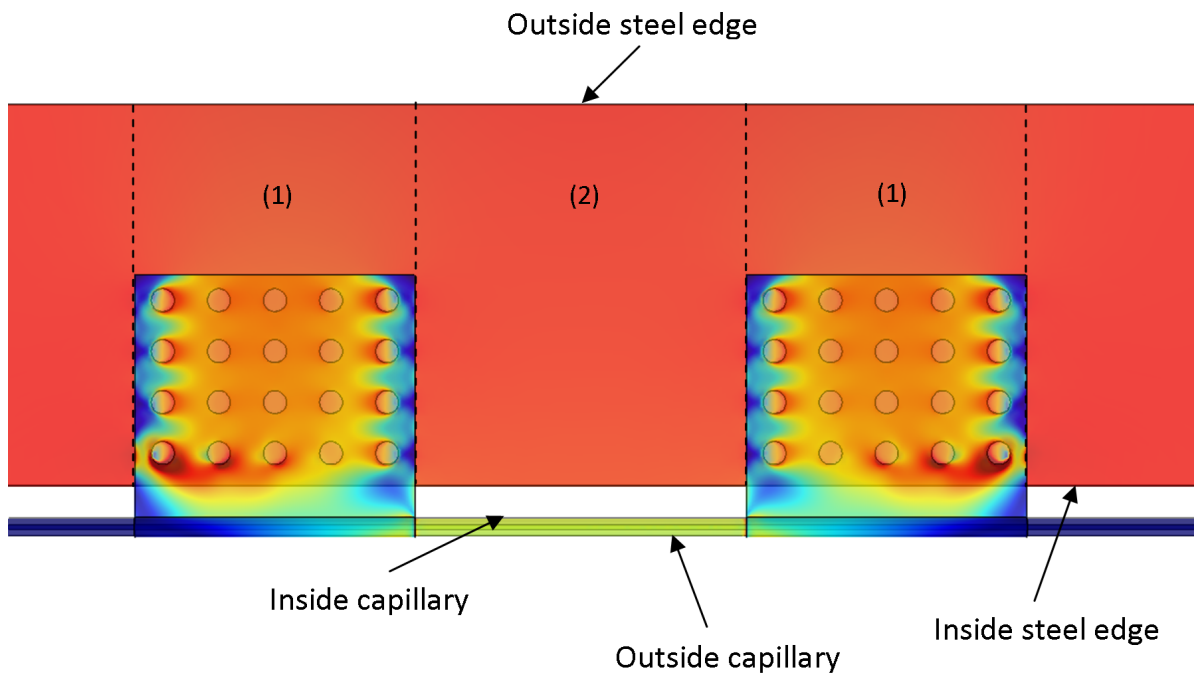


Fig. 5.31 Sensor package on a stressed substrate. The substrate was stressed to 1300 MPa. Stress concentration at the spot welds can be seen, along with varying stress where the shim surrounds the capillary. Two areas, (1) and (2) are labelled to allow comparisons with the strain shown in Figures 5.32 and 5.33.

The varying shim stress from the first model was applied to the second model, Figure 5.33. Here the strain induced on the fibre is about $3.8 \text{ m}\epsilon$, corresponding to strain transfer of 54%. Changing the position of the fixed point increases the strain transfer if it is moved towards the centre of the capillary and vice versa. The models show that the strain transfer of the sensor will not be as high as a bare FBG bonded to the substrate. However, this will be beneficial for this application where high strain is involved.

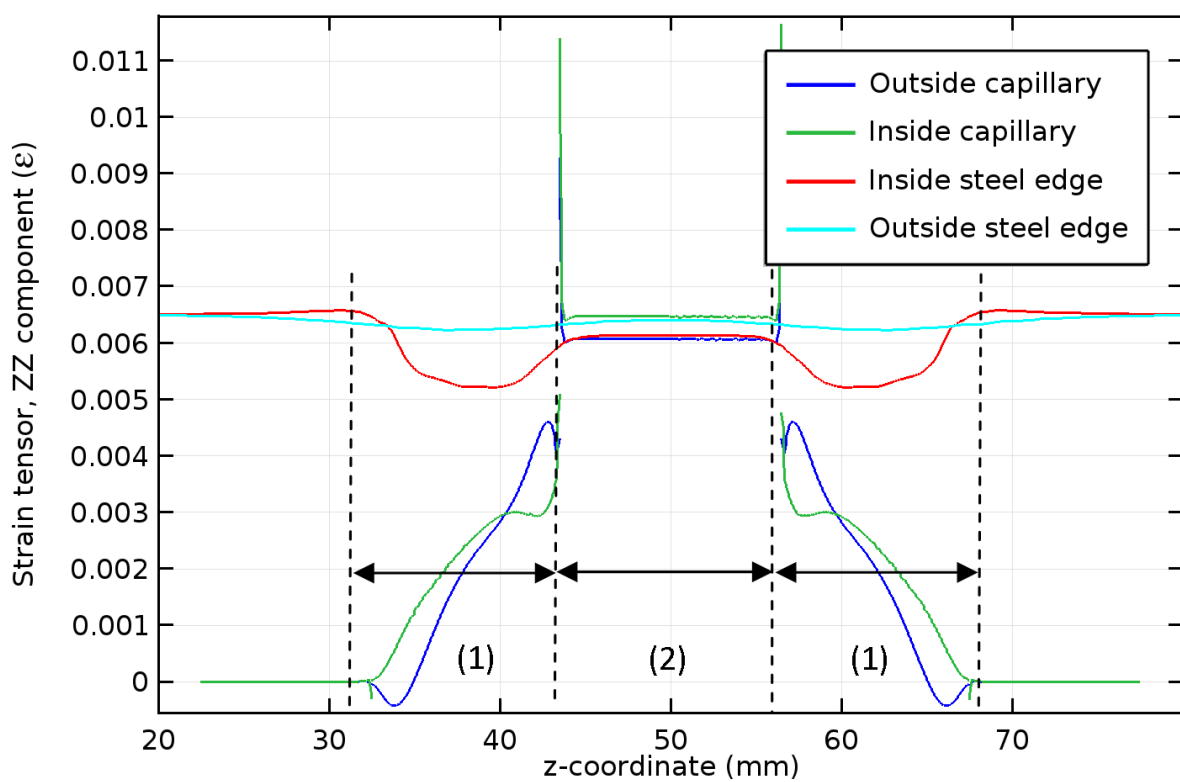


Fig. 5.32 Substrate and capillary model strains, area (1) and (2) correspond to the areas shown in Figure 5.31. In the section of capillary between the shims the strain transfer is close to 1.

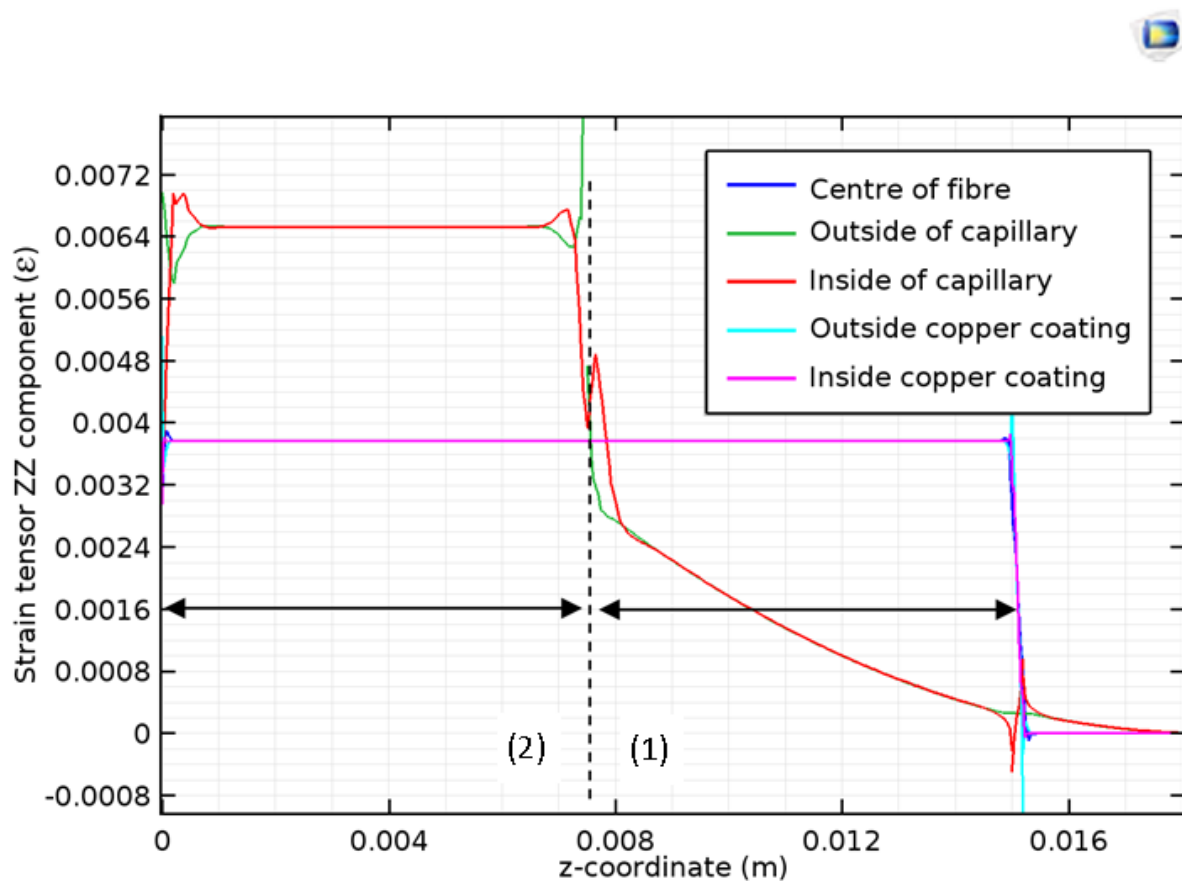


Fig. 5.33 Capillary and fibre model strains, area (1) and (2) correspond to the areas shown in Figure 5.31. The strain in the fibre is lower because the fibre is fixed to the section of capillary where the shim is attached. The strain in this section is lower than the strain in the middle section of the capillary.

5.7 Sensor relaxation from vice stressing

It is likely that the brazing process introduces some residual thermal stress in the brazed joints [136]. This is due to the high temperature needed to melt the brazing solder and the subsequent rapid cooling of the joint. In a previous study an instrumented strand underwent four stress cycles up to 1300 MPa. The strand was held at 1300 MPa for four minutes each cycle. It was found that the sensor response exhibited relaxation characteristics which were attributed to the residual stress within the brazed joints [126]. As a consequence, strain sensors were subject to a series of stressing cycles with a custom made vice. This helped to relax the sensor brazed joints, allowing the sensors to measure strain correctly without having to unnecessarily load cycle the strands.

The vice was designed so that the contact surface where the shims were attached, matched the geometry of the tendon surface. The sensors were mounted onto the vice and stressed so that the peak wavelength shifted by about 3.5 nm, corresponding to a strain of $4.5 \text{ m}\epsilon$ assuming the strain coefficient was that of bare optical fibre ($0.78 \text{ }\epsilon^{-1}$). They were held for several minutes and this was repeated several times. The response of the sensors was also checked on the vice to ensure that the peak wavelength shifted consistently.

The vice was not able to measure the force on the sensor or the strain induced to an accurate value, therefore only a qualitative description of the sensor performance could be obtained from the stressing vice. However, whilst stressing the sensors on the vice, relaxation was clearly seen (first stress cycle of Figure 5.34). This was characterised by an exponential decrease in the wavelength similar to that seen in steel. Another important feature revealed through these tests was that once the sensors had been stressed, if the subsequent stressing was below the maximum wavelength reached previously, the relaxation was reduced. This can be clearly seen in Figure 5.34, where stressing cycle two and four reach a smaller maximum wavelength than the previous stressing, indicating that the stressing vice is able to relax the sensors to a significant extent. This suggests the sensors should be stressed above the level of stress they will experience during service, allowing the relaxation in service to be significantly reduced to measure tendon strain more accurately from the beginning.

5.8 Single wire tensile tests

To demonstrate that the fabrication method is able to produce sensors that can monitor strain for extended periods of time, a strain and temperature sensor were attached to a low relaxation steel rod with a 7 mm diameter. The sensors shims were symmetrically attached to the rod,

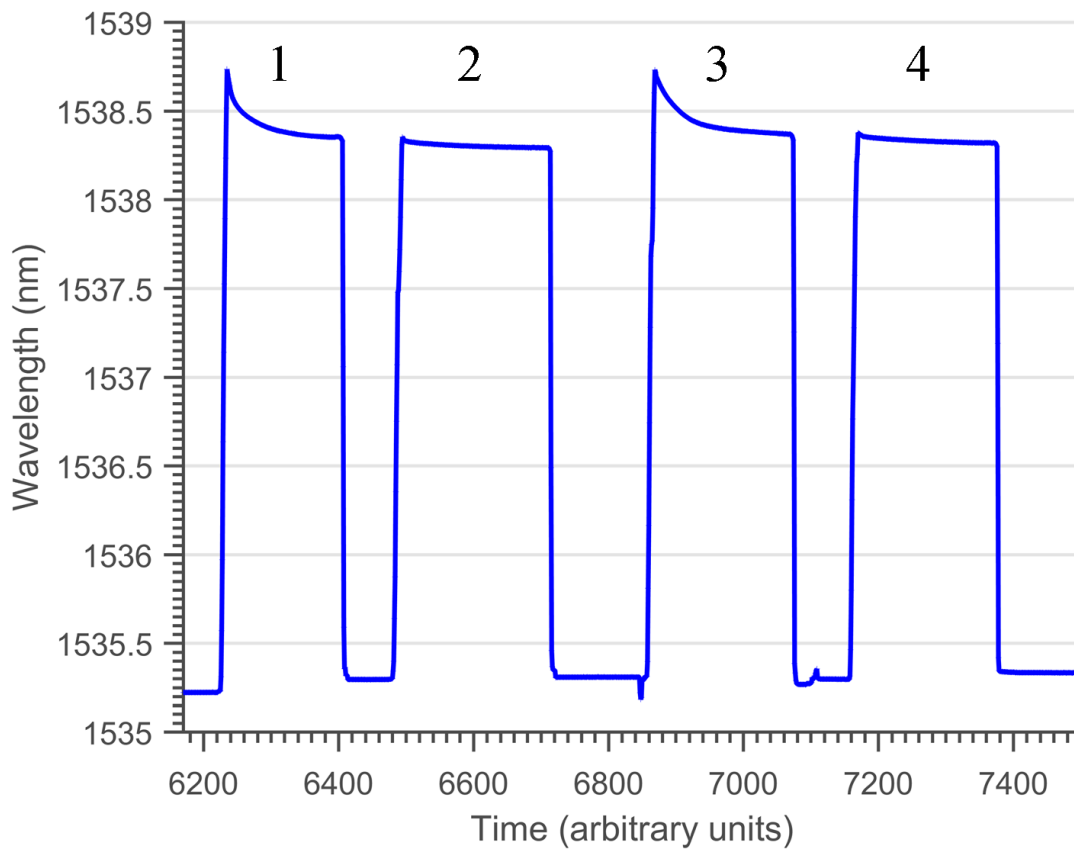


Fig. 5.34 Example of stress relaxation in a strain sensor mounted onto the stressing vice. Stress cycles two and four show reduced relaxation as they were stressed at stress levels below those of the previous cycle. This indicates that the technique has the potential to provide sufficient relaxation of the sensors prior to their deployment.

unlike the asymmetrical attachment that is required to attach them to the prestressing strands. The rod was stressed to 1300 MPa, in two different tests, on a tensile machine and left for an extended period of time at constant displacement. The peak wavelength of both the temperature and strain FBG was measured throughout the experiment. After completion, the strain sensor was temperature compensated and the wavelength was converted to a strain measurement using the strain-optic coefficient. This was then compared to the strain response from the tensile machine, and in the two separate tests with a strain camera and a displacement gauge lasting 110 and 66 hours respectively.

The tensile machine was programmed to provide constant cross-head displacement throughout the test. Therefore the strain sensor response was expected to be constant, while the stress in the strand was expected to decrease due to steel relaxation. There is a significant amount of research on steel relaxation during tensile experiments [37, 137, 138]. However, these were carried out at constant strain (with the exception of [37]) and at constant temperature, which was not the case in these experiments as discussed below. It is possible to compare basic stress trends in the current experiments but the temperature fluctuations that the steel rod experienced will cause small time-scale variations in stress. Temperature variation can be incorporated into empirical equations for steel relaxation [139], although the aim of these experiments was to test the optical sensors so the added complication has not been included.

5.8.1 110hr constant displacement

This experiment ran for 110 hours, and a strain camera was used for an independent measurement of strain. The temperature FBG sensor was able to follow the fluctuations in the thermocouple temperature (Figure 5.35, a). However initially the thermocouple and FBG temperature sensor do not match, this was probably because the thermocouple was situated at the base of the rod in contact with the tensile machine. Ideally it should be placed in thermal equilibrium with the steel rod.

After removing the temperature response of the strain FBG, several features can be seen in Figure 5.35, b). The strain sensor features have similarities with the stress data and the fluctuations match in time. The machine stress decreased over time, while the FBG response was relatively flat ignoring the obvious fluctuations. Figure 5.35 shows the limitations of converting tensile machine stress to strain via the modulus of elasticity under certain conditions. The decrease in machine strain was probably due to stress relaxation. The fluctuations seen in both the machine and FBG sensor strain can be explained by the temperature variation during the experiment (Figure 5.35, a). Machine strain is measured as displacement of the cross-head,

so while this was constant throughout the experiment, temperature fluctuations still had an effect on the rod and therefore strain measured by the FBG sensor. There was a significant increase in the stress when the temperature decreased by $1.5\text{ }^{\circ}\text{C}$ over 5 hours. Likewise, there was a significant decrease in stress when the temperature increased by $2.5\text{ }^{\circ}\text{C}$ over 5 hours. This was consistent with previous findings [140].

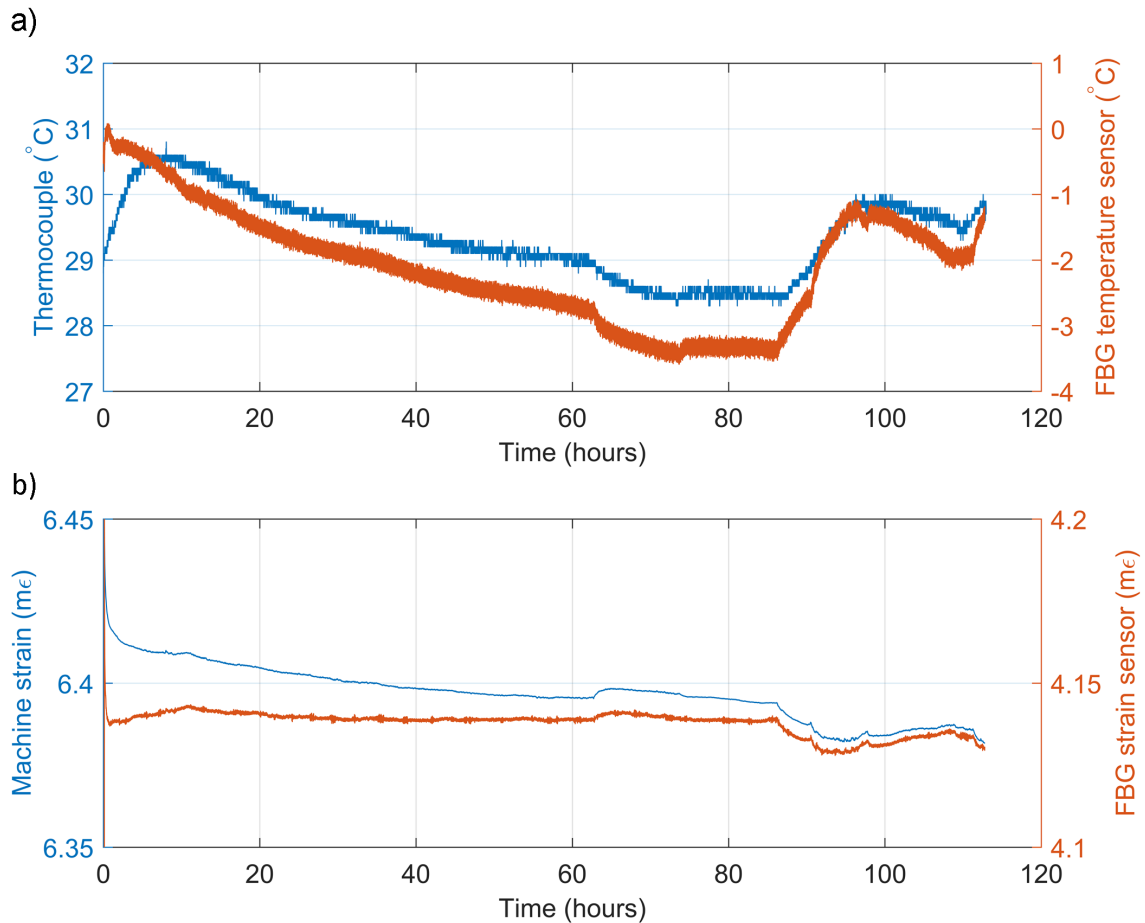


Fig. 5.35 Temperature, a) and strain, b) measurements during a 110 hr constant displacement tensile test. FBG wavelength was converted to strain using the strain-optic coefficient.

The initial strain measured by the camera was about $6.5\text{ m}\epsilon$ (comparable to $6.4\text{ m}\epsilon$ calculated from the stress data) but does not show the initial strain decrease measured by the machine and FBG sensor in the first hour. Due to a malfunction, the strain camera only recorded measurements for the first 30 minutes. Additionally, the strain camera measurements had large noise, so the variations in strain would not have been resolved by the strain camera. The strain FBG measured $4.14\text{ m}\epsilon$ after ~ 10 hours compared to $6.42\text{ m}\epsilon$ measured by the tensile machine. The difference between these values can be explained by the strain transfer properties of the

sensor packaging. This difference ($\sim 65\%$) compares well with previous measurements of these particular symmetrical sensors [126]. The response of the strain FBG throughout the experiment cannot be independently verified by the strain camera due to the malfunction but the small fluctuations do match in time with the machine data.

5.8.2 60hr constant displacement

In the second test, the strain camera was replaced with a displacement gauge to independently verify the FBG strain measurements. Figure 5.36 shows that the converted strain response of the FBG was comparable to the previous experiment; for a stress of $1280 \pm 6\text{MPa}$ the strain from the FBG sensor was calculated as $4.14\text{ m}\epsilon$ and $4.16\text{ m}\epsilon$ for the first and second test respectively. Steel relaxation can be seen in the machine stress converted to strain whilst the strain sensor had a flatter response. Strain in the rod was recorded for the entire experiment with a physical displacement gauge. Its initial response as the steel rod was stressed to $\sim 1300\text{MPa}$ corresponded well with the response from the strain FBG. However, after 20 minutes there was a significant difference in the strain measurement. The displacement gauge measured an increase of $0.15\text{ m}\epsilon$ while the FBG measured a decrease of less than $0.01\text{ m}\epsilon$. As the machine strain also showed a decrease of $\sim 0.01\text{ m}\epsilon$, the displacement gauge data must be discounted. Furthermore, the strain variation in the displacement data cannot be explained by temperature variation during the experiment. Therefore, it was likely that the displacement gauge was not correctly fixed to the steel rod.

The temperature sensor had the same feature at the start of the measurements as with previous experiment (Figure 5.36). The temperature response of the thermocouple increased by $0.5\text{ }^\circ\text{C}$ over the first 6 hours but this was not seen by the temperature FBG. The thermocouple was in the same position as the previous experiment so this discrepancy could once again be explained by the difference in position.

Both independent strain measurements failed to provide confirmation that the FBG strain sensor was measuring strain correctly. However this was due to failure of the strain camera and displacement gauge rather than the FBG sensor. FBG sensor strains match those measured by the machine but the overall decreasing trend in the machine strain is due to steel relaxation. Steel relaxation with varying strain and temperature can be modelled if necessary [139]. Although in terms of validating the FBG sensor response it would be more useful to rerun the tests with a properly functioning independent strain measurement. The remaining option for this would be to attach an electrical strain gauge to the rod, however this was not possible at the time. The

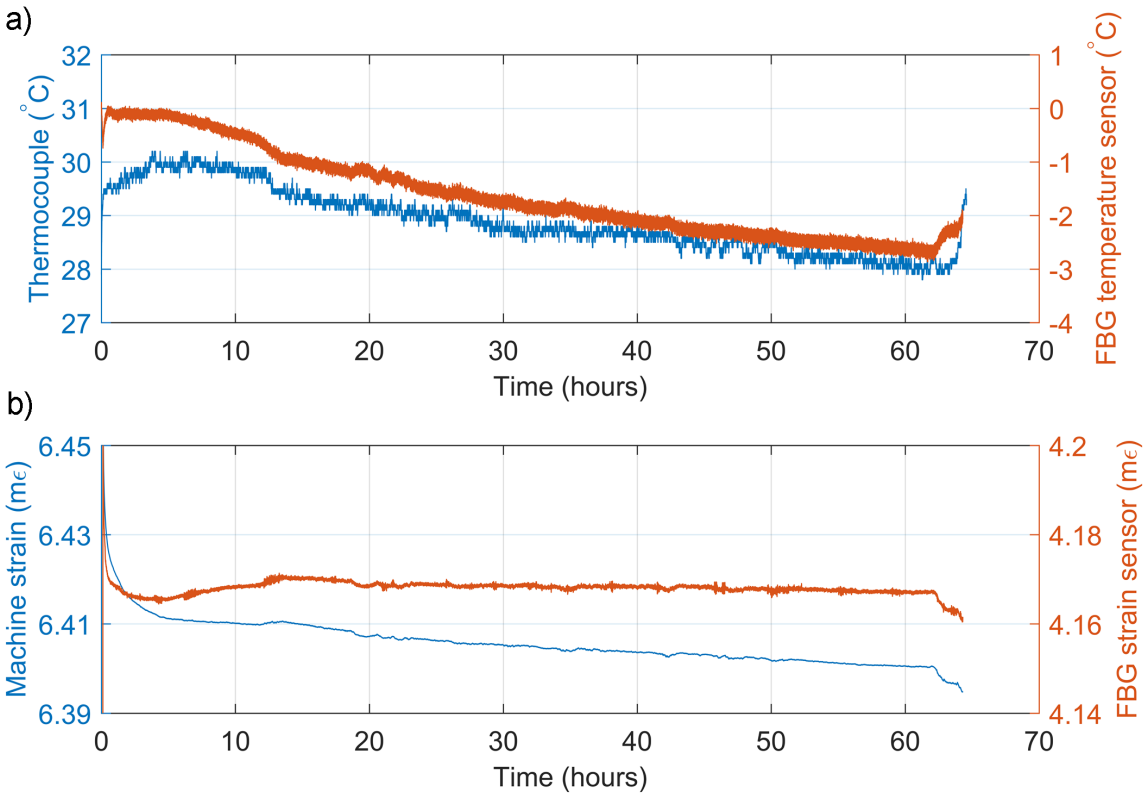


Fig. 5.36 Temperature, a) and strain, b) measurements during a 66 hr constant displacement tensile test. FBG wavelength was converted to strain using the strain-optic coefficient.

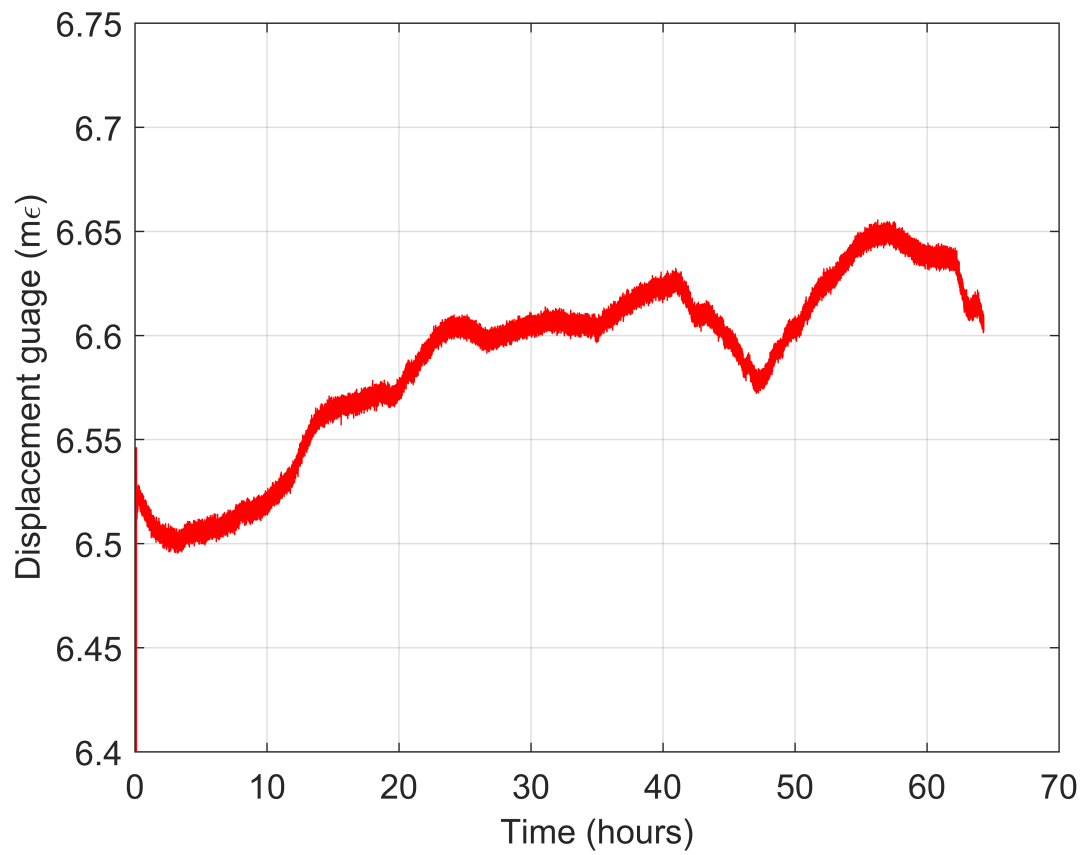


Fig. 5.37 Strain measured by a displacement gauge during a 66 hr constant displacement tensile test. The displacement gauge did not match the machine and FBG sensor strain, so it was likely that it was not attached correctly to the rod.

stressing experiments show that the temperature FBG sensor was able to accurately record temperature variations when compared to the thermocouple.

5.9 Summary

Metal coated fibre can be sealed into metal capillaries via induction heating. Induction heating causes the brazing paste to melt and capillary flow draws the molten solder into the capillary to form a joint between the capillary and fibre. Kovar was found to be the most suitable capillary material due to its Curie transition protecting the FBG from the high temperature reached during brazing. This technique allowed sensors to be made from an all metal construction removing the need for epoxy which is potentially beneficial in high-stress nuclear environments. Temperature and strain sensors were made using this fabrication process and through monitoring the wavelength and reflectivity of the encapsulated FBG, the process was shown to not cause significant deterioration to the FBGs.

Fabricated sensors must be calibrated for both temperature and strain. Several temperature calibration techniques were developed specifically for this application as the long length of the strands causes practical issues when trying to temperature calibrate the strain sensors. In-situ temperature calibration by local induction heating and natural temperature fluctuations showed that, within the error, the calibration obtained from these two techniques was comparable to that carried out in an environmental chamber. The temperature error of a typical temperature sensor was found to be less than 0.06 °C for a calibration range of 60 °C. Strain calibration of the strain sensors is also problematic as the strands cannot be practically stressed outside of the tendon ducts. Therefore, the sensors should be calibrated before attachment to the strands. Calibration after attachment should then be performed by bending the strands around several cylinders with different diameters to obtain consistent measurement points of the full strain range. A final check of the calibration can be carried out with a stress cycle upon installation. A strain transfer FEM model was developed to provide an indication of the strain transfer that can be expected. The model predicted that the strain transfer would be no more than 50 %, and depending on the location of the brazed joint compared to the shim, it may be as low as 10 %.

Strain sensors were tested on a manual stressing vice. The wavelength response showed that the sensors undergo relaxation. This is likely due to the thermal stress caused by the brazing process. If the sensors were stressed to lower stress levels than those previously reached, the relaxation was smaller. Finally, to demonstrate that the brazing fabrication process is able to produce sensors that can measure the required strain levels, a strain sensor was mounted on a high strength steel rod and stressed to 1300 MPa in two tests of 66 and 110 hours. The sensor

was able to measure strain comparable to that measured by the tensile machine although an independent verification of the strain measurement was not achieved due to a malfunctioning strain camera and extensometer. It must be noted that this sensor had symmetrical attachment to the rod via shims, whereas in the application the attachment will be asymmetric.

In this chapter, all the stages to fabricate temperature and strain sensors and instrument prestressing strands have been demonstrated. Sensors were able to measure strain up to the required $6.5 \text{ m}\epsilon$. The next chapter concentrates on more detailed tensile machine tests of the sensors in order to properly characterise their strain response.

Chapter 6

Tensile machine tests

6.1 Sensor package tensile strength

Section 5.4 showed that the kovar capillary was the first component of the metal sensor package to fail during stress testing. Consequently, the bare sensor package was tested on a tensile machine to check that the kovar would be able to withstand the stress applied to it when attached to stressed prestressing strands. A set of grips were machined to match the ones on the manual stressing vice described in Section 5.7. Predictions from the material properties of kovar indicate that the capillaries should fail between 160 and 250 N, therefore a load cell with maximum force capacity of 250 N was installed on the load machine. Figure 6.1 shows a typical stress versus machine displacement plot of a sensor package. It shows that the capillaries did not fail at the predicted force and that the displacement is much greater than expected. This is a clear indication of the sensor package slipping in the grips. While the sensor could not be properly fixed to the grips during this project, this test shows that the kovar capillaries are able to withstand a higher force than predicted and are therefore a suitable material to use. The variation in tensile strength of the kovar is possibly due to annealing.

6.2 Strain calibration

A number of strain sensors were tested with a tensile machine to ensure that they were able to measure strains of up to $6.5 \text{ m}\epsilon$ and to measure their strain sensitivity. They were attached to high strength (CS95 grade) steel dumbbell specimens. The steel had a Rockwell hardness of 50-52, equivalent to a tensile strength of 1663-1725 MPa. Dimensions were chosen so that the steel could be stressed upwards of 1400 MPa on a 10 kN tensile machine; this resulted in the

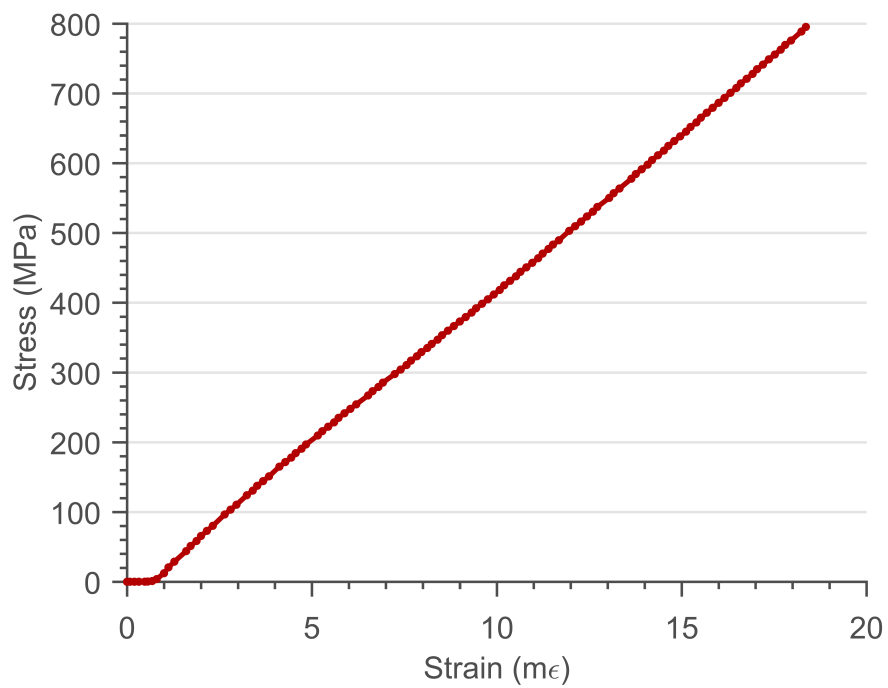


Fig. 6.1 Sensor package stressed on tensile machine. The sensor package did not fail during the stressing. The large strain measured is a clear indication of the package slipping in the machine grips.

steel having a width and thickness of 7 mm and 1 mm respectively. The required stress was achieved by tensioning the specimen to a force of 9.8 kN.

The steel specimen was mounted on a 10 kN tensile machine (Figure 6.2) and a step-like test profile was programmed for different strain ranges. For example, the maximum force the specimens were tested to was 10 kN; in this case, the force was increased in multiples of 1 kN and held for 20 seconds at each stage as seen in Figure 6.3. This was repeated for three cycles. During these experiments, the FBG sensors were interrogated continuously on separate channels of a National Instruments PXI-4844 interrogator. Force measured by an external load cell was also recorded. Additionally, temperature was measured by a thermocouple to compensate the strain sensors. The maximum temperature change during the experiments was 0.02 °C. The strain sensors had an average temperature sensitivity of 15 pm/°C. While the National Instruments interrogator has an accuracy of 1 pm, therefore the result of this temperature change was negligible, especially considering the wavelength changes due to stressing the sensors.

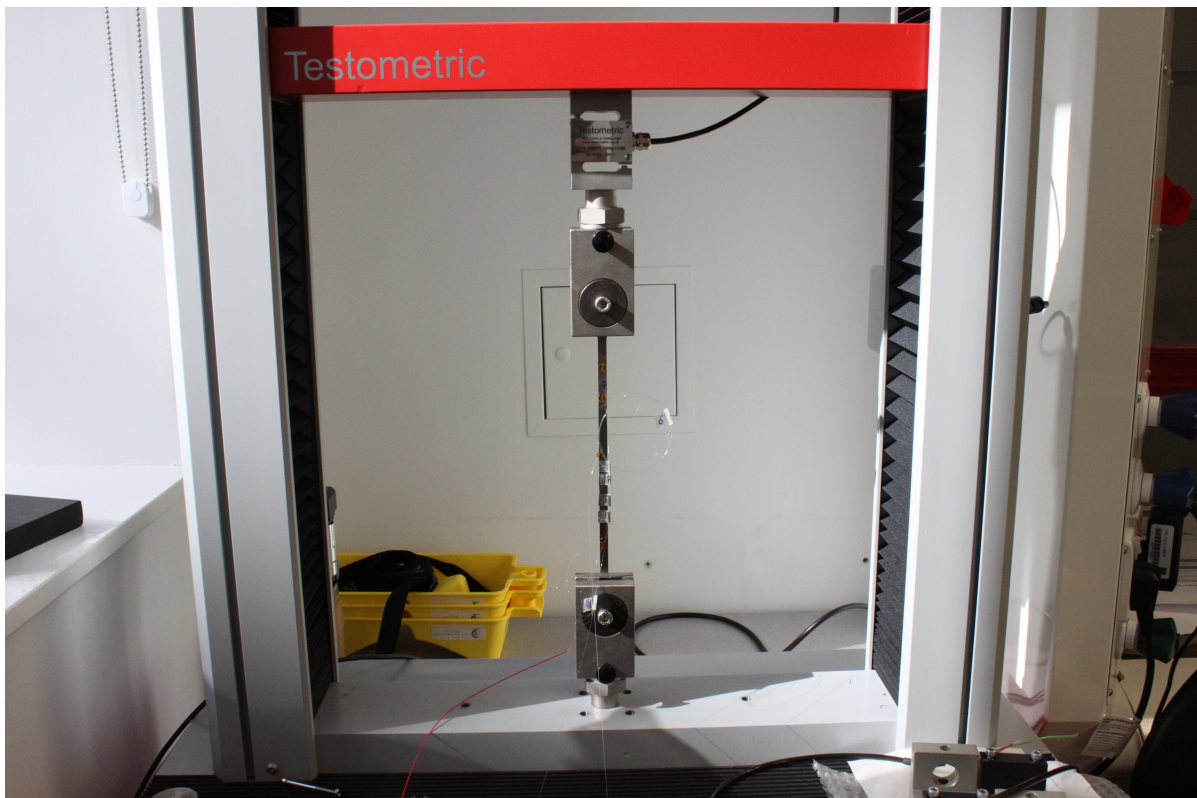


Fig. 6.2 Steel specimen mounted on a tensile machine. The sensors were tested by cycling the specimen up to 1400 MPa in several cycles.

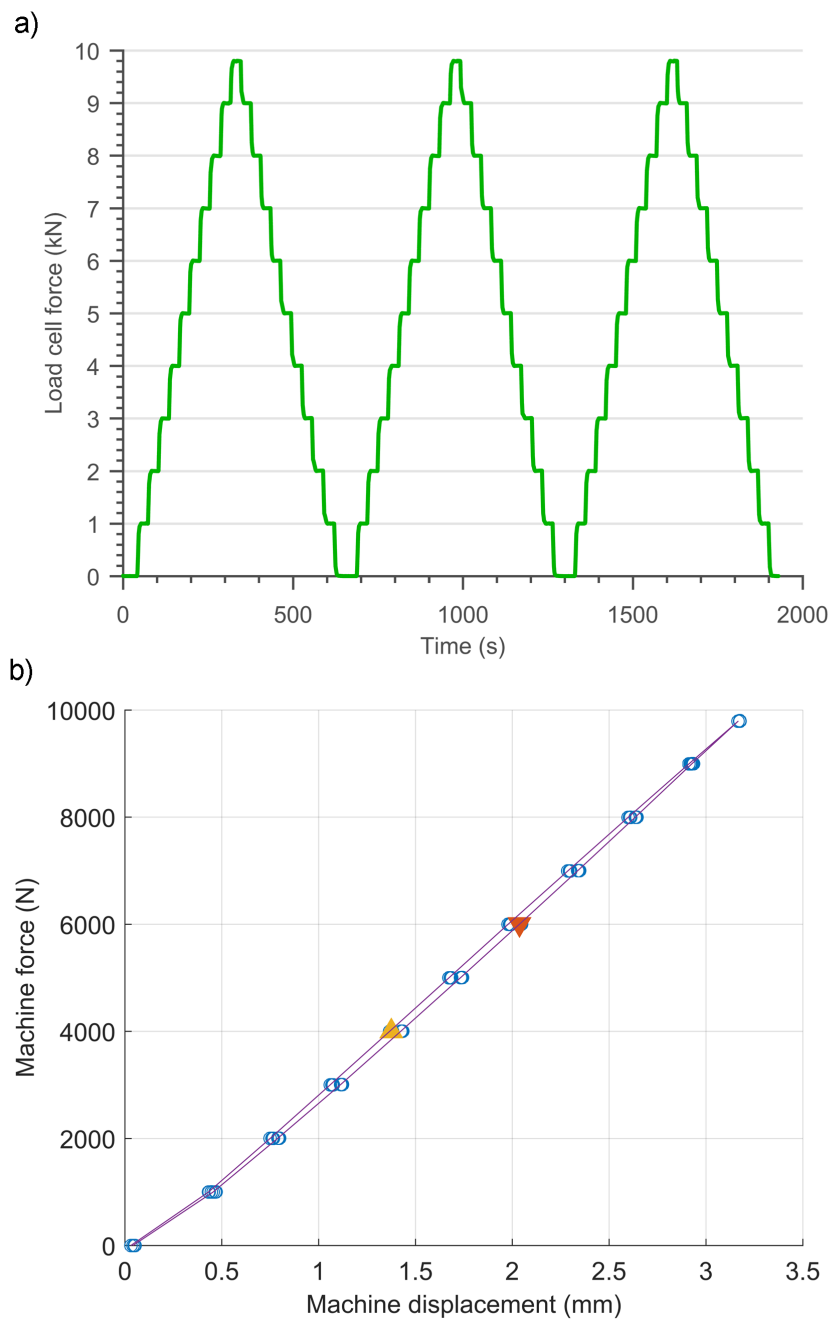


Fig. 6.3 Example of a tensile machine calibration test. a) The tensile machine was programmed to increase force in steps to calibrate the strain sensors when they were attached to steel specimens. In this case the specimen was stressed to 1400 MPa. b) A small amount of hysteresis can be seen when comparing machine displacement to load cell force. Increasing and decreasing force are shown by the triangle pointing upward and downward in the vertical direction, respectively.

In order to calibrate the strain sensors, the load cell force was converted to strain using the modulus of elasticity of the specimen (193 MPa). Figure 6.3 b) shows the force-displacement relationship measured by the machine during force cycling of one of the specimens. There are two things to note here: there is a small amount of hysteresis, and the machine displacement at 9.8 kN converts to a strain of $\sim 11 \text{ m}\epsilon$ which is over $3.3 \text{ m}\epsilon$ more than the expected strain of the specimen. This suggests the machine extension is not a reliable measurement to use as a comparison to the strain sensors. This is further supported by the results from calibrating epoxied FBGs, they show negligible hysteresis between loading and unloading as will be discussed in Section 6.3. The larger than expected displacement is due to machine displacement measurements including grip and load cell extension and frame compression and the results here are consistent to previous findings [141, 142]. If necessary, tensile machine frame stiffness can be calculated and used to compensate machine displacement so that it more accurately represents specimen strain [143, 144]. Strain determined from the load cell measurement is more accurate and therefore was used for the calibration. Future work would benefit from using an external extensometer or electric strain gauges.

The derived strain was compared with the wavelength measurements from the strain sensors. The wavelength and strain readings used for the calibration were taken midway through the 20 second period when the tensile machine was holding a given force. Least squares fitting was used to determine the strain transfer, K_ϵ , of the individual sensors. This assumed a perfect strain transfer would change the wavelength of the FBG by 0.78ϵ .

The sensors that were attached to specimens were first calibrated to $3.3 \text{ m}\epsilon$ several times and then up to $7.2 \text{ m}\epsilon$. This was partly so that data could be recorded from the sensors before they were subject to high strain where they could possibly fail and partly to determine if the sensors had a different sensitivity for different strain ranges. Figure 6.4 shows an example of two sensors being calibrated up to $3.3 \text{ m}\epsilon$. Both sensors displayed hysteresis.

6.2.1 Hysteresis during tensile testing

Hysteresis is commonly seen during tensile machine tests, a small amount can be seen in Figure 6.3. The underlying cause of hysteresis is material viscoelasticity and specifically anelasticity. A viscoelastic material has a time dependent component to its response to stress or strain. For example when held at constant force, the strain of a viscoelastic material will increase over time. Similarly, when held at constant strain, stress in the material decreases. This is known as relaxation and was described in Section 2.3. Anelasticity is the time-dependent recovery of creep strain after unloading [145]. The time dependent nature of these effects causes a

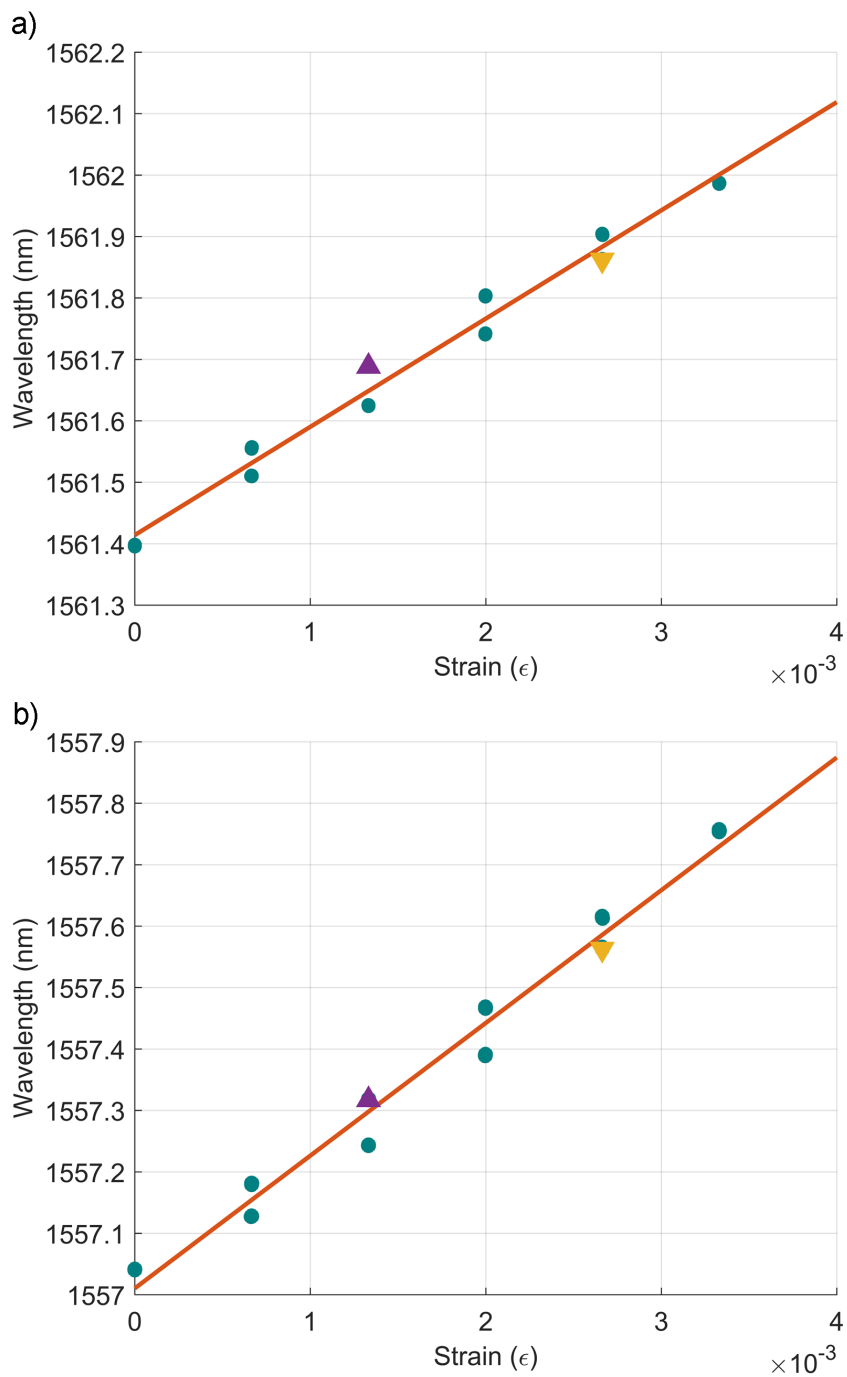


Fig. 6.4 Two different strain sensors (a and b) calibrated up to $3.3 \text{ m}\epsilon$.

difference in material properties for tensile tests at different stress/strain rates. This is because the stress rate determines the combination of elastic and anelastic strain. For a specimen that is rapidly loaded, anelastic strain approaches zero. Whereas, a specimen that is slowly loaded will show greater anelastic strain [141]. Therefore, a specimen that is loaded slowly will have a smaller measured modulus of elasticity compared to one that is loaded quickly.

We can assume that at the two extremes, the specimen is either loaded fast enough that it is in a completely unrelaxed state or that the loading is so slow that the specimen is fully relaxed as it is loaded. Practical tensile tests are carried out at a speed that is somewhere between these two extremes. Therefore, test speed can have an effect on the measured properties of the specimen being tested. It can also have an effect on the stress-strain curve, causing deviations from a linear correlation. A short time after loading or unloading the curve will be closer to an unrelaxed state compared to later in the curve where some relaxation will have occurred. This causes hysteresis in the stress-strain curve; near the point of loading or unloading the curve is steeper as the specimen is stiffer.

This was probably the cause of the hysteresis in the sensor calibration graphs. The response was repeatable over several cycles, which suggests wavelength changes were not permanent because the strain was recoverable, at least in these tests. Chapter 9 investigates this effect in more detail and further characterises the behaviour of the sensors.

6.2.2 Sensor hysteresis

Figure 6.5 shows load cell force against strain sensor wavelength. This is equivalent to a stress-strain curve as force and wavelength are proportional to stress and strain respectively. The sensor hysteresis loop direction is reversed when compared to a regular hysteresis curve from a tensile machine test. In other words, for a given force, the wavelength during loading was higher than the one during unloading. However, this is expected if it is the brazed joint between the capillary and fibre that is exhibiting viscoelastic behaviour.

The FBG peak shift is not a measurement of the strain in the brazed joint itself, it is a measurement of the stress and strain transferred from the kovar capillary to the brazed joint and then to the fibre. If there is viscoelastic behaviour in the brazed joint the elongation in the fibre will reduce over time because less stress/strain will be transferred to the fibre. Therefore, viscoelastic behaviour of the brazed joint would cause smaller wavelength during unloading for a given force. The hysteretic behaviour of the sensor wavelength response during loading and unloading was due to the joint between the capillary and fibre.

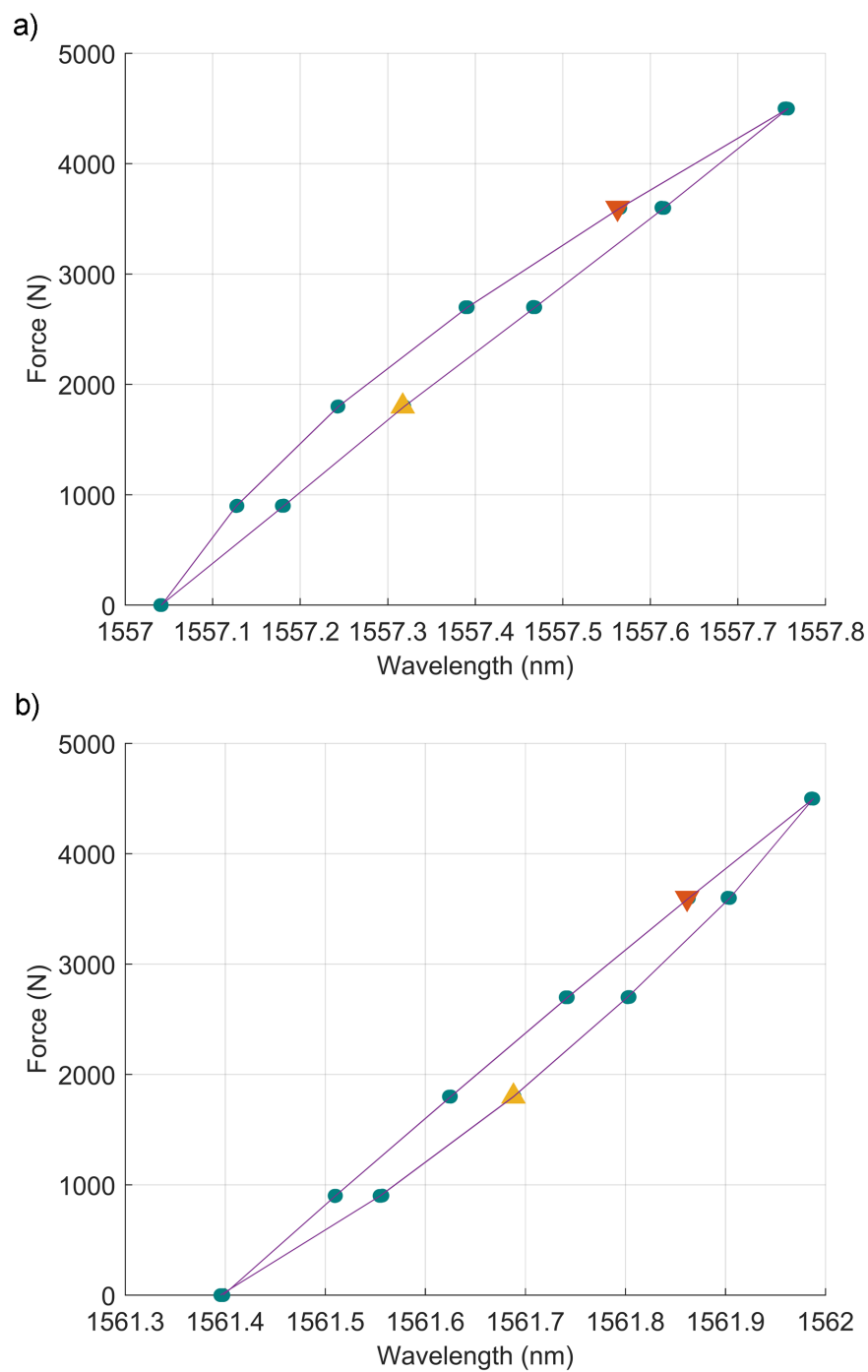


Fig. 6.5 Load cell force against sensor wavelength during $3.3 \text{ m}\epsilon$ calibration for two different sensors. This graph is similar to Figure 6.4 but the axes have been switched around. This graph represents a stress-strain graph. The hysteresis loop is reversed compared to the stress strain graph of specimen. This is because relaxation is occurring in the brazed joint.

6.2.3 Sensor strain sensitivity

Figure 6.6 and 6.7 show two examples of sensors being calibrated up to $7.2 \text{ m}\epsilon$. Their response is similar to that seen during calibration at smaller strain. Table 6.1 shows the best fit slope of the three sensors shown in the figures in this section. The strain sensitivity at $3.3 \text{ m}\epsilon$ is larger than it is for $7.2 \text{ m}\epsilon$. This can, in part, be explained by relaxation. The calibration cycles were carried out at the same speed so a sensor being loaded to higher force will experience force for a longer period than when being loaded to a lower force. This means that the sensor will have had a longer time to relax leading to a reducing sensitivity. This is investigated in more detail in Chapter 9.

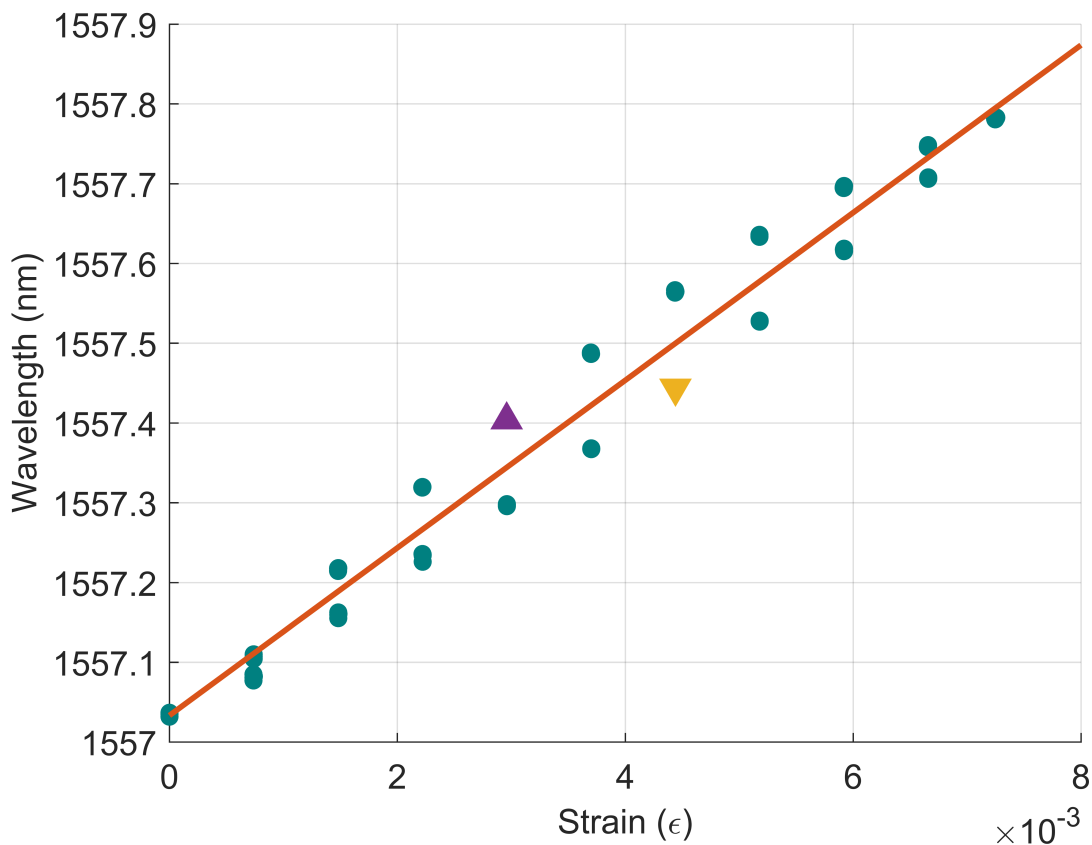


Fig. 6.6 A strain sensor calibrated up to $7.2 \text{ m}\epsilon$.

Compared to the FEM model predictions, the measured strain transfer of the sensors was significantly lower. The models predict approximately 50 % strain transfer, however sensors showed strain transfers that were closer to 10-20 %. Sensor strain sensitivity decreased with calibration to higher strains. Following this, the highest strain transfer was 36 % and was

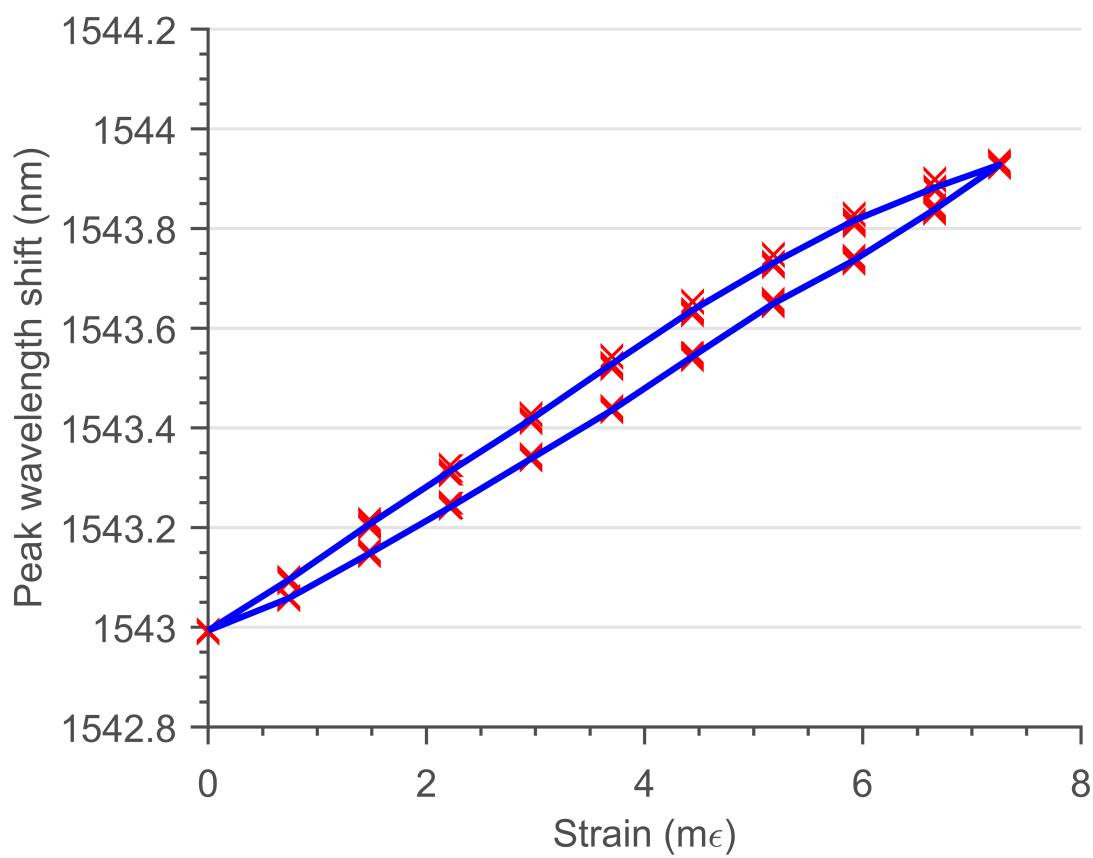


Fig. 6.7 A metal packaged sensor calibrated with a tensile machine.

measured during calibration to $0.5 \text{ m}\epsilon$. The strain sensitivity has some dependence on the chosen modulus of elasticity of the steel specimen as the strain used for the calibrations was converted from load cell force. There is only a $\sim 1 \%$ change in the strain transfer if the modulus of elasticity is altered by 10 GPa, so this is not likely to change the strain transfer by a significant amount. The FEM models assume perfect contact between the specimen and spot welded shim, however this is not likely to be the case. Additionally, non-linear mechanical effects such as creep and relaxation were not included in the model. It is obvious from the calibration graphs and previous discussion that these effects have a significant effect on the performance of the sensors.

Table 6.1 Strain sensitivity of several sensors. Strain sensitivity was determined by a least squares linear best fit. The strain transfer of a sensor was calculated by assuming a perfect normalised wavelength strain sensitivity of 0.78.

Sensor	Strain sensitivity (nm/ ϵ)		Strain transfer (%)	
	3.3 m ϵ	7.2 m ϵ	3.3 m ϵ	7.2 m ϵ
Sensor A	216	107	17.8	8.7
Sensor B	176	-	14.5	-
Sensor C	-	133	-	10.8

6.3 Epoxy sensor tensile tests

During several of the metal packaged sensor tests, FBGs were epoxied to the same specimen to give a direct comparison. Figure 6.8 shows an example of the wavelength change of such an FBG. The response is linear up to $7.2 \text{ m}\epsilon$ with high repeatability and sensitivity. The strain transfer of this particular sensor was 95 %, but this is consistent with other epoxied FBGs, the minimum strain transfer found has been 90 %. These sensors did not show any measurable hysteresis.

Although the majority of the epoxied FBGs showed a repeatable response over several cycles, some of the sensors showed signs of an unreliable contact between the epoxy and fibre. An example can be seen in Figure 6.9. The wavelength for each subsequent cycle occurred at a lower value for all strains. This shows that proper curing of the epoxy is important for repeatable behaviour. From a practical perspective curing epoxy in an industrial environment, often in wet

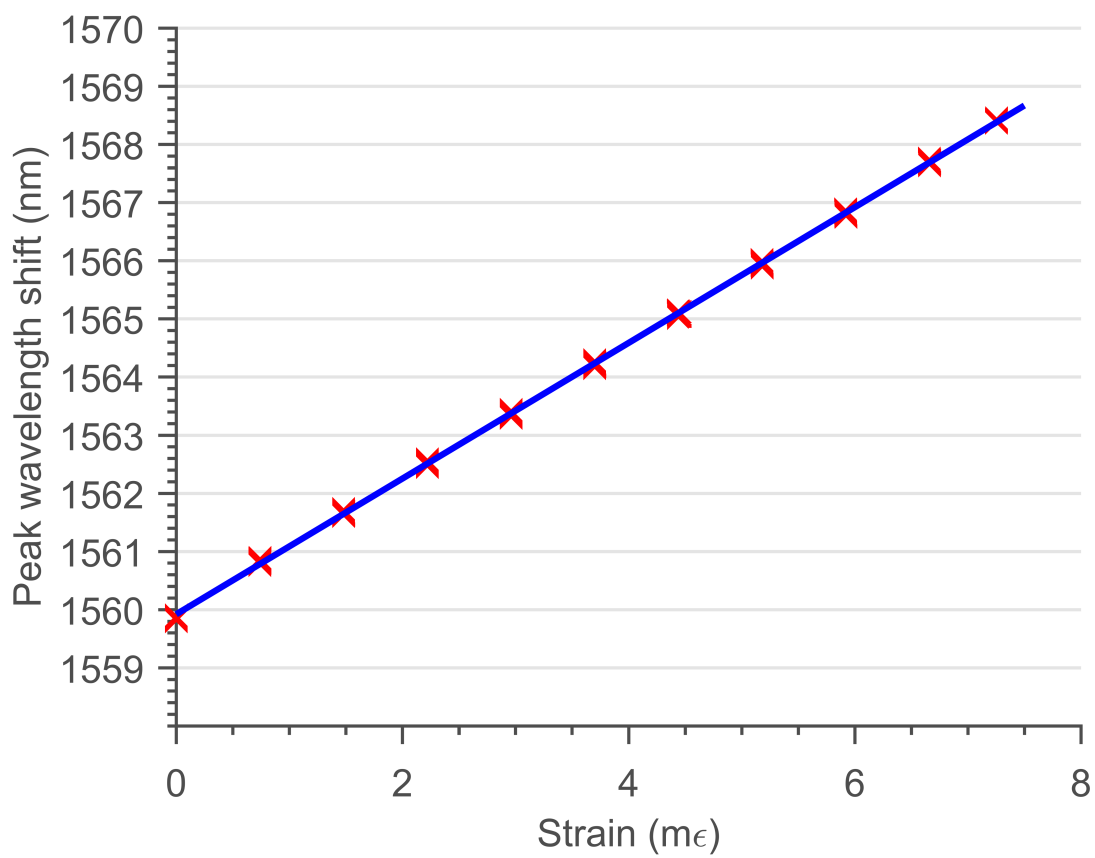


Fig. 6.8 Epoxied FBG calibrated with a tensile machine. The strain sensitivity of the FBG was $1166 \text{ nm}/\epsilon$

ambient conditions will likely impact the consistency of the attachment. Additionally, without protection the epoxied sensor is vulnerable to damage as the fibre is exposed.

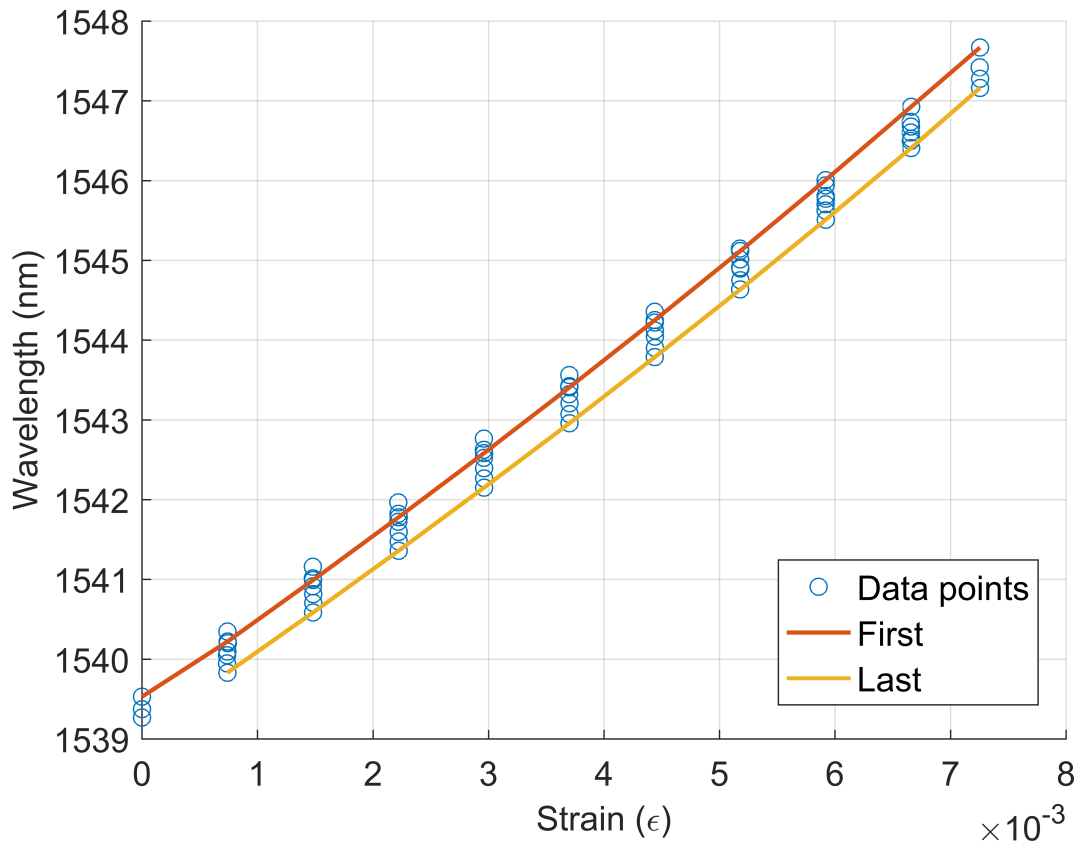


Fig. 6.9 Epoxied FBG calibrated with a tensile machine. The first and last loading cycles show that the sensor does not have a repeatable response.

6.4 Strain resolution and accuracy

6.4.1 Metal packaged sensor

The resolution of the strain sensors is dependent on the interrogator resolution and the sensor strain sensitivity. Based on the results of Table 6.1 an average sensitivity of $0.2 \text{ pm}/\mu\epsilon$ and $0.12 \text{ pm}/\mu\epsilon$ were used for strains up to $3.3 \text{ m}\epsilon$ and $7.2 \text{ m}\epsilon$ respectively. For an interrogator with a 1 pm resolution, the experimental resolution of the sensors was approximately $5 \mu\epsilon$ at $3.3 \text{ m}\epsilon$ and $8.5 \mu\epsilon$ at $7.2 \text{ m}\epsilon$. The strain resolution is not great enough to resolve day to day strain changes when a reactor nears the end of its lifetime. There are two options for improving the resolution;

either increase the sensor strain sensitivity, or improve the interrogator resolution. It is not likely that the strain sensitivity of the sensors could be improved in their current design, so improving the interrogator resolution is considered. In order to achieve a 10 nε resolution that would be required to measure strain changes from day to day near the end of a reactor lifetime, the interrogator resolution would need to be approximately two femtometres. Interrogators with this resolution have been developed using interferometry [146, 147]. Although some limitations currently exist, such as temperature stability [146] and the number of sensors that can be interrogated [147]. It can be assumed that in the future improvements will be made to these interrogation systems in terms of number of sensors and stability.

The resolution of a temperature compensated strain measurement includes the temperature resolution of temperature sensor converted into an equivalent strain. This can be expressed with the following equation:

$$\delta\epsilon_{res} = \frac{\delta\lambda_{res}[\text{pm}] + K_{Tstrain}[\text{pm}/^\circ\text{C}] \frac{\delta\lambda_{res}[\text{pm}]}{K_{Temp}[\text{pm}/^\circ\text{C}]}}{K_\epsilon[\text{pm}/\mu\epsilon]} \quad (6.1)$$

where $\delta\lambda_{res}$ is the interrogator resolution, $K_{Tstrain}$ and K_ϵ are the temperature and strain sensitivity of the strain sensor and K_{Temp} is the temperature sensitivity of the temperature sensor. The units for this specific calculation are noted in square brackets. For an interrogator resolution of 1 pm the strain resolution of the strain sensors is approximately 11 με for a strain of 3.3 mε and approximately 18 με for a strain of 7.2 mε. These values were calculated assuming typical temperature sensitivities of 15 and 18 pm/°C for the temperature and strain sensor, respectively.

The results from the strain calibration can be used alongside those from the temperature calibration in Section 5.6.1 to calculate the total strain error in a strain measurement. The error is a combination of the accuracy of the strain calibration and the error introduced from using an additional temperature sensor to compensate for temperature fluctuations. A derivation of the strain errors introduced during a temperature compensated strain measurement can be found in Appendix A.5. Assuming no temperature influence and that the strain reference has an error of 1 μm¹, the strain sensor measurement error, $\delta\epsilon_z$, reduces to:

$$\delta\epsilon_z \approx \frac{\delta K_\epsilon \epsilon_z}{K_\epsilon} \quad (6.2)$$

¹A displacement gauge with an accuracy of 1 μm would have a percentage error of approximately 0.5 % at 7 mε if it was attached to the strain sensor package (25 mm length) during calibration. The error would be an order of magnitude greater than the wavelength error from the interrogator. The strain reference error could be reduced by attaching the displacement gauge to either end of the specimen so that it measures a larger displacement while assuming the strain is constant throughout the specimen.

where δK_ε is the error in the strain transfer coefficient. If the strain reference error can be reduced, then the wavelength error must be considered as well:

$$\delta \varepsilon_z^2 = \left(\frac{K_\varepsilon \lambda}{\Delta \lambda} \right)^2 \left(\left(\frac{\delta \lambda}{\Delta \lambda} \right)^2 + \left(\frac{\delta \lambda}{\lambda} \right)^2 + \left(\frac{\delta K_\varepsilon \varepsilon_z}{K_\varepsilon} \right)^2 \right) \quad (6.3)$$

For an interrogator accuracy of 1 pm, a strain calibration error of 0.5 % and a strain sensor with a strain transfer of 10 %, the strain error is 33.5 $\mu\varepsilon$. If the strain calibration error is reduced to 0.1 %, the strain error reduces to 10.5 $\mu\varepsilon$. To further improve the accuracy below 1 $\mu\varepsilon$, both the interrogator accuracy and strain calibration error must be improved. The accuracy of the strain measurements worsen considerably when taking into account the error introduced from the temperature compensation, see Appendix A.5 for details. For a strain and temperature sensor with typical temperature sensitivities of 15 and 18 pm/ $^\circ\text{C}$ respectively, a strain calibration error of 0.1 %, a 10 % strain transfer for the strain sensor and a 1 pm accuracy interrogator, the strain measurement accuracy is approximately 35 $\mu\varepsilon$. The majority of the error originates from the temperature compensation.

For this application it may be sufficient to be able to resolve the small strain changes near the end of the reactors lifetime without certifying their accuracy to the same degree. At that point the sensors will have collected over 20 years of data and a model could be fitted to the data, with high confidence in the prediction of strain levels in future years.

6.4.2 Epoxy sensor

The strain sensitivity of the epoxy sensor was an order of magnitude greater than the metal packaged sensors, resulting in strain resolutions of approximately 2.0 $\mu\varepsilon$ and 0.9 $\mu\varepsilon$ with and without temperature compensation being taken into account. Consequently the interrogator resolution requirements are relaxed to approximately 11.5 fm to achieve a strain resolution of 10 n ε ; however, the majority of commercial interrogators cannot resolve this wavelength increment. The strain transfer of the epoxy sensors was approximately 95 % which is approaching the strain in the specimen. This demonstrates that even if the sensor measures 100 % of the specimen strain, it is likely that a high resolution interrogator is needed to monitor strain changes in the later stages of a reactors lifetime. As expected the strain measurement accuracy also improves with a 95 % strain transfer. An accuracy of approximately 1.1 $\mu\varepsilon$ without temperature influence, and 3.6 $\mu\varepsilon$ with temperature compensation is achieved for the same values considered for the metal packaged sensor with the exception of a 95 % strain transfer.

6.5 Summary

Tensile tests on the metal sensor package showed that the strength of the metal capillary is higher than expected and can survive stresses of 795 MPa. Sensor package strain could not be measured because the package could not be properly fixed to the machine grips. Sensors mounted to specimens were calibrated using the tensile machine up to strains of 7.2 mε. The wavelength response of the sensors showed that viscoelastic behaviour was present in the form of hysteresis between loading and unloading cycles. Related to this, the strain sensitivity was lower when the sensors were calibrated at 7.2 mε compared to when they were calibrated at 3.3 mε. The strain transfer of the sensors ranged from 10-20 %, resulting in a temperature compensated strain resolution and accuracy of 18 and 35 με respectively with a 1 pm interrogator. While the strain transfer is not very high and will limit the absolute strain resolution for a given interrogator, it places less stress on the FBG. The metal packaged strain sensors were compared with bare FBGs epoxied to the specimen. These showed strain transfers above 95 % and were linear with very little hysteresis. They had a resolution of approximately 2.0 με and an accuracy of 3.6 με with temperature compensation. The epoxied FBGs confirm that the hysteresis measured in the metal packaged sensors is predominantly due to the sensor design and fabrication itself. Nevertheless, the metal package sensors were able to measure the required strain with repeatability over the three cycles presented in this section.

Chapter 7

Field trial I: Concrete beam test

The previous chapter showed that the metal packaged strain sensors were able to repeatedly measure up to $7.2 \text{ m}\epsilon$. Consequently, to assess the performance of the metal packaged strain and temperature sensors in an environment similar to the intended application they were tested in two small post-tensioned concrete beams for 170 days.

7.1 Beam design and sensor layout

Two 2.4 metre prestressed concrete beams were cast for the sensors to be tested on. The design was carried out by the Civil Engineering department at the University of Strathclyde with input from EDF. Each beam had two ducts running through it where prestressing strands were inserted. One beam contained straight ducts, the other had a double harp duct geometry. Figure 7.1 shows the technical drawing for the bent duct beam, while Figure 7.2 shows the predicted prestress loss due to the duct geometry. The bent ducts allowed the effects of duct friction to be investigated. Several rebars ran through the beams with rebar cages at each end to provide strength for the concrete beams whilst being moved and to guard against failure upon stressing. The prestressing strands were 18 mm diameter cold drawn 7-wire strands, manufactured according to the BS 5896:2012 standard. After the beams were stressed, they exhibited pre-stress loss effects similar to those in a prestressed containment.

7.1.1 Sensor layout

Each pre-stressing strand had three strain and three temperature sensors equidistantly attached to it, see Figure 7.3. The strain and temperature sensors were connected in series with each other to form two fibre lines. The fibre connecting the sensors was helically wound round the

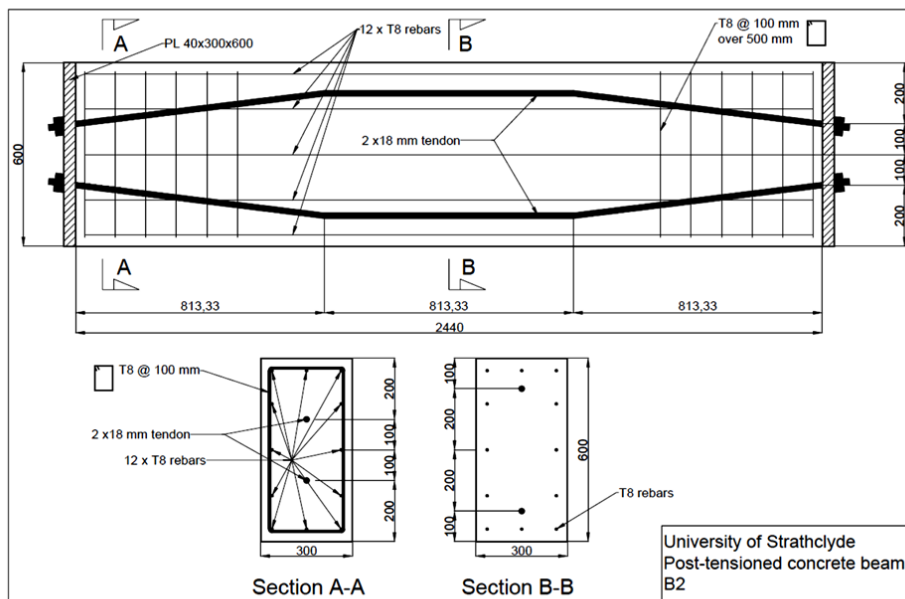


Fig. 7.1 The CAD diagram of the bent duct concrete beam. The straight duct beam was identical to this in terms of dimensions and rebar layout. The beams were designed by the Civil Engineering department at University of Strathclyde with input from the Civil Design Group at EDF.

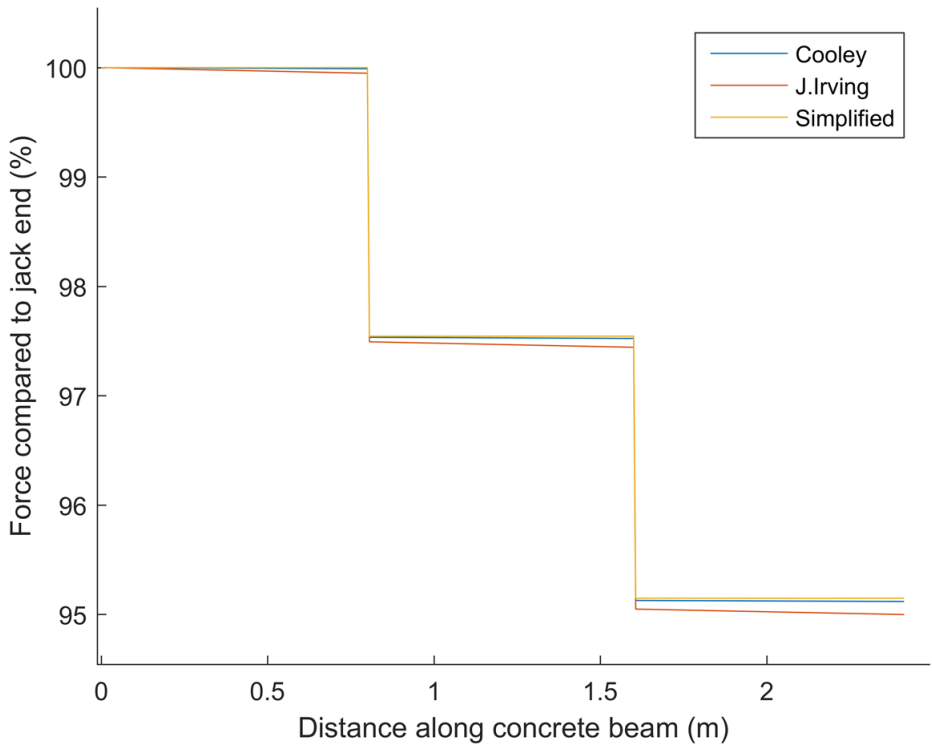


Fig. 7.2 Prediction of prestress loss due to friction in a double harp tendon duct according to three different empirical equations.

strands and sat within the strand grooves ensuring it was protected. The two fibre lines, one strain and one temperature, were connected outside the beam for troubleshooting of the sensor lines. This allowed any potential breakages of either fibres or sensors to be pin pointed. Initially all six sensors from the two lines were connected in series. Later, the two sensor lines were connected by a fibre coupler; this reduced the range of peak reflectivities from the FBGs in the fibre line. Centre wavelength peak detection of all FBGs was more easily achieved in this configuration. The couplers could be replaced with circulators to improve the reflection signal; however, it was discovered that the relative difference between peak reflectivities, not the overall signal level, had a larger impact on peak detection. A commercial system would require some form of automatic gain to equalise the reflectivities or adjust the detection threshold for each FBG individually. Such techniques are readily available. Each instrumented strand was interrogated on one optical channel of the interrogator, meaning six FBG peaks were detected on each channel. Additionally load cells at either end of the beam measured the force in the strands at the bearing plate. It is important to measure the force (and its loss) at the end of the strand because relaxation of steel by definition is a loss of stress at constant strain, see Section 2.3. Therefore the strain sensors are not able to measure the steel relaxation component of the prestress loss. Complimentary load cell force and strain sensor strain measurements are able to determine the complete prestress loss while providing a distributed measurement of strain throughout the strand.

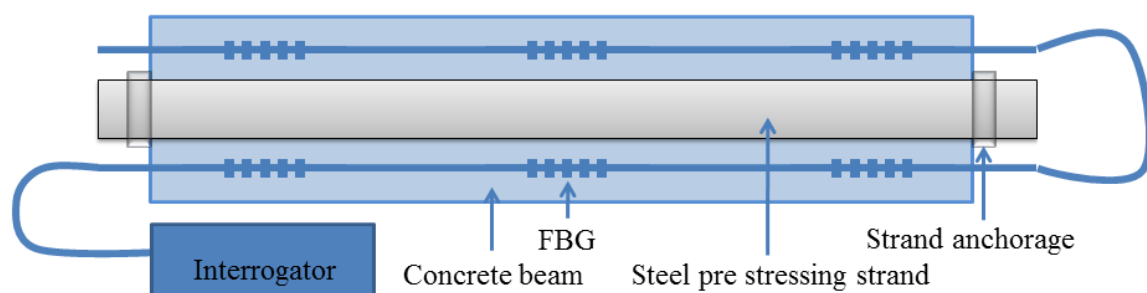


Fig. 7.3 Sensor layout on a prestressing strand.

7.2 Sensor interrogation and data recording

The FBG sensors were interrogated with a commercial interrogator from National Instruments (PXIe-4844) housed within a PXI chassis. The interrogator had four channels with a 10-Hz sampling rate; it had a peak detection accuracy and repeatability of 1 pm ($\sim 1 \mu\epsilon$). The load cells were monitored from the same PXI chassis allowing high levels of synchronisation between the optical and electrical measurements by utilizing a 10-MHz on board reference clock. LabVIEW software was used to create a program to record load cell voltage and FBG sensor wavelength for the duration of the test. The PXI unit was connected to a desktop computer via an Ethernet cable allowing remote monitoring of the concrete beams. Peak reflection wavelengths and load cell force were stored in 12 MB data files (~ 80 mins of data) so data loss was minimised in the event of a power cut. This also allowed easier handling of the files. As the data was acquired and saved on the PXI unit, in the future the acquisition program could be initiated via a laptop. The data could then be periodically collected from the PXI unit. Alternatively the PXI unit could be connected to a local network (via an Ethernet cable) allowing multiple users to monitor the data in real time.

7.3 Strand installation and stressing procedure

7.3.1 Strand installation

The instrumented strands were inserted into the concrete beam strand ducts. The interrogating optical fibres exiting the ends of the strands were fed through the ducts first. All sensors survived the installation into the ducts; however, some of the fibre lines connecting the sensors did not. The fibre lines that broke were protected with copper tubing as shown in Figure 7.4. This protection was shown to be inadequate for fibre protection at the end of the strands, additionally the stress jack did not fit over it. The stress jack jaw has an extremely tight tolerance when fitted onto a strand. Consequently any fibre protection must fit within the strands original cross sectional area. An improved version, Figure 7.5, utilised high strength optical fibre cable. One of the outside wires of the prestressing strand was removed up to 20 cm from the end of the strand. The metal coated fibre was spliced to the high strength optical fibre cable and was secured with epoxy.

In the real application due to the long length of the ducts and the damage that could occur at the end of the strand, it would be more prudent to splice the fibre pigtails onto the metal coated fibre after the instrumented strand has been pulled through. Further development of

the fibre protection at the end of the strands could allow the fibre to be fed through the ducts. This would include smoothing the edge of the cut wire so that the fibre cannot be broken at this section, see Figure 7.5.

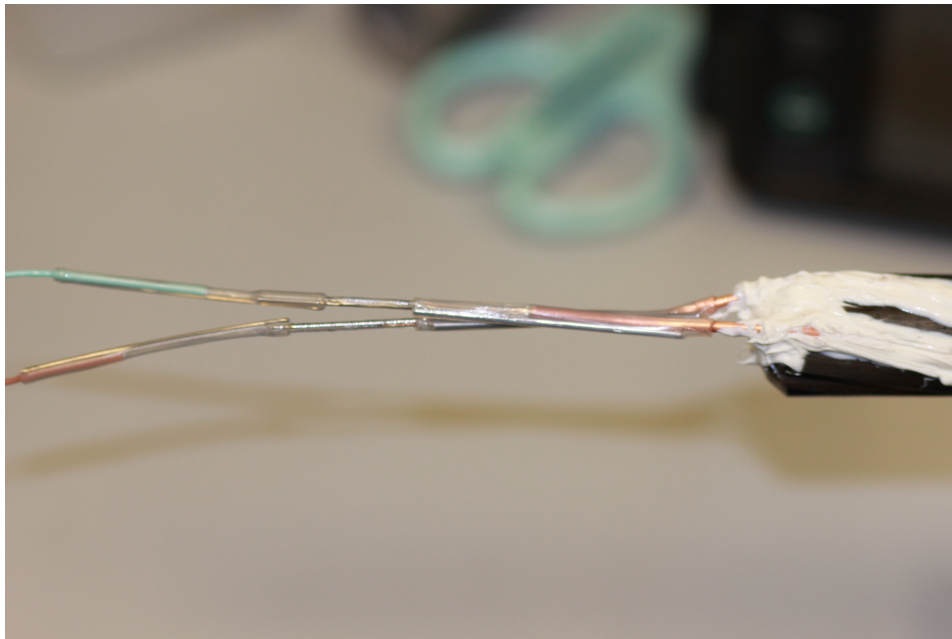
7.3.2 Stressing procedure

The stress jack was calibrated daily by a traceable standard hollow load cell; this ensured the stress jack pressure could be accurately converted to force. Wedges were seated in the barrel at the dead end of the strand, opposite end to the one being stressed, the stress jack was then inserted onto the live end of the tendon. First, the reinforced optical fibre cable was threaded through the stress jack using a metal rod. The stress jack slid over the protected end without issue once the second iteration of fibre protection had been applied. The optical fibre pigtails were reconnected and the sensors were interrogated for the stressing of the strands, see Figure 7.6.

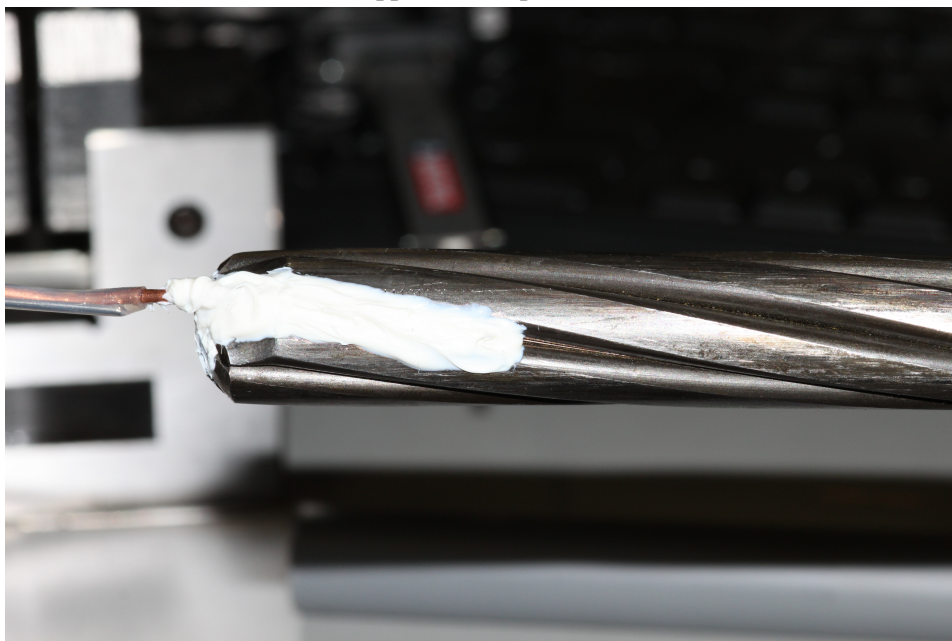
7.3.3 Calibration of strain sensors

Before the final stressing, the strands underwent one load cycle in order to calibrate the strain sensors. Calibration of the sensors when they are permanently attached to the host object is desirable so the strain transfer between the steel strand and the FBG can be determined. The strain transfer is dependent on the sensor package geometry, the attachment method and the interaction of shear strain between the components [107, 111]. Small fabrication and attachment differences between sensors mean that a universal strain transfer ratio would not be accurate¹. Therefore in the final application, sensors should be calibrated using the procedure in Section 5.6.3. For this field trial sensors were calibrated by cycling the strand load. The load was increased in 20-kN steps and held at each point for a few tens of seconds. Once the maximum load had been reached the stress jack reduced the load down to zero in 40-kN steps. The FBG sensors and load cells were monitored constantly throughout this process and were compared to the force measured on the stress jack. To calibrate the strain sensor from the load cell measurements the force in the tendon were converted into a strain. For the straight ducts, it was assumed that there was a constant strain throughout the tendon. However, for the bent ducts friction must be taken into account. There are several empirical equations, including Cooley's formula, that can be applied to calculate this [20]. As the geometry of the tendon was known, as well as the force in the strand due to the stress jack, the distribution of the load in

¹If an automated sensor fabrication facility was developed, capable of manufacturing devices with highly consistent behaviour, on-site calibration could possibly be avoided.



(a) Copper silicon protection 1



(b) Copper silicon protection 2

Fig. 7.4 Protection at tendon ends using copper tubing and splice jackets. However the stress jack would not fit over end of the tendon because the tubing protruded about 2 mm from the strand groove. Figure 7.5 shows the final protection scheme used.



Fig. 7.5 Photos of the cut outer wire and reinforced fibre cable exiting the strand. Epoxy covers the splice protectors and fibre cable holding them in place.

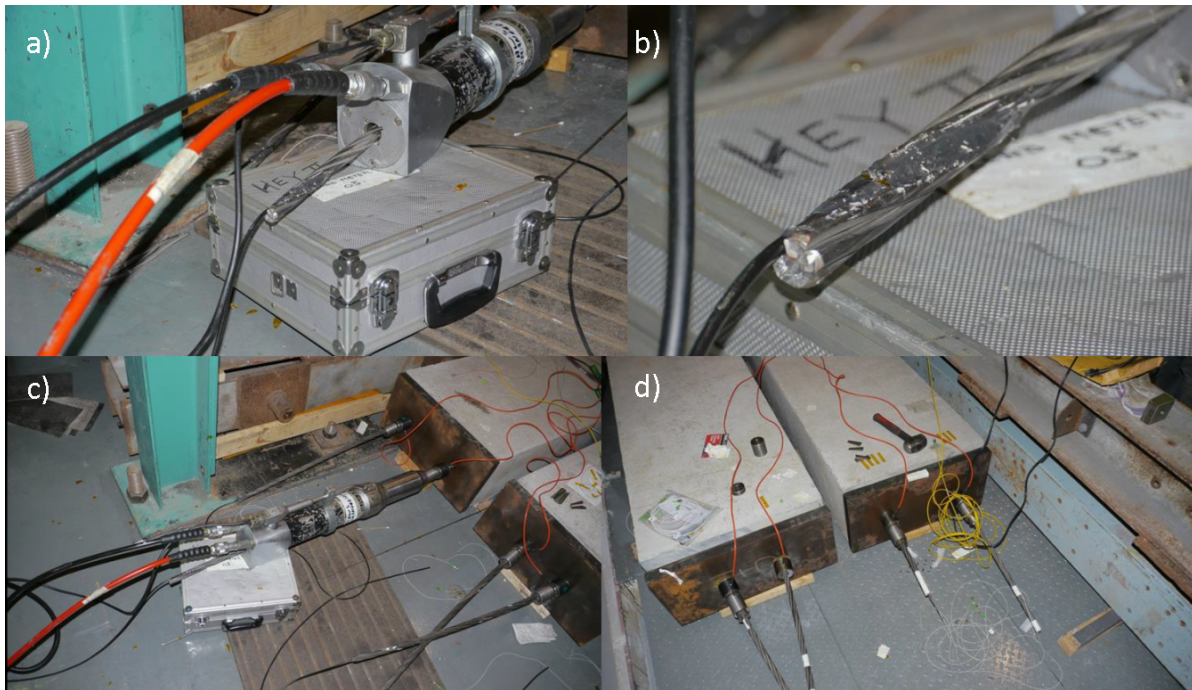


Fig. 7.6 a),c) Stress jack stressing the instrumented strands. b) Strand end after removal of stress jack. d) Overview of the beam ends.

the strand was estimated. This was checked against the readings of the load cells at each end of the strand. The strain at the points where the strain sensors were attached was estimated from this. Further verification of the calibration was obtained by observing the wavelength shifts when the calibration procedure was occurring, to provide an estimate of the strain the FBGs measured.

As noted in Section 5.6.3, prior calibration of the strain sensors is required to measure distributed strand strain. Calibration of the strain sensors is an important aspect of sensor development. Strain calibration of the sensors outside of the vessel is vital for identifying the experimental load profile of the strand without assuming that Cooley's formula holds true. One of the main advantages of distributed strain measurement is that Cooley's formula and the assumptions of friction coefficients can be tested; therefore, a robust calibration method such as calibration by bending the strands around a fixed radius should be investigated in the future.

7.3.4 Load cells

The load cells loads were checked against the stress jack for consistency. As the load cells had a low profile it was important that they were seated properly when the stressing began. If they

were not, the load may be placed through a smaller area of the load cell leading to a higher reading than expected.

7.3.5 Locking off the stressed strands

The wedges were placed in the barrel on the live end for the final stress. Once there was tension in the strand it couldn't be released without placing a destressing stool above the barrel and strand. The final stress procedure was similar to the calibration cycle the strands underwent. The strand was tensioned in 20-kN intervals up to the desired force when the wedges were seated in the barrel and the strand was locked off. The FBGs and load cells were monitored throughout the process allowing the calibration cycles to be checked against the final stressing. When the wedges were seated in the barrel part of the strand extension obtained from stressing was lost; this is known as wedge draw in. This was clearly seen on the load cells and strain sensors. Figure 7.7 shows an example of this effect; here the magnitude of the force/strain 'dip' before the wedges were seated in the barrel varied slightly between the strain sensor and load cell. This varied for each strand. The wedge draw in was relatively large due to the short length of the concrete beams.

7.4 Results from the calibration cycles and final stressing

During the stressing procedure many practical issues arose because instrumented prestressing strands of this nature had not been tested before. One of the main successes of this field trial was the extensive information gathered about the realistic practical implementation of the strain and temperature sensors on the pre-stressing strands. The sections below show the key issues that were encountered.

7.4.1 FBG peak detection

The data acquisition program used for recording the calibration and initial stressing was the same one developed for the extended recording post stressing. During the calibration procedure it became evident that some additional features would have been beneficial to speed up sensor diagnostics during stressing. Due to the interrogator, sensor peak detection parameters had to be saved in a configuration file in a program separate from Labview called OSI Explorer. When using the configuration file, interrogator peak detection relies on setting a fixed wavelength range for each sensor peak to prevent peak overlaps. If a sensor moves out of this range its peak is not detected, the data acquisition program must be stopped and OSI Explorer must then

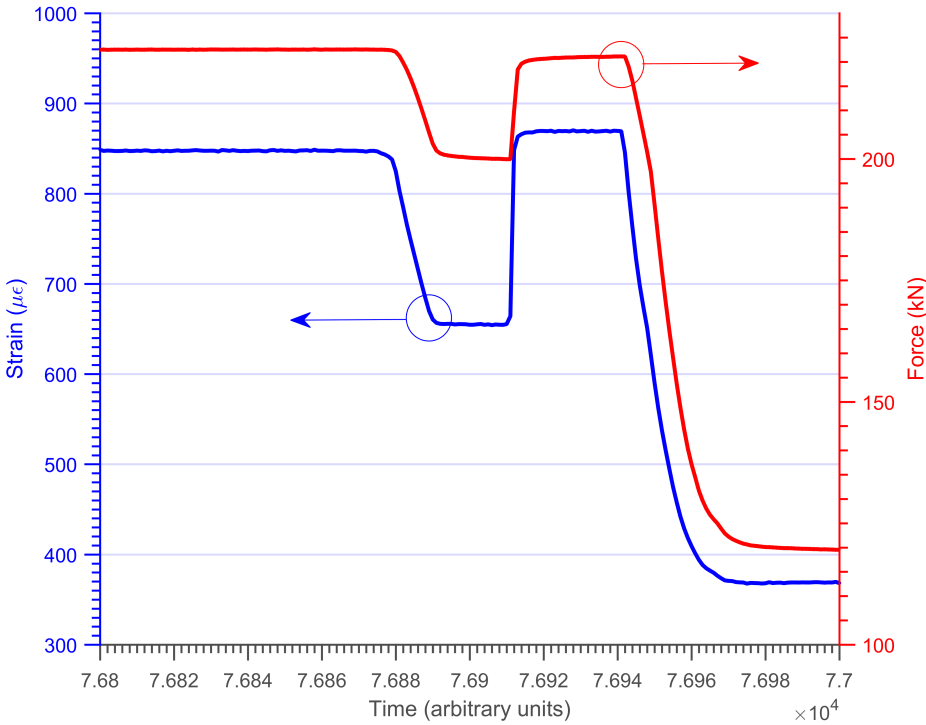


Fig. 7.7 Anchor slippage of one of the strands as measured by a load cell and an FBG strain sensor.

be used to adjust the peak detection parameters. OSI Explorer is slow to execute, therefore a long time was spent adjusting the parameters. Had the temperature sensors not shifted with force this would not have been a problem. However, this was highlighted when they did. In the future, peak detection needs to be adjustable on the fly, ideally automatically. Additionally, this application would benefit from dynamic peak detection bins rather than the static ones offered in OSI Explorer. Finally, it would be useful to view the spectrum of the sensors to check the peak reflectivity and side lobes. This would also highlight any FBGs displaying a split peak due to the strain.

Proper apodisation of the FBGs prior to sensor fabrication must also be ensured. Interrogating increasing numbers of FBGs puts an increasing demand for small side lobes from a peak detection point of view. This is especially true when they are interrogated in series as in this application. Several of the FBGs showed potential signs of side lobes being detected, an example of erroneous peak detection is shown in Figure 7.8.

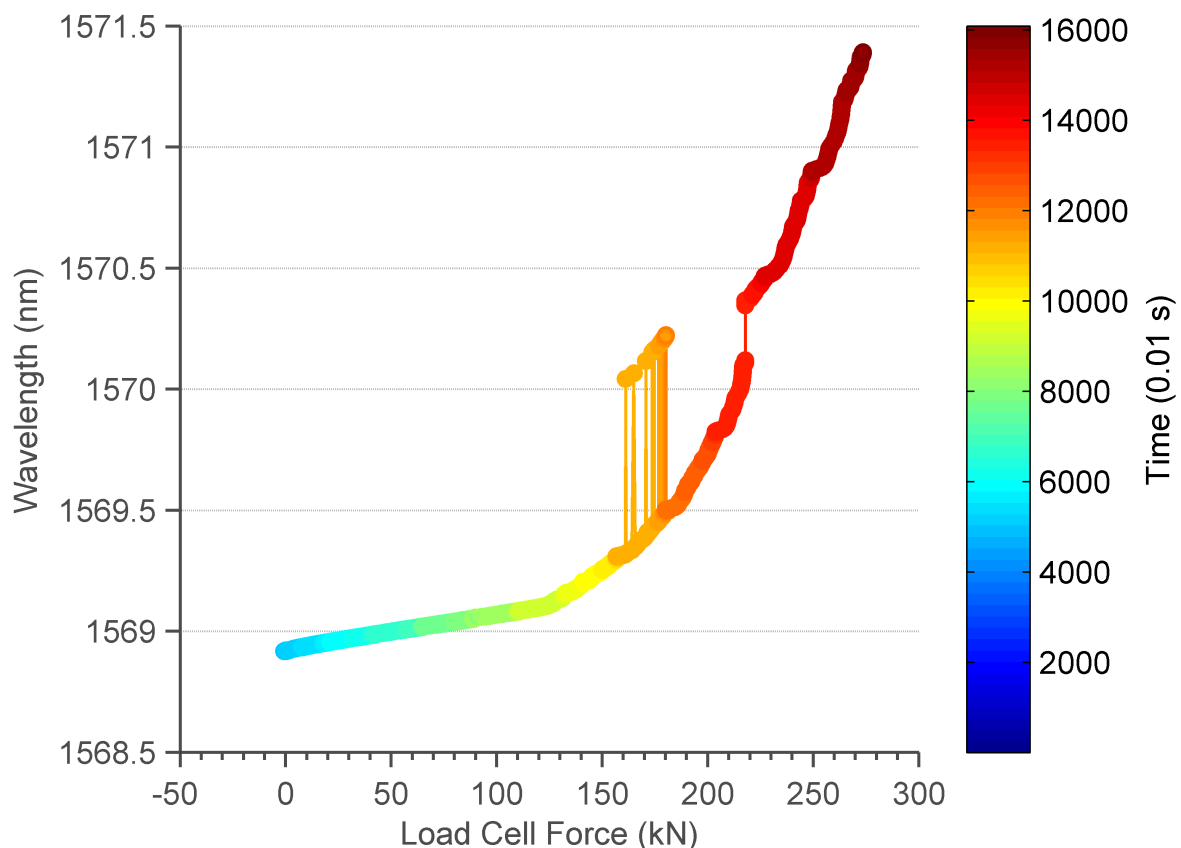


Fig. 7.8 An example of erroneous peak detection; from 150-200 kN the peak detection algorithm intermittently picked up either a side lobe or a splitting FBG peak.

7.4.2 Temperature sensors

While the calibration procedure was taking place it was clear that the temperature sensors were responding to the increasing force in the strand. They displayed a step profile that was comparable to the force profile from the load cells. There was a large variation in the magnitude of the wavelength shift during stressing; the largest shift was 4.5 nm for a force of 200 kN, while the smallest was less than 0.1 nm. Figure 7.9b shows a temperature sensor's wavelength plotted against load cell force for both the calibration cycle and final stressing of the strand. The sensor responded to increasing force from approximately 100kN. A small permanent wavelength shift between the two cycles was also seen.

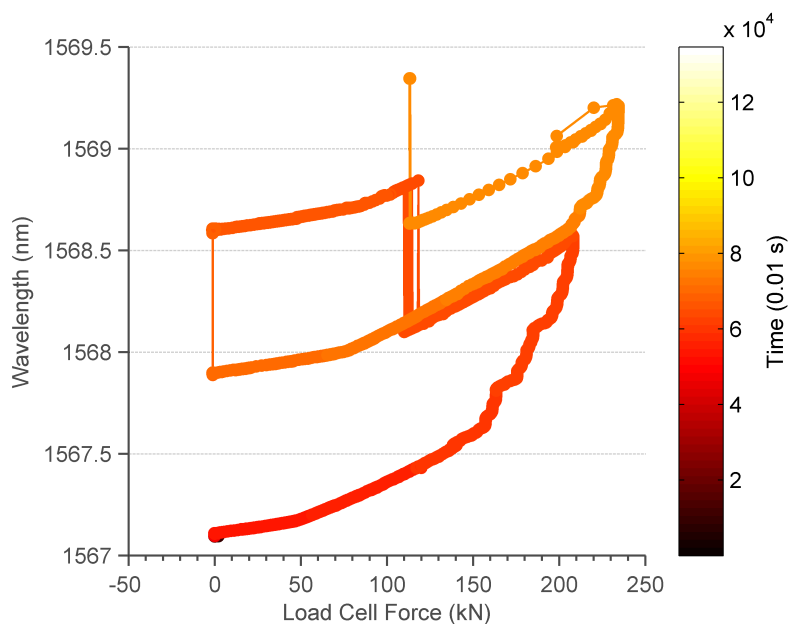
7.4.3 Strain sensors

A typical example of the wavelength response of a strain sensor can be seen in Figure 7.9a. The figure shows the sensor wavelength against load cell force for both the calibration cycle and the final stressing up to ~235 kN. There were two distinct stages of the sensor wavelength response: before and after ~150 kN. Both of the stages were approximately linear but there was an increased strain sensitivity above ~150 kN. There was a permanent wavelength shift of almost 1 nm for this sensor. The strain response was expected to be linear throughout the entire force range, 0-300 kN, however this was not the case. Most of the strain sensors behaved in this way and the graphs of all the strain sensors can be found in Appendix A.6. More specifically, for each sensor the point at which the slope of the line of best fit changed was different. However, it was always in the 100-150 kN range. This call into question whether the strain sensors can be reliably calibrated by the total force measured at the end of the 7-wire strand.

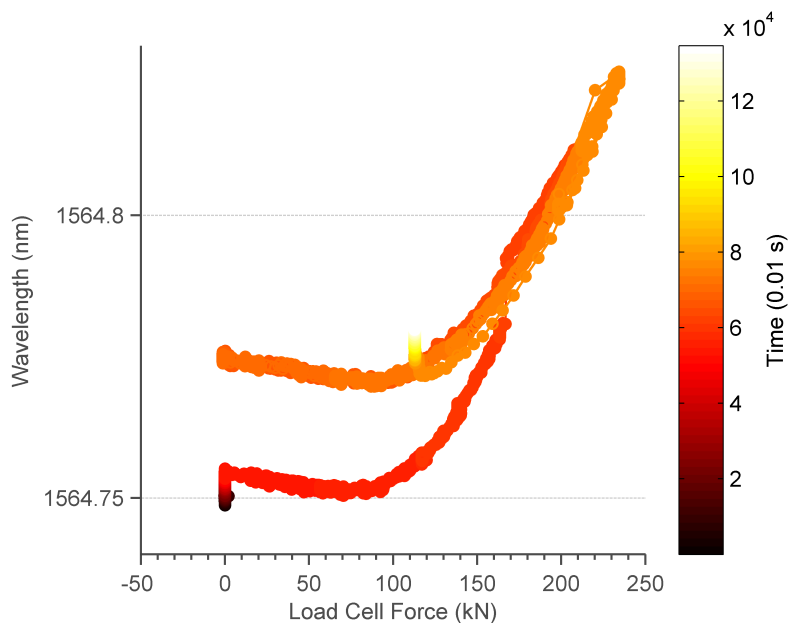
7.4.4 Summary of problems encountered during calibration

To summarise, the main problems affecting the sensors during the calibration cycles were the following:

- Several of the fibre lines interrogating the sensors broke as the force in the prestressing strands increased. In some cases, the sensors could be interrogated from the opposite end of the concrete beam as the interrogating fibres were exposed at both ends.
- The peak reflectivity of some sensors decreased so that they could not be interrogated in series with the other sensors.



(a) An example of the wavelength response of a strain sensor



(b) An example of the wavelength response of a temperature sensor

Fig. 7.9 The strain sensor shows several issues encountered during the procedure: a non-linear strain response, a large increase in strain sensitivity at a certain force and possibly some peak detection problems (the sudden increase and decrease of wavelength over a short time scale). The temperature sensor shows a small permanent shift in the zero strain wavelength from the calibration cycle and also a small strain dependency (80 pm). However, other temperature sensors show much greater strain dependencies.

- Both the strain and the temperature sensors experienced permanent zero strain wavelength shifts between the calibration cycle and the final stressing. The sensors responses to increasing strain were similar between the cycles, but the zero offset had shifted.
- The temperature sensor wavelength increased for increasing force above 100-150 kN.
- The strain sensors sensitivity increased above 100-150 kN.

7.4.5 Possible explanations and solutions of the problems

When the sensors were tested on a single metal rod, the aforementioned problems were not seen and the strain sensor response was linear up to stresses of 1300 MPa [126, 122], equivalent to approximately 300 kN in the pre stressing strands. There were several differences when the sensors were installed into the concrete beams. The most significant of these differences include the use of a multi-wire strand and sensors that were spliced in series. The sensor package was also slightly different to fit in the strand grooves. At the time of this experiment the causes of the sensor responses were unknown. In subsequent chapters these will be identified, however at this point some possible reasons for the problems can be postulated.

Capillary bending

Kovar is relatively ductile compared to steel. This is especially true for the thin tube geometry used to encapsulate the FBGs. Therefore the capillary can be bent, resulting in a permanent shift in the zero-strain wavelength of either a temperature or strain sensor. As has been shown, both types of sensor experienced a permanent shift in their wavelengths during these tests. The temperature sensors were fixed with silicone at one end so it is possible that they could have been bent. However, the strain sensors were fixed at both ends with spot welded shim so there was less chance that this could have happened to them. Furthermore, a bent capillary would be more likely in the bent ducts as the strand was bent when it was inserted into the duct. This could be remedied by further sensor protection such as a encapsulating the Kovar capillary in a steel one or indeed attempting to replace Kovar altogether.

Kovar yielding

A cause of the non-linear strain sensor response could be the Kovar yielding. There are a wide range of values available for the yield and ultimate tensile strength (UTS) of Kovar as these parameters are very dependent on any annealing performed on the material. The UTS of Kovar can range from 520-790 MPa and the yield stress ranges from 276-720 Mpa. For

the capillary dimensions, the yield strain ranges from 2-5.2 $m\epsilon$. Based on the data from the supplier, the yield strain for this particular Kovar should be 2.5 $m\epsilon$. This is relatively low for this application as the strain in the prestressing strands is at least 6.5 $m\epsilon$. However, Kovar has a number of beneficial properties in terms of the sensor fabrication. It has a lower Curie transition temperature than steel as well as a much lower thermal expansion coefficient. Therefore, it is the best suited metal for the sensor fabrication process. If the Kovar capillary is to stay below its yield point, the strain transfer from the prestressing strand must stay below about 40 %, see Figure 7.10. In past experiments the measured strain transfer has been relatively low and below this level. These calculations have been the the total strain transfer from the prestressing strand to the optical fibre. It is possible that the strain transfer from the strand to the Kovar capillary is higher.

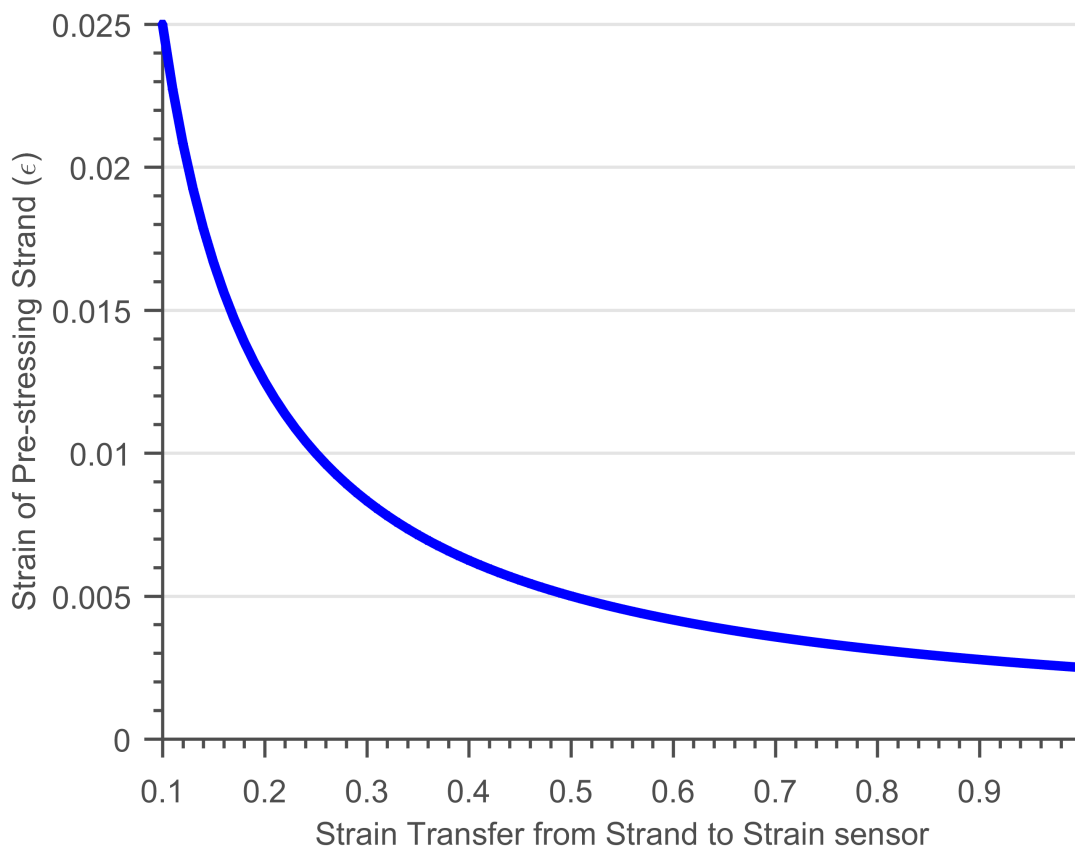


Fig. 7.10 Maximum permissible prestressing strand strain at the yield strain of Kovar for different strain transfers.

Fibre tensioning

As mentioned previously, during stressing, the strain in the pre-stressing strand can be as large as $7.2 \text{ m}\epsilon$. This is equivalent to a change in length of 7 mm over 1 m. The sensors and optical fibre and splices are all subject to the increase in length and must be able to withstand it. The sensors were fabricated on separate sections of fibre, ~ 200 mm long, and spliced together. To secure the splice protectors and fibre, they were attached to the strand groove. Therefore, all the components were subject to increasing strain as the strand force was increased. It is likely that there was a small amount of slack in the fibre before the stressing commenced. If the fibre slack is removed, the fibre will be tensioned which could in turn stress the end of the sensor. Moreover, if the joint securing the fibre into the capillary is not strong enough, the increasing strain of the fibre outside the capillary might be measured by the FBG. This could explain why the temperature sensors responded to strand loading above 100-150 kN and why the strain sensitivity of the strain sensors increased above this force range.

To reduce the lengthening effect on the temperature sensor line, the fibre must be free to move back and forth during stressing. This could be achieved by securing tubing, similar to a splice protector, into the strand groove and threading the fibre through without securing the fibre in the tube. The fibre must be able to move freely at the ends of the strand to allow it to adjust to the new strand length. In this case, the sensors and fibre would not be secured into the groove so there may be additional risk of the fibre being broken. A continuous tube could be used to ensure the fibre does not move out of the strand groove. Another option would be to place the sensors on separate fibre lines in the strand duct but multiplexibility is one of the key advantages of optical fibre sensing. To mitigate this effect from the strain sensors, if it is significant, the fibre-capillary joint must be strong enough to withstand the strain applied.

Uneven force distribution

Finally, the strain sensor response could also be explained by the relative movement of the individual wires that make up the strand. Anecdotal evidence suggests the central wire takes most of the force during the initial stages of stressing the strand and there may be uneven load distribution between the wires. The strain sensor responses would be consistent with a large increase in force through an individual wire compared to the overall force in the strand. If the force is distributed unevenly between the individual wires and this varies with time, the strain in an individual wire compared to the overall force measured by the load cell would not linearly correlate. Again further investigations are needed to determine the distribution of force between the wires and whether this varies as the strand load is increased. Moreover, if this was

indeed the reason for the behaviour seen in the figures above, additional sensors would likely be required to “sample” more wires for the determination of the average strain in a specific location along the strand.

7.5 Longterm results

Fibre line breakages meant that only three of the strands had strain sensors that could be interrogated. A thermocouple was taped to the side of one of the concrete beams to measure ambient temperature fluctuations. It was placed there one day after the experiment began to determine if the temperature sensors were correctly measuring temperature because some of the temperature sensors showed a response to strain during stressing. This could lead to temperature errors and could mask decreasing strain measured by the strain sensors. It was hoped that the thermocouple could be used to compensate the strain sensors if necessary, however as it was located outside the concrete beam, the temperature fluctuations of the FBG sensors lagged the thermocouple due to the time taken for heat to transfer in and out of the concrete beam. Additionally, as the thermocouple sample rate was 1 Hz it was difficult in practice to compensate the FBG strain sensors with the thermocouple. This was achieved by resampling the FBG measurements to 1 Hz and aligning both signals, but meant that the compensated FBG wavelength contained more noise than if the compensation was carried out with another FBG sensor.

Figure 7.11 shows the thermocouple temperature and an FBG temperature sensor wavelength converted to degrees Celsius. The temperature FBG sensor corresponds well with the thermocouple, in terms of temperature change and variation, but lags behind it slightly because the room temperature fluctuations take time to affect the temperature inside the strand ducts in the concrete beam. The temperature for the complete experiment can be seen in Figure 7.12, it shows that the temperature varied at most by approximately 7 °C over the 170 days. There are several trends in the data including fluctuations on a daily and weekly basis due to heating in the laboratory and a general increasing temperature trend due to the experiment starting in spring. Similar temperature variations can be expected during the real implementation of these sensors on a nuclear site. There is a small difference between the long term trend of the thermocouple and the FBG sensor. The FBG sensor temperature measurements had a small decreasing trend compared to the thermocouple, possibly showing that the FBG sensor was strained during stressing and that the strain was decreasing over time.

The force decrease from one of the load cells can be seen in Figure 7.13, this is the total force in the strand. The strain sensors were compensated with their corresponding temperature

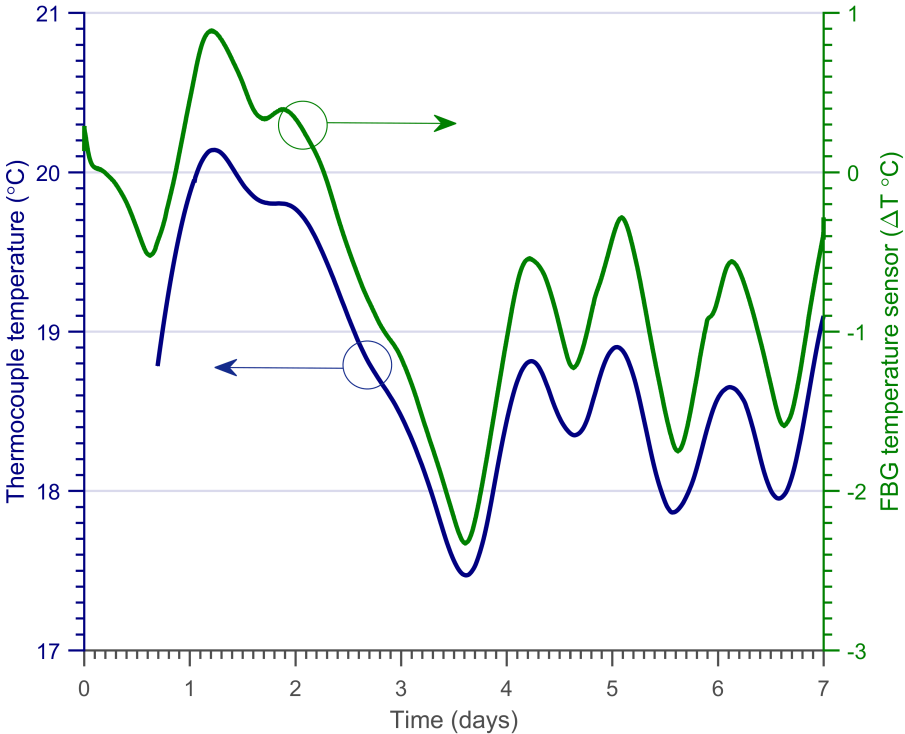


Fig. 7.11 Thermocouple and FBG sensor temperature for the first week.

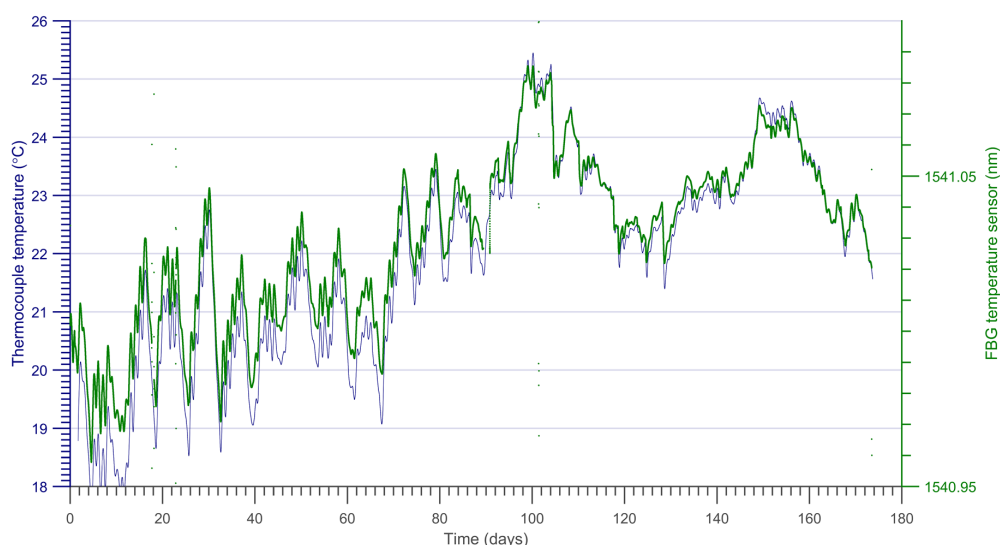


Fig. 7.12 Temperature measured by the thermocouple and wavelength of an FBG temperature sensor. The temperature varied by approximately 7 °C over 170 days. Daily and weekly fluctuations can be seen due to heating of the laboratory.

sensors and compared to the force of the nearest load cell. The results of several sensors can be seen in Figures 7.14, 7.15, 7.16 and 7.17. The FBG sensor signals are displayed in terms of raw wavelength due to the non linearity during calibration. Strain is directly proportional to wavelength so comparisons can still be made. Three of the four sensors shown here display a decreasing strain that is comparable to that determined from the load cells. The load cell should have measured a larger force decrease because steel relaxation also contributes to the prestress loss. Although it must be noted that after locking off, the stress in some of the strands was not above 40 % so the effect of stress relaxation may have been negligible. Temperature fluctuations can be seen in both the load cell force and the strain measurements. The load cells were not compensated for temperature fluctuations so they were due to the intrinsic temperature sensitivity of the load cell and the thermal expansion of the concrete beam and strands. The strain sensors have been temperature compensated but there was still some residual influence. This is because the temperature compensation coefficient did not fully account for all the temperature dependencies of the concrete beam. The temperature coefficient for each strain sensor was obtained whilst they were attached to the steel strands, so it accounted for the intrinsic temperature sensitivities of the sensor and also the thermal

expansion of the prestressing strand. Therefore the fluctuations seen were due to concrete and anchor plate thermal expansion.

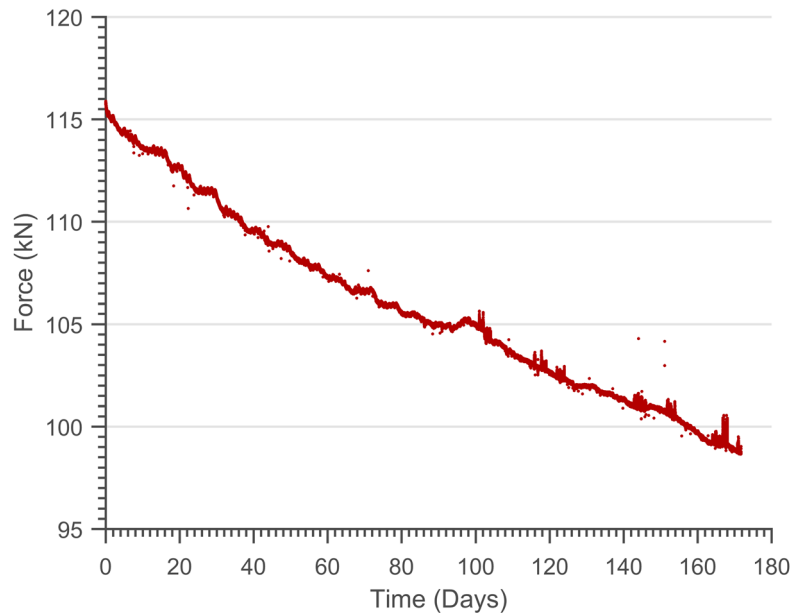


Fig. 7.13 Total strand force measured by a load cell. There was an 18 kN force loss over 170 days.

Figure 7.14 and 7.15 show two strain sensors that had a decrease in wavelength of 60 and 50 pm respectively. While, Figure 7.16 shows a sensor that had a 30 pm decrease for the entire experiment. The temperature sensor next to this particular strain sensor could not be interrogated, therefore it was compensated with a temperature sensor from the adjacent strand. This compensated sensor wavelength contains more noise than Figures 7.14 and 7.15 and the compensation could have also caused an erroneous strain reading as the magnitude of strain change during the experiment was small. An example of a sensor that could still be interrogated but that was not correctly measuring strand strain can be seen in Figure 7.17 a), the change in wavelength was close to the interrogator resolution.

Concentrating on one strain sensor, Figure 7.18 shows sensor wavelength converted to strand force compared to load cell force for the complete experiment. The FBG sensor was temperature compensated by a Bayesian algorithm that is described in Section 11.2 and converted to force by considering the sensors wavelength response during calibration, which can be seen in Figure 7.9a. A conversion factor of 0.00024578 m/mN was calculated. The graph shows that the overall force decrease measured by the strain sensor was approximately

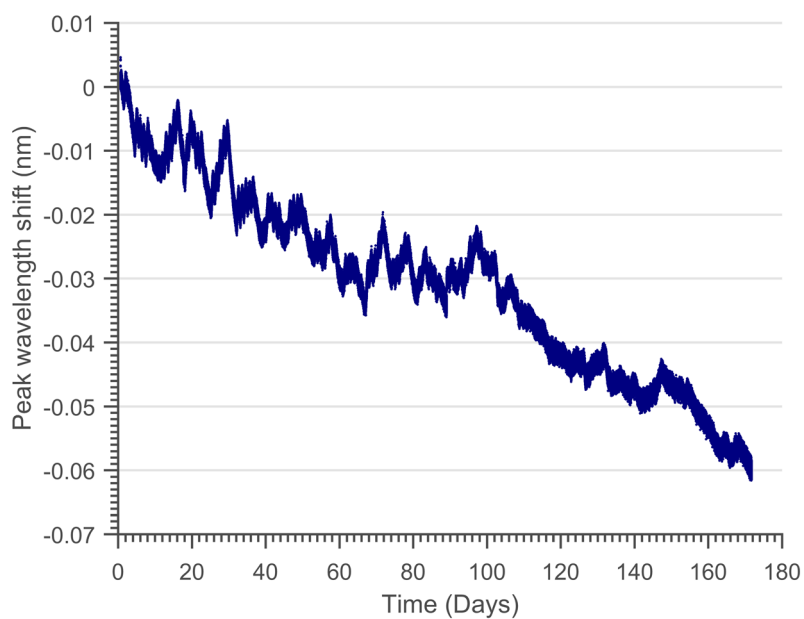


Fig. 7.14 Strain sensor wavelength decrease. There was a total decrease of 60 pm over 170 days. The sensor reading has been temperature compensated but still has a temperature dependence. In this case the sensor's temperature coefficient was measured before the sensor was attached to the strand. Therefore the residual temperature dependence is the steel thermal expansion.

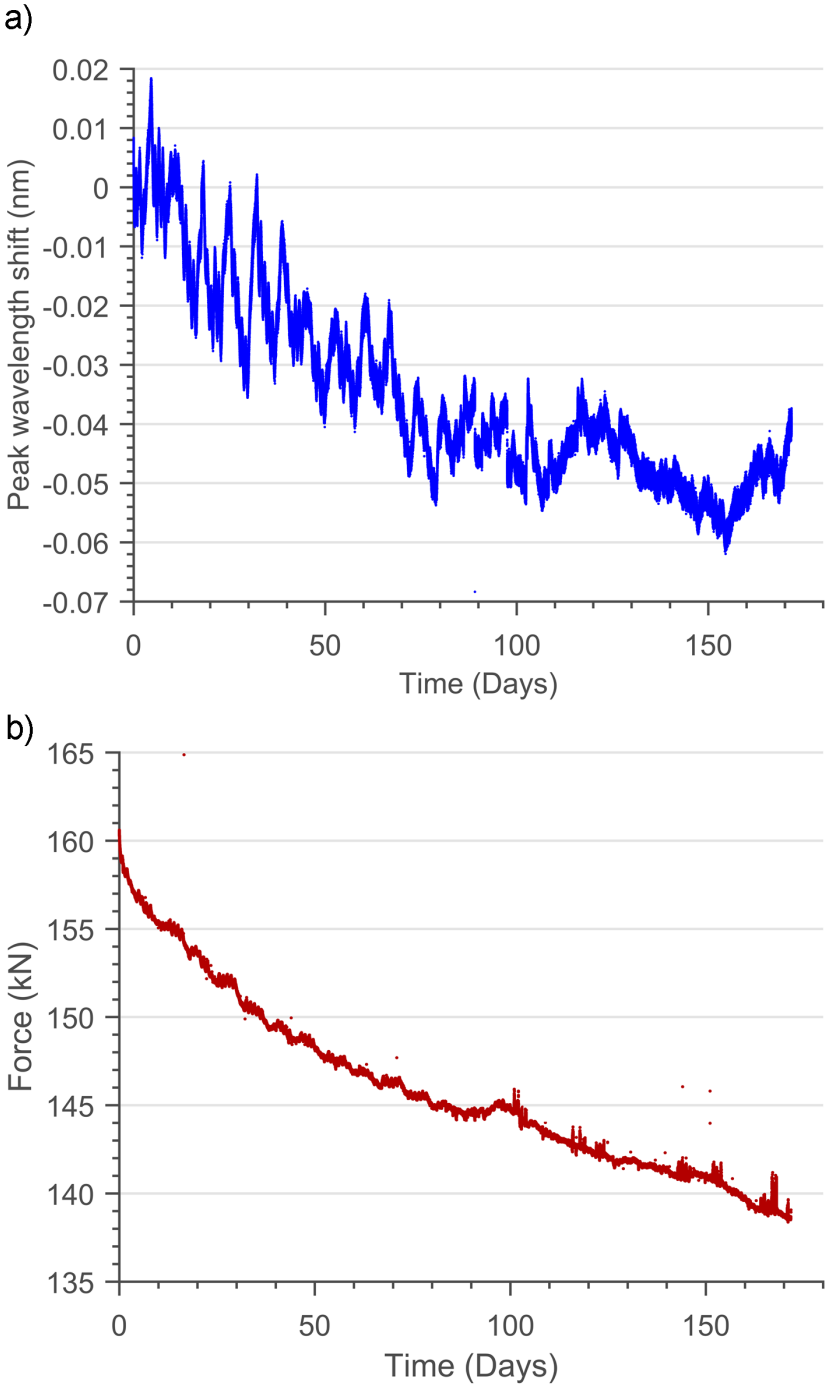


Fig. 7.15 Example of strain sensor wavelength a) compared to load cell force b). This particular sensor measured a wavelength decrease of 50 pm.

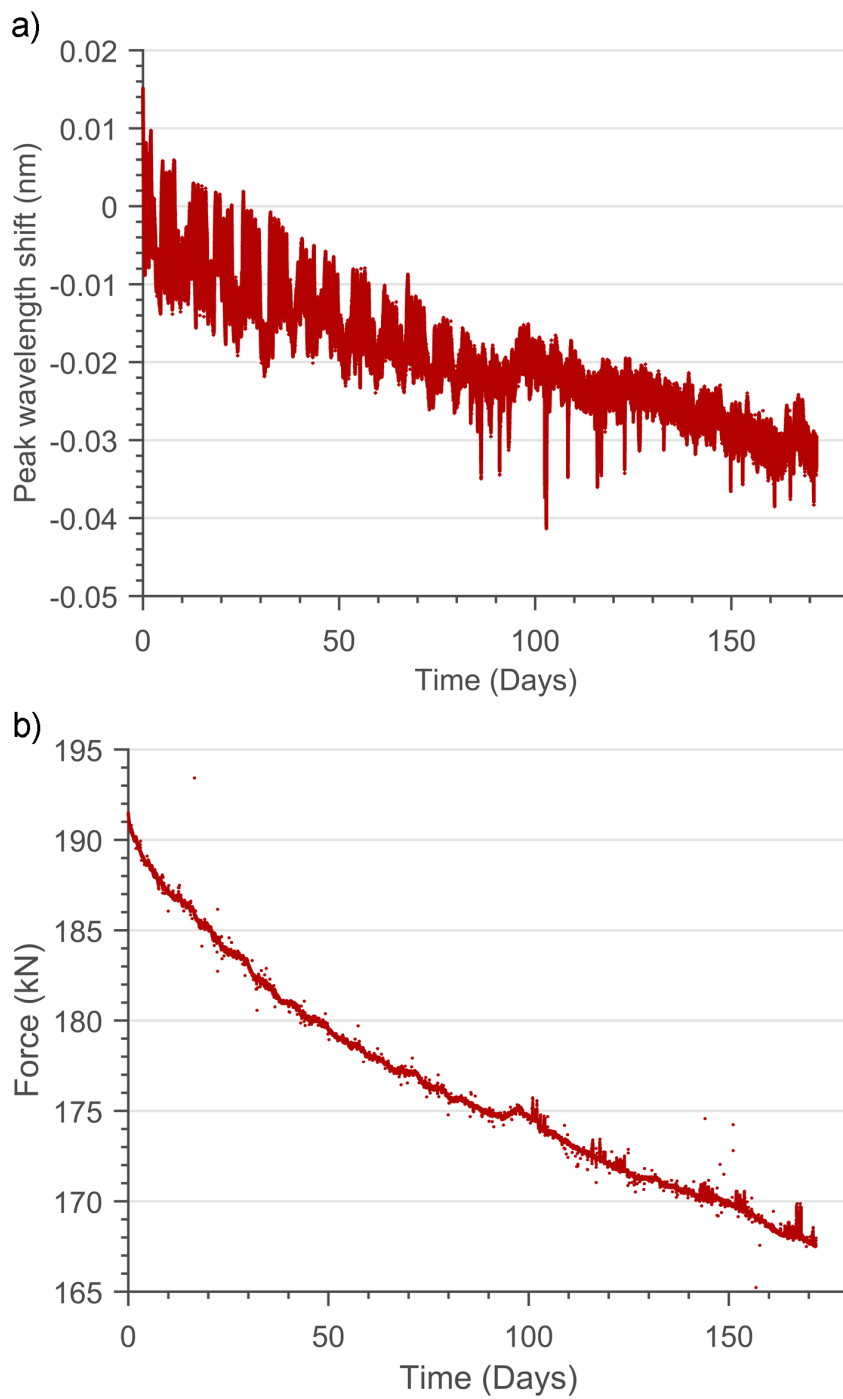


Fig. 7.16 Example of strain sensor wavelength a) compared to load cell force b). This particular sensor measured a wavelength decrease of 30 pm.

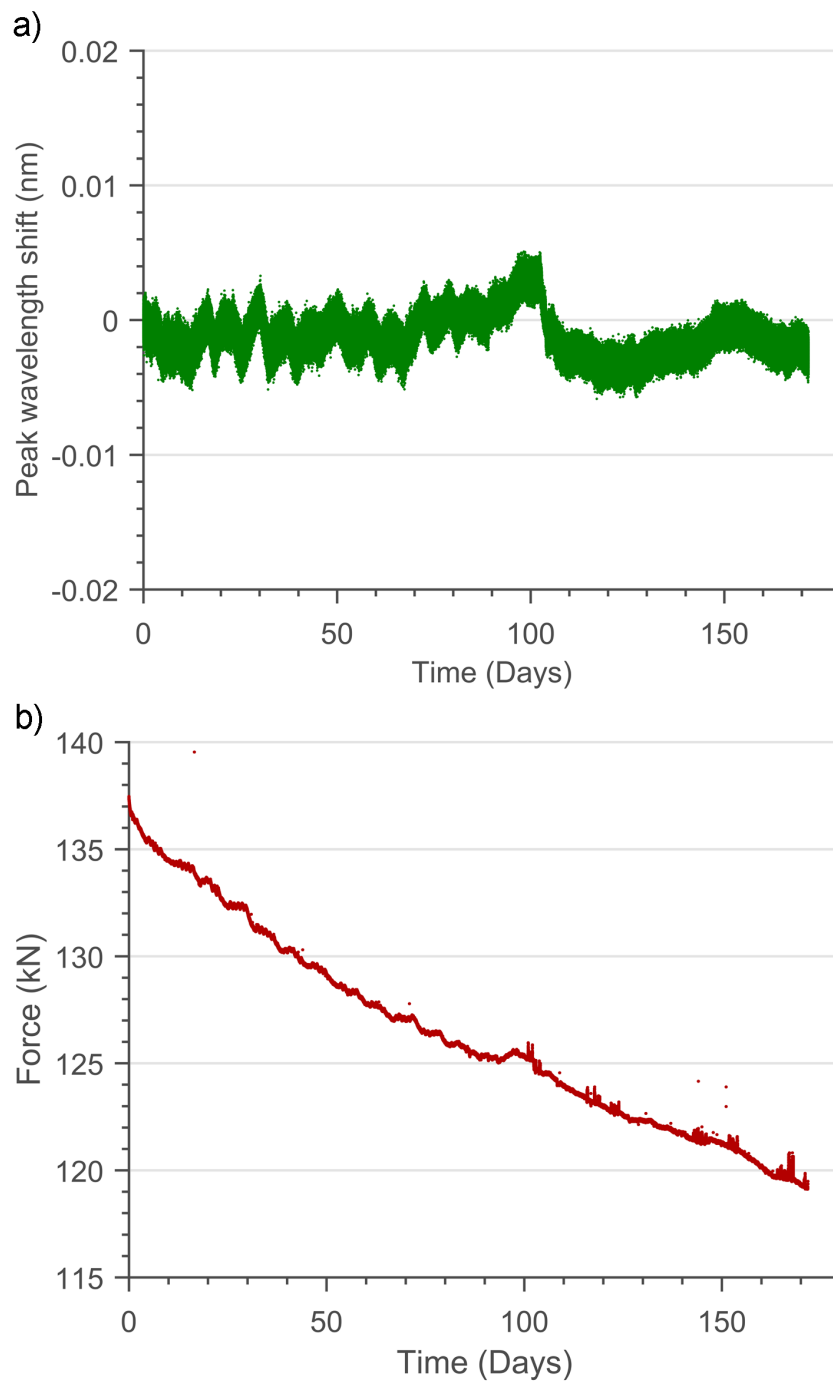


Fig. 7.17 Example of strain sensor wavelength a) compared to load cell force b). There was no wavelength decrease for this sensor showing that it did not correctly measure strand strain during the experiment.

11 kN, compared to the load cell which measured approximately 16 kN. The curve of both the strain sensor and load cell are similar, if the strain sensor force is multiplied by 1.45 the two curves overlap to a high degree. This shows that the strain sensor is measuring prestress loss of the strand, however it does not measure as large a force decrease as the load cell. The most likely explanation for the discrepancy is that the strain sensor calibration is not correct. The wavelength during the calibration cycles gives an indication to the wavelength magnitude change per force increment but due to the non-linearity and permanent shifts the calibration cycles cannot be relied upon with a high degree of confidence.

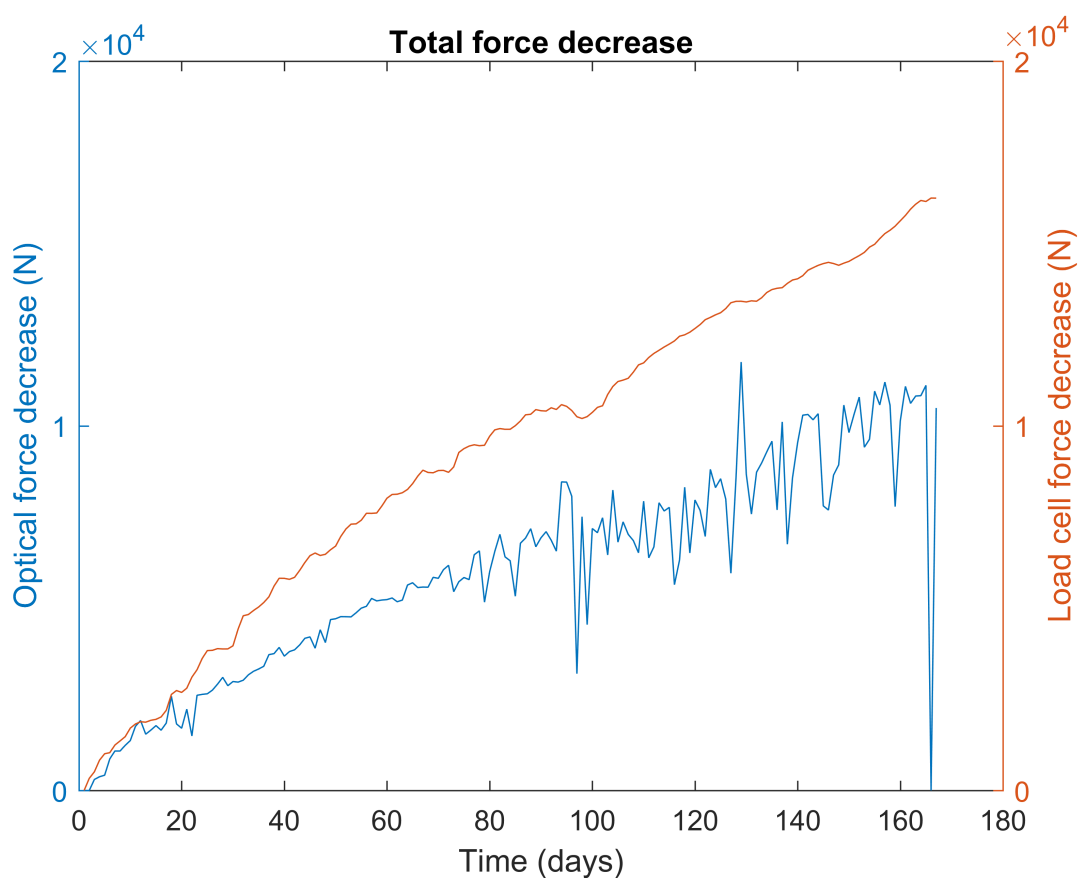


Fig. 7.18 Prestress force loss measured by a strain sensor. The wavelength change measured by this strain sensor is shown in Figure 7.14. In this graph the sensor was temperature compensated using a Bayesian approach outlined in Section 11.2. Sensor wavelength was then converted to strain and force using the calibration cycles. Compared to its corresponding load cell, the strain sensor measures a smaller loss. This is likely due to the calibration.

The difference in force at the end of each strand in the bent duct beam was larger than the prediction shown in Figure 7.2 with a difference of 80 % and 85 % for the two strands. This was due to the duct material being different from that used in a PCPV/PCC. The results

indicate that the coefficient of friction for the ducts used lies in the range 0.6-0.8, compared to the assumed value of 0.2. This demonstrates that potentially significant deviations from assumed friction values can be expected in reality.

7.6 Summary

A number of problems, which are summarised in Section 7.4.4, were encountered during the installation and initial stressing of the instrumented prestressing strands. The possible uneven force distribution and nonlinear strain sensor response is investigated further in the second field test described in Chapter 8. This made calibration of the strain sensors difficult, therefore most sensor responses in this section have been shown in wavelength. The sensor results show that despite the problems encountered with the interrogating fibre during installation and stressing of the strands, sensors that could be interrogated survived stressing of the prestressing strands. Temperature sensor measurements were consistent with thermocouple temperature and strain sensors were able to monitor decreasing strain comparable to the decreasing force measured by the load cells, for the entire test of 170 days.

Chapter 8

Field trial II: Multi strand test

In the previous field trial instrumented prestressing strands were installed in two post-tensioned concrete beams. Twenty four sensors, 12 strain and 12 temperature, were attached to two sets of strands. There were several problems, such as fibre breakages, encountered during the installation; and a non-linear response of the remaining sensors during the initial stressing. The test at Vinci Technology Centre aimed to test improved fibre and sensor protection and determine the reasons for the sensor responses previously observed. The test was carried out on a calibration rig that Vinci uses to calibrate their 28-strand stressing jack. The calibration rig, shown in Figure 8.1, is a metal structure and the strands are stressed in a linear direction. This was a simpler scenario compared to the previous experiment with the concrete beams.

8.1 Aims

Specifically the aims of the test were:

- Check the sensors survive 1300 MPa whilst attached to a multi wire strand.
- Investigate the force distribution of the wires within the strand.
- Test the improved optical fibre system and sensors.

8.2 Sensor design

During the previous field trial, it was found that several aspects of the sensor design and fibre system needed to be improved. There were fibre failures at the end of the sensor capillary and where the fibre was attached at the end of the strand; as well as where the bare fibre lay in the



Fig. 8.1 28-strand calibration rig. The rig is used to calibrate a 28-strand stress jack, seen at the top, with a Statimeter load cell.

strand groove. Therefore, a few changes were made. A small section of capillary was added to each end of the sensor package, see Figure 8.2. This ensured the brazed joint between the fibre and capillary was covered by the shim, protecting it further. The fibre was put through a small-diameter flexible silicone tube that fit inside the strand grooves. This prevented the fibre from exiting the groove whilst allowing it to move freely. Finally, the fibre at the end of the strand was covered with silicone tubing and completely sealed with epoxy as shown in Figure 5.18.

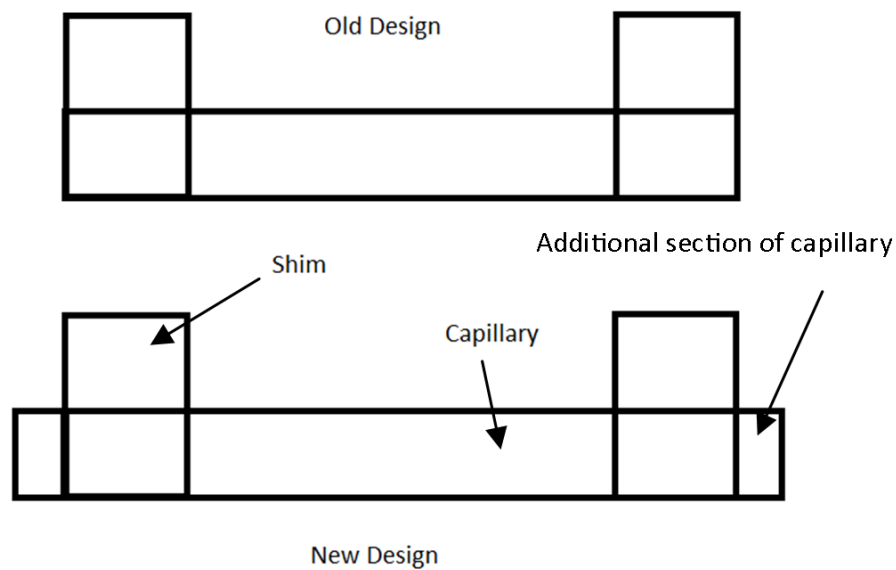


Fig. 8.2 Improved sensor design. The new sensor design had two small sections of capillary at each end to protect the brazed joint.

Two strands were instrumented in this way. One had three strain and one temperature sensor attached to it; the other had two strain sensors and one temperature sensor. The strain sensors were spot welded onto different wires of the same strand to investigate the force distribution between the wires, see Figure 8.3. A third strand had sensors attached without protected interrogating fibres, so that if any problems occurred there was the potential to fix them when on site. In the end this was not required. Two epoxied FBG sensors were attached to the third strand for comparison with the metal packaged sensors. Epoxied FBGs have shown high resolution and linear behaviour in the laboratory and so acted as a comparison for the metal packaged sensor.

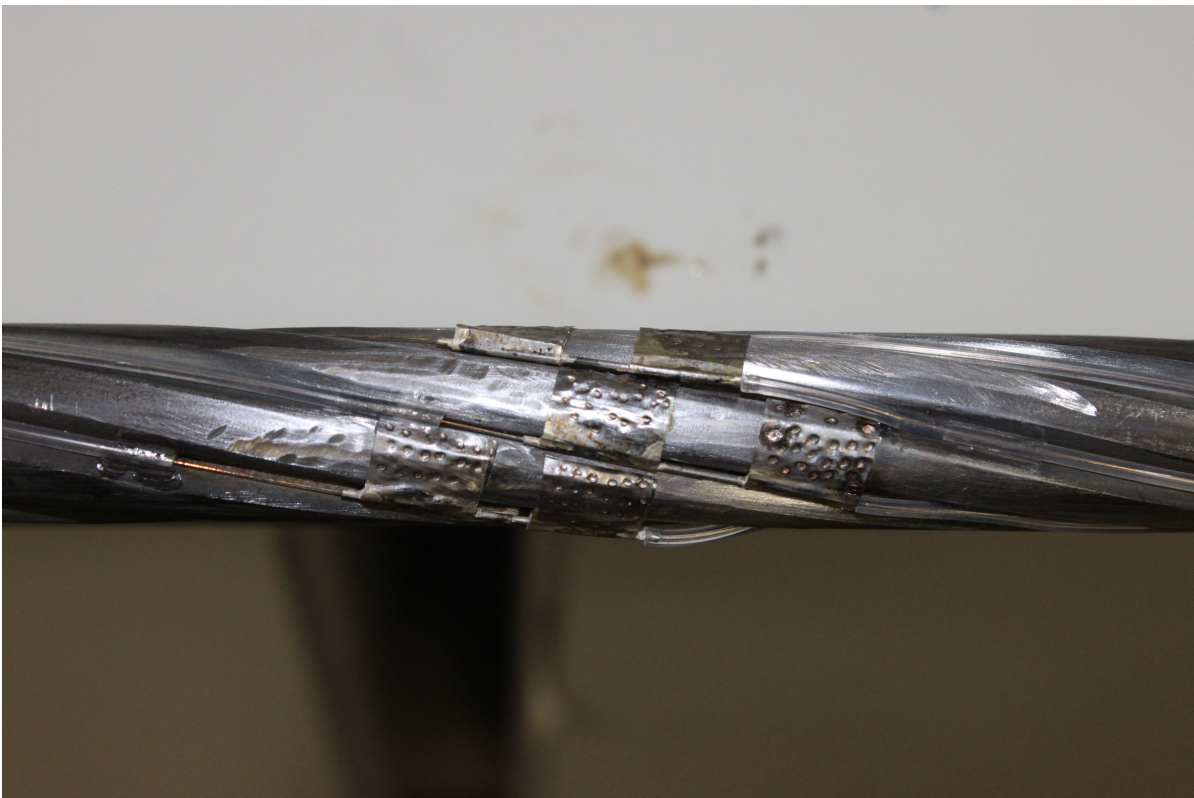


Fig. 8.3 Three sensors attached to different wires of a prestressing strand.

8.3 Installation of the instrumented strands

Strand installation was improved compared to when instrumented strands were put into the concrete beams previously. The strand that had unprotected fibre was inserted into the calibration rig without the hydraulic jack on top. The fibre was then connected to the interrogator and tidied away. The hydraulic jack was lowered onto the strand and calibration rig. After this, the two instrumented strands with protected fibre were inserted into their holes on the rig. A load cell was placed at the top of each instrumented strand followed by a barrel and set of wedges. The interrogating fibres were then connected to the interrogator to check the sensors and the rest of the 28 strands were set up. Figure 8.4 shows the procedure.

The sensors on the strands had to be fitted into 19mm holes and this was done successfully for the strands with protected fibre. One sensor on the unprotected strand could not be interrogated as the fibre connecting the sensors broke. However there were 5 sensors working on this strand.

8.4 Stressing procedure

All 28 strands, including 3 instrumented ones, were stressed simultaneously using a 28-strand hydraulic jack. The gauge on the hydraulic jack measured pressure. To determine the applied force a Statimeter load cell was attached to the calibration rig. A pressure of 9500 psi in the hydraulic jack corresponded to 750 tons on the load cell. The load cell was calibrated at the National Physical Laboratory and a linear relationship was determined, in which the slope coefficient was 9.9675 kN/ton.

The strands were stressed to 9500 psi which is equivalent to a force of 267 kN in each strand. The hydraulic jack was increased in 1000 psi steps until 4000 psi, then the pressure increment was reduced to 500 psi. Figure 8.5 shows the load cell force during stress cycle 4. At each pressure level the sensors were checked to see if their peaks were being properly detected. If they were not then the force was reduced to zero and the peak detection parameters were adjusted. This happened twice; therefore the strands were subject to 5 cycles where the maximum force for each cycle was 200 kN, 250 kN, 280 kN, 280 kN and 280 kN per strand respectively¹.

¹Note that these forces were measured by the individual strand load cells and not the hydraulic jack. They measured a higher force than the predicted 267 kN.

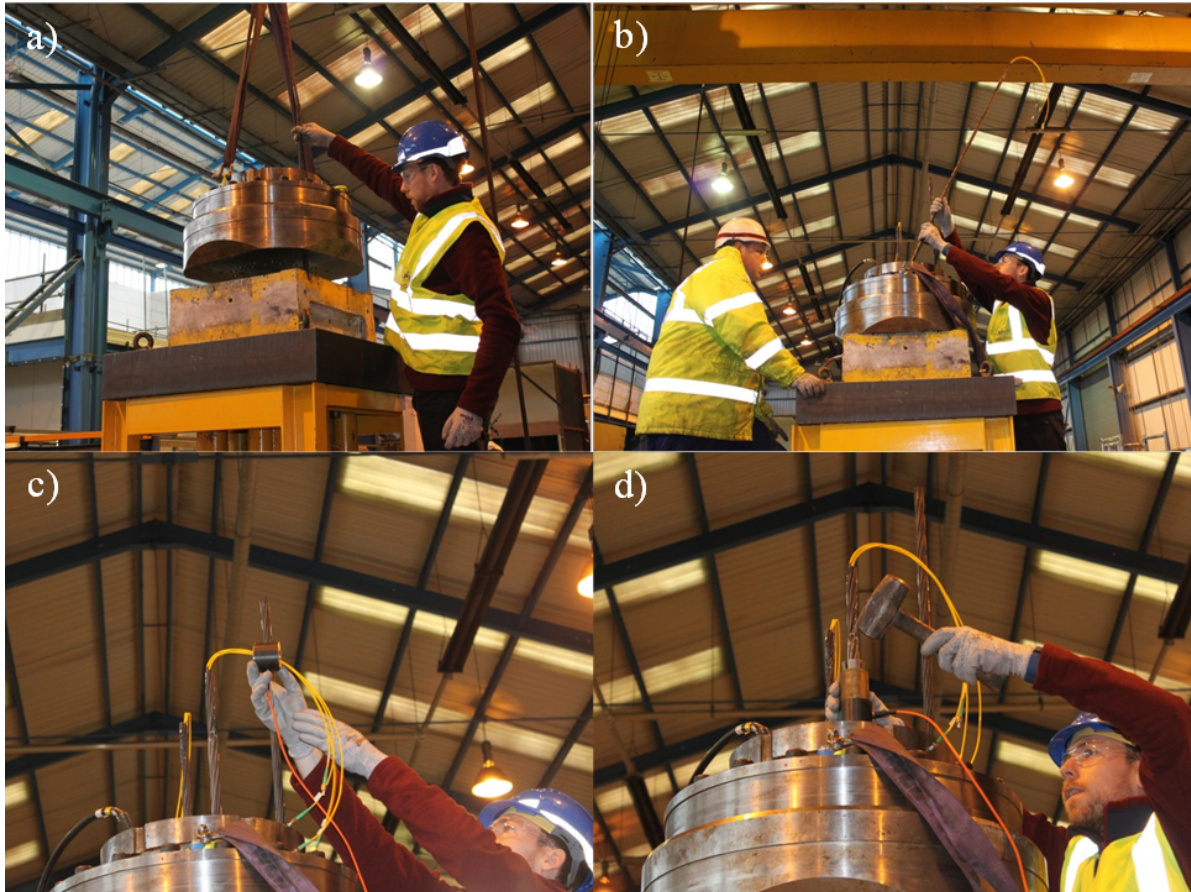


Fig. 8.4 Installing the instrumented strands into the calibration rig. (a) The hydraulic jack was lowered onto the unprotected strand. (b) The other two instrumented strands were inserted afterwards. (c) A load cell was placed beneath the barrel and wedges. (d) The wedges were secured by tapping them with a hammer. The rest of the 28 strands were inserted in their slots.

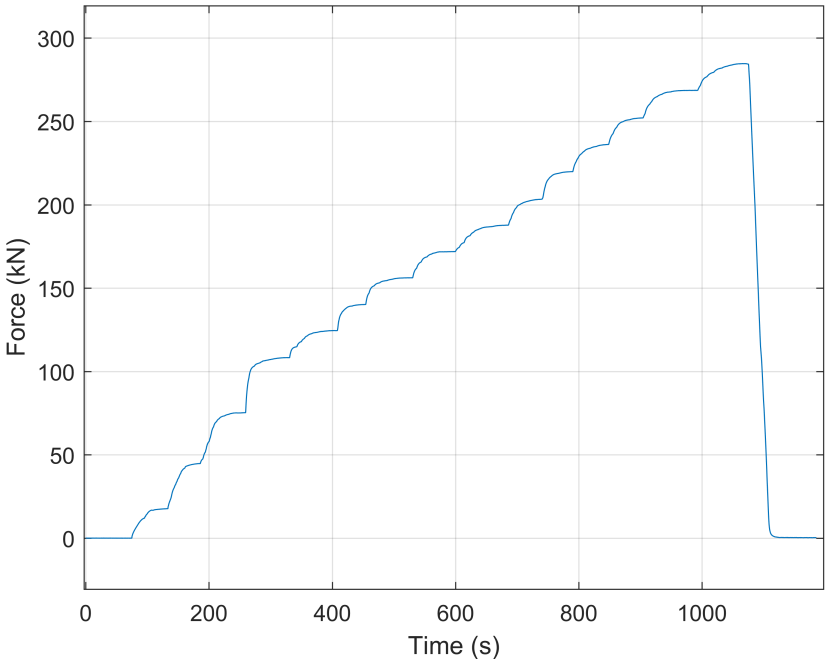


Fig. 8.5 Load cell force during stress cycle 4. The strands were stressed with a step profile to determine if the sensors were stable at constant force. The hydraulic jack pressure was increased in 1000 psi steps until 4000 psi (~ 100kN) was reached, after which the steps were reduced to every 500 psi.

8.5 Sensor results and observations

Although the installation of the strands was more successful compared to the previous test, the recorded sensor responses displayed characteristics that were very similar to the previous attempt. All the metal packaged strain sensors had a non-linear response above a threshold force, see Figure 8.6. The force with which the non-linear response began was higher for each subsequent stressing cycle which was consistent with what had been observed before. This type of behaviour has been noted in all previous experiments with 7-wire prestressing strands. Below the threshold force, the sensor responses were approximately linear (Figure 8.6b-f). The wavelength response from three sensors was very jagged, see Figure 8.6a. There were rapid increases in wavelength that did not correspond to increases in force measured by the load cell. This has not been seen before, but could have been due to the fibre slipping incrementally in the capillary. Figure 8.6b and 8.6e show that permanent, large zero-force wavelength shifts after stressing were observed. These ranged from tens of pico-metre up to 3 nm for one sensor.

In general the epoxy sensors performed very well although they also had problems with peak detection (see Figure 8.7 Sensor 1) and in one case the epoxy sensor peak was too low to interrogate after cycle five. Inspection of the sensor spectrum indicated that the FBG had been subject to such a high strain that it was permanently damaged. For each cycle the epoxy sensor response was linear when compared to the load cell force as shown in Figure 8.7. This shows this type of sensor may have a good potential for future use if the strain transfer can be reduced and it can be protected properly. Both of these can be achieved with well designed sensor packaging.

Table 8.1 shows least squares fits for the most linear metal packaged sensor and the two epoxy sensors. Comparing the strain sensitivity, the slope, of the two types of sensors shows that the metal packaged sensors were approximately ten times less sensitive than the epoxy sensors. This is consistent with that measured on the tensile machine in the laboratory. The metal packaged sensor had a 500 pm change in zero-force wavelength, the intercept, between cycle 3 and 4. The intercept of epoxy sensor 1 decreases constantly during the stress cycling showing that the sensor was deteriorating, this was the epoxy sensor that failed after cycle five. Epoxy sensor 2 shows excellent zero-force repeatability with a 6 pm variation throughout the cycles. Epoxy sensor 2 also had the most repeatable strain sensitivity. The difference in performance between the two epoxy sensors demonstrates the importance of consistency in epoxy mixing and curing.

Some of the metal packaged sensors failed during the stress cycles. In this experiment, a failure was classified as either the loss of an FBG peak (Figure 8.6d) at the interrogator, or the

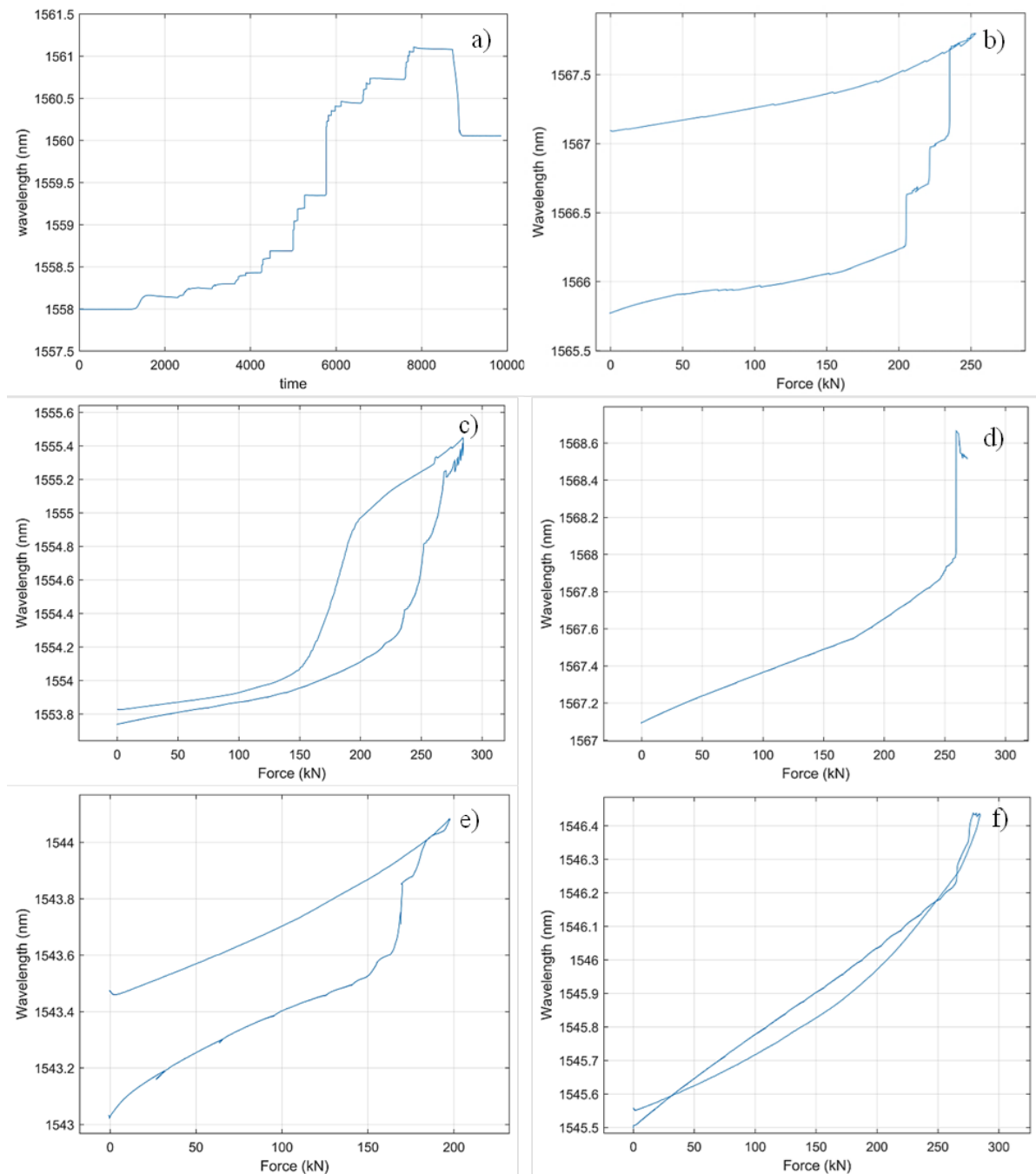


Fig. 8.6 Typical metal packaged sensor responses during stressing including: a) jagged wavelength response from one sensor which didn't follow the step loading applied to the strands. b) Permanent wavelength shift at 0 N after loading. c) Non-linear sensor wavelength response. d) Sensor interrogating fibre failure. e) Permanent wavelength shift at 0 N after loading. e) Non-linear sensor wavelength response.

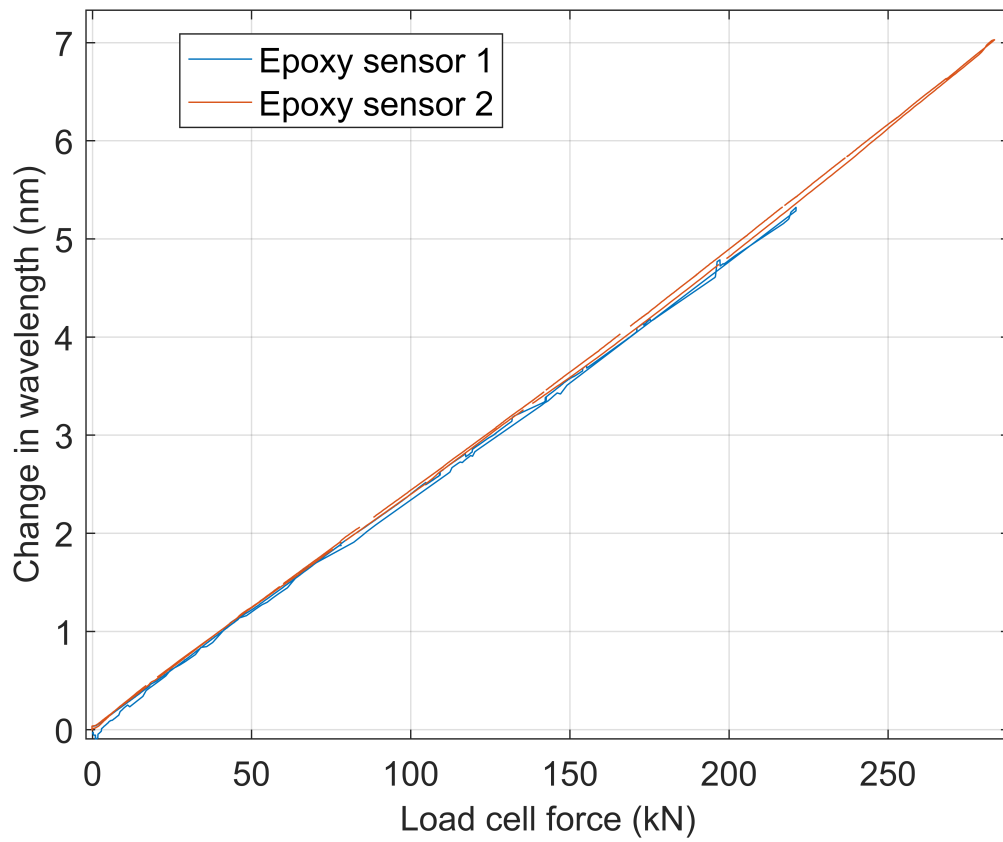


Fig. 8.7 Strain response of the two epoxy sensors during the 3rd loading cycle. Both sensors have a linear response, although the peak reflectivity of Sensor 1 reduced each cycle making it difficult to detect.

Table 8.1 Least squares fit for one metal packaged and two epoxied FBG strain sensors. The fit for the metal packaged sensor was taken from the linear region from 0-250 kN, see Figure 8.6(f).

Sensor type	Stress cycle 3		Stress cycle 4		Stress cycle 5	
	S (pm/kN)	I (nm)	S (pm/kN)	I (nm)	S (pm/kN)	I (nm)
Metal	2.82	1545.064	2.66	1545.505	2.68	1545.557
Epoxy 1	23.9	1529.605	24.2	1529.571	23.4	1529.455
Epoxy 2	24.7	1569.834	24.8	1569.840	24.6	1569.836

S: Slope, I: Intercept.

FBG peak did not shift with increasing strain. The loss of an FBG peak was caused by failure of the interrogating fibre; whilst capillary-fibre joint failure resulted in the FBG not responding to increasing strain. The first sensor failed at 200 kN (75% of the required force) during the second stress cycle; the peak could not be detected. Two more failed at 250 kN during the second cycle but their peaks could still be detected. Finally, a sensors interrogating fibre failed at the capillary at 250 kN during the third cycle. In total four sensors failed out of 11; three strain sensors and one temperature. The temperature sensor responded to strain for the first two stress cycles. Additionally, as mentioned previously, one of the two epoxied sensors could not be interrogated after five cycles because the peak reflection had deteriorated too much.

In terms of the practical installation and protection of the fibres and sensors, the experiment was mostly successful. The silicone tubing that ran along the strands protected the fibre properly, particularly from the barrel and wedges. It also protected the fibre at the end of the strand and allowed the whole area to be covered in epoxy. However the fact that the fibre was attached to the strand at certain points may have caused the non-linear sensor response. This is discussed in more detail in Section 8.6.

Problems were also encountered with peak detection in the LabVIEW software. The first two stress cycles were stopped at 200 kN and 250 kN, so that the peak detection parameters could be adjusted. This has happened previously and dynamic peak bin trending was suggested to remedy this. However, part of this problem was due to permanent wavelength shifts from some of the sensors. This would not happen if the sensors were to behave in a repeatable manner. Additionally, some of the FBG peaks reduced in reflectivity to such a large extent that they could not be detected. This was because other peaks on the same channel had not reduced in reflectivity.

8.6 Outcome of the field trials

The two separate field trials show that the current sensor design and implementation needs to be improved. The sensors have been shown to perform adequately when mounted to a steel specimen on a tensile machine, see Figure 6.7; the sensors display hysteresis characteristics but it was repeatable. However, when the sensors were mounted on a prestressing strand and protected, the sensor response became non-linear after a certain force. Before the second field trial, one of the hypotheses to explain this was that the force within one of the strands wires does not linearly correlate with the total force measured by a load cell at the end of a strand. But the epoxy FBGs showed a very linear correlation compared to the metal packaged sensors. Therefore this effect was not the cause of the responses seen from the metal packaged sensors. The sensor response was due to either the sensor design or the way the sensors were attached to the prestressing strand.

When the sensors were tested on the tensile machine, the fibre exiting the capillary was not attached to the strand. Whereas for the field trials, the splice protector was glued to the strand. On average the splice protector was located 15 cm from the end of the sensor which resulted in a fibre-length change that was six times greater than the fibre-length change inside the capillary. The interrogating fibre becoming tensioned at a certain elevated force could explain the sudden increase in sensitivity during stressing. Furthermore, it could also explain why there were some fibre failures at the end of the metal capillary. After the stress cycles took place the sensors were inspected. There were a number of sensors which had a bare section of fibre at the end of the capillary, see Figure 8.8. This section of fibre should be completely covered by metal, providing further evidence that the fibre may have become tensioned. Furthermore, after the 28-strand calibration rig field trials some of the sensors FBG peaks could be moved by manually pulling on the fibre exiting the capillary, suggesting that the joint had failed.

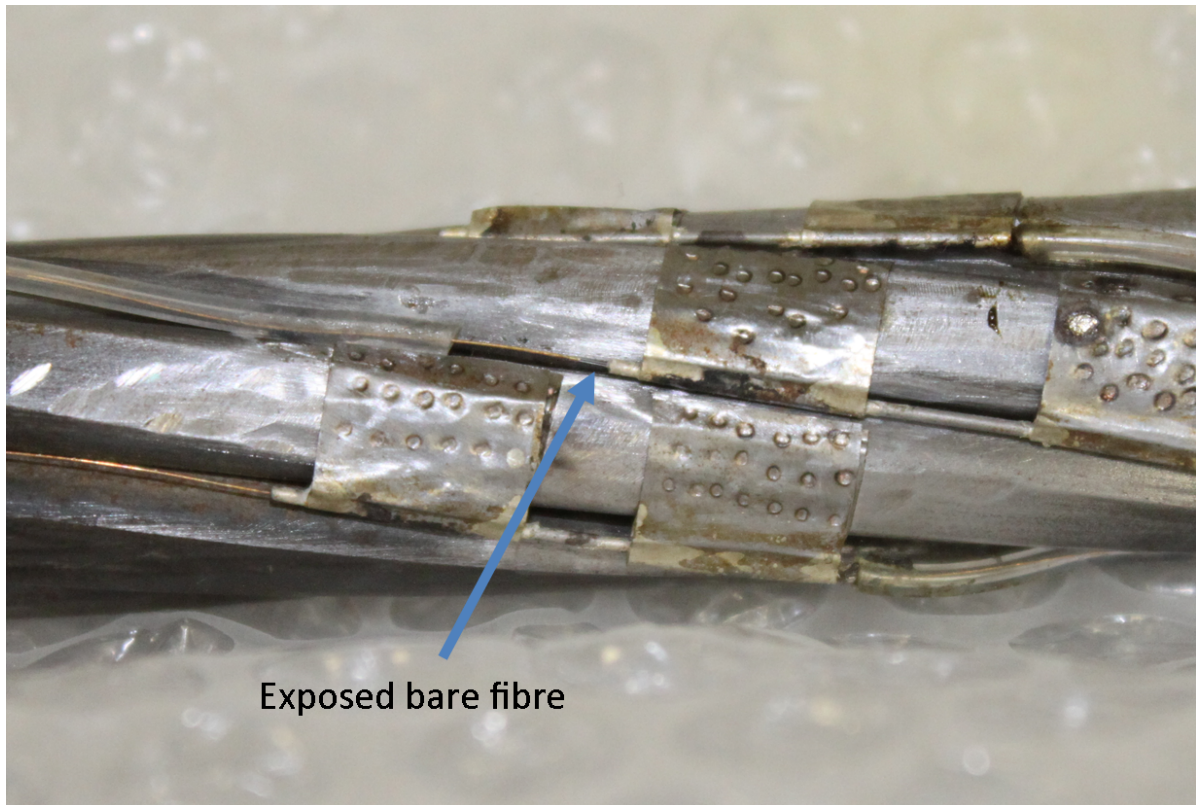


Fig. 8.8 Bare fibre exposed after strand stressing. The fibre should be covered with a copper layer on top of a carbon layer. However silica glass can be seen. This suggests the fibre has been pulled out of the capillary.

8.7 Summary

The strain and temperature sensors were tested in two field trials. In the first, real time monitoring of prestress loss in two concrete beams in ambient conditions was demonstrated. The sensors survived installation and stressing to ~ 1000 MPa. However, some of the sensor interrogation lines did not, indicating that additional measures were needed to protect the fibre. Comparison of the strain measured by the strain sensors and load cell force revealed that possibly individual wires in the strand shared the total force unequally. The second field trial was used to determine the cause of the non-linear sensor response during sensor calibration and test improvements to the fibre protection. The additional fibre protection helped to protect the interrogating fibre, however there were still some fibre failures. These were potentially due to the interrogating fibre becoming tensioned during stressing. Through comparisons with epoxied FBGs, uneven force distribution between strand wires was discounted as a reason for the non-linear strain response of the sensors. This leaves two remaining hypotheses: the

interrogating fibre becomes tensioned and causes failure of the fibre-capillary joint or the Kovar capillary is stressed past its yield stress; these are investigated in Chapter [9](#).

Chapter 9

Investigations into the non-ideal sensor responses

9.1 Non-linear wavelength response

The strain sensors exhibited non-linear strain responses in both the field trials. After the first field trial, where instrumented prestressing strands were tested in concrete beams, it was thought that the non-linear response could have been due to non-uniform force distribution between the strands. This was discussed in detail in Section 7.4.5 and has indeed been measured experimentally [103]. Non-uniform force distribution between the strands was discounted after the second field trial when epoxied FBGs showed a linear response. Therefore there are currently two valid hypotheses;

- The interrogating fibre pulls the end of the sensor causing the brazed joint to fail.
- The stress in the Kovar capillary exceeds its yield stress.

To distinguish between these effects, attempts were made to replicate the non-linear response on the tensile machine in the lab. To check if the tensioned interrogating fibre influences the sensor wavelength, a sensor was mounted onto a steel specimen and stressed to 1300 MPa (80 % UTS), its interrogating fibre was fixed with epoxy 15 cm from the sensor location, see Figure 9.1 (top). There was no slack in the fibre before the specimen was stressed. The specimen was stressed in three cycles up to 5 kN, equivalent to 3.5 $\text{m}\epsilon$. The load cell force and sensor wavelength were compared every 1 kN.

During the stress cycles it was clear that the fibre external to the capillary was under tension. During the third stress cycle at 3.5 $\text{m}\epsilon$ the fibre inside the capillary failed and the FBG could

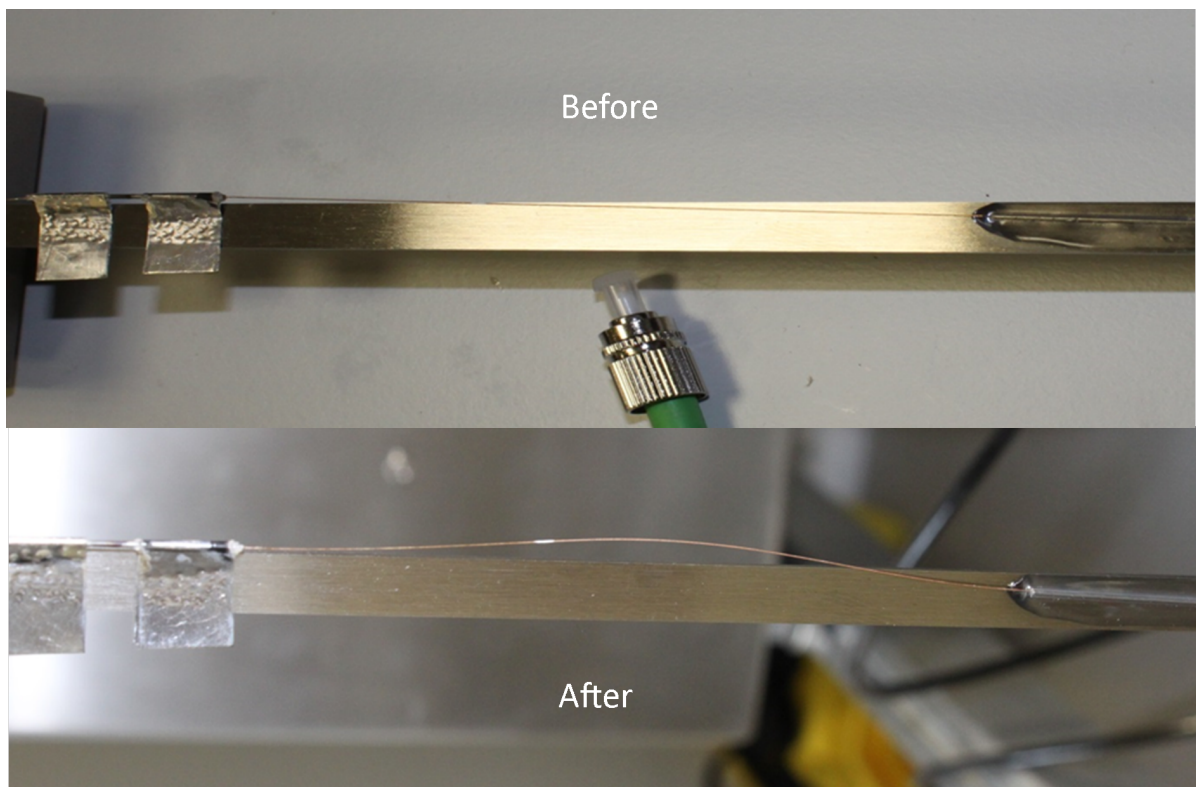


Fig. 9.1 The sensor and interrogating fibre before and after three stress cycles. Slack in the fibre is present after the stress cycles as the fibre has been pulled out of the capillary.

no longer be detected. Figure 9.1 shows the fibre and sensor before and after the stress cycles, the fibre was slacker afterwards, showing that the fibre was pulled out of the capillary leading to its failure.

The wavelength results from the sensor show that at lower strain the sensor behaved in a linear manner, Figure 9.2. But around 4 kN, there was a large increase in the strain sensitivity. This is consistent with what was seen from the sensors on the calibration rig at Vinci. Therefore it is extremely likely that the cause of the non-linear response is due to external force causing the fibre-capillary joint to fail. This is due to the larger absolute length change between the sensor end and the point where the fibre is attached to the specimen compared to the absolute length change of the fibre inside the capillary, which puts increased stress on the brazed joint.

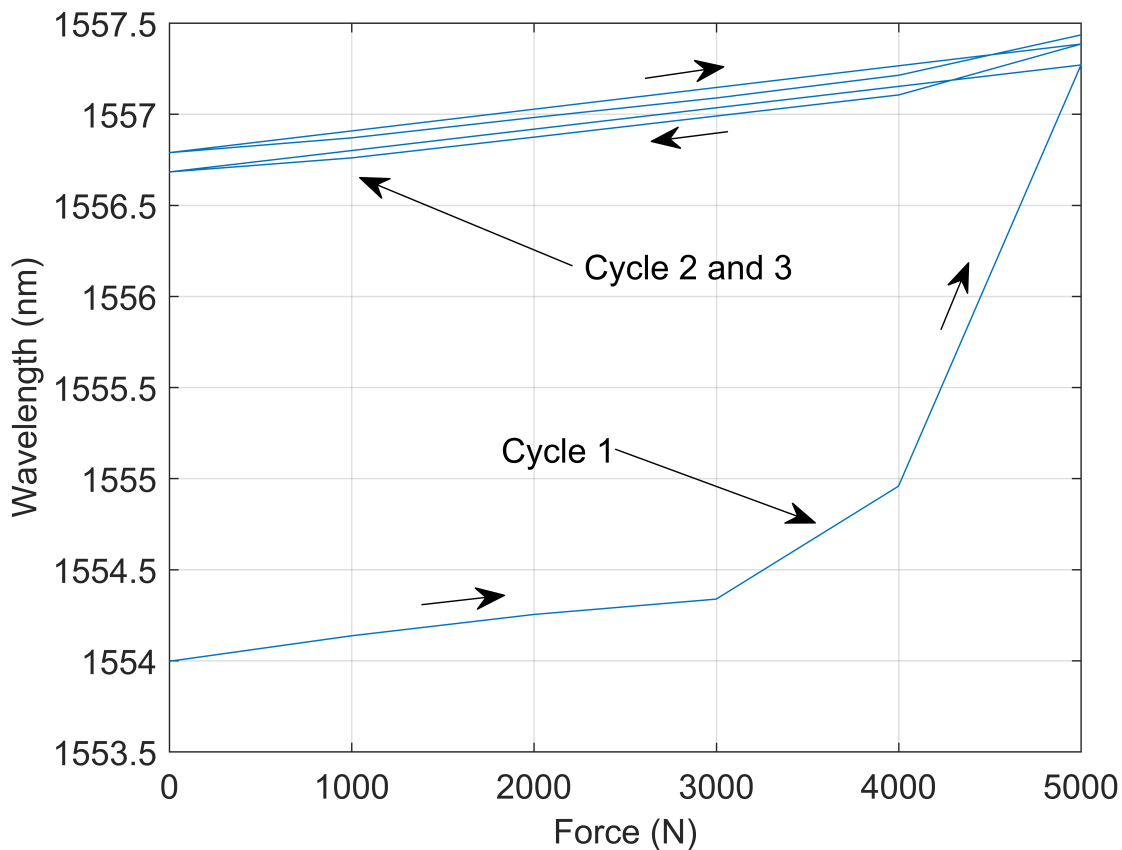


Fig. 9.2 Sensor response when the interrogating fibre is fixed to the specimen. The sensor strain sensitivity increased at 3 kN as the interrogating fibre became tensioned, resulting in enough slack in the interrogating fibre for a normal response during cycle 2 and 3.

To confirm that the fibre is pulled out of the capillary when the splice protector is attached to the specimen, two sensors were mounted to a specimen with different amounts of slack in

the interrogating fibre. Figure 9.3 shows the force profile of each cycle. It was expected that the sensor with the least slack in its interrogating fibre would display a large increase in strain before the other sensor. This is what happened as shown in Figure 9.4. Both sensors had a linear response for cycle 1 up to 4 kN. During cycle 2, the strain response for sensor 1 increased, while the response of sensor 2, with more slack in its fibre, remained linear. When the specimen was stressed to 10 kN, both sensors showed large increases in strain sensitivity. The first sensor increased in sensitivity beyond 4 kN ($2.9 \text{ m}\epsilon$), while the other increased in sensitivity at 7 kN ($5 \text{ m}\epsilon$). The sensors showed permanent wavelength shifts similar to previous experiments. Both optical fibres failed during the experiment. Sensor 2 failed inside the capillary at the opposite end compared to the interrogating fibre, the other failed near the splice protector.

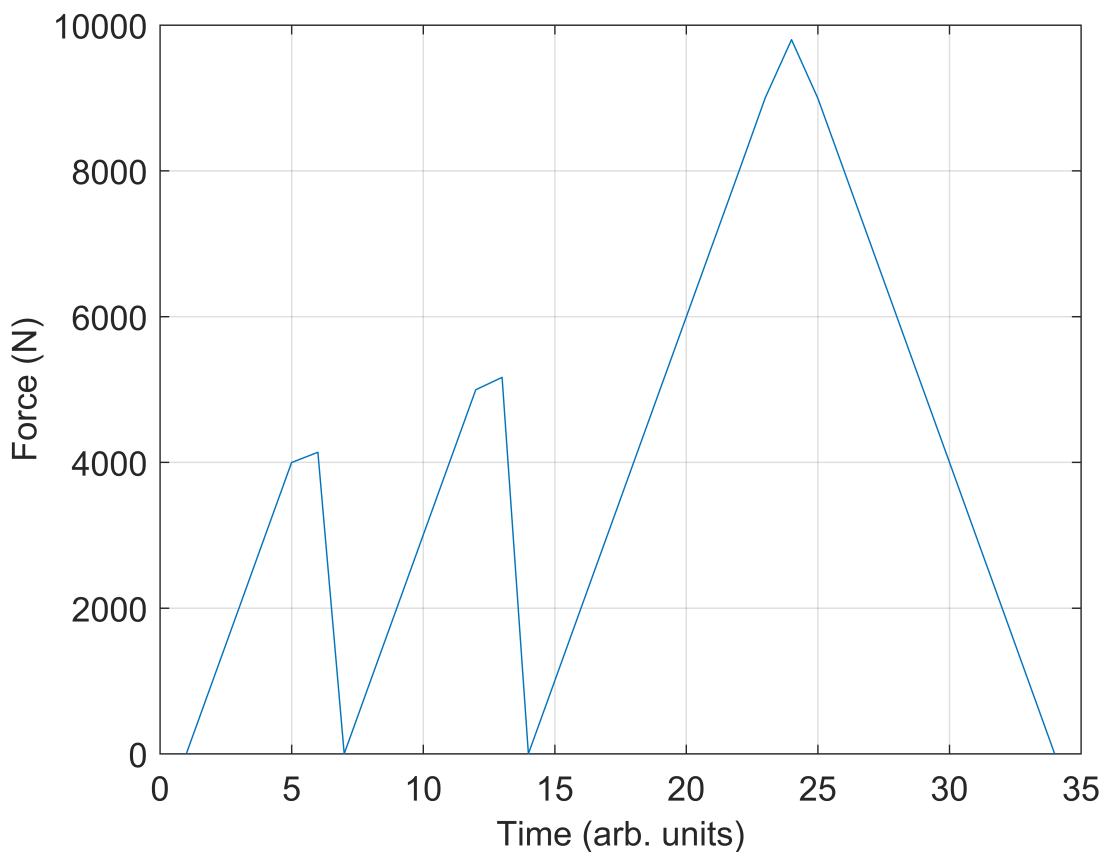


Fig. 9.3 Force profile for second non-linear sensor response experiment.

When the specimen was removed from the tensile machine, the fibre was found to be unattached to the capillary on sensor 2. The fibre had failed at the bare section where the FBG was written. This was the result of the fibre-capillary joint failing and there was evidence of

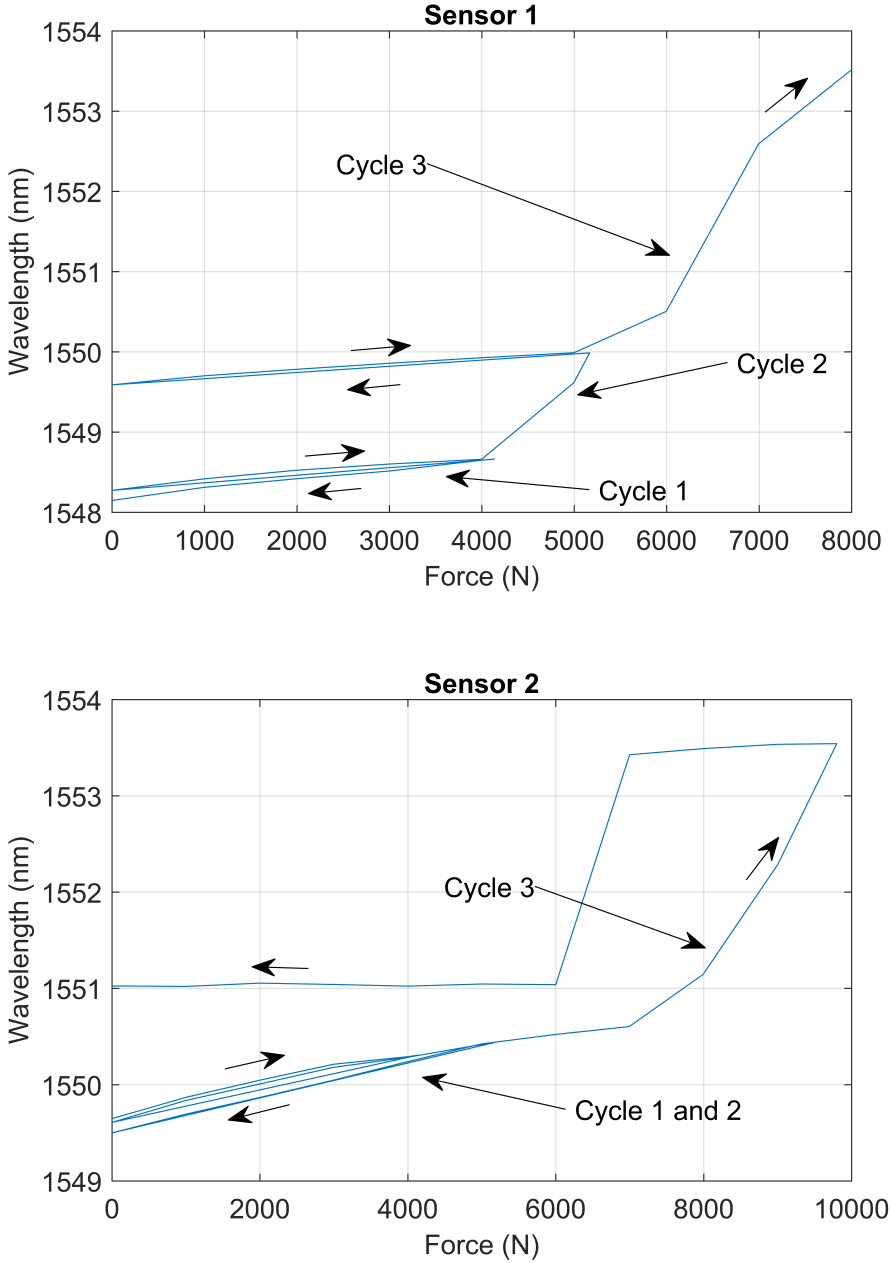


Fig. 9.4 Sensor wavelength for second non-linear sensor response experiment. Sensor 1 had less slack in its interrogating fibre at the beginning of the experiment so its sensitivity was expected to increase first. This happened in cycle 2, while it did not for sensor 2.

deformation of the copper coating at the joint area. Figure 9.5 shows an image of the fibre joint section where the copper coating has ruptured and separated from the fibre.

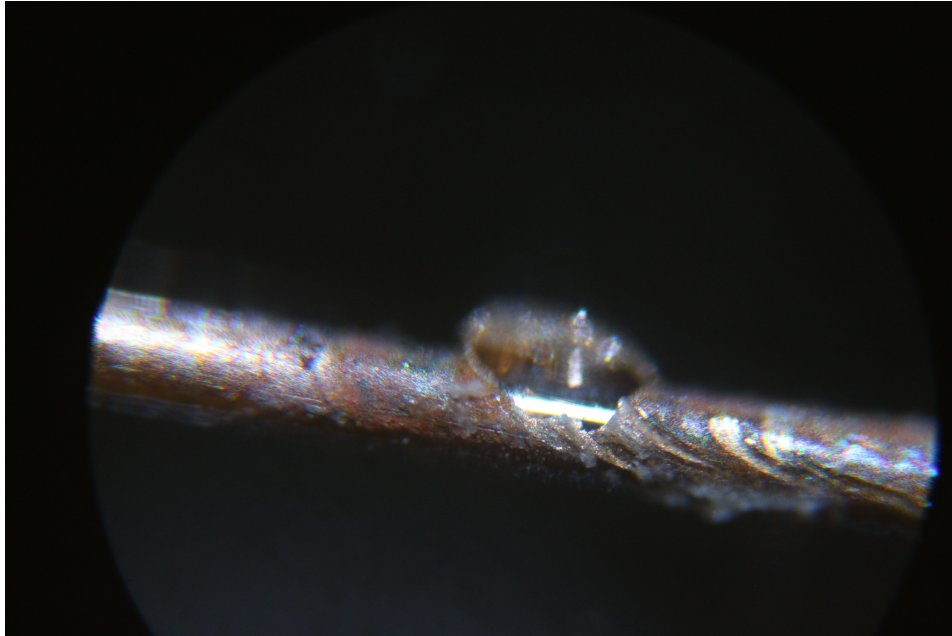


Fig. 9.5 Rupture in fibre copper coating due to it being pulled out of the capillary.

These experiments confirmed that the non-linear sensor response was due to the sensors interrogating fibre being attached to the strained specimen. The relatively long length of the fibre section causes a larger force from the outside of the brazed joint compared to the internal force inside the sensor. This causes the joint to fail resulting in a large increase in strain sensitivity. If the fibre is strained further it eventually fails completely. When the sensors have been tested in realistic conditions, there have been several sensor failures, it is highly likely that this is the reason. In order to use the sensors, the problem must be mitigated potentially by fixing the capillary end to the specimen or increasing the strength of the sensor end. Alternatively, there must be enough slack in the interrogating fibre between sensors to ensure that the fibre does not become tensioned as the strand elongates.

9.2 Sensor hysteresis

During strain calibration the strain sensor wavelengths displayed hysteresis during loading and unloading, suggesting that the sensors had viscoelastic properties. This was investigated in further detail by stress cycling the sensors a number of times, attention was paid to wavelength repeatability at the maximum and zero forces, the evolution of the hysteresis curve and the

hysteresis area. While it is not strictly necessary for sensors in this application to perform repeatedly for so many stress cycles, testing the sensors in this way has allowed insight into the various unknown effects that the sensors displayed.

Three metal package strain sensors were compared to epoxied FBGs in separate tests. The sensors were mounted on steel specimens of the same specifications as in Section 6.2 and tests were carried out as follows:

- 100 cycles at a force of 5 kN.
- 100 cycles in total, 20 cycles each at forces of 1, 2.5, 5, 7.5, 2.5 kN.
- 100 cycles in total, 20 cycles each at forces of 1, 2.5, 5, 7.5, 2.5 kN.
- 100 cycles at a force of 5 kN.

The tests were carried out at a constant speed of 5 mm/min and the specimen and sensors were placed in an environmental chamber at 32 ± 0.03 °C to remove any temperature influence during the comparisons. While the temperature of the chamber, steel specimen and sensors was stabilising the tensile machine crosshead was constantly adjusted so that there was no stress on the specimen as the various components thermally expanded. The optical signals and load cell voltage were synchronised using a National Instruments PXI unit and interrogated at 10 Hz.

To calculate the hysteresis area, first the beginning and end of each stress cycle was identified by using a peak finding algorithm. Then, both the sensor wavelength and load cell voltage shift were normalised to their maximum value and had their offset removed. Finally, the hysteresis area was calculated using numerical integration via the trapezoidal method. The calculated area was a normalised hysteresis area, so that sensor sensitivity changes were not measured and small differences in maximum force or permanent wavelength shifts did not affect the measurement. These effects were investigated separately with plots of load cell voltage against sensor wavelength so that they were comparable to stress-strain curves and the same as Figure 6.5, for example.

The epoxy sensors are considered first. Figure 9.6 shows an epoxy sensor on a specimen stressed to 5 kN for two tests. Recall that the sensors underwent two sets of 20 cycles each of 1, 2.5, 5 and 7.5 kN in between the two sets of 5 kN cycles. The figure shows that the sensor response is repeatable with no noticeable change in sensitivity or permanent wavelength shift. This shows that we can be confident that the specimen does not undergo significant creep during these tests and any creep behaviour seen can be attributed to the metal packaged sensors themselves. The normalised hysteresis area, shown in Figure 9.7, is also repeatable across the

two sets of 100 cycles, there is a consistently decreasing trend with increasing cycle number. This is consistent with observations from load cycling electrical strain gages [106]. One epoxy sensor did show sign of a permanent wavelength shift between the two tests. This can be seen in Figure 9.8, where there was approximately a 40 pm decrease in wavelength for all forces when comparing test 2 with test 1.

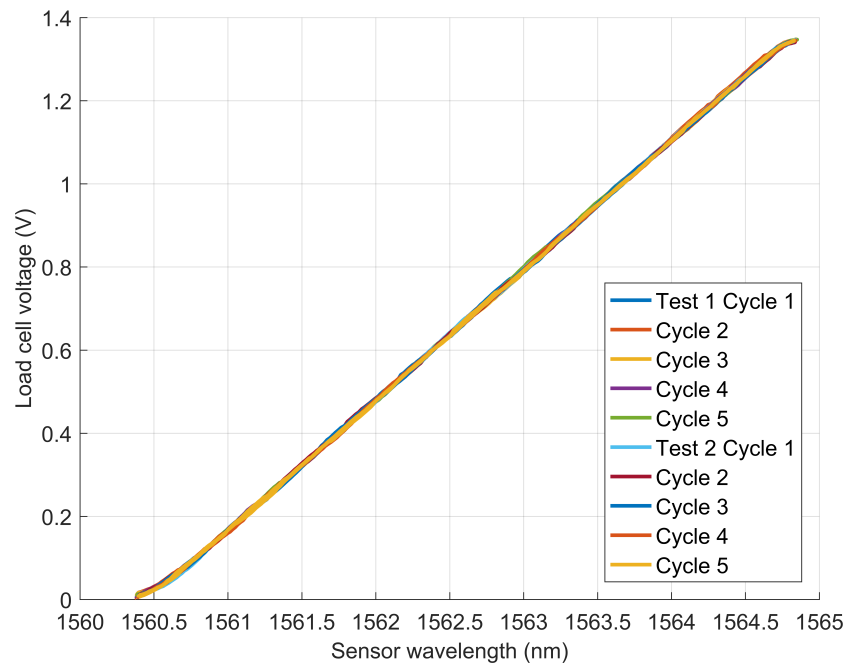


Fig. 9.6 Epoxy sensor wavelength during 200 cycles at 5 kN. The graph shows two separate 100 cycle tests. In between the tests the sensor was stressed in two sets of 1, 2.5, 5 and 7.5 kN 20 times each. The sensor response shows negligible difference between the two tests.

The sensor responses of the metal packaged sensors during repeated cycling were more complicated with several changes happening to the sensors. The evolution of the hysteresis loops across both tests can be seen in Figure 9.9. The direction of the hysteresis loop does not change throughout the tests and is the same as in Section 6.2. However its shape does change, it is clear that the sensors absolute wavelength has changed between test 1 and 2. This can be seen more clearly in Figure 9.10, which shows the first cycle of test 1 and the last cycle of test 2 with wavelength plotted on the y-axis. The sensor wavelength has decreased for the entire force range suggesting there was a permanent change to the fibre capillary joint of the sensor. Additionally, there was a slight decrease in strain sensitivity, the hysteresis loop of test 2 in Figure 9.10 is not as steep as the one for test 2. The hysteresis loops for test 2 appear to be more consistent than those in test 1. The normalised hysteresis area for the metal sensor was an

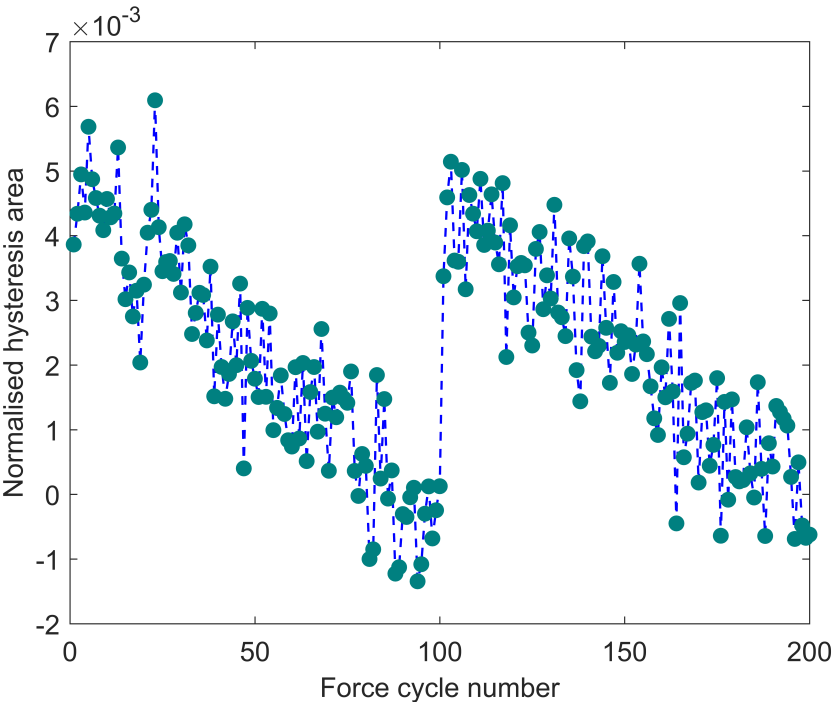


Fig. 9.7 Normalised hysteresis area for an epoxy sensor for two separate 100-cycle tests to 5 kN. The decrease in area is consistent with observations from load cycling specimens with attached electrical strain gages [106].

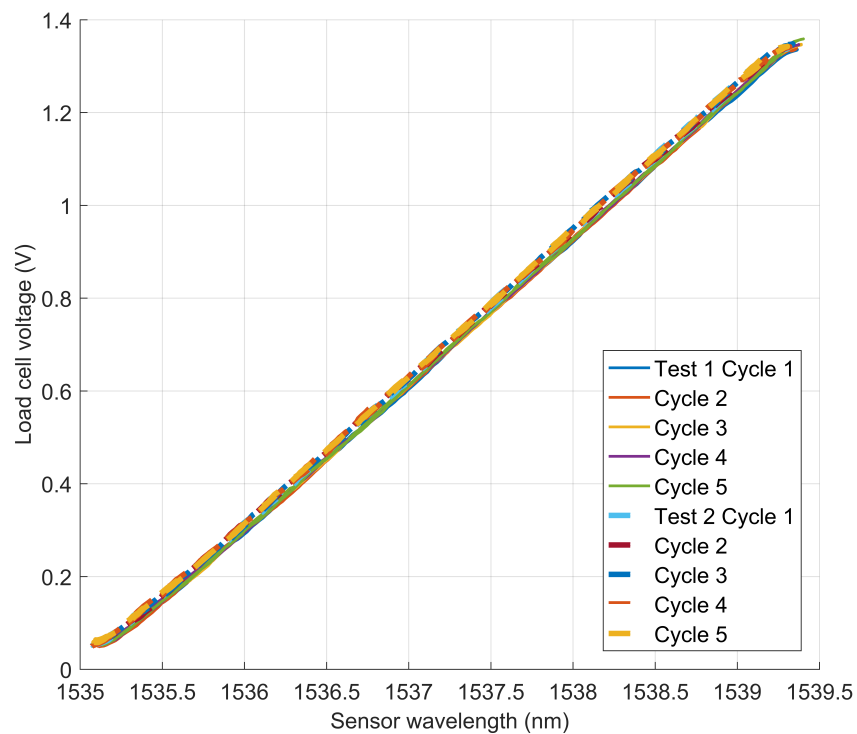


Fig. 9.8 Epoxy sensor wavelength during 200 cycles at 5 kN. The graph shows two separate 100 cycle tests. In between the tests the sensor was stressed in two sets of 1, 2.5, 5 and 7.5 kN 20 times each. There is a small shift in sensor wavelength for all forces when comparing test 1 and 2.

order of magnitude larger than the epoxied FBG. It also does not behave consistently between the two tests, see Figure 9.11. In the second test the metal sensor hysteresis matches the epoxy hysteresis in terms of the magnitude of the decrease. This further suggests that the sensor is more consistent during the second test.

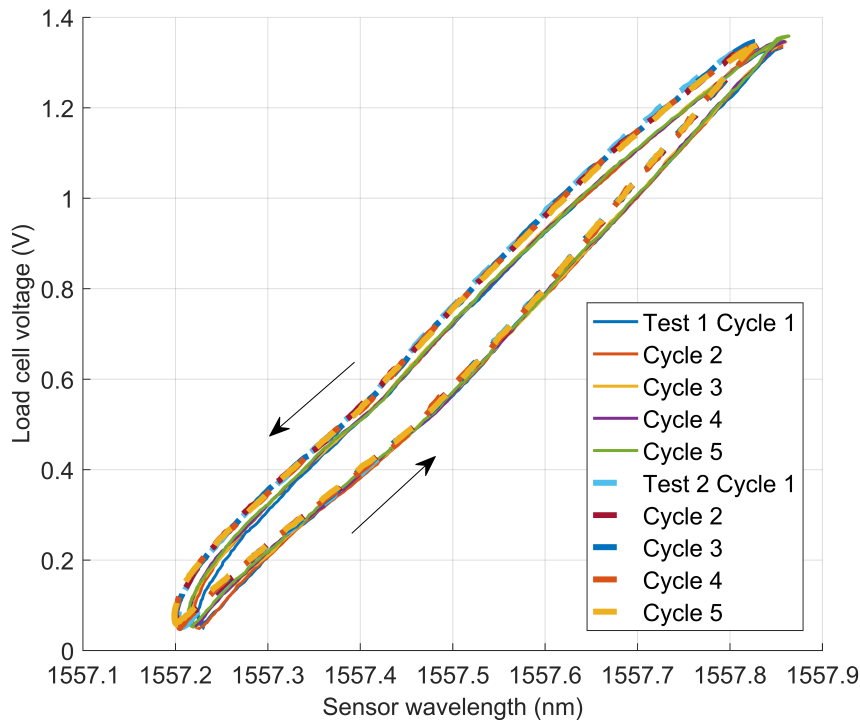


Fig. 9.9 Metal packaged sensor wavelength during 200 cycles at 5 kN.

In between the two force cycling tests at 5 kN, the sensors were tested at different forces to investigate the hysteresis effects in more detail. The machine displacement, Figure 9.12, shows that some of the sensor hysteresis could be due to the specimen. The graph shows that for smaller forces the stress-strain curves are marginally steeper, implying a larger modulus of elasticity. This is consistent with the theory discussed in Section 6.2 and indeed a small amount of hysteresis is seen in the epoxy sensor, although it is too small to be seen in Figure 9.13. This suggests that hysteresis in the metal packaged sensor can be partly attributed to viscoelastic effects in the specimen itself. However, the hysteresis of the epoxy sensor is an order of magnitude less than the metal sensor even though the strain transfer of the epoxy sensor is approximately 80 % greater. Therefore, the large majority of the hysteresis present in the metal packaged sensor strain response is due to the sensor itself. Many of the characteristics that have been already mentioned in this section and in Section 6.2 can be seen in the metal packaged

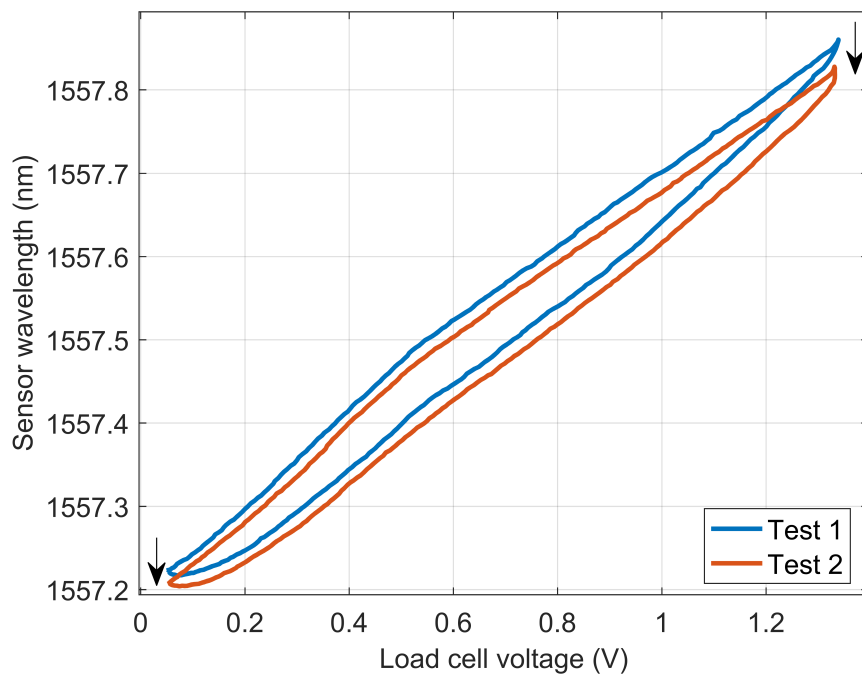


Fig. 9.10 First stress cycle of test 1 and last stress cycle of test 2.

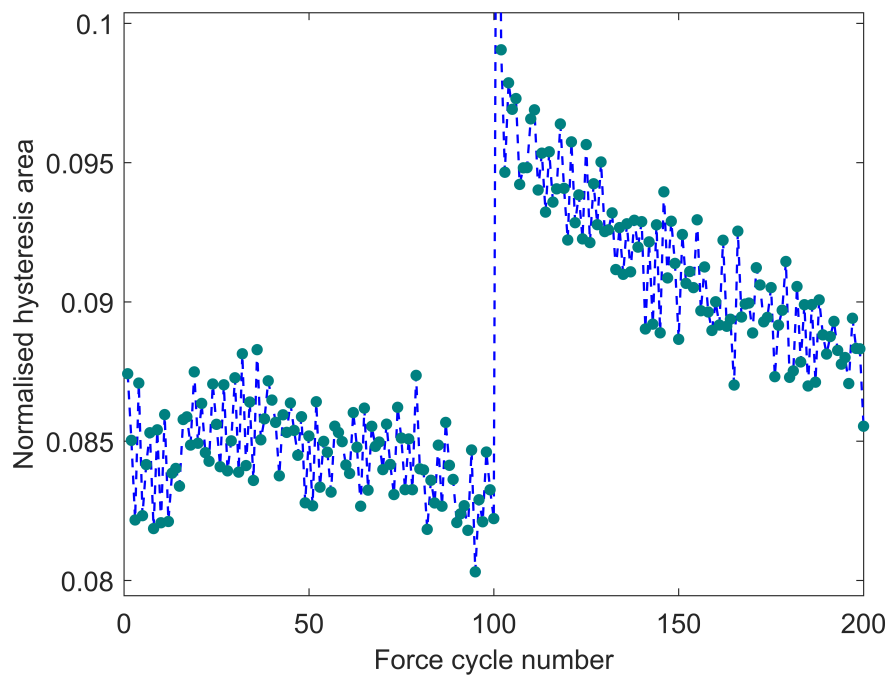


Fig. 9.11 Normalised hysteresis area for a metal sensor for two separate 100-cycle tests to 5 kN.

sensors when they were stressed in cycles of different forces. Figure 9.14 shows hysteresis loops from two sets of cycles of 1, 2.5, 5, 7.5 kN. The graph shows that hysteresis width, in either the x- or y-direction is larger for larger forces. There is a reduction in wavelength for the same force in test 2, this is labelled with arrow B. Interestingly the cycles up to 7.5 kN are the most repeatable. Finally, there is a reduction in strain sensitivity for larger forces.

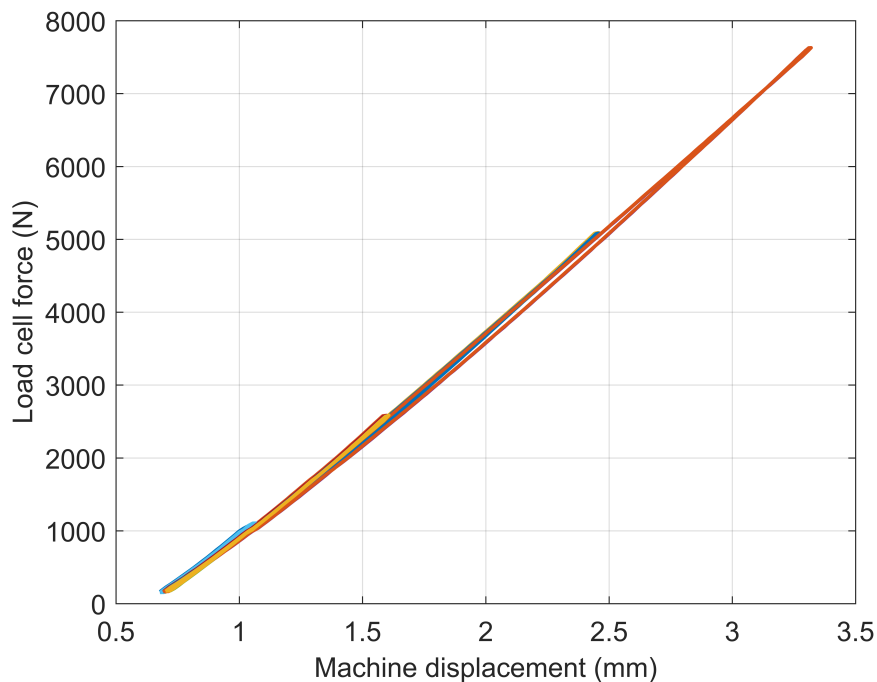


Fig. 9.12 Load cell force and machine displacement for different forces.

The normalised hysteresis area for both the epoxy and metal packaged sensor can be seen in Figure 9.15. The epoxy sensor hysteresis area is similar to that with the machine displacement. The different forces can be distinguished but there is an overall decreasing trend in the two tests. This is similar to what was seen in the 5 kN cycles in Figure 9.7. The metal sensor is more inconsistent, the cycle at 7.5 kN can clearly be seen with an increase in the hysteresis area. This is possibly because the sensors have been cycled at the lower force of 5 kN, indicating that the sensors may undergo a form of work hardening. This idea is further reinforced by the fact that the second set of 5kN cycles are more repeatable than the first.

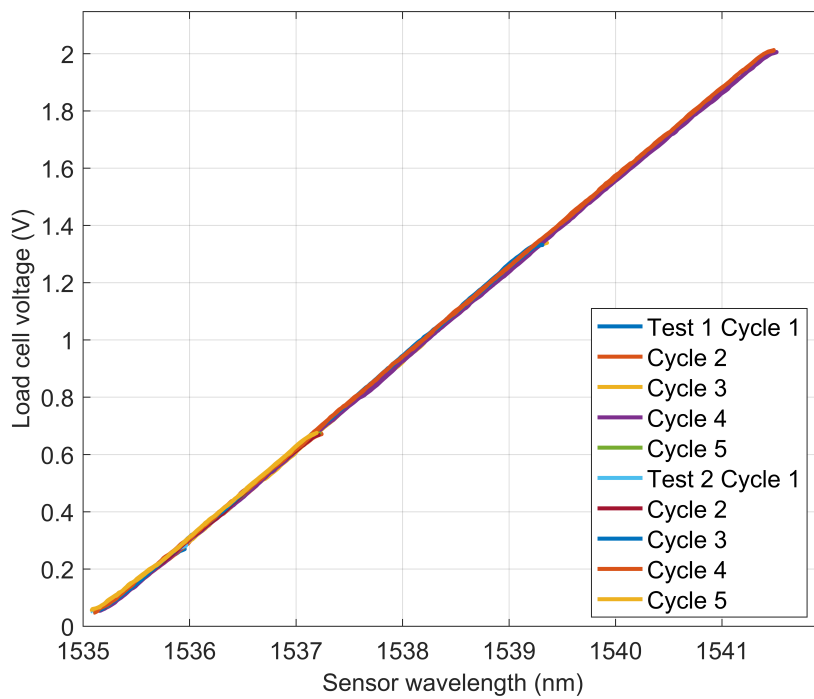


Fig. 9.13 Epoxy sensor hysteresis loops for different forces.

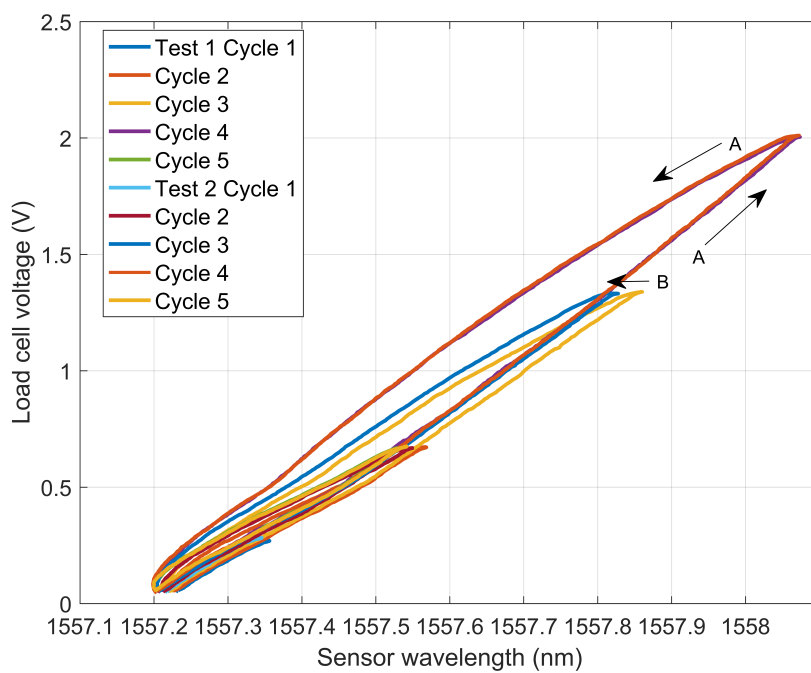


Fig. 9.14 Metal packaged sensor hysteresis loops for different forces.

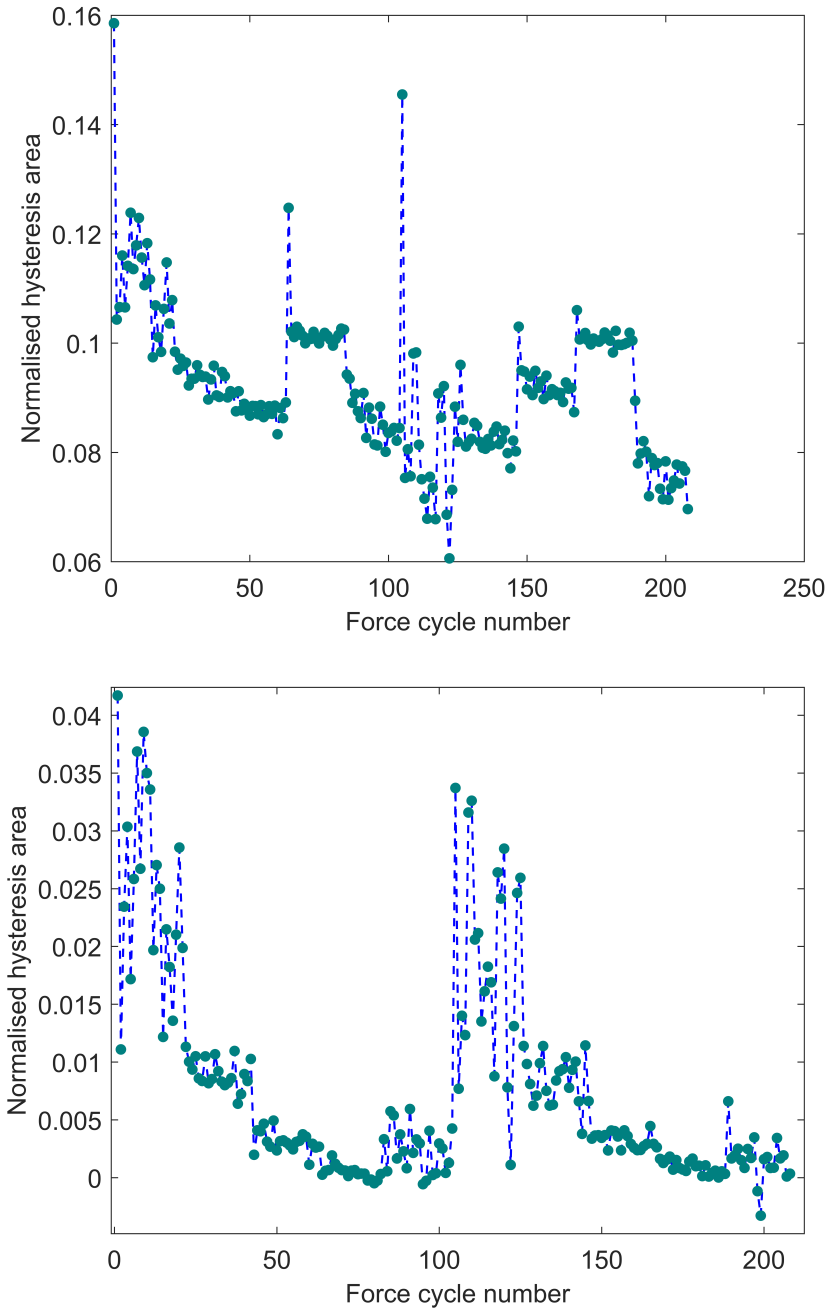


Fig. 9.15 Normalised hysteresis area for cycles of 1, 2.5, 5, 7.5 kN. The sensors were subject to twenty cycles at each force in two tests. The top graph shows a metal packaged sensor, with an epoxy sensor on the bottom graph.

9.3 Long term calibration

One sensor was calibrated up to $3.3 \text{ m}\epsilon$ a number of times to investigate the long term stability of the calibration. In between the calibration cycles the sensor was subject to a number of different tests such as those described in Section 9.2. Figure 9.16 shows one cycle from 8 different calibrations, the wavelength offset has been removed so that the strain sensitivity between each calibration can be compared more easily. The maximum wavelength reached in each calibration decreases, showing that the strain sensitivity of the sensor has decreased over time. The first large decrease in sensitivity, C4 to C5, occurred when the sensor was calibrated up to $7.2 \text{ m}\epsilon$ in three cycles. The second large decrease in sensitivity, C7 to C8, occurred when the sensor was subject to 100 cycles at a force of 9 kN, equivalent to $\sim 6.5 \text{ m}\epsilon$. The sensitivity decrease can be clearly seen during the 9 kN force cycling, Figure 9.17, this happened near the beginning of the test from approximately cycle 1-20. Figure 9.17 again shows the sensor reaching a relatively stable period of operation near the end of the test. Returning to the sensors calibration history, interestingly the sensor was subject to 200 cycles at 5 kN and 40 cycles each at 1, 2.5, 5, 7.5 kN between calibrations C6 and C7. This did not effect the strain sensitivity of the sensor to a large extent. These observations are consistent to those observed within Section 9.2; the wavelength response gradually stabilises over a number of cycles when a sensor is stressed by a certain amount. If the sensor is stressed to a level below this, it performs relatively consistently. If the sensor is stressed above this level, it must adjust to the new stress level.

9.4 Sensor response discussion

From the various experiments on the sensors, the following effects have been seen:

- Reduction in sensitivity for higher strain ranges with constant machine speed.
- Hysteresis during loading and unloading.
- Permanent wavelength shifts during repeated force cycles.
- The sensor response reaching a ‘stable’ period after a few cycles at a particular force.
- The sensor adjusting to a higher stress/strain in the first cycle. Either the fibre-joint deforms or the fibre slips inside the capillary.

These characteristics arise from complex non-linear material behaviour which varies from sensor to sensor. If these effects were due to one of the bulk materials such as the kovar

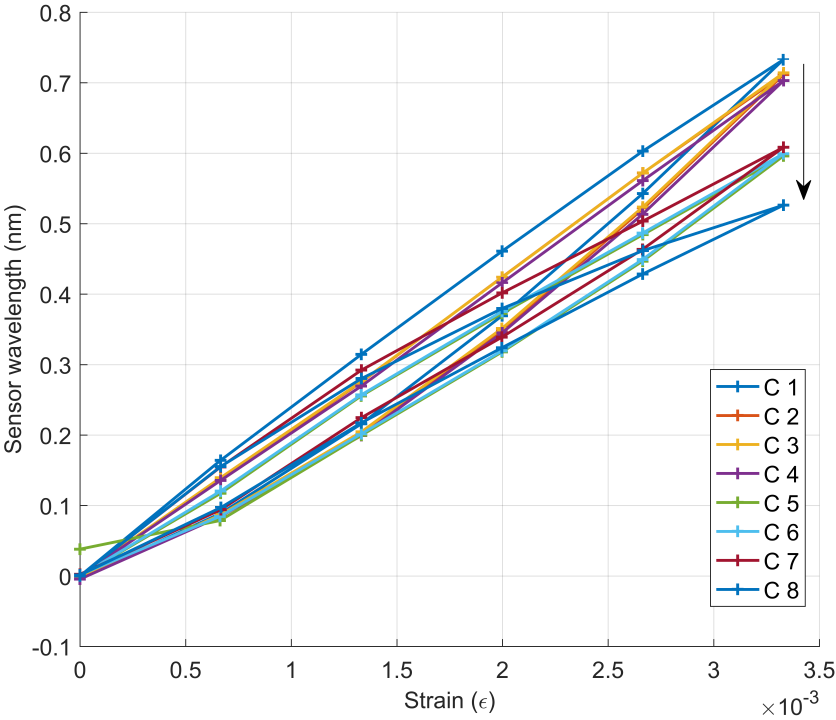


Fig. 9.16 Long term calibration evolution at $3.3 \text{ m}\epsilon$. The same sensor was calibrated up to $3.3 \text{ m}\epsilon$ 8 times, one cycle from each calibration is labelled C1-C8. In between some of the calibrations the sensor underwent multi-cycle tests like those described in Section 9.2. The overall trend is a decreasing strain sensitivity. Note wavelength offset of each cycle has been removed so that it is easier to compare the strain sensitivity.

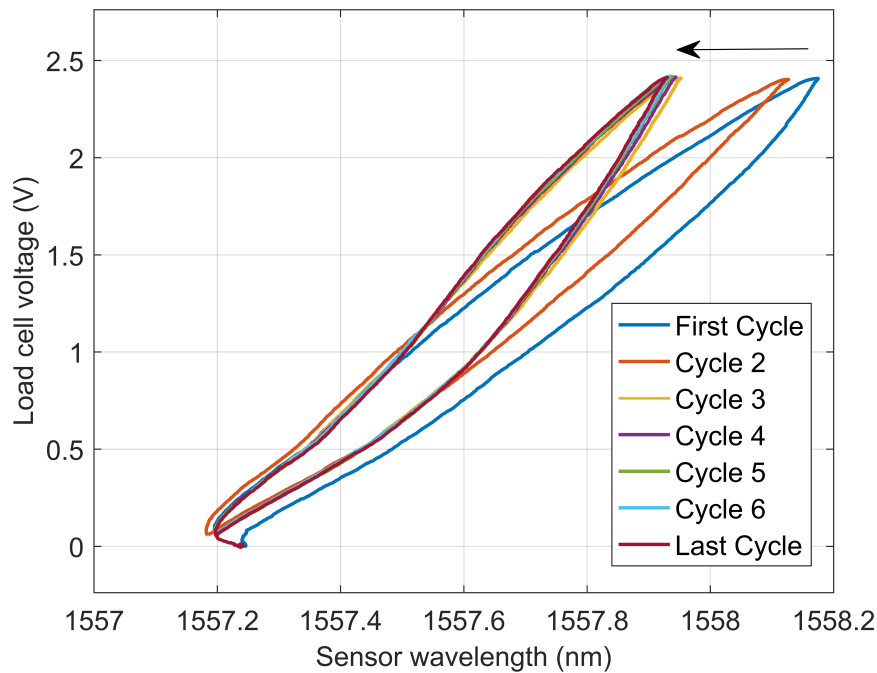


Fig. 9.17 Metal packaged sensor hysteresis loops during 100 cycles at 9 kN.

capillary, it could be expected that the sensor behaviour would be repeatable between sensors. As this is not the case the most likely component is the brazed joint between the capillary and the fibre. This is supported by the following observations:

- The hysteresis loop direction is opposite to that expected from tensile tests of visco-elastic and visco-plastic behaviour in a bulk material.
- The sensor wavelength decreases when the sensor is held at constant non-zero strain.
- Strain sensitivity of the sensor decreases over time.
- Tension in the interrogating fibre causes failure of the fibre-capillary joint.

The sensor wavelength is not an intrinsic measurement of the material that is deforming. Therefore, the sensor response can be expected to behave in the opposite manner when compared to direct strain measurement of the sensor component that has visco-elastic and plastic behaviour. This is due to the fibre being suspended from said sensor components. It is not clear whether it is the brazed material itself, the bond between the brazed material and the capillary or fibre, or possibly even deformation of the copper coating on the fibre. These problems will be difficult to prevent as they are properties of the key part of the sensor where strain is transferred from the

sensor package to the FBG. Therefore, a different solution to this problem is possibly required. Consistent fabrication of sensors would allow these effects to be characterised properly and as a repeatable period of operation has been demonstrated, the various effects could be compensated for.

9.5 Improving the sensor design

9.5.1 Altering the shim design

During calibration up to $7.2 \text{ m}\epsilon$ there were some failures of shim spot welds. An example of this can be seen in Figure 9.18, the sensor wavelength shows a large decrease after $6 \text{ m}\epsilon$ and this was caused by a spot weld near to the capillary failing. Therefore, an alternative shim design was proposed to prevent this happening. Stress on the spot welds is not uniformly distributed between the individual welds due to the asymmetric nature of the sensor package, this can be seen in Figure 5.31. The area of highest stress is close to the capillary at the extreme edges of the shim. The modified shim was shaped differently so that load on the leading edge of the shim was more evenly distributed. Additionally, the length of the shim was increased so that more spot welds could be fitted onto it. This resulted in the shim design seen in Figure 9.19. The gap between the shims decreased due to the use of longer shims and a longer length of capillary was not available at the time of testing. The new shim design was tested up to $7.2 \text{ m}\epsilon$, Figure 9.20. The spot welds of the shim did not fail so the design was an improvement in this respect. However, the wavelength still decreased after $4 \text{ m}\epsilon$ on the first cycle. This was due to movement in the joint between the capillary and the fibre.

9.5.2 Reducing stress at sensor end

Another problem that was only encountered during the field trials was a highly non-linear strain response. This was replicated and the results are shown in the first section of this chapter. The results demonstrated that the FBG was being stressed due the interrogating fibre outside the capillary becoming tensioned. In order to prevent this, the sensor end was strengthened by attaching a copper capillary with epoxy. This was tested using the same procedure as before, the fibre exiting the capillary was fixed to the specimen 15 cm from the sensor location. In this case the fibre was fixed so that no slack was present. This tested the strengthened fibre end with the worst case scenario that the fibre is already tensioned before a prestressing strand is stressed. The sensor wavelength response during loading was linear until the fibre failed above $6 \text{ m}\epsilon$, this can be seen in Figure 9.21. It should be noted that during normal instrumentation

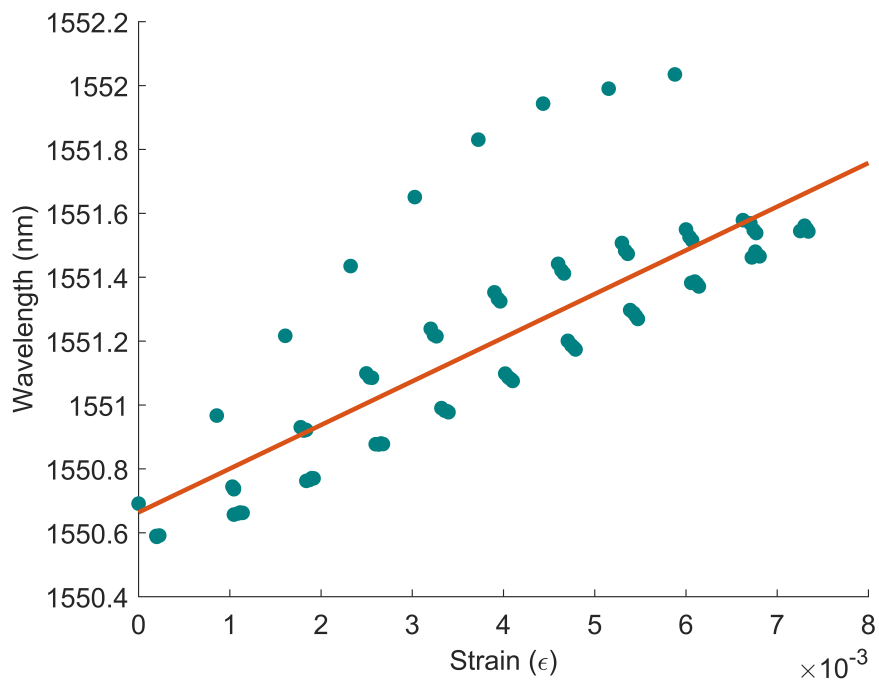


Fig. 9.18 Sensor with old shim design calibrated up to 7.2 $m\epsilon$. The sensor had a high sensitivity for the first force cycle until 6 $m\epsilon$ when some spot welds failed, resulting in a rapid decrease in wavelength.

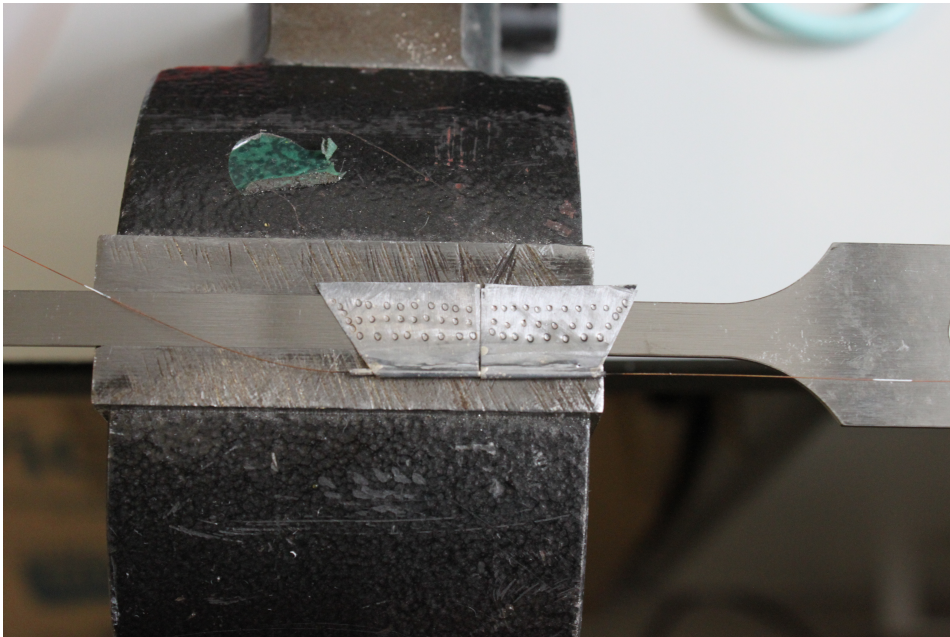


Fig. 9.19 Revised shim design, this helped distribute stress more evenly between the spot welds.

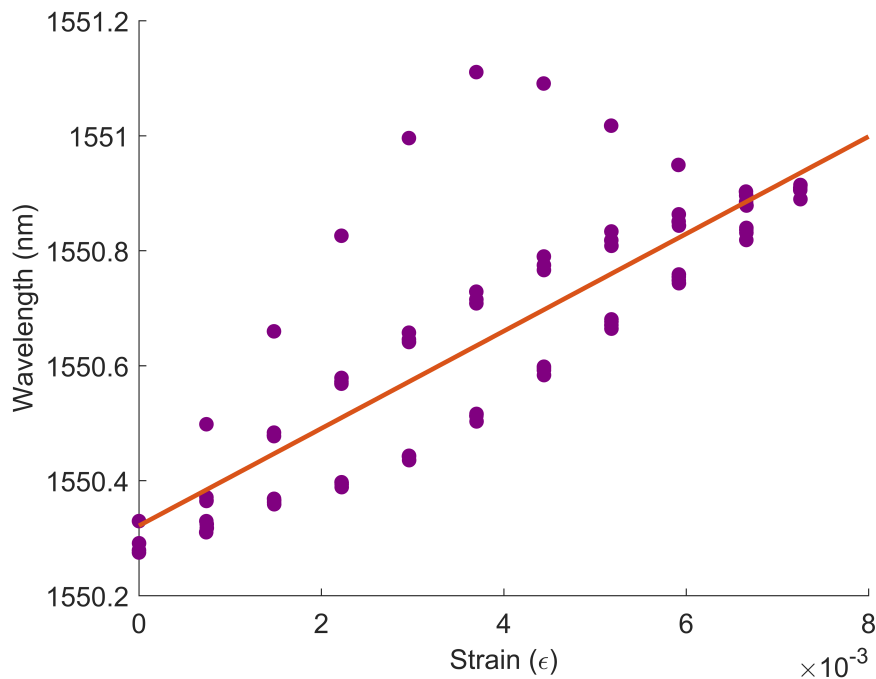


Fig. 9.20 Sensor with new shim design calibrated up to $7.2 \text{ m}\epsilon$

of a prestressing strand there would be some slack in the fibre before the strand is stressed. Therefore it is expected that the strengthened fibre end will allow the sensor to be isolated from strain in the interrogating fibre. This problem can be further mitigated by encasing the interrogating fibre inside a 2-4 mm diameter metal tube, allowing additional fibre length to accommodate strand elongation.

9.5.3 Fibre in metal tube

Adding an additional length of interrogating fibre between sensors would reduce the stress in the fibre at the end of the sensor by allowing the strand to elongate without stressing the interrogating fibre. The additional length of fibre needed can be simply calculated as the change in length of a particular strand section when the strain is $6.5 \text{ m}\epsilon$. It is proposed that the interrogating fibre between sensors is placed in a small diameter (2-4 mm) metal tube, with the tube being secured into the groove. The metal diameter must be large enough to allow enough to accommodate additional fibre, but small enough to not interfere with other strands or the duct wall. The fibre will sit loose inside the tube.

Figure 9.22 demonstrates the situation when enough additional fibre can be fed into the metal capillary. In case A, the specimen is in an unstressed state, while case B shows the

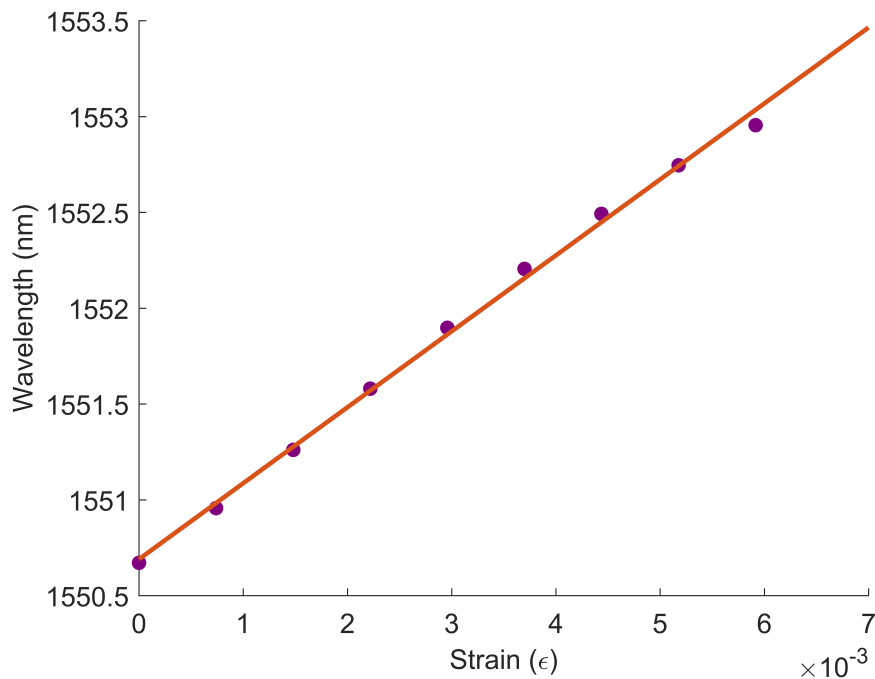


Fig. 9.21 Sensor with strengthened ends stress until failure.

specimen in a fully stressed state. The fibre slack has been removed due to the specimen elongation but the stress in the fibre remains negligible. The FBG in the fibre is to test the concept, in the real application there will be no sensors in these sections of fibre.

Method for testing the concept

The concept was tested on a tensile machine by measuring fibre strain inside a 2mm-diameter metal tube mounted on a steel specimen. The concept was tested with a 16 cm length of metal tube so that it would fit onto the high strength steel specimens available. This meant that to compensate for a specimen strain of $7\text{ m}\epsilon$, 1.12 mm of additional fibre had to be inserted into the tube. The testing procedure was as follows:

- The metal tube was fixed to a high strength steel specimen with epoxy.
- A fibre with an FBG written into it was inserted into the tube.
- The fibre was fixed at one end of the tube.
- FBG wavelength was recorded as the additional fibre length was manually inserted and removed from the metal tube. This gave a baseline for the FBG wavelength shift expected from stressing the specimen.

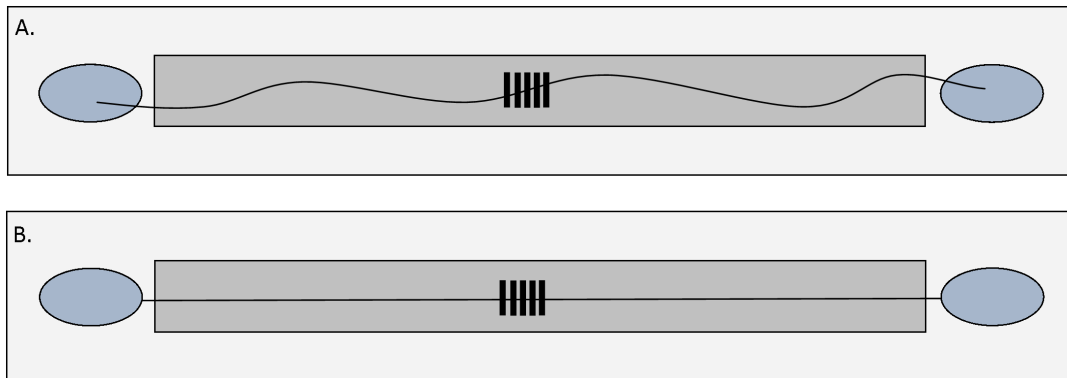


Fig. 9.22 Un-stressed, A, and stressed, B, fibre in a metal tube. The fibre between sensors should have some slack to allow for strand elongation when stressed. The concept was tested by monitoring fibre strain within the metal tube with an FBG.

- The fibre was secured at the other end of the tube with additional slack inserted.
- The specimen was subject to two step-profile force tests; one to 4.5 kN (3.3 m ϵ) and another to 9.8 kN (7.2 m ϵ). The FBG wavelength was recorded continuously during these tests.

With sufficient additional fibre fed into the metal the FBG wavelength was not expected to change significantly. The FBG wavelength change during stressing on the tensile machine was compared to the wavelength change when fibre was manually inserted into the tube. With no specimen elongation, fibre inside the metal tube will be under compression, therefore there will be a small decrease in FBG wavelength. When the specimen is fully stressed, the fibre should experience close to zero stress. Therefore, the FBG wavelength response will have a positive shift as the specimen is stressed, but this will be greatly reduced compared to an FBG that is securely attached to the specimen.

Results

The FBG wavelength when the fibre was manually inserted into the metal tube can be seen in Figure 9.23. The behaviour was as expected, the FBG wavelength decreased when fed into the tube showing that fibre is under compression. The wavelength shift was approximately 0.3 nm, therefore wavelength shifts in this range during the tensile machine stressing were assumed to be due to the fibre transitioning from a compressed to a non-compressed state.

Figure 9.24 shows the FBG wavelength compared to the tensile machine load cell force while stressing the specimen in steps up to 4.5 kN, equivalent to 3.4 m ϵ . There is correlation between the load cell force and FBG wavelength as expected. The maximum wavelength shift

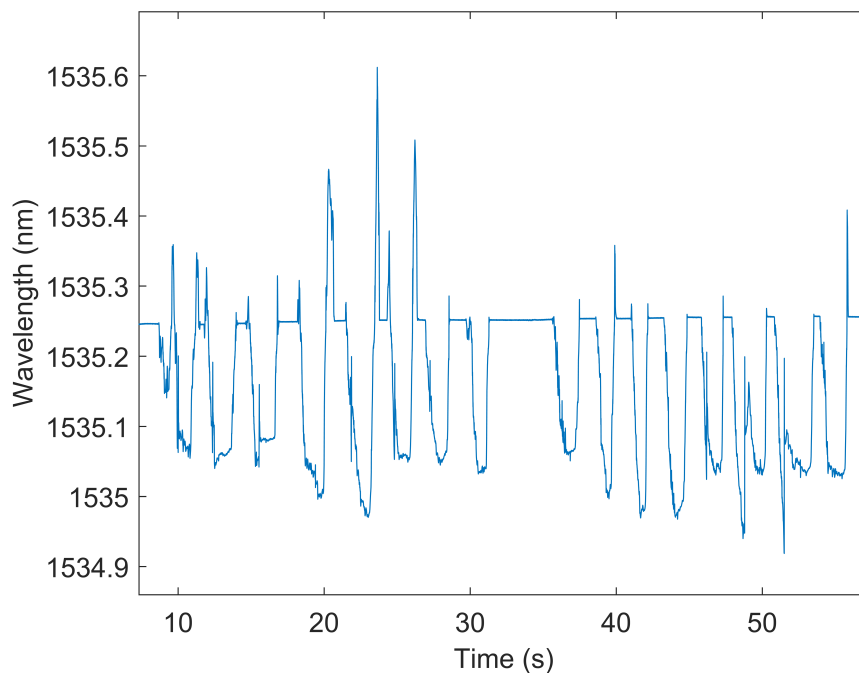


Fig. 9.23 Fibre manually fed into metal tube. The FBG wavelength decreases due to fibre compression, with a maximum shift of approximately 0.3 nm.

at 4.5 kN was approximately 0.25 nm, which was less than the wavelength shift when the fibre was manually inserted into the metal tube. As a comparison, an FBG epoxied directly onto the specimen would have a wavelength shift of approximately 4 nm at 4.5 kN.

When the specimen was stressed up to 9 kN, the metal tube became detached from the specimen at 6 kN. The metal tube was re-attached with stronger epoxy and the test was repeated. Figure 9.25 shows that the FBG wavelength change for the total force range was less than 0.1nm. This, like the previous test, was less than the maximum shift measured when the fibre was manually inserted into the metal tube. Therefore, these experiments demonstrate placing the fibre inside a metal tube can help to reduce stress in the interrogating fibre and better isolate the strain sensor.

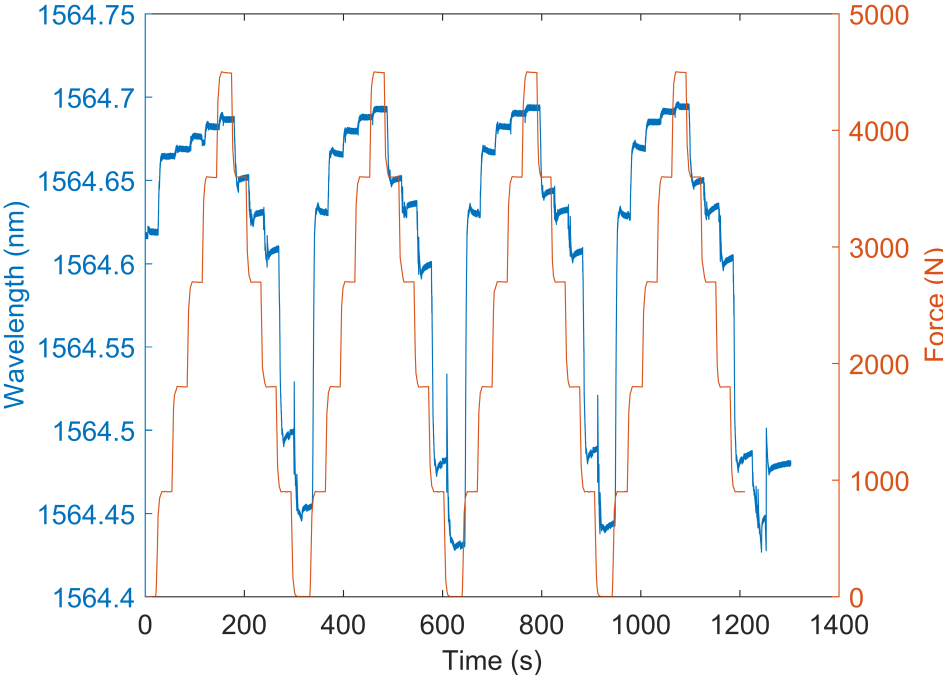


Fig. 9.24 Testing the fibre in metal tube up to 3.2 mε. The FBG wavelength showed correlation with the load cell as expected but the maximum wavelength shift was within the 0.3 nm range from manually inserting the fibre.

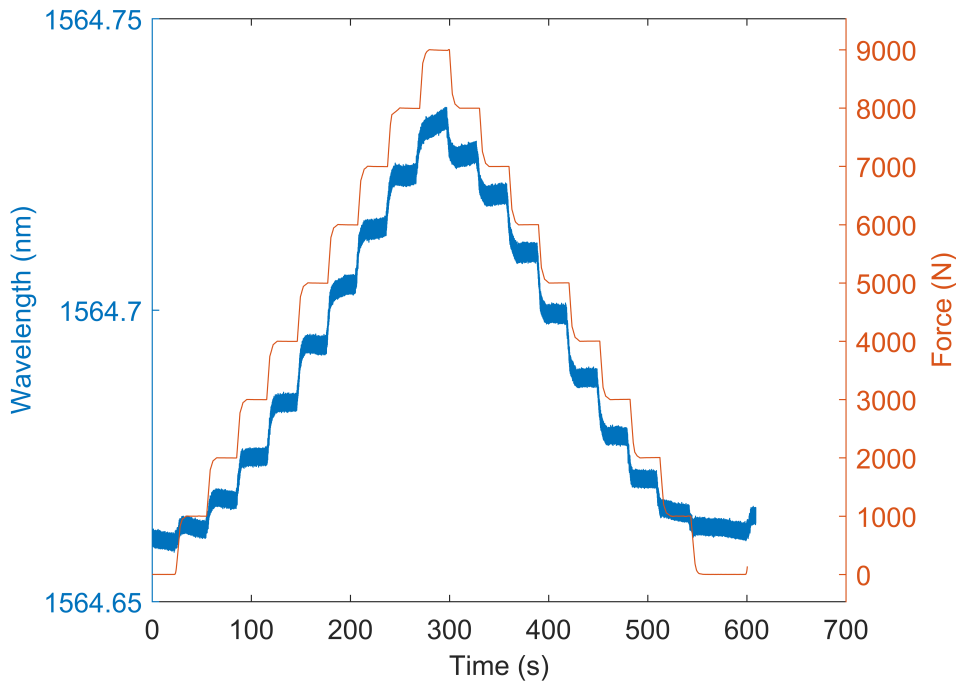


Fig. 9.25 Testing the fibre in metal tube up to $6.7 \text{ m}\epsilon$. The FBG wavelength shifted by less than 0.1 nm for a strain of $6.7 \text{ m}\epsilon$, showing that there is enough additional fibre in the metal tube to compensate for the specimen elongation.

9.6 Summary

The sensors were subjected to stress cycling and long term calibration on a tensile machine. These experiments confirmed that the joint between the fibre and capillary is insufficient to withstand the applied stresses of this application. A variety of non-linear material phenomena were observed. If the sensors were able to be fabricated consistently, these effects could be characterised and compensated for in the field. However, currently the fabrication process produces mixed results due to the number of variables and the somewhat unpredictable flow of the molten brazing paste.

During the two tests where prestressing strands were involved, the sensors displayed a non-linear response and permanent wavelength shifts. These effects were only seen when sensors were attached to prestressing strands and were determined to be because of elongation of the interrogating fibre stressing the sensor end causing the joint between the capillary and fibre to fail. This is an important issue as it will affect any type of FBG sensor attached to the prestressing strands in series. It was remedied by strengthening the end of the sensor with an additional copper capillary. In addition to strengthening the sensor end, it was demonstrated

that placing additional interrogating fibre inside a metal tube reduces stress in the fibre. Finally, a revised shim was designed to prevent spot welds from failing near the capillary where they are subject to higher stress.

Chapter 10

Deploying the optical system on a working nuclear site

Chapters 5-8 have laid out the majority of the work required to implement Bragg grating sensors in an operational containment vessel. While the particular sensor design has shown issues with wavelength repeatability, the practical details of sensor installation can be readily applied to any FBG strain monitoring system. This chapter will describe the stages of installing the system on an operational containment vessel with a focus on the additional stages that have not yet been described. The majority of the additional steps are in instrumenting the strands as they will be significantly longer than those tested previously.

10.1 Number of sensors

Individual sensors are to be fabricated as described in Section 5.4. The number of sensors needed for each strand may vary due to the differences in strand length, the spatial resolution requirements and whether force profile of the strand is being measured. At least 6 sensors are needed to resolve the 'M' shape force profile due to duct friction, although more than 9 sensors, with 3 on each section of the 'M' profile will provide better accuracy as the force gradients can be fitted with at least 3 data points.

The number of measurement points is also somewhat dependent on strain transfer and the interrogator bandwidth. For a strain transfer of 10-20 %, at $7 \text{ m}\epsilon$ a wavelength shift of 0.8-1.6 nm can be expected. In addition to this we might expect shifts from temperature variations of $20 \text{ }^\circ\text{C}$ and 10 years of neutron and gamma radiation to cause shifts of approximately 0.25 nm. A conservative estimate would be to allow 3 nm bandwidth per sensor, this would give 6 nm per temperature-compensated strain measurement allowing 15 strain measurement points per

fibre line for a 90 nm bandwidth, which is typical of commercial interrogators. This would be more than adequate for monitoring one strand per interrogator channel.

10.2 Instrument prestressing strand

It is likely that the prestressing strands being instrumented will be over 30 metres in length, this requires a proper methodology to instrument them. Before their installation, the correct length of strand is wound onto a drum approximately 2.5 metres in diameter for transportation. To instrument these strands it is proposed that the strand is wound from one drum to another placed 10 metres away. The straight length of strand will rest on stools to allow it to be instrumented. The fibre and sensors will be attached in sections with the newly instrumented section of strand wound onto the new reel. This can take place outside of the main reactor building.

The strand instrumentation will proceed as follows. The first strain sensor is spliced at each end to a long length of metal coated fibre. This sensor is attached to the section of the prestressing strand. The strand will be cleaned by light abrading and application of solvent at the sensor locations prior to sensor attachment. Five metre sections of 2-4mm diameter metal tube are threaded onto the fibre up to the end of the sensor, the sections of metal tubing are epoxied into the strand groove. The fibre can be thread through the 5m metal tube sections by attaching it to a small diameter rod for guidance. Additional fibre must be inserted into each section of metal tube to allow for elongation of the prestressing strand. Once each section is secured the strand is wound further onto the new drum. As the strand is wound onto the drum it is covered in grease to protect against corrosion.

Temperature sensors will be placed inside a double metal capillary as this has been shown to isolate the FBG from strain [148]. They will then be placed loose inside the metal tubes that are fixed to the prestressing strands. Once all the sensors and metal tubing have been fixed to the strand the fibre will be glued to the very end of the strand. Reinforced fibre similar to that seen in Figure 5.19 will not be spliced onto the metal coated fibre until the strand has been pulled through the duct because the strand must move past other strands and will potentially come into contact with the duct surface.

10.3 Calibration

Both temperature and strain sensors will be calibrated in an environmental chamber before being attached to the prestressing strands. The temperature coefficient measured in the chamber will be valid for the temperature sensors as they are isolated from strain. While for the strain

sensors, chamber calibration will provide a baseline for when they have been spot welded to the strands. Attachment to the prestressing strands will increase the temperature coefficient by the thermal expansion of the steel taking into account the sensor strain transfer.

After attachment the strain sensors will be further temperature calibrated according to Section 5.6.1 using the portable induction heating setup. Additionally, every time the strand is placed in a different location, the strain and temperature sensors will be monitored for a number of hours. This will allow the induction temperature calibration procedure to be confirmed with stable temperature measurements at several points along the calibration curve.

Strain sensors will be strain calibrated using the procedure detailed in Section 5.6.3:

- Sensors are to be strain calibrated on a tensile machine before they are attached to the prestressing strands, providing an initial calibration and checking that the sensor response is consistent.
- Once sensors are attached, the prestressing strand is to be bent around several cylinders of different radii. Cylinders with radii between 9 and 1.29 m are required to obtain strain measurement points between 1 and 7 $m\epsilon$.
- The sensor calibration can be confirmed when the instrumented strands are finally stressed inside the PCC or PCPV by comparing the sensor response to the load cell, taking into account the expected friction.

10.4 Installing strands in concrete vessel

For standard telecomms fibre, strands must be located at least one metre from the reactor liner. Radiation resistant fibre may be used to allow monitoring of ducts nearer to the liner, however this fibre must be tested thoroughly beforehand. It may be possible to use currently empty ducts to install the instrumented strands. As this would be untested territory for the reactor operator, installing the strands in empty ducts will reduce the risk associated with this new activity. Risk is reduced in the following ways:

- Instrumented strands will be surplus to the requirements of stressing the vessel, therefore it would not be essential that they were stressed to 1300 MPa.
- Strands do not have to pass others that are already in place, significantly reducing the risk of sensor or fibre failure.

- Interstrand friction and interaction would not occur allowing duct friction to be investigated more easily.
- A demonstration of the type will increase confidence that the strands can provide adequate prestress levels and prestress monitoring.

Instrumented strands will be inserted into the tendon ducts in a similar way to normal prestressing strands. The new strand is welded to the old de-stressed strand, the old strand is then pulled out of the duct from the opposite end until the new strand is located in place of the old one. Once in place, the reinforced interrogating fibre can be spliced to the metal coated fibre and fixed to the end of the strand. The strand must be at least one metre longer than a standard strand to accommodate the fibre protection at the end and that the epoxy must have cured before stressing can begin. Splicing interrogating fibres to both ends of the fibre system will provide some redundancy to the sensor interrogating fibre system. Sensors could also be placed on several fibre lines per strand, allowing some sensors to be interrogated in the event of a fibre breakage.

10.5 Stressing the strand

The reinforced fibre cable is thread through the stress jack and the jack is placed onto the strand. Before the wedges are placed in the barrels to anchor the strands at the correct stress, several stress cycles will be carried out to calibrate the strain sensors. This was completed during the concrete beam field trial, see Chapter 7. Two different stress jacks have been tested in the field trials and both were able to stress the strands without failure of the interrogating fibre at the stressing jack jaws. A mono-strand stress jack was used to stress the instrumented strands in the concrete beams, while a 28-strand stress jack was used on the calibration rig, as described in Chapters 7 and 8. It is expected that the fibre protection will work with other stressing jacks, but this must be tested beforehand.

10.6 Monitoring strand stress with the sensors

During installation locating the sensor interrogator and laptop/PC in the stressing gallery will aid sensor checks and allow the stressing to be monitored allowing parameters such as peak threshold detection to be adjusted quickly. Once the instrumented strands are stressed to the required level, the interrogator and PC must moved be to a permanent location. Optical fibre will need to be secured in the stressing gallery and properly routed to the required location.

Chapter 11

Structural information from sensor data

The primary use of the strain sensor data is to determine the prestress load in the tendons; from this the total prestress load on the concrete vessel can be calculated. If the vessel is under the minimum design load either the reactor pressure must be decreased or the prestressing tendons can be re-stressed. Once data has been acquired for a few months it can be used to predict the date at which the prestress level will drop below the minimum design load. This chapter will describe how this can be achieved and why using a rigorous mathematical procedure, such as Bayesian analysis, is beneficial for this type of application.

11.1 Bayesian data analysis

Generally in structural health monitoring the aim is to determine the state of a structure from measurements carried out on that structure. The property of interest of the structure is not normally directly measured, for example to detect if a structure is damaged it is necessary to infer this from measurements of strain, displacement or force. These measurements or observations are assumed to determine the state of the structure according to a proposed engineering model. However, in the real world the structural observations and models are often uncertain. For example, Section 2.3.2 showed that concrete creep and shrinkage models could have strain errors of up to 20 %. Bayesian inference sets out a rigorous mathematical framework to incorporate uncertainty in the model and measurements. At a more fundamental level, the state of a system is a logical inference based on observations and the prior knowledge of the system, and how these relate to its state through a model [149]. Therefore, Bayesian inference is well suited for use in SHM.

Bayes' theorem can be written as [149]:

$$P(\boldsymbol{\theta}|y) = \frac{P(y|\boldsymbol{\theta})P(\boldsymbol{\theta})}{P(y)} \quad (11.1)$$

In this case, the notation is defined in terms of parameter identification. The probability of the values of a set of parameters, $\boldsymbol{\theta}$ given the data, y is equal to: the probability of the data occurring given the values of the parameters multiplied by the prior knowledge of the values of the parameters. Bayes' theorem relates the quantity of interest, the probability of the values of $\boldsymbol{\theta}$, with a term that can be calculated more easily, the probability that the data is observed if the values of $\boldsymbol{\theta}$ are true [150].

The right-hand term in the numerator of Equation 11.1 is the prior probability: the knowledge of the parameters before experimental data has been gathered. The left-hand term is called the likelihood of the data, this updates the prior probability of the parameters with experimental measurements. The likelihood for a set of n uncorrelated measurements is:

$$P(y|\boldsymbol{\theta}) = \prod_{i=1}^n P(y_i|\boldsymbol{\theta}) \quad (11.2)$$

This is the product of the likelihood of individual measurements. The term on the denominator is called the evidence, it is a normalisation constant and is obtained by summing over all possible scenarios. The evidence can be ignored in some cases, including parameter estimation, as it does not depend explicitly on the hypothesis [150].

11.2 Bayesian temperature compensation

Temperature and strain sensors are calibrated before attachment to the prestressing strands. This is carried out in an automated environmental chamber ensuring the temperature of the sensors is very close to that of the temperature reference. Therefore, this calibration is more accurate than the calibration procedures developed to calibrate sensors in-situ. This section describes a rigorous mathematical procedure to temperature calibrate the strain sensors whilst they are attached to the prestressing strands and measuring strand strain. It takes into account the prior knowledge of the temperature coefficient measured in the environmental chamber. The main advantages of this procedure over conventional temperature compensation are:

- Once installed the strain sensor temperature sensitivity may be different from the prior calibration due to effects such as concrete and anchor plate thermal expansion.
- The procedure results in one mechanical-strain value and one temperature sensitivity coefficient per sensor per day.

- The strain sensor temperature sensitivity can be tracked during the experiment, giving an indication of sensor degradation.
- Each parameter is represented by a Gaussian probability distribution with associated mean and variance.

The procedure provides a single value of each parameter per day to check, which simplifies the monitoring. If there is an anomalous wavelength reading for one day this can be investigated further by looking into the raw data. Additionally, the temperature coefficient of the strain sensor can be tracked over time giving an indication if the sensor is reducing in sensitivity. Before the procedure is described, the sensor measurements and how they relate to the temperature compensation model must be described in detail.

11.2.1 Temperature compensation model

The overall aim of the temperature compensation is to remove any temperature influence from the strain sensor reading. The wavelength measured by the strain sensor is dependent on mechanical and thermal strain as well as the intrinsic temperature dependence of the strain sensor. This is given by the following relationship [149]:

$$\hat{\lambda}(t) = \lambda_0 + \alpha(\hat{T}(t) - T_0) \quad (11.3)$$

The parameter λ_0 is the sensor wavelength without temperature influence and is therefore directly proportional to the mechanical strain, ε through the sensors strain transfer coefficient. While any temperature influence on the sensor is given by the change in temperature ($\hat{T}(t) - T_0$) multiplied by the sensors unknown temperature sensitivity, α . The strain sensor wavelength, λ_i and temperature, T_i determined by measurements from the sensors at time t_i are related to the physical wavelength, $\hat{\lambda}$ and temperature, \hat{T} by:

$$\begin{aligned} \lambda_i &= \hat{\lambda}(t_i) + g(\sigma_\lambda) \\ T_i &= \hat{T}(t_i) + g(\sigma_T) \end{aligned} \quad (11.4)$$

where $g(\sigma_\lambda)$ and $g(\sigma_T)$ are the wavelength and temperature error represented by zero mean uncorrelated Gaussian noise. The relationship between parameters and observations is non-linear as the standard deviation of the temperature noise depends on α . It is, however, convenient to assume that noise is independent of α . This results in a linear Gaussian model where temperature, T is a dependent variable of $\hat{\lambda}$. This can be written in matrix form as [151]:

$$\hat{\lambda}(T; \lambda_0, \alpha) = \begin{bmatrix} 1 & (T - T_0) \end{bmatrix} \begin{bmatrix} \lambda_0 \\ \alpha \end{bmatrix} + \begin{bmatrix} g \end{bmatrix} = \mathbf{X}\boldsymbol{\theta} + \mathbf{g} \quad (11.5)$$

Where $\boldsymbol{\theta}$ is a vector of the parameters, X is a vector of the dependent measurements and g is the error of each measurement. Equation 11.5 can be solved by finding the linear fit, where λ_0 is the intercept and α is the gradient.

11.2.2 Parameter identification

The temperature compensation proceeds as follows:

- Sensor data is grouped for each day.
- Temperature sensor wavelength is converted to a change in temperature $\Delta T = T - T_0$, where T_0 is the temperature at the start of the experiment.
- Prior distributions are assigned to the parameters λ_0 and α , that take the form of Gaussian distributions with $Norm\{\boldsymbol{\mu}, \boldsymbol{\sigma}^2\}$.
- The linear fit to the data was calculated as the maximum likelihood estimate (MLE) of a multivariate Gaussian distribution with mean $\boldsymbol{\mu}_{y|\boldsymbol{\theta}}$ and covariance matrix $\boldsymbol{\Sigma}_{y|\boldsymbol{\theta}}$. The covariance matrix was of the form $\sigma_y^2 I_n$ where I_n is the identity matrix:

$$I_n = \begin{bmatrix} 1 & 0 \\ 0 & 1 \end{bmatrix} \quad (11.6)$$

implying that observations are uncorrelated and with variance, σ_y^2 . Provided this is the case and that a uniform prior is assumed for the parameters, the MLE is equivalent to minimising the sum of square residuals which is given in matrix form by:

$$\begin{aligned} \boldsymbol{\Sigma}_{y|\boldsymbol{\theta}} &= (\mathbf{X}^T \mathbf{X})^{-1} \sigma_y^2 \\ \boldsymbol{\mu}_{y|\boldsymbol{\theta}} &= \mathbf{X}^+ \mathbf{y} \quad \mathbf{X}^+ = (\mathbf{X}^T \mathbf{X})^{-1} \mathbf{X}^T \end{aligned} \quad (11.7)$$

Where y is the strain sensor observations, X is a matrix of the temperature observations of the same form given in Equation 11.5 and σ_y^2 is the variance of the MLE for the observations.

- Finally the prior and likelihood distributions are combined using Bayes equation to give the posterior mean and covariance matrix for the parameters¹:

$$\begin{aligned}\Sigma_{\theta|y}^{-1} &= \Sigma_{y|\theta}^{-1} + \Sigma_{\theta}^{-1} \\ \mu_{\theta|y} &= \Sigma_{\theta|y} \left(\Sigma_{y|\theta}^{-1} \mu_{y|\theta} + \Sigma_{\theta}^{-1} \mu_{\theta} \right)\end{aligned}\tag{11.8}$$

The assumptions of the algorithm are:

- Strain does not change significantly during one day.
- Temperature sensors correctly measure temperature changes.
- Gaussian noise assumption is valid for this application.
- Temperature change in one day is sufficient to fit the temperature coefficient.

11.2.3 Temperature compensation results

The algorithm was applied to the sensors in the field trial described in Section 7. The parameters λ_0 and α for the same strain sensor as Figure 7.14 are shown in Figure 11.1. The results show that the change in wavelength over the entire experiment was 60 pm, which is the same for both compensation methods. The temperature coefficient was relatively consistent throughout the experiment, however there was a small downward trend, suggesting there may have been a decrease in the temperature sensitivity of the strain sensor. This may also have been due to the decreased temperature difference during one day in the latter part of the experiment. This caused the parameter estimation to have a larger variation from day 100 onwards, as seen clearly for both λ_0 and α .

For this reason, the temperature compensation was applied to 2-day data windows for comparison, the results show that both λ_0 and α have less variation, see Figure 11.2, which is confirmed by the standard deviation from the parameter identification shown in Figure 11.3. Following this, the extreme case would be to identify the sensor parameters from the complete dataset. However, this would result in a single measurement of λ_0 which is not useful for this application as the decrease in strain would be averaged out. Therefore, for this algorithm there is a trade off between the number of strain measurements and the temperature variation in a given data window during the experiment. A small temperature variation will cause the fitting to have a large variance.

¹This is the result of combining two Gaussian distributions with known variance.

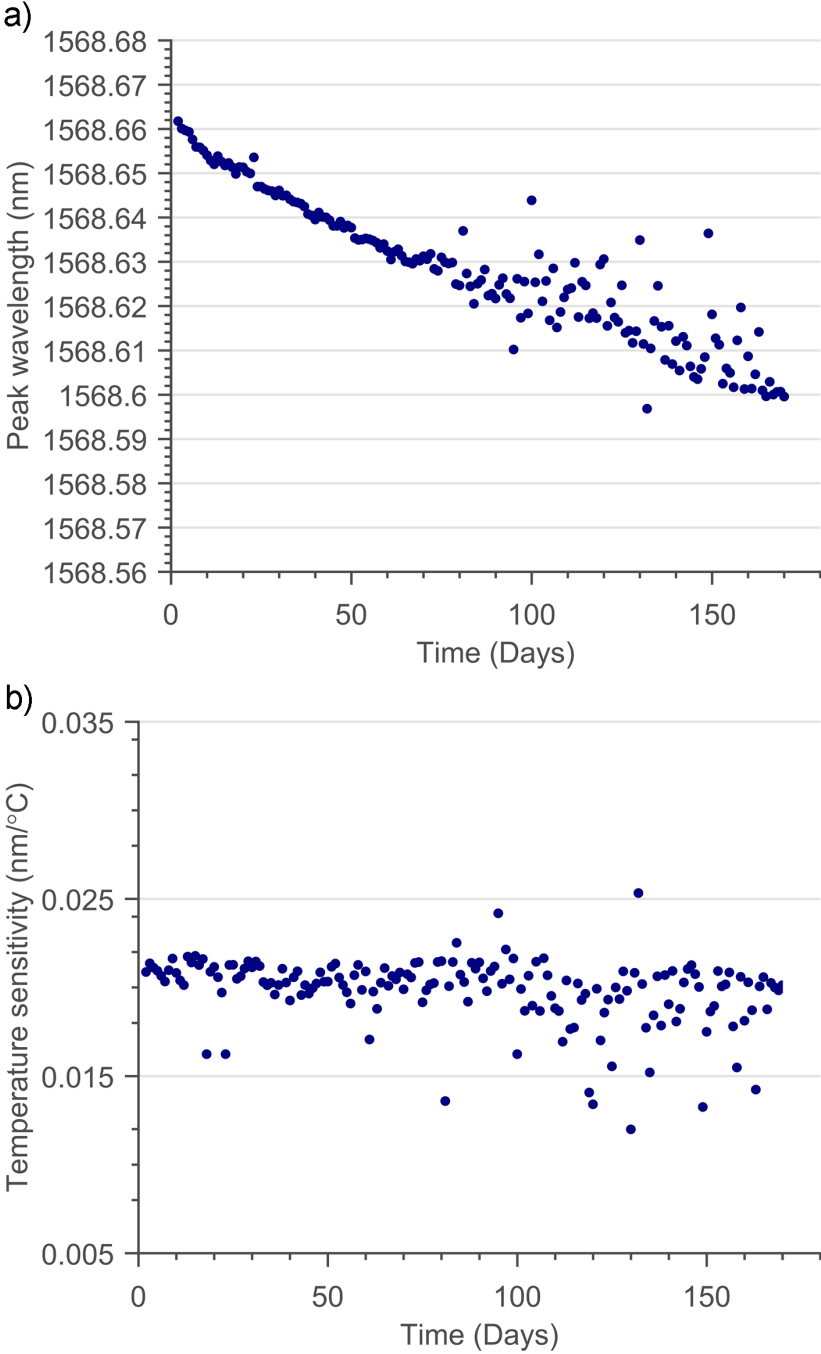


Fig. 11.1 Parameters λ_0 , a) and α , b) calculated from data windows of one day.

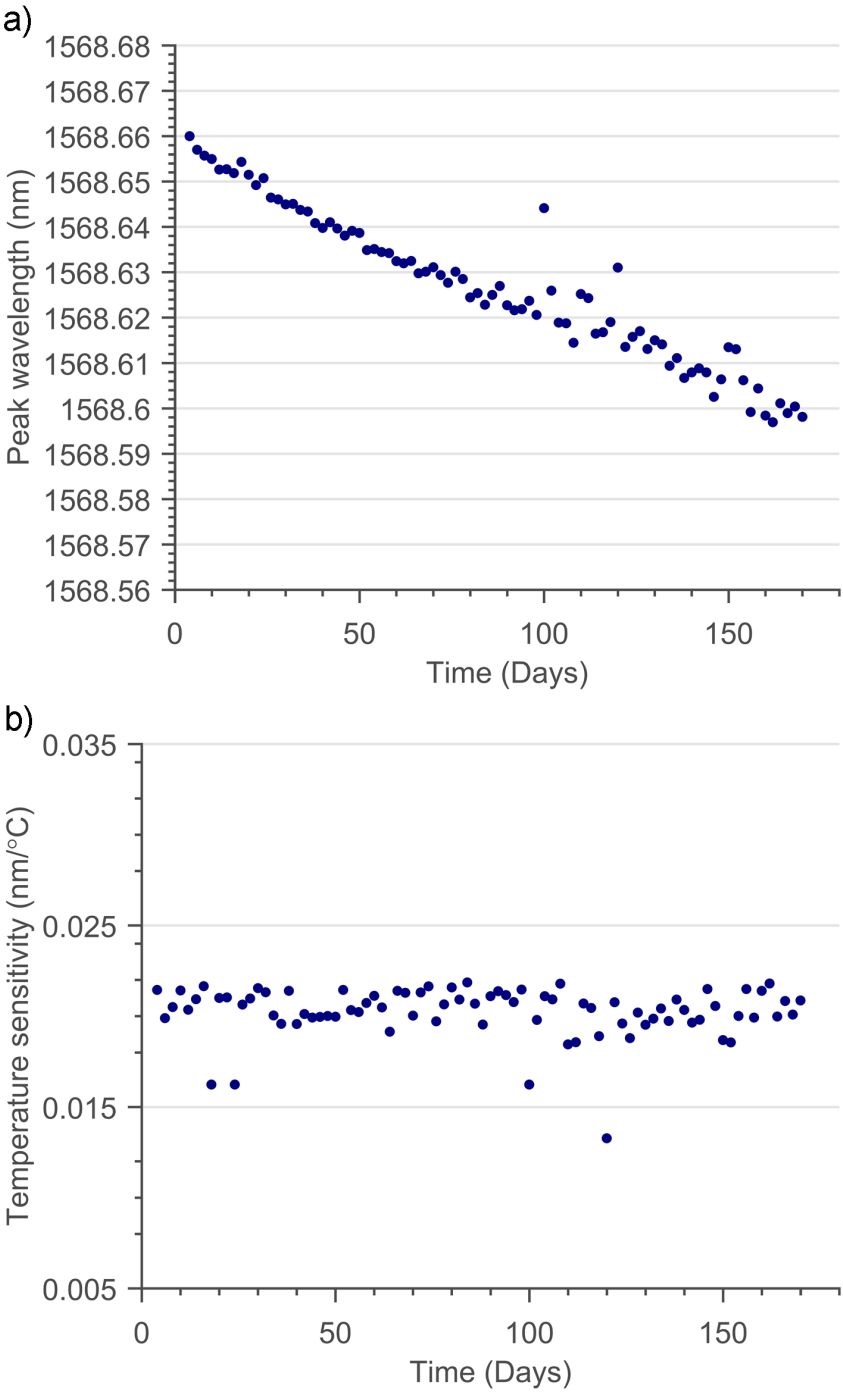


Fig. 11.2 Parameters λ_0 , a) and α , b) calculated from data windows of two days.

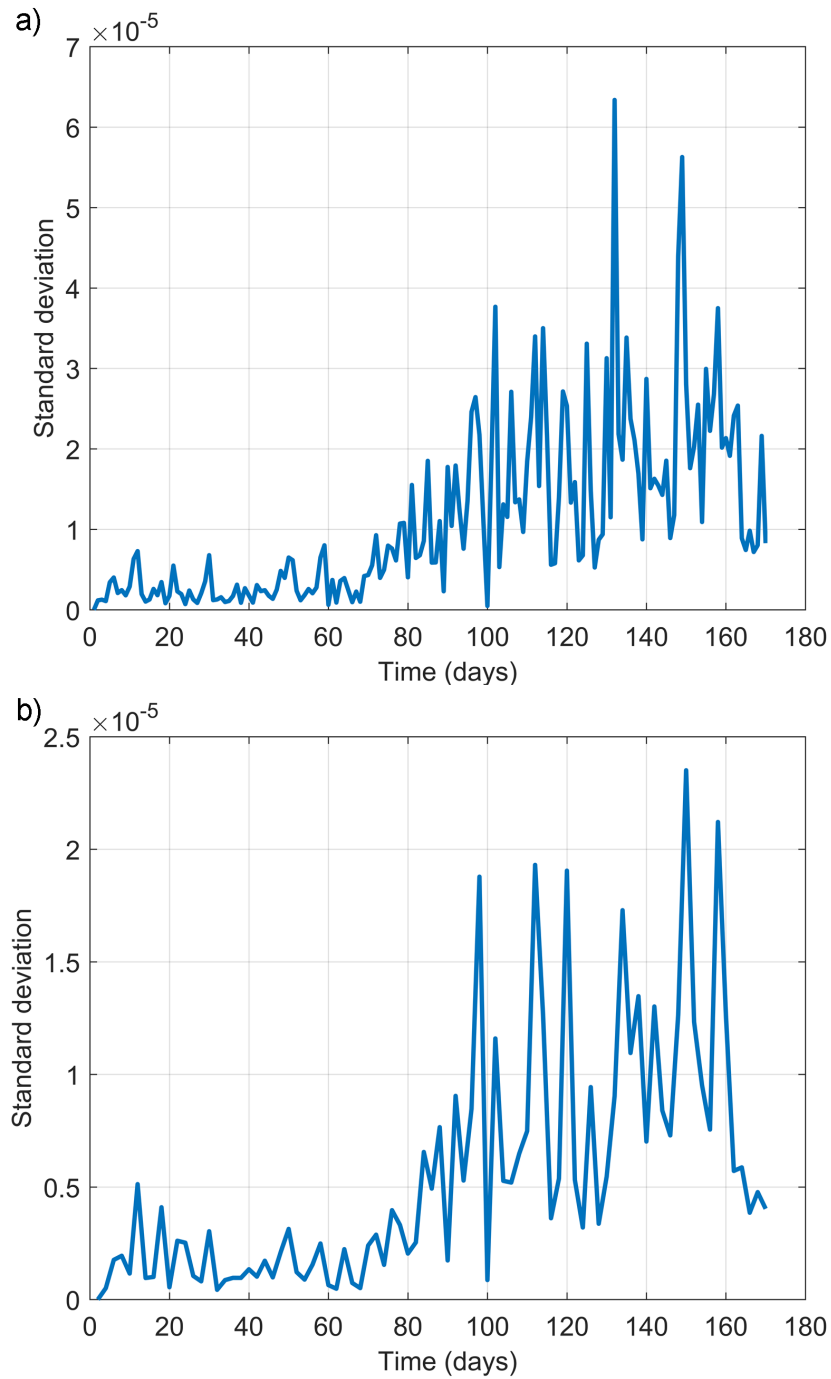


Fig. 11.3 Standard deviation for λ_0 measurements from temperature compensation. a) The error when taking one-day windows of data, while b) shows error from two-day windows of data. The error in the λ_0 measurements, which is directly proportional to ϵ_0 , is smaller when the parameters are determined from two day windows of data.

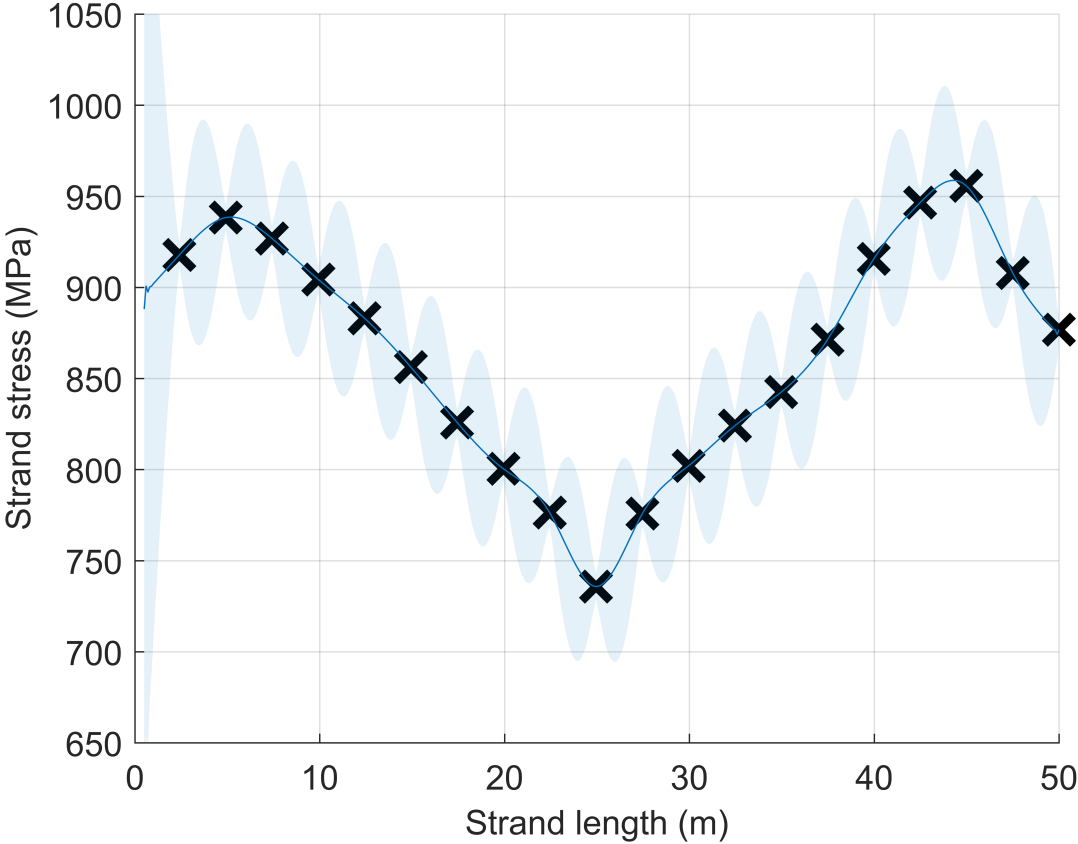


Fig. 11.4 Distributed strand force profile with 20 measurements. The shaded area is the error in the interpolation. The error is lower where there is a measurement point, as expected. The standard deviation of each measurement has been arbitrarily set to 5 kN in this example.

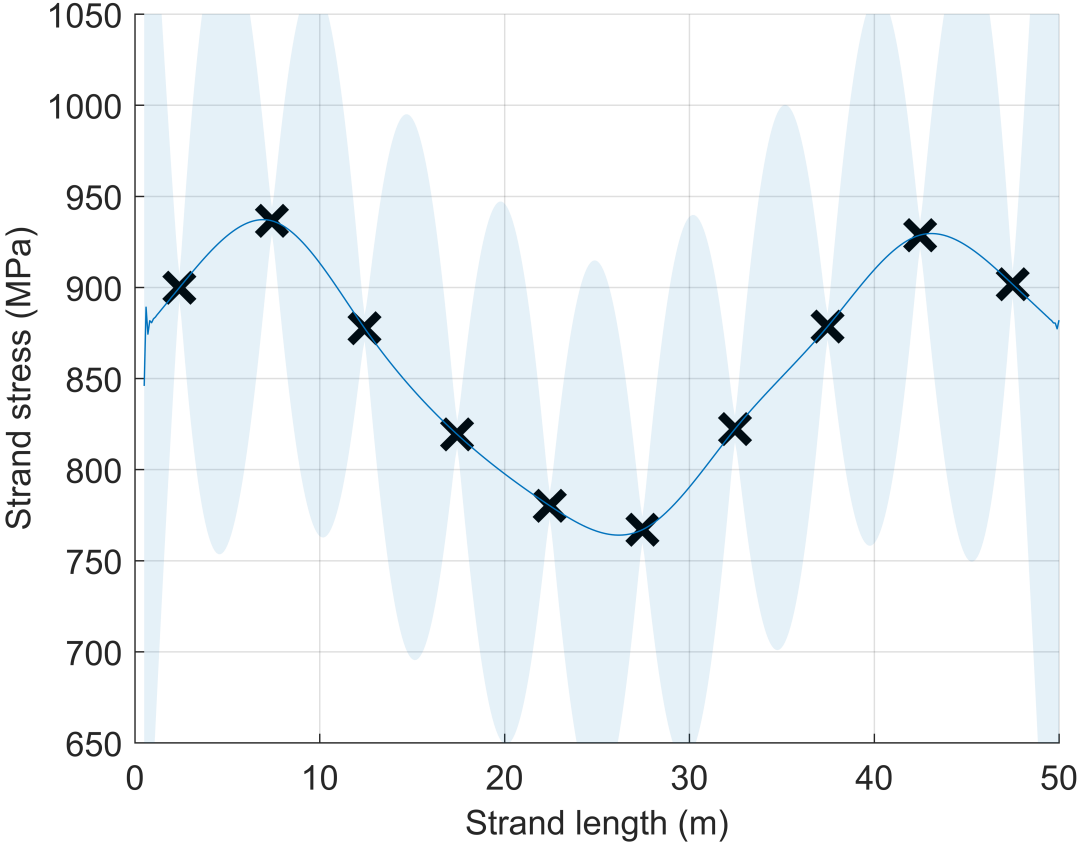


Fig. 11.5 Distributed strand force profile with 10 measurements. When compared to 11.4 there is larger uncertainty due to fewer measurements along the strand. The standard deviation of each measurement has been arbitrarily set to 5 kN in this example.

11.4 Sensor fusion and model fitting

As noted in Section 2.3.2, concrete creep and shrinkage models can vary significantly from experimental results. This was seen in the prestressed concrete beam experiment detailed in Chapter 7. Figure 11.6 shows the CEB model prediction for prestress loss compared to the force measured by an FBG strain sensor and a load cell for one of the prestressing strands in the straight-duct concrete beam. In order to predict prestress loss more accurately, it is possible to adjust the model as sensor data from the structure of interest becomes available. First, the load cell and FBG strain sensor measurements will be combined, taking into account their relative measurement errors.

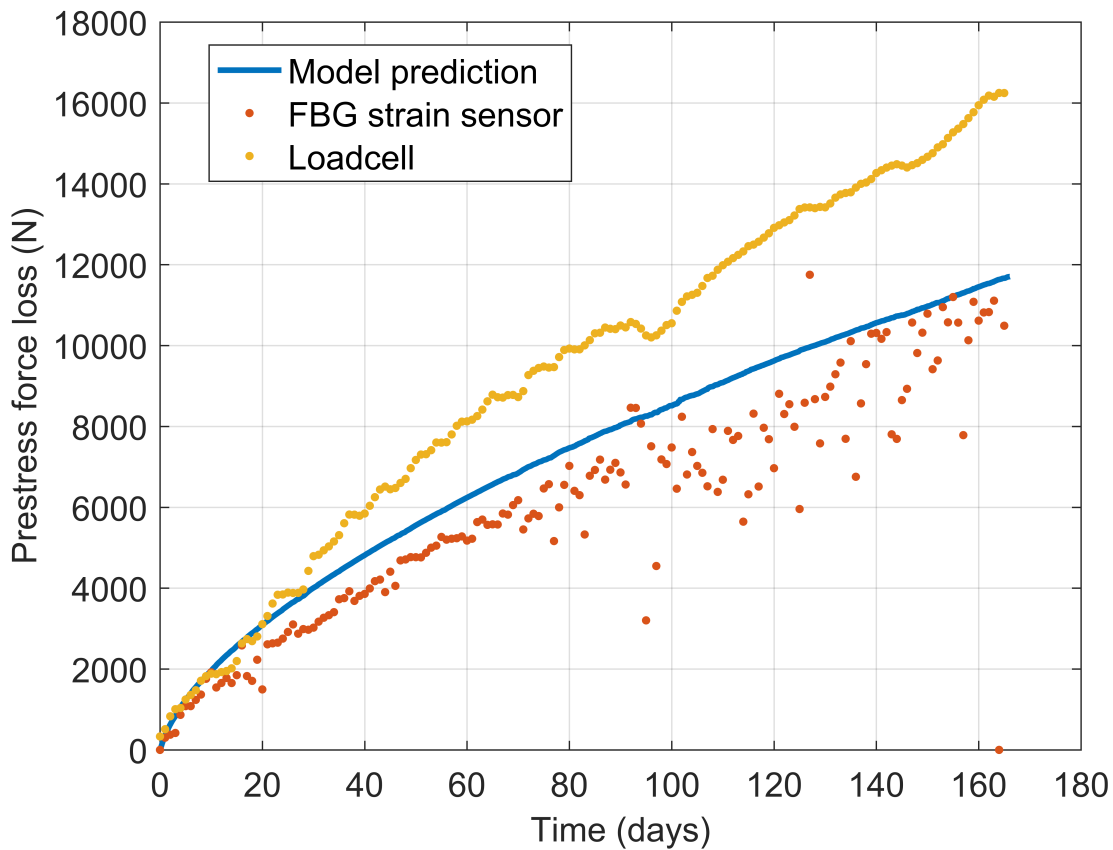


Fig. 11.6 Model prediction of prestress loss compared to an FBG strain sensor and a load cell measuring the same prestressing strand

11.4.1 Sensor fusion

This problem is often termed 'sensor fusion'; the aim is to combine data from multiple sources with different errors [96]. This presentation is based on Murphy, 2012 [153]. Adopting a Bayesian approach, the posterior mean $p(\mu|D)$ of the combined sensor measurements D is:

$$p(\mu|D) \propto p(\mu)p(D_x|\mu, \lambda_x)p(D_y|\mu, \lambda_y) \quad (11.13)$$

Where D_x and D_y are data from the two different measurement devices. The precisions of both devices can be integrated out, by marginalisation, as follows:

$$p(\mu|D) \propto p(\mu) \int p(D_x|\mu, \lambda_x)p(\lambda_x|\mu)d\lambda_x \int p(D_y|\mu, \lambda_y)p(\lambda_y|\mu)d\lambda_y \quad (11.14)$$

The priors assigned to the mean and precisions are $p(\mu) \propto 1$, $p(\lambda_x|\mu) \propto 1/\lambda_x$ and $p(\lambda_y|\mu) \propto 1/\lambda_y$. As the x and y terms are symmetric, the following focusses on the x term. With a Gaussian likelihood, the posterior distribution can be shown to be:

$$p(\mu|D) \propto \int \lambda_x^{-1} (\lambda_x)^{n_x/2} \exp\left(-\frac{n_x}{2}\lambda_x(\bar{x} - \mu)^2 - \frac{n_x}{2}\lambda_x s_x^2\right) d\lambda_x \quad (11.15)$$

Where $s_x^2 = 1/n \sum_{i=1}^n (x_i - \bar{x})^2$. Equation 11.15 is proportional to the integral of an un-normalised Gamma density:

$$Ga(\lambda|a, b) \propto \lambda^{a-1} e^{-\lambda b} \quad (11.16)$$

Where $a = n/2$ and $b = \frac{n}{2}((\bar{x} - \mu)^2 + s_x^2)$. Therefore the integral in Equation 11.15 is proportional to the normalising constant of the Gamma distribution, $\Gamma(a)b^{-a}$. Remembering there are two sets of measurements, x and y , the posterior is proportional to:

$$p(\mu|D) \propto \left(\frac{n}{2}((\bar{x} - \mu)^2 + s_x^2) \frac{n}{2}((\bar{y} - \mu)^2 + s_y^2)\right)^{-n/2} \quad (11.17)$$

The Bayesian temperature compensation algorithm, Section 11.2, was applied to the load cell and FBG strain sensor measurements, resulting in one measurement each per day. These were then combined using Equation 11.17. Figure 11.7 shows the posterior distribution of combining the load cell and FBG strain sensor data for each day during the experiment. Within the first 20 days of the experiment both measurements are similar, this results in a narrow distribution, with a high amplitude, as seen in Figure 11.7. As the two data sets begin to differ, the end result is more uncertain. Load cell measurements were assigned a smaller standard

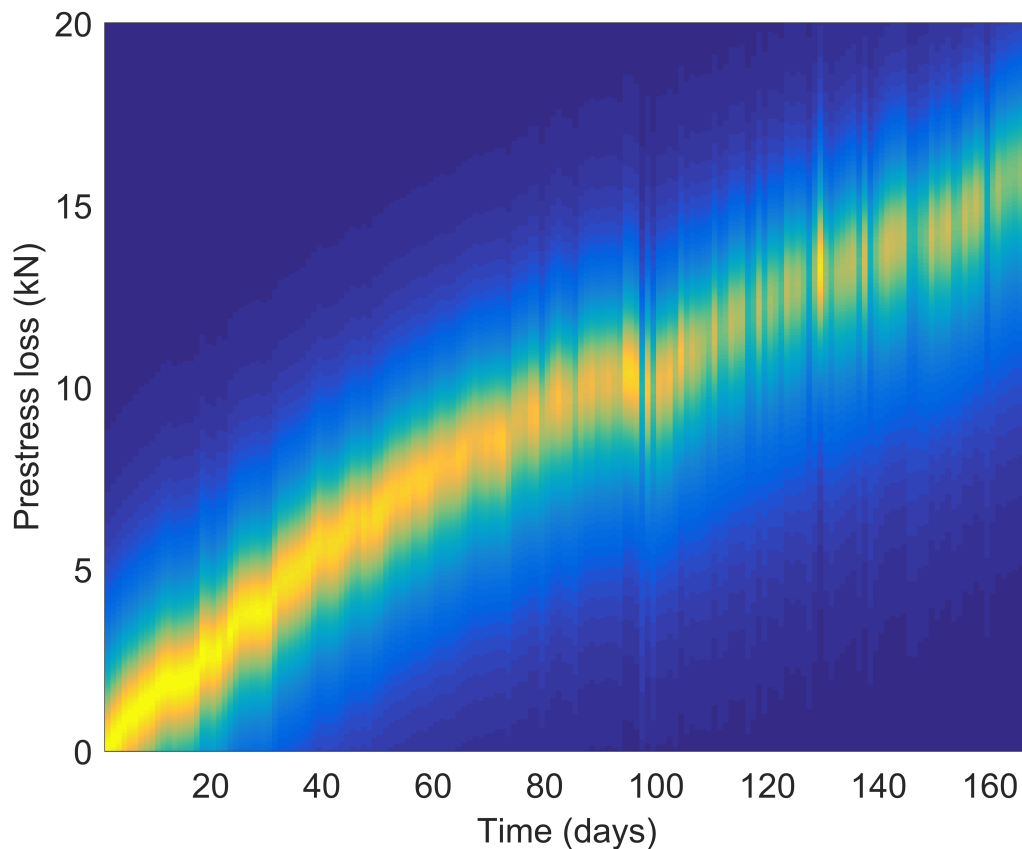


Fig. 11.7 Load cell force measurements combined with FBG strain sensor measurements. The graph shows the probability distribution of the combined measurements for each day. For a given day, the MLE is the force with the largest amplitude (closest colour to yellow); The MLE can be seen in Figure 11.8 for reference. The load cell measurements were assigned a smaller measurement error, therefore when the two sets of measurements are combined, they have a larger weighting.

deviation during the analysis to account for the inaccurate calibration of the FBG strain sensor². Consequently, the load cell measurements are weighted more heavily in the output of the sensor fusion; the overall trend in Figure 11.7 follows that of the load cell measurements.

²Details of the FBG strain sensor calibration can be found in Section 7.5.

11.4.2 Fitting the prestress loss model to experimental data

Prestress loss in a prestressing strand can be described by a combination of concrete creep and shrinkage³. The following simplified equations from the CEB model⁴ were adjusted to fit the experimental data. Prestress loss due to creep at time t after prestressing at time t_0 is given by:

$$F_{creep}(t) = A_{ps} \frac{E_s}{E_c} \phi_0 \left(\frac{t - t_0}{\beta_H + (t - t_0)} \right)^{0.3} \quad (11.18)$$

Where A_{ps} and E_s are the cross sectional area and modulus of elasticity of the steel strand. E_c is the modulus of elasticity of the concrete, β_H is the humidity constant and ϕ_0 is the notional creep coefficient. Prestress loss due to shrinkage at time t after curing at time t_c is given by:

$$F_{shrinkage}(t) = A_{ps} E_s \epsilon_{cs0} \left(\frac{t - t_c}{350 \left(\frac{V/S}{(V/S)_0} \right)^2 + (t - t_c)} \right)^{0.5} \quad (11.19)$$

Where V/S is the volume to surface ratio in mm, $(V/S)_0$ is a constant equal to 50 mm and ϵ_{cs0} is the shrinkage coefficient. The notional creep coefficient ϕ_0 and the shrinkage coefficient ϵ_{cs0} can be fitted to the MLE of the combined sensor measurements shown in Figure 11.7. The equation describing this is simply:

$$F_{MLE}(t) = \phi_0 a(t) + \epsilon_{cs0} b(t) \quad (11.20)$$

Here the constants in Equations 11.18 and 11.19 have been gathered together into $a(t)$ and $b(t)$ respectively. Now all that remains is to use least squares fitting to find the values of ϕ_0 and ϵ_{cs0} that fit the experimental data. Figure 11.8 shows the model fitted to the MLE of the sensor fusion results. This approach can be implemented as soon as sensor measurements are recorded, therefore it can be used to predict the prestress loss at a given time in the future. As more sensor measurements are gathered the prediction will become more accurate. This can help indicate the time at which the prestress levels reach the minimum design load.

³In the case of the experiment described in Chapter 7 steel relaxation was negligible because large prestress loss due to wedge draw-in resulted in strand stresses below 40 % UTS.

⁴The equations are described in their complete form in Appendix A.1 and A.2

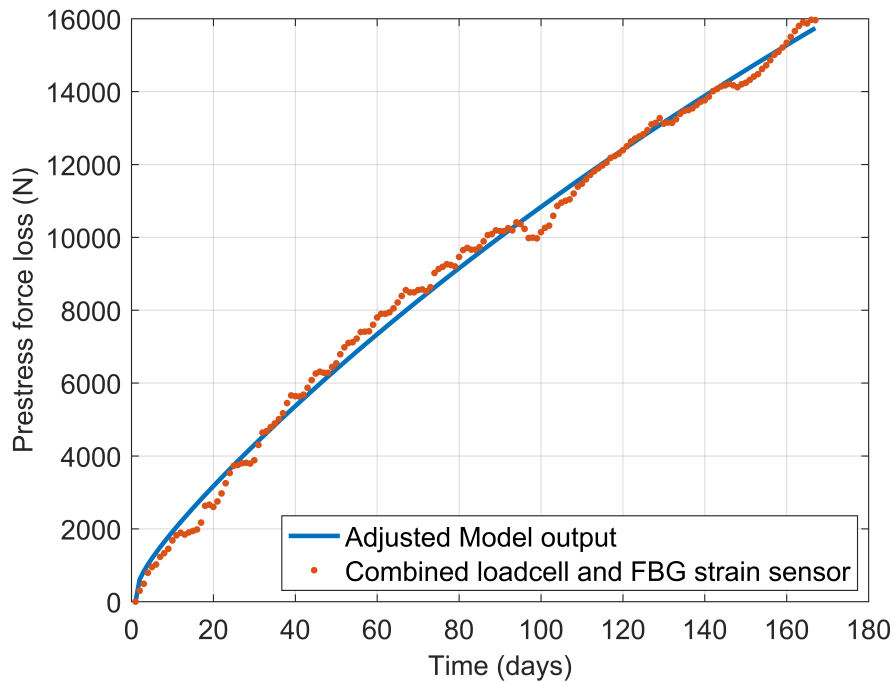


Fig. 11.8 Concrete model fitted to the combined prestress loss measurements.

11.5 Summary

This chapter presented three mathematical procedures based on Bayesian analysis that facilitate the primary goal of the fibre optic system in determining prestress levels in the PCC or PCPV and predicting the date at which the prestress level will fall below the minimum design load. A temperature calibration procedure to calibrate strain sensors after installation and during operation was developed. This is useful as a sensor's temperature sensitivity may be different when it is installed, due to the thermal expansion of the structure. It also allows the temperature sensitivity to be monitored over time, potentially providing an indication of sensor degradation. Reconstruction of a strand force profile was demonstrated through interpolation of simulated distributed sensor measurements. Finally, strain sensor and load cell measurement were combined and the prestress loss model was adjusted to fit the experimental data collected in Chapter 7, providing a prediction of the prestress loss evolution over time that can be updated as more data becomes available.

Chapter 12

Conclusion and further work

12.1 Conclusion

A fibre optic sensor system with metal packaged strain and temperature sensors for monitoring prestress levels in a prestressed concrete containment (PCC) or prestressed concrete pressure vessel (PCPV) has been developed and tested in this project. An online monitoring system like this could replace existing prestress inspections and provide additional benefits because prestress loss would be monitored remotely and continuously providing an early indication of prestress levels. It would also allow distributed force measurements which are not currently possible. Post-tensioned prestressed concrete is not unique to nuclear reactors; therefore, this technology could be applied to other structures such as bridges, dams and oil tanks.

In the PCPV concrete shielding of neutron and gamma radiation allows standard metal coated SMF-28 fibre to be used up to one metre from the reactor lining. Temperature and strain sensors were fabricated from copper coated fibre by induction brazing type I fibre Bragg gratings into kovar capillaries. The Curie transition of kovar at 430°C protected the gratings from the high temperature needed to melt the brazing solder to form a bond between the fibre and capillary. The strain sensors were attached to the prestressing strands with 0.5mm steel shims via resistance spot welding.

Sensors were temperature calibrated, before attachment to the strands, in an environmental chamber. This calibration is adequate for the temperature sensors, while strain sensors require further calibration once attached due to the thermal expansion of the prestressing strands. Two in-situ techniques were developed for this: an active heating method where the strand section around the sensor was induction heated, and a passive method where sensor wavelengths were recorded during ambient temperature fluctuations. Sensors calibrated by these methods were able to replicate, within the error, calibration coefficients obtained in the environmental

chamber. During a comparison with one sensor, the temperature sensitivity determined by the induction heating and room temperature methods were $14.9 \pm 1.5 \text{ pm}/^\circ\text{C}$ and $15.3 \pm 0.9 \text{ pm}/^\circ\text{C}$ respectively, and the calibration in the environmental chamber was $15.9 \pm 0.6 \text{ pm}/^\circ\text{C}$. Defect screening during environmental chamber calibration was able to identify faulty sensors. A strain calibration procedure has been proposed which includes the following stages: sensors should initially be calibrated before attachment to the prestressing strands. To determine the strain transfer coefficients and check the spot weld attachment of the sensors, the strands should be bent around several cylinders with different diameters to obtain consistent measurement points of the full strain range. A final calibration check can be performed when the strand is installed in the containment building and stressed.

In this project, the fabricated metal packaged strain sensors were attached to high strength steel and calibrated up to 3.3 and 7.2 mε (680 and 1400 MPa) with consistent wavelength response during 3 cycles. They had strain transfers in the range of 10-20 %, with a lower sensitivity when calibrated to a higher strain. When calibrated up to 7.2 mε, the temperature compensated strain resolution and accuracy was found to be approximately 18 and 35 με, respectively for a 1 pm resolution and accuracy interrogator. Strain resolutions of the order of 10s nε are required as a reactor nears the end of its lifetime, therefore a high resolution (femtometre) interrogator is required for this application. The strain sensor wavelength also displayed hysteresis; this and the decreasing strain sensitivity for increasing strain were attributed to viscoelastic behaviour in the sensor. The direction of the hysteresis loop was opposite to that expected during tensile tests of a bulk material, leading to the conclusion that the viscoelastic behaviour originated from the fibre-capillary joint.

To test the sensor system in realistic conditions, prestressing strands were instrumented with sensors and stressed within two prestressed concrete beams. The strain sensor wavelength was non-linear, during stressing, when compared to strand force measured at the ends of the concrete beams by load cells. The source of the non-linear behaviour could have been due to several different effects, including uneven force distribution of individual wires in the prestressing strand or the tensioned fibre at the end of the capillary affecting the FBG. Sensors that survived stressing were able to monitor temperature and strain for the duration of the 170 day experiment. A second field trial determined, through comparisons with epoxied FBGs, that the non-linear wavelength response of the strain sensors was not caused by non-uniform force distribution of individual wires in a strand. The field trial also demonstrated improved fibre protection on the prestressing strands.

The non-linear wavelength response during the two field trials was investigated in the lab and identified as the fibre at the capillary end becoming tensioned and causing failure of

the fibre-capillary joint. This was remedied by strengthening the end of the sensor with an additional copper capillary and tested with a sensor showing a linear response up until the interrogating fibre failed.

Several strain sensors were tested extensively on a tensile machine with stress cycling and long term strain calibration. The results showed that the sensor wavelength displays a variety of non-linear behaviour including permanent wavelength shifts, decreasing strain sensitivity over time and the sensor adjusting to higher strain during the first stress cycle. These effects were attributed to an inadequate bond between the fibre and metal capillary for the stress levels applied in this application. Consistent sensor fabrication would allow these effects to be characterised and compensated during the prestress monitoring, however the fabrication process is currently inconsistent due to the number of variables and the somewhat unpredictable flow of the molten brazing paste.

Uncertainty in measurements and the complexity of the PCPV/PCC mean that including uncertainty in sensor data analysis is important. Bayesian data analysis is a framework capable of this and was used for a temperature compensation algorithm that also allows the sensor temperature sensitivity to be tracked. The results of the temperature compensation were comparable to the conventional method. Also presented was a method to interpolate the force between sensor measurements and fit a concrete model to the experimental data. This type of data analysis could aid engineers when making important decisions about the structures as they provide an uncertainty with each result and allow the information obtained from a prestress monitoring system to be presented in a clear manner.

The specific strain sensor design investigated during this project was not able to meet the requirements for monitoring prestress loss of prestressing strands in terms of sensor measurement consistency. The application would also benefit from an improved strain sensitivity so that the expected strain changes near the end of a reactors' life can be resolved. However, this would place higher stress on the fibre capillary joint and cause the sensor wavelength response to be more inconsistent. Nevertheless, the experimental results and information gathered during this project will facilitate the development of an improved prestress monitoring system. Provided a different strain sensor design is able to reliably measure up to $7 \text{ m}\epsilon$ and fit within the prestressing strand grooves, it can be readily used with the calibration procedures in Chapter 5, deployment strategy laid out in Chapter 10 and data analysis in Chapter 11.

12.2 Further work

There are a number of factors that need to be investigated before the fibre optic system described in this thesis can be applied on a working reactor.

12.2.1 Sensor fabrication

Sensor fabrication must become more consistent if the metal packaged sensors are to be used for this application. Sensor hysteresis and creep are inevitable when measuring such a high stress and strain and the large majority of strain sensors will exhibit these characteristics [106]. However, if sensors are fabricated consistently these characteristics can be properly characterised, compensated for and will not lead to inaccurate strain measurements. Currently, the results of sensor fabrication are somewhat unpredictable, therefore sensors must be characterised individually. Consistent sensor fabrication may prove difficult with the current induction heating set up due to the nature of the process. If the brazing process could be automated and brazing took place in a controlled inert atmosphere, then potentially the fibre-capillary joint consistency could be improved.

The current sensor design would also benefit from metal coated FBGs. This would provide an additional layer of protection for the FBG which would be beneficial for strengthening the FBG section which is weaker than the fibre itself. Metal coated FBGs were not commercially available during this project, however they are now available from Technica with a gold recoating [154]. The composition of the brazing paste would need to be altered to optimise bonding with gold, but the extra protection may prove beneficial. Fibres are now commercially available with several different metal coatings including gold and aluminium; these may also improve the performance of the strain sensors.

12.2.2 Different sensor design

Tests with epoxied FBGs in this project have shown that they have a high strain sensitivity and linearity, suggesting that a sensor whose principal attachment between the fibre and sensor package is epoxy may perform better than the current design at these strain levels. A sensor package would be necessary to reduce the stress on the FBG and it must be hermetically sealed; metal sealing techniques may still be useful for this.

12.2.3 Radiation, humidity and corrosion

If sensors are to be used closer than one metre to the reactor liner they will need to be characterised under neutron and gamma radiation¹. Additionally, the effect of radiation on the temperature and strain sensitivity of the sensors should be investigated. Relating to this, it needs to be confirmed that the sensors strain sensitivity is not different for different temperatures. It would also be prudent to test sensors that have been subject to accelerated corrosion testing to confirm that this does not adversely affect sensor responses. All of these tests should be carried once the sensors can be strain characterised in a repeatable manner.

12.2.4 Strain calibration by bending

The calibration procedure proposed in Section 5.6.3 needs to be tested properly. Calibrating the sensors by bending the strands around a set radius has not been tested experimentally; this needs to be investigated to ensure that it is a valid method to strain calibrate the sensors.

12.2.5 Fibre in metal tube

The test to reduce the stress in the interrogating fibre was carried out on a short length of metal tube, therefore this must be tested on longer tubes to check if it is possible to feed enough fibre into the tube. For example, an elongation of approximately 7 cm is expected for a 10 metre length of tube. Several smaller lengths of tube between sensors may be needed for long prestressing strands. The metal tube will be wound around the prestressing strand and attached to the groove. Due to the strand geometry, the metal tube will compress against the prestressing strand upon stressing, further securing it.

12.2.6 Strand instrumentation procedure and final field trial

An instrumentation procedure for instrumenting the long strand lengths that are required in a PCC or PCPV was detailed in Chapter 10. The procedure must be tested to determine if it is practically feasible and to determine the time and resources needed for such an activity. The test could coincide with a demonstration of the technology being installed in one of the empty ducts on a PCC or PCPV. A demonstration like this would test the instrumented strands in conditions that are very close to the final application.

¹Radiation resistant FBGs have become commercially available recently [155]. These would be beneficial if the sensors are to be placed within one metre of the reactor lining

12.2.7 Grouted ducts

The instrumented strands developed in this project may have a greater benefit for containments where the tendons are grouted into the ducts. It is not possible to use the lift off technique on grouted tendons and the instrumented strands could provide measurements of these tendons. The tendons are sheathed in a polyethylene sleeve and the duct is filled with the grout at high pressure, therefore tests must be carried out with the instrumented strands to determine whether the fibre and sensors can survive the additional disturbance.

12.2.8 Sensor Interrogating system

Although beyond the scope of this thesis, interrogator resolution and accuracy also play an important role in the absolute accuracy of the strain sensors. If the sensor response repeatability is improved the interrogator will become the limiting factor in both resolution and accuracy. Interferometric interrogators have shown strain resolutions in the region of nano-strain and may provide improvements in sensor accuracy if proper thermal stabilisation can be achieved [146].

References

- [1] Nuclear Power in the United Kingdom |UK Nuclear Energy - World Nuclear Association, September 2017.
- [2] K. Kharecha and J. Hansen. Coal and gas are far more harmful than nuclear power. *Climate Change: Vital Signs of the Planet*, April 2013.
- [3] S. J. Mihailov. Fiber Bragg Grating Sensors for Harsh Environments. *Sensors*, 12(12):1898–1918, February 2012.
- [4] M. Perry, P. Niewczas, and M. Johnston. Effects of Neutron-Gamma Radiation on Fiber Bragg Grating Sensors: A Review. *IEEE Sensors Journal*, 12(11):3248–3257, November 2012.
- [5] Uranium Enrichment | Enrichment of uranium - World Nuclear Association.
- [6] F. Carre and G. Fiorini. Status of the Generation IV Initiative on Future Nuclear Energy Systems, March 2011.
- [7] M. Perry. *Optical Fibre Sensors for Monitoring Prestressed Concrete Structures in Nuclear Power Plants*. PhD thesis, University of Strathclyde, June 2013.
- [8] W. Hannum, G. Marsh, and G. Stanford. Smarter use of nuclear waste. *Scientific american*, pages 84–91, December 2005.
- [9] Licence condition handbook. Technical report, Office for Nuclear Regulation, February 2017.
- [10] *Fundamentals of Prestressed Concrete Design*. Prestressed Concrete Institute., 2 edition, 1968.
- [11] R. M. Megahid, A. S. Makarious, and M. A. El-Kolaly. Attenuation of reactor thermal neutrons in a bulk shield of ordinary concrete. *Annals of Nuclear Energy*, 8(2):79–85, 1981.
- [12] J. M. Verbeke, C. Hagmann, and D. Wright. Simulation of neutron and gamma ray emission from fission and photofission. *Lawrence Livermore National Laboratory, Livermore CA, UCRL-AR-228518*, 4:40, 2010.
- [13] A. Aminian and M. R. Nematollahi. Determination of shielding parameters for different types of concretes by Monte Carlo methods. volume 38 of 50, Turkey, 2007. International Nuclear Information System.

- [14] *Defence in depth in nuclear safety: a report*. Number 10 in INSAG. International Atomic Energy Agency, Vienna, 1996.
- [15] D. Darwin, A. Scanlon, P. Gergely, A. G. Bishara, H. L. Boggs, M. E. Brander, R. W. Carlson, W. L. Clark Jr, F. H. Fouad, M. Polvika, and others. Cracking of concrete members in direct tension. *J. Am. Concr. Inst*, 83(1):3–13, 1986.
- [16] X. H. Vu, Y. Malecot, and L. Daudeville. Strain measurements on porous concrete samples for triaxial compression and extension tests under very high confinement. *The Journal of Strain Analysis for Engineering Design*, 44(8):633–657, November 2009.
- [17] P. Domone and J. Illston. *Construction Materials: Their Nature and Behaviour*, Fourth Edition, May 2010.
- [18] M. K Hurst. *Prestressed concrete design*. E & FN Spon, London; New York, 1998.
- [19] The British Standards Institution. *BS 5896:2012 High tensile steel wire and strand for the prestressing of concrete. Specification*. BSI Standards Limited, 2 edition, May 2012.
- [20] E. G. Nawy. *Prestressed concrete A fundamental approach*. Prentice Hall, New Jersey, USA, 5 edition, 2010.
- [21] J Irving. The measurement of tendon loads in prestressed concrete pressure vessels and containment buildings, appendices to volume 3: The theory and practice of tendon loads based on a case study of measurements and tests on the Hinkley Point B PCPVs. Technical report PCPV/3166/V03, February 2000.
- [22] M. N. Hassoun and A. A. Al-Manaseer. *Structural concrete: theory and design*. Wiley, Hoboken, N.J, 5th ed edition, 2012.
- [23] K. M. Shrestha and B. Chen. Aging coefficient, creep coefficient and extrapolating aging coefficient from short term test for sealed concrete. *Journal of Wuhan University of Technology-Mater. Sci. Ed.*, 26(1):154–159, February 2011.
- [24] Z. P. Bažant, G. Cusatis, and L. Cedolin. Temperature effect on concrete creep modeled by microprestress-solidification theory. *Journal of engineering mechanics*, 130(6):691–699, 2004.
- [25] American Concrete Institute and ACI Committee 209–Creep and Shrinkage, editors. *Guide for modeling and calculating shrinkage and creep in hardened concrete*. Number 209.2R-08 in ACI standard. American Concrete Institute, Farmington Hills, MI, 2008.
- [26] G. Pickett. The Effect of Change in Moisture-Content on the Creep of Concrete Under a Sustained Load. *Journal Proceedings*, 38, February 1942.
- [27] Z. P. Bažant. Prediction of concrete creep and shrinkage: past, present and future. *Nuclear Engineering and Design*, 203(1):27–38, 2001.
- [28] Z. P. Bažant and Y. Xi. Continuous retardation spectrum for solidification theory of concrete creep. *Journal of Engineering Mechanics*, 121(2):281–288, 1995.

- [29] Z. P. Bazant, A. B. Hauggaard, S. Baweja, and F. J. Ulm. Microprestress-solidification theory for concrete creep. I: Aging and drying effects. *Journal of Engineering Mechanics*, 123(11):1188–1194, November 1997.
- [30] Z. P. Bazant, F. H. Wittman, J. K. Kim, and F. Alou. Statistical Extrapolation of Shrinkage Data - Part 1: Regression. *ACI Materials Journal*, 84(1):20–34, 1987.
- [31] Z. P. Bazant and S. Baweja. Creep and shrinkage prediction model for analysis and design of concrete structures: Model B3. *ACI Special Publications*, 194:1–84, 2000.
- [32] British Standards Institute, editor. *BS EN 1992-1-1:2004+A1:2014 Eurocode 2: Design of concrete structures. General rules and rules for buildings*. BSI, London, December 2004.
- [33] N. J. Gardner and M. J. Lockman. Design Provisions for Drying Shrinkage and Creep of Normal-Strength Concrete. *Materials Journal*, 98(2):159–167, March 2001.
- [34] R. L’Hermite, M. Mamillan, and C. Lefevre. Nouveaux Resultats de Recherche sur la Deformation et la Rupture du Beton. *Supplement aux Annales de Institut Technique du Batiment et des Travaux Publics*, 207/208:325, 1958.
- [35] J. R. Keeton. Study on Creep in Concrete. Technical report R333-1, R333-2, R333-3, U.S. Navy Civil Engineering Laboratory, 1965.
- [36] D. McHenry. A New Aspect of Creep in Concrete and its Application to Design., *Proceedings ASTM*, 43:1069–1084, 1943.
- [37] D. Magura, M.A. Sozen, and C. P. Siess. A study of stress relaxation in prestressing reinforcement. *Journal of prestressed concrete institute*, 9(2):13–57, April 1964.
- [38] J. Trevino and A. Ghali. Relaxation of steel in prestressed concrete. *PCI JOURNAL*, page 83, 1985.
- [39] British Standards Institute. *BS 4975:1990 British standard specification for prestressed concrete pressure vessels for nuclear reactors*. BSI Standards Limited, 1990.
- [40] S. Khan. Reactor 4 PCPV Statutory examination report 2008, Revision 000. Technical report E/REP/BNCB/0222/HPB/08, January 2009.
- [41] C. Grant. 2009 Statutory examination of the R2 pre-stressed concrete pressure vessel, revision 000. Technical report E/REP/BNCB/0241/TOR/09, July 2009.
- [42] Multi-Design Consultants Ltd. The measurement of tendon loads in prestressed concrete pressure vessels and containment buildings: Volume 1: The design, installation and in-service monitoring of PCPV and PCC prestressing systems. Technical report MDF/3166/V01, January 2000.
- [43] P. Anderson. Thirty years of measured prestress at Swedish nuclear reactor containments. *Nuclear Engineering and Design*, 235(21):2323–2336, October 2005.
- [44] K McNally. A statistical Analysis of PCPV Tendon loads at Hinkley Point B Power Station. Technical report MSU/2008/17, September 2008.

- [45] C. Malings and M. Pozzi. Conditional entropy and value of information metrics for optimal sensing in infrastructure systems. *Structural Safety*, 60:77–90, May 2016.
- [46] M. Majumder, T. Gangopadhyay, A. Chakraborty, K. Dasgupta, and D.K. Bhattacharya. Fibre Bragg gratings in structural health monitoring—Present status and applications. *Sensors and Actuators A: Physical*, 147(1):150–164, September 2008.
- [47] J. Lopez-Higuera, L. Rodriguez Cobo, A. Quintela Incera, and A. Cobo. Fiber Optic Sensors in Structural Health Monitoring. *Journal of Lightwave Technology*, 29(4):587–608, February 2011.
- [48] R. Paschotta. Encyclopedia of Laser Physics and Technology - numerical aperture, NA, optical fiber, lens, objective, acceptance angle.
- [49] A. Ghatak and K. Thyagarajan. *An Introduction to Fiber Optics by Ajoy Ghatak*. June 1998.
- [50] Corning Incorporated. Corning SMF-28 Optical Fiber Datasheet, November 2014.
- [51] B. Brichard, P. Borgermans, A. F. Fernandez, K. Lammens, and A. Decreton. Radiation effect in silica optical fiber exposed to intense mixed neutron-gamma radiation field. *IEEE Transactions on Nuclear Science*, 48(6):2069–2073, 2001.
- [52] B. Brichard, A. F. Fernandez, H. Ooms, and F. Berghmans. Fibre-optic gamma-flux monitoring in a fission reactor by means of Cerenkov radiation. *Measurement Science and Technology*, 18(10):3257–3262, October 2007.
- [53] B. D. Evans. The role of hydrogen as a radiation protection agent at low temperature in a low-OH, pure silica optical fiber. *IEEE Transactions on Nuclear Science*, 35(6):1215–1220, 1988.
- [54] L. W. Hobbs, F. W. Clinard, S. J. Zinkle, and R. C. Ewing. Radiation effects in ceramics. *Journal of Nuclear Materials*, 216:291–321, October 1994.
- [55] K. Gill, R. Grabit, M. Persello, G. Stefanini, and F. Vasey. Gamma and neutron radiation damage studies of optical fibres. *Journal of non-crystalline solids*, 216:129–134, 1997.
- [56] M. Van Uffelen, F. Berghmans, A. Nowodzinski, Ph Jucker, B. Brichard, F. Vos, and M. Decréton. Fiber-optic link components for maintenance tasks in thermonuclear fusion environments. In *Radiation and Its Effects on Components and Systems, 1999. RADECS 99. 1999 Fifth European Conference on*, pages 491–496. IEEE, 1999.
- [57] F Berghmans, B Brichard, A F Fernandez, A. Gusarov, M. Van Uffelen, and Sylvain Girard. *Optical Waveguide Sensing and Imaging: An Introduction to Radiation Effects on Optical Components and Fiber Optic Sensors*. NATO science for peace and security series B: physics and biophysics. Springer, Dordrecht, 2008.
- [58] M. Lezius, K. Predehl, W. Stower, A. Turler, M. Greiter, Ch. Hoeschen, P. Thirolf, W. Assmann, D. Habs, A. Prokofiev, C. Ekstrom, T. W. Hansch, and R. Holzwarth. Radiation Induced Absorption in Rare Earth Doped Optical Fibers. *IEEE Transactions on Nuclear Science*, 59(2):425–433, April 2012.

- [59] T. Wijnands, L. K. De Jonge, J. Kuhnenn, S. K. Hoeffgen, and U. Weinand. Optical Absorption in Commercial Single Mode Optical Fibers in a High Energy Physics Radiation Field. *IEEE Transactions on Nuclear Science*, 55(4):2216–2222, August 2008.
- [60] W. J. Bock, I. Gannot, and S. Tanev. *Optical Waveguide Sensing and Imaging*. Springer Netherlands, 2008.
- [61] A. F. Fernandez, F. Berghmans, B. Brichard, P. Borgermans, A. I. Gusarov, M. Van Uffelen, P. Mégret, M. Decréton, M. Blondel, and A. Delchambre. Radiation-resistant WDM optical link for thermonuclear fusion reactor instrumentation. *IEEE Transactions on Nuclear Science*, 48(5), 2001.
- [62] S. Rehman and L. Norin. Specialty optical fibers for harsh environments. *Photonics Spectra*, Laurin Publishing, (October), October 2010.
- [63] A. Pal, A. Dhar, A. Ghosh, R. Sen, B. Hooda, V. Rastogi, M. Ams, M. Fabian, T. Sun, and K. T. V. Grattan. Sensors for Harsh Environment: Radiation Resistant FBG Sensor System. *Journal of Lightwave Technology*, 35(16):3393–3398, August 2017.
- [64] P. Russell. Photonic crystal fibers. *Science*, 299(5605):358–362, 2003.
- [65] S. Girard, J. Baggio, and J.-L. Leray. Radiation-induced effects in a new class of optical waveguides: the air-guiding photonic crystal fibers. *IEEE Transactions on Nuclear Science*, 52(6):2683–2688, December 2005.
- [66] H. Henschel, J. Kuhnenn, and U. Weinand. High radiation hardness of a hollow core photonic bandgap fiber. Anaheim, Calif, 2005.
- [67] G. Cheymol, H. Long, J. F. Villard, and B. Brichard. High Level Gamma and Neutron Irradiation of Silica Optical Fibers in CEA OSIRIS Nuclear Reactor. *IEEE Transactions on Nuclear Science*, 55(4):2252–2258, August 2008.
- [68] B. Glisic. Influence of the gauge length on the accuracy of long-gauge sensors employed in monitoring of prismatic beams. *Measurement Science and Technology*, 22(3):035206, March 2011.
- [69] E. Udd and W. Spillman. *Fiber Optic Sensors: An Introduction for Engineers and Scientists*. John Wiley & Sons, October 2011.
- [70] K. O. Hill, Y. Fujii, D. C. Johnson, and B. S. Kawasaki. Photosensitivity in optical fiber waveguides: Application to reflection filter fabrication. *Applied Physics Letters*, 32(10):647–649, May 1978.
- [71] T. Erdogan. Fiber grating spectra. *Journal of lightwave technology*, 15(8):1277–1294, 1997.
- [72] S. J. Mihailov, C. W. Smelser, P. Lu, R. B. Walker, D. Grobncic, H. Ding, G. Henderson, and J. Unruh. Fiber Bragg gratings made with a phase mask and 800-nm femtosecond radiation. *Optics Letters*, 28(12):995–997, 2003.
- [73] J. Canning. Fibre gratings and devices for sensors and lasers. *Laser & Photonics Review*, 2(4):275–289, August 2008.

- [74] J. Canning, M. Stevenson, S. Bandyopadhyay, and K. Cook. Extreme Silica Optical Fibre Gratings. *Sensors*, 8(10):6448–6452, October 2008.
- [75] K. O. Hill and G. Meltz. Fiber Bragg grating technology fundamentals and overview. *Journal of lightwave technology*, 15(8):1263–1276, 1997.
- [76] G. Flockhart, R. Maier, J. Barton, W. MacPherson, J. Jones, K. Chisholm, L. Zhang, I. Bennion, I. Read, and P. Foote. Quadratic behavior of fiber Bragg grating temperature coefficients. *Applied optics*, 43(13):2744–2751, 2004.
- [77] V. B. Neustruev. Colour centres in germanosilicate glass and optical fibres. *Journal of Physics: Condensed Matter*, 6(35):6901, 1994.
- [78] A. Gusarov, A. F. Fernandez, S. Vasiliev, O. Medvedkov, M. Blondel, and F. Berghmans. Effect of gamma–neutron nuclear reactor radiation on the properties of Bragg gratings written in photosensitive Ge-doped optical fiber. *Nuclear Instruments and Methods in Physics Research Section B: Beam Interactions with Materials and Atoms*, 187(1):79–86, 2002.
- [79] A. I. Gusarov, F. Berghmans, A. F. Fernandez, O. Deparis, Y. Defosse, D. Starodubov, M. Decreton, P. Mégret, and M. Bondel. Behavior of fibre Bragg gratings under high total dose gamma radiation. *IEEE Transactions on Nuclear Science*, 47(3):688–692, 2000.
- [80] A. Gusarov, S. Vasiliev, O. Medvedkov, I. Mckenzie, and F. Berghmans. Stabilization of Fiber Bragg Gratings Against Gamma Radiation. *IEEE Transactions on Nuclear Science*, 55(4):2205–2212, August 2008.
- [81] A. Fernandez, B. Brichard, F. Berghmans, and M. Decreton. Dose-rate dependencies in gamma-irradiated fiber bragg grating filters. *IEEE Transactions on Nuclear Science*, 49(6):2874–2878, December 2002.
- [82] H. Henschel, D. Grobnic, S. K. Hoeffgen, J. Kuhnenn, S. J. Mihailov, and U. Weinand. Development of Highly Radiation Resistant Fiber Bragg Gratings. *IEEE Transactions on Nuclear Science*, 58(4):2103–2110, August 2011.
- [83] A. F. Fernandez, B. Brichard, P. Borgermans, F. Berghmans, M. Decreton, P. Megret, M. Blondel, and A. Delchambre. Fibre Bragg grating temperature sensors for harsh nuclear environments. In *Optical Fiber Sensors Conference Technical Digest, 2002. OFS 2002, 15th*, pages 63–66. IEEE, 2002.
- [84] S. Lin, N. Song, J. Jin, X. Wang, and G. Yang. Effect of Grating Fabrication on Radiation Sensitivity of Fiber Bragg Gratings in Gamma Radiation Field. *IEEE Transactions on Nuclear Science*, 58(4):2111–2117, August 2011.
- [85] A. F. Fernandez, A. I. Gusarov, S. Bodart, K. Lammens, F. Berghmans, M. Decre, P. Me, M. Blondel, A. Delchambre, and others. Temperature monitoring of nuclear reactor cores with multiplexed fiber Bragg grating sensors. *Optical Engineering*, 41(6):1246–1254, 2002.

- [86] A. Gusarov, C. Chojetzki, I. Mckenzie, H. Thienpont, and F. Berghmans. Effect of the Fiber Coating on the Radiation Sensitivity of Type I FBGs. *IEEE Photonics Technology Letters*, 20(21):1802–1804, November 2008.
- [87] A. Gusarov. Long-Term Exposure of Fiber Bragg Gratings in the BR1 Low-Flux Nuclear Reactor. *IEEE Transactions on Nuclear Science*, 57(4):2044–2048, August 2010.
- [88] M F. Ashby, H. Shercliff, and D. Cebon. *Materials: Engineering, Science, Processing and Design*. Butterworth-Heinemann, December 2013.
- [89] W. Urbanczyk, E. Chmielewska, and W. Bock. Measurements of temperature and strain sensitivities of a two-mode Bragg grating imprinted in a bow-tie fibre. *Measurement Science and Technology*, 12(7):800, 2001.
- [90] S. W. James, M. L. Dockney, and R. P. Tatam. Simultaneous independent temperature and strain measurement using in-fibre Bragg grating sensors. *Electronics Letters*, 32(12):1133–1134, 1996.
- [91] M. G. Xu, J.-L. Archambault, L. Reekie, and J. P. Dakin. Discrimination between strain and temperature effects using dual-wavelength fibre grating sensors. *Electronics letters*, 30(13):1085–1087, 1994.
- [92] J. Echevarria, A. Quintela, C. Jauregui, and J. M. Lopez-Higuera. Uniform fiber Bragg grating first-and second-order diffraction wavelength experimental characterization for strain-temperature discrimination. *IEEE Photonics Technology Letters*, 13(7):696–698, 2001.
- [93] B. Glisic and D. Inaudi. *Fibre Optic Methods for Structural Health Monitoring*. Wiley, October 2007.
- [94] D. Inaudi and B. Glisic. Long-Range Pipeline Monitoring by Distributed Fiber Optic Sensing. *Journal of Pressure Vessel Technology*, 132(1):011701, 2010.
- [95] B. Glisic and D. Inaudi. Development of method for in-service crack detection based on distributed fiber optic sensors. *Structural Health Monitoring*, 11(2):161–171, March 2012.
- [96] D. Zonta, F. Bruschetta, R. Zandonini, M. Pozzi, M. Wang, B. Glisic, D. Inaudi, D. Posenato, and Y. Zhao. Sensor Fusion on Structural Monitoring Data Analysis: Application to a Cable-Stayed Bridge. *Key Engineering Materials*, 569-570:812–819, July 2013.
- [97] Case Study–Nuclear Power, Robert E.Ginna Nuclear Generating Station Pilot Project, Assessing the Condition of Concrete Containment Structures, 2012.
- [98] E Hughs, Z Liang, R Idriss, and C. Newtonson. In-place modulus of elasticity for high-performance concrete bridge. *ACI materials journal*, 102(6):454–458, 2005.
- [99] RI Idriss. Monitoring of a prestressed high performance concrete bridge from construction through service using an embedded optical fiber sensor system. In *Bridge Maintenance, Safety, Management, Resilience and Sustainability*, Bridge Maintenance, Safety and Management, pages 3198–3205. CRC Press, June 2012.

- [100] H Abdel-Jaber and B Glisic. A method for the on-site determination of prestressing forces using long-gauge fiber optic strain sensors. *Smart Materials and Structures*, 23(7):075004, July 2014.
- [101] Z. Zhou, J. He, G. Chen, and J. Ou. A Smart Steel Strand for the Evaluation of Prestress Loss Distribution in Post-tensioned Concrete Structures. *Journal of Intelligent Material Systems and Structures*, 20(16):1901–1912, November 2009.
- [102] C. Lan, Z. Zhou, and J. Ou. Monitoring of structural prestress loss in RC beams by inner distributed Brillouin and fiber Bragg grating sensors on a single optical fiber: Methodology and component of monitoring prestress loss. *Structural Control and Health Monitoring*, 21(3):317–330, March 2014.
- [103] S. Kim, Y. H. Park, S. Park, K. Cho, and J. R. Cho. A Sensor-Type PC Strand with an Embedded FBG Sensor for Monitoring Prestress Forces. *Sensors*, 15(1):1060–1070, January 2015.
- [104] J. W. Chin, K. Aouadi, and T. Nguyen. Effects of Environmental Exposure on Fiber-Reinforced Plastic (FRP) Materials Used in Construction. *Journal of Composites Technology & Research*, 19(4):205–213, October 1997.
- [105] A. Zaman, S. A. Gutub, and M. A. Wafa. A review on FRP composites applications and durability concerns in the construction sector. *Journal of Reinforced Plastics and Composites*, 32(24):1966–1988, December 2013.
- [106] K. Hoffmann. *An introduction to measurements using strain gages*. Hottinger Baldwin Messtechnik Darmstadt, 1989.
- [107] L. Hong-Nan, Z. Guang-Dong, R. Liang, and L. Dong-Sheng. Strain transfer coefficient analyses for embedded fiber Bragg grating sensors in different host materials. *Journal of engineering mechanics*, 135(12):1343–1353, 2009.
- [108] W.Y. Li, C.C. Cheng, and Y.L. Lo. Investigation of strain transmission of surface-bonded FBGs used as strain sensors. *Sensors and Actuators A: Physical*, 149(2):201–207, February 2009.
- [109] L. Dongsheng, L. Hongnan, and R. Liang. *Mechanical property and strain transferring mechanism in optical fiber sensors*. INTECH Open Access Publisher, 2012.
- [110] J. Zhou, Z. Zhou, and D. Zhang. Study on Strain Transfer Characteristics of Fiber Bragg Grating Sensors. *Journal of Intelligent Material Systems and Structures*, 21(11):1117–1122, July 2010.
- [111] H. P. Wang and Z. Zhi. A Review on Strain Transfer Mechanism of Optical Fiber Sensors. *Pac. Sci. Rev*, 14:248–252, 2012.
- [112] K-OP-A: Configurable Armored Optical Sensors Chain | HBM.
- [113] H. W. Bonin, V. T. Bui, and P. E. Poirier. Effects of neutrons and gamma radiation on high polymer epoxy adhesives. In *Proc. 16th Annual Conf. Canadian Nuclear Society*, pages 4–7, 1996.

- [114] P. Majda and J. Skrodzewicz. A modified creep model of epoxy adhesive at ambient temperature. *International Journal of Adhesion and Adhesives*, 29(4):396–404, June 2009.
- [115] B. De Nève and M. E. R. Shanahan. Effects of humidity on an epoxy adhesive. *International Journal of Adhesion and Adhesives*, 12(3):191–196, 1992.
- [116] J.S. Hwang and R.M. Vargas. Solder Joint Reliability—Can Solder Creep? *Soldering & Surface Mount Technology*, 2(2):38–45, February 1990.
- [117] S. K. Ferguson. Patent Number: US 2006/0285813 A1, Fiber anchoring method for optical sensors, December 2006.
- [118] E. Suhir and B. Poborets. Solder-glass attachment in cerdip/cerquad packages: thermally induced stresses and mechanical reliability. In *Electronic Components and Technology Conference, 1990., 40th*, pages 1043–1052. IEEE, 1990.
- [119] F. Jin. Material Requirements For Optoelectronic Packaging—Fiber Soldering. *San Jose State Univ., San Jose, CA, Tech. Rep.*, 2003.
- [120] D. R. H. Jones and M. F. Ashby. *Engineering Materials 1: An Introduction to Properties, Applications and Design*. Butterworth-Heinemann, Amsterdam ; Boston, 4 edition edition, September 2011.
- [121] M. Perry, P. Niewczas, M. Johnston, K. Cook, and J. Canning. Induction Brazing of Type-I Fiber Bragg Gratings Into Kovar Ferrules Exploiting Curie Transition. *IEEE Sensors Journal*, 13(2):816–823, February 2013.
- [122] G. Fusiek, M. Perry, P. Niewczas, and M. Johnston. Deformation monitoring in prestressing tendons using fibre Bragg gratings encapsulated in metallic packages. In *SPIE 9157, 23rd International Conference on Optical Fibre Sensors*, volume 9157A6, June 2014.
- [123] Z Mei and J.W. Morris. Superplastic creep of low melting point solder joints. *Journal of Electronic Materials*, 21(4):401–407, April 1992.
- [124] S. Bandyopadhyay, J. Canning, M. Stevenson, and K. Cook. Ultrahigh-temperature regenerated gratings in boron-codoped germanosilicate optical fiber using 193 nm. *Optics letters*, 33(16):1917–1919, 2008.
- [125] C. Barbosa, N. Costa, L. A. Ferreira, F. M. Araújo, H. Varum, A. Costa, C. Fernandes, and H. Rodrigues. Weldable fibre Bragg grating sensors for steel bridge monitoring. *Measurement Science and Technology*, 19(12):125305, December 2008.
- [126] M. Perry, Z. Yan, Z. Sun, L. Zhang, P. Niewczas, and M. Johnston. High stress monitoring of prestressing tendons in nuclear concrete vessels using fibre-optic sensors. *Nuclear Engineering and Design*, 268:35–40, March 2014.
- [127] J Zhou and Z Zhao. Encapsulation Techniques for FBGs and Smart Monitoring for Bridges with FBG Sensors. Stanford University, January 2003. DEStech Publications.
- [128] Q. Tan and Y. C. Lee. Soldering technology for optoelectronic packaging. In *Electronic Components and Technology Conference, 1996. Proceedings., 46th*, pages 26–36. IEEE, 1996.

- [129] S. R. Baker, H. N. Rourke, V. Baker, and D. Goodchild. Thermal decay of fiber Bragg gratings written in boron and germanium codoped silica fiber. *Lightwave Technology, Journal of*, 15(8):1470–1477, 1997.
- [130] D. C. Ripple, R. Davis, B. Fellmuth, J. Fischer, G. Machin, T. Quinn, P. Steur, O. Tamura, and D. R. White. The Roles of the *Mise en Pratique* for the Definition of the Kelvin. *International Journal of Thermophysics*, 31(8-9):1795–1808, September 2010.
- [131] B. Fellmuth, J. Fischer, G. Machin, S. Picard, P. P. M. Steur, O. Tamura, D. R. White, and H. Yoon. The kelvin redefinition and its *mise en pratique*. *Philosophical Transactions of the Royal Society A: Mathematical, Physical and Engineering Sciences*, 374(2064):20150037, March 2016.
- [132] H. Preston-Thomas. The International Temperature Scale of 1990 (ITS-90). *Metrologia*, 27:3–10, 1990.
- [133] pt100 temperature sensor | Omega Engineering.
- [134] E. Doebelin. *Measurement Systems, Application and Design*. Mechanical and Industrial Engineering. McGraw-Hill Publishing Company, fourth edition, 1990.
- [135] B. McGinty. Beam Bending.
- [136] Wen-Chun Jiang, Jian-Ming Gong, Hu Chen, and S. T. Tu. Finite Element Analysis of the Effect of Brazed Residual Stress on Creep for Stainless Steel Plate-Fin Structure. *Journal of Pressure Vessel Technology*, 130(4):041203, 2008.
- [137] R. J. Glodowski and J. J. Lorenzetti. Method for predicting prestress losses in a prestressed concrete structure. *Journal of precast/prestressed concrete institute*, 17(2), March 1972.
- [138] J. D. Buckler and C. F. Scribner. Relaxation characteristics of prestressing strand. Technical report, University of Illinois Engineering Experiment Station. College of Engineering. University of Illinois at Urbana-Champaign., 1985.
- [139] Z. P. Bažant and Q. Yu. Relaxation of Prestressing Steel at Varying Strain and Temperature: Viscoplastic Constitutive Relation. *Journal of Engineering Mechanics*, 139(7):814–823, July 2013.
- [140] F. S. Rostásy, K.-Ch Thienel, and K. Schütt. On prediction of relaxation of cold drawn prestressing wire under constant and variable elevated temperature. *Nuclear engineering and design*, 130(2):221–227, 1991.
- [141] J. Davis, editor. *Tensile testing*. ASM International, Materials Park, Ohio, 2. ed edition, 2004.
- [142] H.B. Motra, J. Hildebrand, and A. Dimmig-Osburg. Assessment of strain measurement techniques to characterise mechanical properties of structural steel. *Engineering Science and Technology, an International Journal*, 17(4):260–269, December 2014.
- [143] J. Hockett and P. Gillis. Mechanical testing machine stiffness: Part II—Application to data reduction. *International Journal of Mechanical Sciences*, 13(3):265–275, 1971.

- [144] J. Hockett and P. Gillis. Mechanical testing machine stiffness: Part I—Theory and calculations. *International Journal of Mechanical Sciences*, 13(3):251–264, 1971.
- [145] A. Rao, P. John Bouchard, S. Northover, and M. Fitzpatrick. Anelasticity in austenitic stainless steel. *Acta Materialia*, 60(19):6851–6861, November 2012.
- [146] M. Perry, P. Orr, P. Niewczas, and M. Johnston. Nanoscale Resolution Interrogation Scheme for Simultaneous Static and Dynamic Fiber Bragg Grating Strain Sensing. *Journal of Lightwave Technology*, 30(20):3252–3258, October 2012.
- [147] Technobis. PalawanGator - High Resolution / Multi Parameter | Technobis.
- [148] G. Fusiek, T. Rubert, P. Niewczas, J. McAlorum, and M. Perry. Preliminary characterization of metal-packaged fiber Bragg gratings under fatigue loading. In *2017 IEEE International Instrumentation and Measurement Technology Conference (I2MTC)*, pages 1–4, May 2017.
- [149] D. Zonta. Sensor data analysis, reduction and fusion for assessing and monitoring civil infrastructures. In *Sensor Technologies for Civil Infrastructures*, pages 33–66. Elsevier, 2014.
- [150] D. S. Sivia. *Data Analysis: A Bayesian Tutorial*. Clarendon Press, 1996.
- [151] D. Zonta, M. Pozzi, H. Y. Wu, and D. Inaudi. Bayesian Logic Applied to Damage Assessment of a Smart Precast Concrete Element. *Key Engineering Materials*, 413-414:351–358, June 2009.
- [152] D. Calvetti and E. Somersalo. *An Introduction to Bayesian Scientific Computing - Ten | Daniela | Springer*, volume 2. Springer-Verlag New York, 2007.
- [153] K. Murphy. *Machine Learning: A Probabilistic Perspective*. MIT Press, Cambridge, MA, September 2012.
- [154] Technica. T25 Gold Coated FBG with Hermetic Seal.
- [155] Technica. T80 Radiation Hard & Radiation Proof FBG.

Appendix A

A.1 Shrinkage strain in concrete

In the CEB MC90-99 model, shrinkage ϵ_{shr} , at day t after concrete curing t_c , is split into autogenous ϵ_{cas} and drying shrinkage ϵ_{cds} strain¹:

$$\epsilon_{shr}(t, t_c) = \epsilon_{cas}(t) + \epsilon_{cds}(t, t_c) \quad (\text{A.1})$$

A.1.1 Autogenous shrinkage

Autogenous shrinkage is calculated from an autogenous shrinkage coefficient ϵ_{cas0} , and a time dependent term $\beta_{as}(t)$:

$$\epsilon_{cas}(t) = \epsilon_{cas0}(f_{cm28})\beta_{as}(t) \quad (\text{A.2})$$

The autogenous shrinkage coefficient is dependent on the mean concrete compressive strength at 28 days (in *MPa*):

$$\epsilon_{cas0}(f_{cm28}) = \left[-\alpha_{as} \left(\frac{f_{cm28}/f_{cm0}}{6 + f_{cm28}/f_{cm0}} \right)^{2.5} \right] \times 10^{-6} \quad (\text{A.3})$$

where

$$f_{cm0} = 10\text{MPa} \quad \alpha_{as} = 700 \quad (\text{A.4})$$

The time dependent term at day t , is calculated as follows:

¹Consult [25] for more details.

$$\beta_{as}(t) = 1 - \exp\left(-0.2\left(\frac{t}{t_1}\right)^{0.5}\right) \quad (\text{A.5})$$

where $t_1 = 1$.

A.1.2 Drying shrinkage

Drying shrinkage is dependent on a notional drying shrinkage coefficient $\epsilon_{cds0}(f_{cm28})$, the effect of relative humidity $\beta_{RH}(h)$ and a time development term $\beta_{ds}(t - t_c)$:

$$\epsilon_{cds}(t, t_c) = \epsilon_{cds0}(f_{cm28})\beta_{RH}(h)\beta_{ds}(t - t_c) \quad (\text{A.6})$$

The notional coefficient is calculated from the mean concrete compressive strength at 28 days as follows:

$$\epsilon_{cds0}(f_{cm28}) = \left[(220 + 110\alpha_{ds1}) \exp\left(-\alpha_{ds2} \frac{f_{cm28}}{f_{cm0}}\right) \right] \times 10^{-6} \quad (\text{A.7})$$

For normal hardening concrete:

$$\alpha_{ds1} = 4 \quad \alpha_{ds2} = 0.12 \quad (\text{A.8})$$

The relative humidity term is:

$$\beta_{RH}(h) = -1.55 \left(1 - \left(\frac{h}{h_0} \right)^3 \right) \text{ for } 0.4 \leq h < 0.99 \quad (\text{A.9})$$

where h is the humidity as a fraction. The time dependent term is given by:

$$\beta_{ds}(t - t_c) = \left[\frac{(t - t_c)/t_1}{350 \left(\frac{(V/S)}{(V/S)_0} \right)^2 + (t - t_c)/t_1} \right]^{0.5} \quad (\text{A.10})$$

where V/S is the volume to surface ratio of the concrete in mm , and:

$$h_0 = 1 \quad (V/S)_0 = 50mm \quad (\text{A.11})$$

A.2 Creep strain in concrete

The creep compliance, J is made up of two terms²:

$$J(t, t_0) = \frac{1}{E_{cm28}} [\eta(t_0) + \phi_{28}(t, t_0)] = \frac{1}{E_{cmt_0}} + \frac{\phi_{28}(t, t_0)}{E_{cm28}} \quad (\text{A.12})$$

The first term is the initial strain per unit stress at loading time t_0 . The second term, a combination of the 28-day creep coefficient ϕ_{28} and the mean modulus of elasticity at 28-days E_{cm28} , models the development of creep strain in the concrete. The first term is calculated from the modulus of elasticity of the concrete at loading time:

$$E_{cmt_0} = E_{cm28} \exp \left(\frac{S}{2} \left(1 - \left(\frac{28}{t/t_1} \right)^{0.5} \right) \right) \quad (\text{A.13})$$

where $S = 0.25$ for normal hardening concrete with strength of less than 60 MPa. The modulus of elasticity at 28 days, E_{cm28} is calculated as:

$$E_{cm28} = 21,500 \left(\frac{f_{cm28}}{f_{cm0}} \right)^{1/3} \quad (\text{A.14})$$

$$f_{cm28} = f_c + 8.0$$

where f_c is the specified compressive cylinder strength in MPa. The 28-day creep coefficient is a combination of the notional creep coefficient ϕ_0 and a time dependent term $\beta_c(t - t_0)$:

$$\phi_{28}(t, t_0) = \phi_0 \beta_c(t - t_0) \quad (\text{A.15})$$

where the notional creep coefficient is calculated from the following equations:

$$\phi_0 = \phi_{RH}(h) \beta(f_{cm28}) \beta(t_0)$$

$$\beta(f_{cm28}) = \frac{5.3}{(f_{cm28}/f_{cm0})^{0.5}} \quad \beta(t_0) = \frac{1}{0.1 + \left(\frac{t_0}{t_1} \right)^{0.2}}$$

$$\phi_{RH}(h) = \left[1 + \frac{1 - h/h_0}{\left(0.1 \frac{(V/S)}{(V/S)_0} \right)^{1/3}} \alpha_1 \right] \alpha_2 \quad (\text{A.16})$$

$$\alpha_1 = \left[\frac{3.5 f_{cm0}}{f_{cm28}} \right]^{0.7} \quad \alpha_2 = \left[\frac{3.5 f_{cm0}}{f_{cm28}} \right]^{0.2}$$

The time dependent term is calculated and adjusted for humidity as follows:

²Consult [25] for more details.

$$\beta_c(t-t_0) = \left[\frac{(t-t_0)/t_1}{\beta_H + (t-t_0)/t_1} \right]^{0.3}$$

$$\beta_H = 150 \left[1 + (1.2(h/h_0)^{18}) \frac{(V/S)}{(V/S)_0} + 250\alpha_3 \right] \leq 1500\alpha_3 \quad (\text{A.17})$$

$$\alpha_3 = \left[\frac{3.5 f_{cm0}}{f_{cm28}} \right]^{0.5}$$

The 28-day creep coefficient, in Equation A.15, can be adjusted for temperature fluctuations T (in °C), after prestressing, by the following:

$$\phi_{28}(t, t_0, T) = \phi_0 \beta_c(t-t_0) + \Delta\phi_T$$

$$\Delta\phi_T = 0.0004(T-20)^2 \quad (\text{A.18})$$

A.3 Temperature dependence of Bragg peak wavelength

Differentiating Equation 4.6 with respect to temperature, T gives:

$$\frac{\partial \lambda_B}{\partial T} = 2 \left(\Lambda \frac{\partial n_{eff}}{\partial T} + n_{eff} \frac{\partial \Lambda}{\partial T} \right) = \lambda_B \left(\frac{1}{n_{eff}} \frac{\partial n_{eff}}{\partial T} + \frac{1}{\Lambda} \frac{\partial \Lambda}{\partial T} \right) \quad (\text{A.19})$$

The first term is the temperature dependency of the refractive index, named the thermo-optic coefficient, α_n . The second term, α_Λ is the effect of thermal expansion of the glass on the periodicity:

$$\alpha_n = \frac{1}{n_{eff}} \frac{\partial n_{eff}}{\partial T} \quad \alpha_\Lambda = \frac{1}{\Lambda} \frac{\partial \Lambda}{\partial T} \quad (\text{A.20})$$

Resulting in the simplified equation:

$$\Delta \lambda_B = \lambda_B (\alpha_n + \alpha_\Lambda) \Delta T \quad (\text{A.21})$$

A.4 Strain dependence of Bragg peak wavelength

Differentiating Equation 4.6 with respect to length, l gives:

$$\frac{\partial \lambda_B}{\partial l} = 2 \left(n_{eff} \frac{\partial \Lambda}{\partial l} + \Lambda \frac{\partial n_{eff}}{\partial l} \right) = \lambda_B \left(\frac{1}{\Lambda} \frac{\partial \Lambda}{\partial l} + \frac{1}{n_{eff}} \frac{\partial n_{eff}}{\partial l} \right) \quad (\text{A.22})$$

Which can be rearranged as:

$$\frac{\partial \lambda_B}{\lambda_B} = \frac{\partial l}{\Lambda} \frac{\partial \Lambda}{\partial l} + \frac{\partial l}{n_{eff}} \frac{\partial n_{eff}}{\partial l} \quad (\text{A.23})$$

The first term in the equation is ε_z , as a change in periodicity is analogous to strain. Strain in the fibre reduces the effective refractive index due to decreased material density and increased polarisability. This effect is described by Pockel's coefficients, p_{11} and p_{12} in terms of axial, ε_z and radial, ε_r strain on the fibre:

$$\frac{\partial l}{n_{eff}} \frac{\partial n_{eff}}{\partial l} = -\frac{n^2}{2} (p_{11}\varepsilon_r + p_{12}(\varepsilon_r + \varepsilon_z)) \quad (\text{A.24})$$

Assuming radial strain on the fibre is solely due to the Poisson effect results in:

$$\varepsilon_r = -\nu\varepsilon_z \frac{\partial l}{n_{eff}} \frac{\partial n_{eff}}{\partial l} = -\varepsilon_z \frac{n^2}{2} (p_{12} - \nu(p_{11} + p_{12})) \quad (\text{A.25})$$

The constants are grouped together and termed the strain-optic coefficient, p_e , resulting in the simplified equation:

$$\frac{\Delta \lambda_B}{\lambda_B} = (1 - p_e)\varepsilon_z \quad (\text{A.26})$$

A.5 FBG strain and temperature sensor error analysis

A.5.1 Strain error

The strain ε_z of an FBG strain sensor that is compensated with a temperature FBG sensor that measures temperature ΔT is given by:

$$\varepsilon_z = \frac{\frac{\Delta \lambda_{B1}}{\lambda_{B1}} - K_{T1}\Delta T}{K_\varepsilon} = \frac{a}{b} = \frac{c + d}{b} \quad (\text{A.27})$$

where λ_{B1} and $\Delta \lambda_{B1}$ are the Bragg peak wavelength and the change in wavelength, respectively, measured by the strain sensor. The strain sensor has a strain and temperature sensitivity of K_ε and K_{T1} . The expression can be simplified by defining new terms:

$$b = K_\varepsilon \quad c = \frac{\Delta \lambda_{B1}}{\lambda_{B1}} \quad d = K_{T1}\Delta T \quad (\text{A.28})$$

The error in the strain measurement can be approximated using conventional propagation of error analysis, with the assumption of uncorrelated variables, as follows:

$$\left(\frac{\delta\epsilon_z}{\epsilon_z}\right)^2 \approx \left(\frac{\delta a}{a}\right)^2 + \left(\frac{\delta b}{b}\right)^2 = \left(\frac{\delta c^2 + \delta d^2}{a^2}\right) + \left(\frac{\delta b}{b}\right)^2 \quad (\text{A.29})$$

$(\delta c)^2$ is a combination of the error of the absolute Bragg peak wavelength and the error in the measured shift in the Bragg peak wavelength during the measurement period:

$$(\delta c)^2 = \left(\frac{\Delta\lambda_{B1}}{\lambda_{B1}}\right)^2 \left(\left(\frac{\delta\lambda}{\Delta\lambda_{B1}}\right)^2 + \left(\frac{\delta\lambda}{\lambda_{B1}}\right)^2 \right) \quad (\text{A.30})$$

Both these errors are due to the interrogator accuracy, therefore the same error is assigned to them, typically 1 pm. This is stated explicitly as $\delta\Delta\lambda_{B1} = \delta\lambda_{B1} = \delta\lambda$.

The δd term contains the error from temperature compensation. The temperature is measured by a second FBG sensor, therefore the change in temperature is calculated with the following equation:

$$\Delta T = \frac{1}{K_{T2}} \frac{\Delta\lambda_{B2}}{\lambda_{B2}} \quad (\text{A.31})$$

The absolute and change in peak wavelength of the temperature sensor are denoted with $B2$ and its temperature sensitivity is K_{T2} . Replacing ΔT in d gives:

$$d = \frac{K_{T1}}{K_{T2}} \frac{\Delta\lambda_{B2}}{\lambda_{B2}} \quad (\text{A.32})$$

Using similar analysis as before the $(\delta d)^2$ expression becomes:

$$(\delta d)^2 = \left(\frac{K_{T1}}{K_{T2}} \frac{\Delta\lambda_{B2}}{\lambda_{B2}}\right)^2 \left(\left(\frac{\delta K_{T1}}{K_{T1}}\right)^2 + \left(\frac{\delta K_{T2}}{K_{T2}}\right)^2 + \left(\frac{\delta\lambda_{B2}}{\Delta\lambda_{B2}}\right)^2 + \left(\frac{\delta\lambda_{B2}}{\lambda_{B2}}\right)^2 \right) \quad (\text{A.33})$$

Replacing $a = K_\epsilon \epsilon_z$ and $b = K_\epsilon$ leads to the error in ϵ_z as:

$$\delta\epsilon_z^2 = \frac{\delta c^2 + \delta d^2}{K_\epsilon^2} + \frac{\delta K_\epsilon^2 \epsilon_z^2}{K_\epsilon^2} \quad (\text{A.34})$$

Replacing $(\delta c)^2$ and $(\delta d)^2$ with Equation A.30 and A.33 results in the final expression for the strain error of a temperature compensated measurement.

A.5.2 Temperature error

The temperature sensitivity K_T of a sensor is found by temperature calibration. The Equation to calculate K_T is the same as Equation A.31 but in this case the temperature is recorded with a known temperature reference. The error is calculated using the same method as above with an additional term to account for the error in fitting a line of best fit to the data. The error is therefore given by:

$$\left(\frac{\delta K_{T2}}{K_{T2}}\right)^2 \approx \left(\frac{\delta \lambda}{\Delta \lambda_{B2}}\right)^2 + \left(\frac{\delta \lambda}{\lambda_{B2}}\right)^2 + \left(\frac{\delta T_{ref}}{\Delta T_{ref}}\right)^2 + \left(\frac{1}{K_{T2}}\right)^2 \sigma_{fit}^2 \quad (\text{A.35})$$

ΔT_{ref} and δT_{ref} are the temperature range measured by the temperature reference and its error, respectively.

The absolute temperature error from the temperature FBG sensor can be calculated by incorporating the temperature sensitivity error calculated previously (again using an expression equivalent to Equation A.31):

$$\delta T_{FBG}^2 = T_{FBG}^2 \left(\left(\frac{\delta \lambda}{\Delta \lambda_{B2}}\right)^2 + \left(\frac{\delta \lambda}{\lambda_{B2}}\right)^2 + \left(\frac{\delta K_{T2}}{K_{T2}}\right)^2 \right) \quad (\text{A.36})$$

A.6 Concrete beam sensor calibration cycles

Responses of each sensor during the concrete beam calibration cycles.

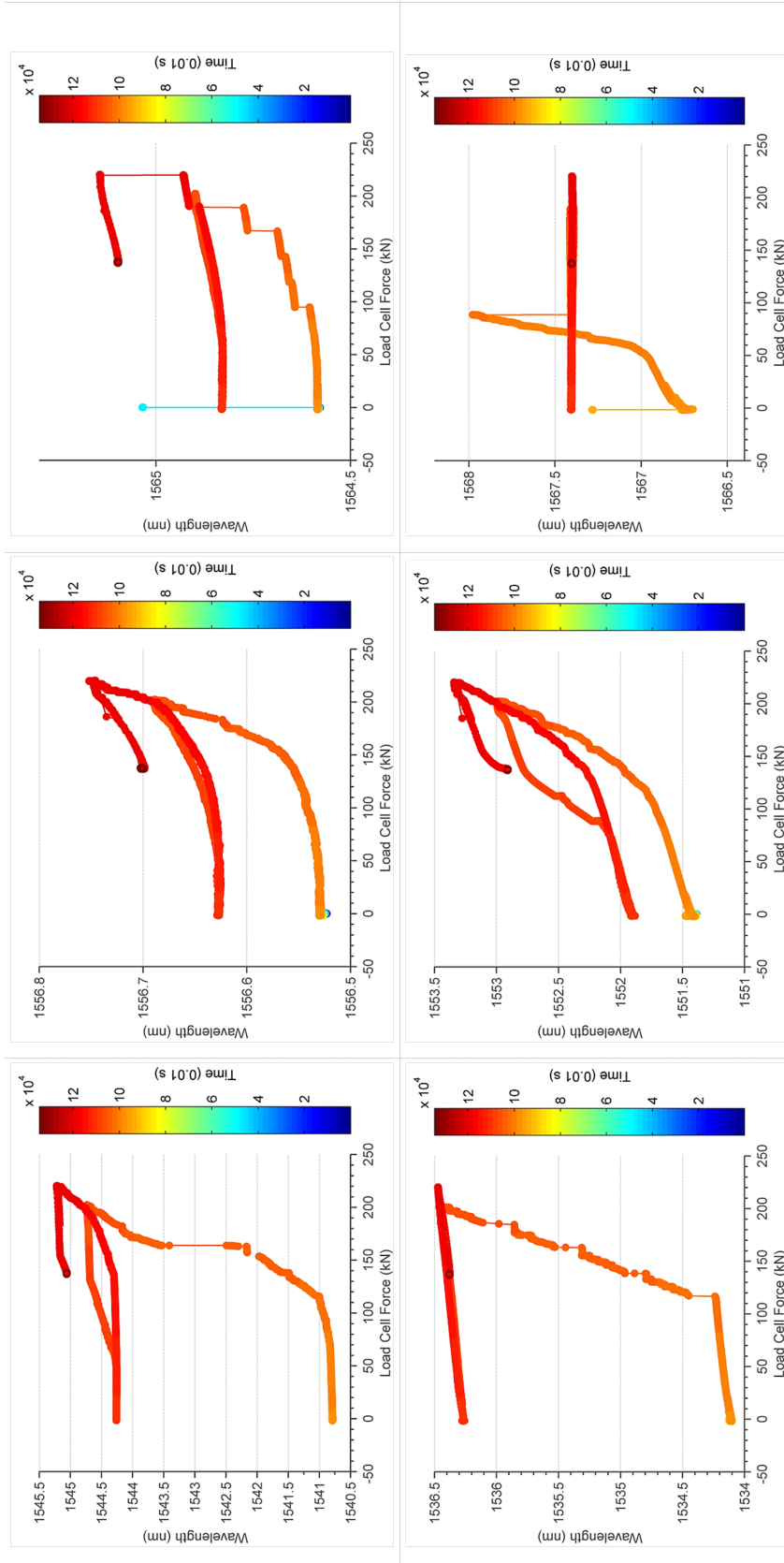


Fig. A.1 Strand 1 (bent duct) calibration graphs. The wavelength from all sensors was plotted against the live end load cell. The temperature (top) and strain (bottom) sensor attached in the same place on the tendon are in line with each other. Data from the calibration cycle and final stress with wedges in the barrels is shown. The colour gradient bar shows increasing time; therefore the colour corresponding to the shortest time shows the start of the calibration cycle.

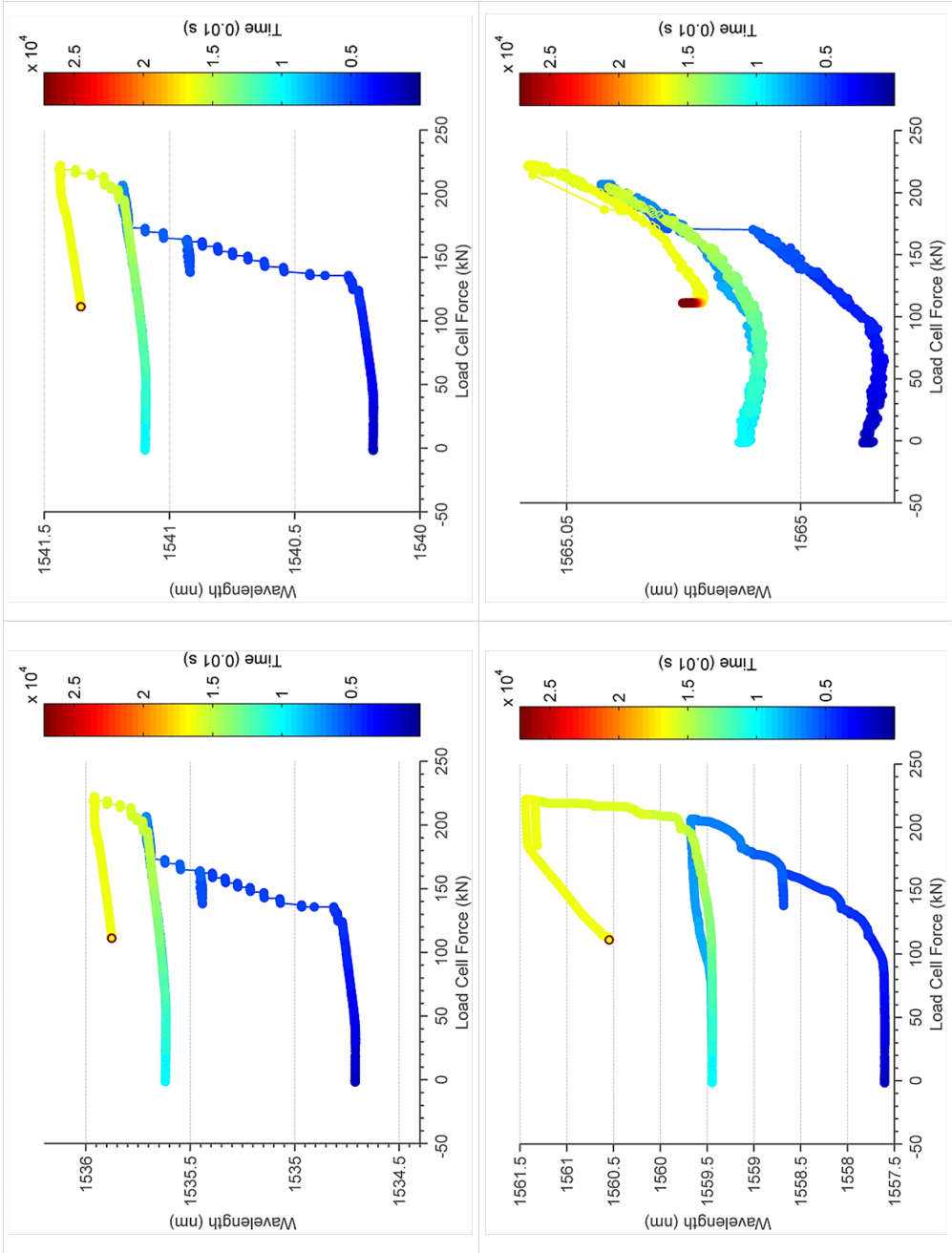


Fig. A.2 Strand 2 (bent duct) calibration graphs. The wavelength from all sensors was plotted against the live end load cell. Data from the calibration cycle and final stress with wedges in the barrels is shown. The colour gradient bar shows increasing time; therefore the colour corresponding to the shortest time shows the start of the calibration cycle. For this particular strand the strain sensor fibre line was broken at the beginning of the calibration cycle, therefore it was not possible to interrogate the strain sensors.

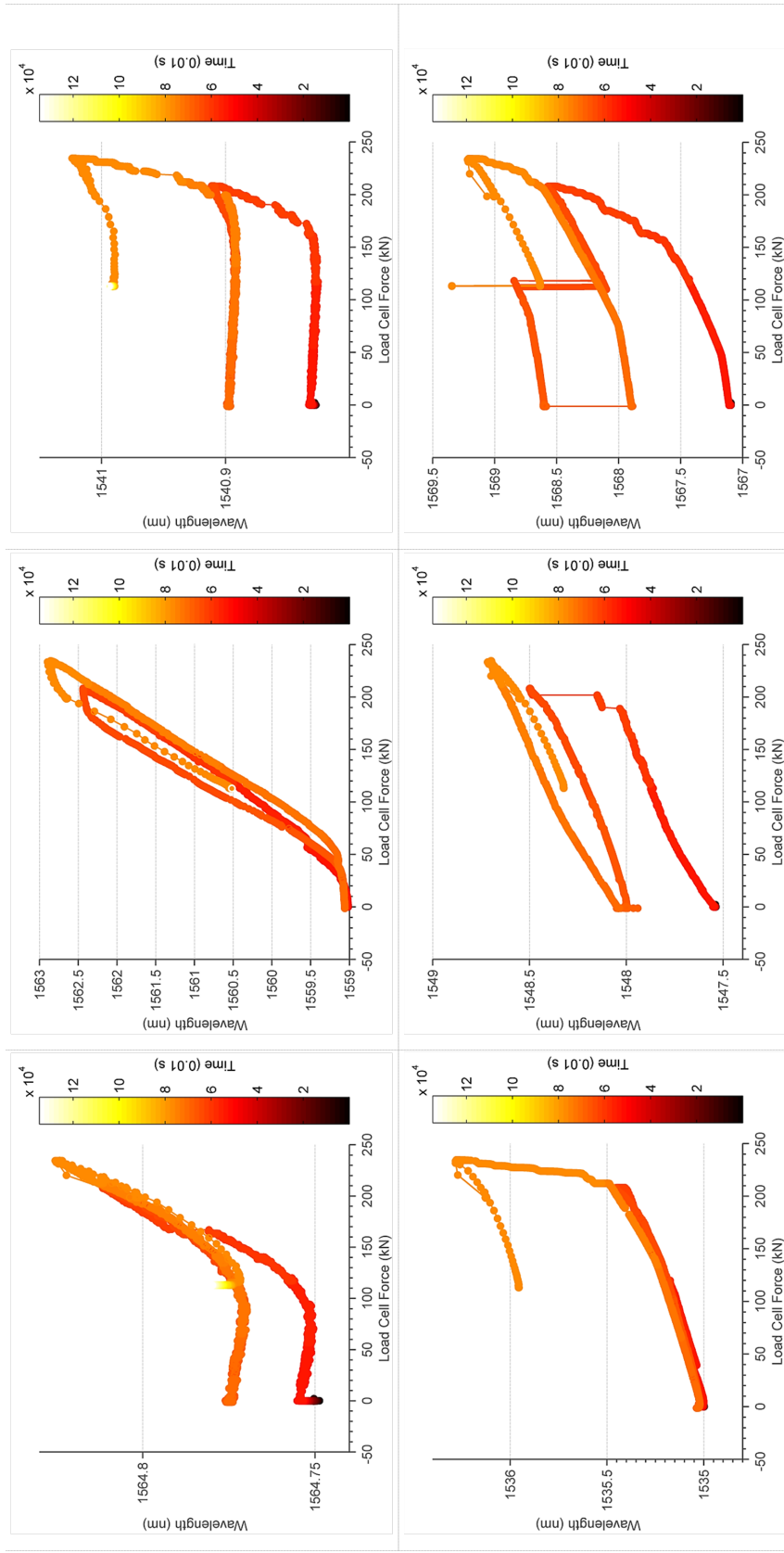


Fig. A.3 Strand 3 (straight duct) calibration graphs. The wavelength from all sensors was plotted against the live end load cell. The temperature (top) and strain (bottom) sensor attached in the same place on the tendon are in line with each other. Data from the calibration cycle and final stress with wedges in the barrels is shown. The colour gradient bar shows increasing time; therefore the colour corresponding to the shortest time shows the start of the calibration cycle.

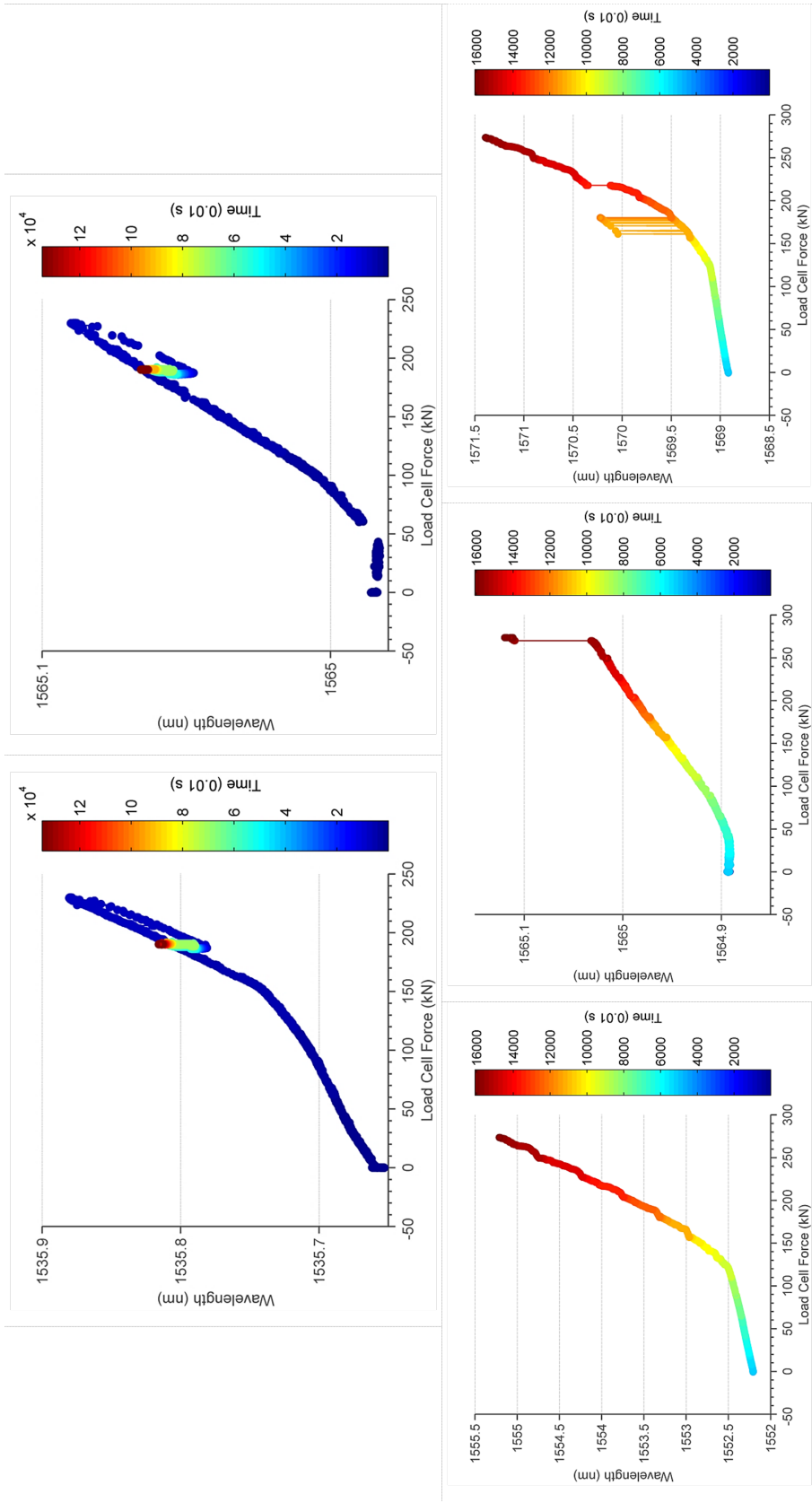


Fig. A.4 Strand 4 (straight duct) calibration graphs. Bottom row shows sensors (two strain sensors left and right, one temperature sensor middle) recorded during the first half of the calibration cycle. After reaching the maximum force the fibre line interrogating the sensors broke. The two sensors on the top row (strain sensor left and temperature sensor right) were interrogated from the opposite end of the concrete beam for the final stressing. The wedge draw in can be seen on the top two sensors, after this their wavelength increases while the load cell force remains the same. This is due to an increasing temperature was seen on other unstressed (at this point) sensors.

